INSTITUTE OF PHYSICAL CHEMISTRY
POLISH ACADEMY OF SCIENCES

Maciej Zieliński

Structure dynamics of heterogeneous catalysts based on nanocrystalline gold in oxidation-reduction (REDOX) reactions

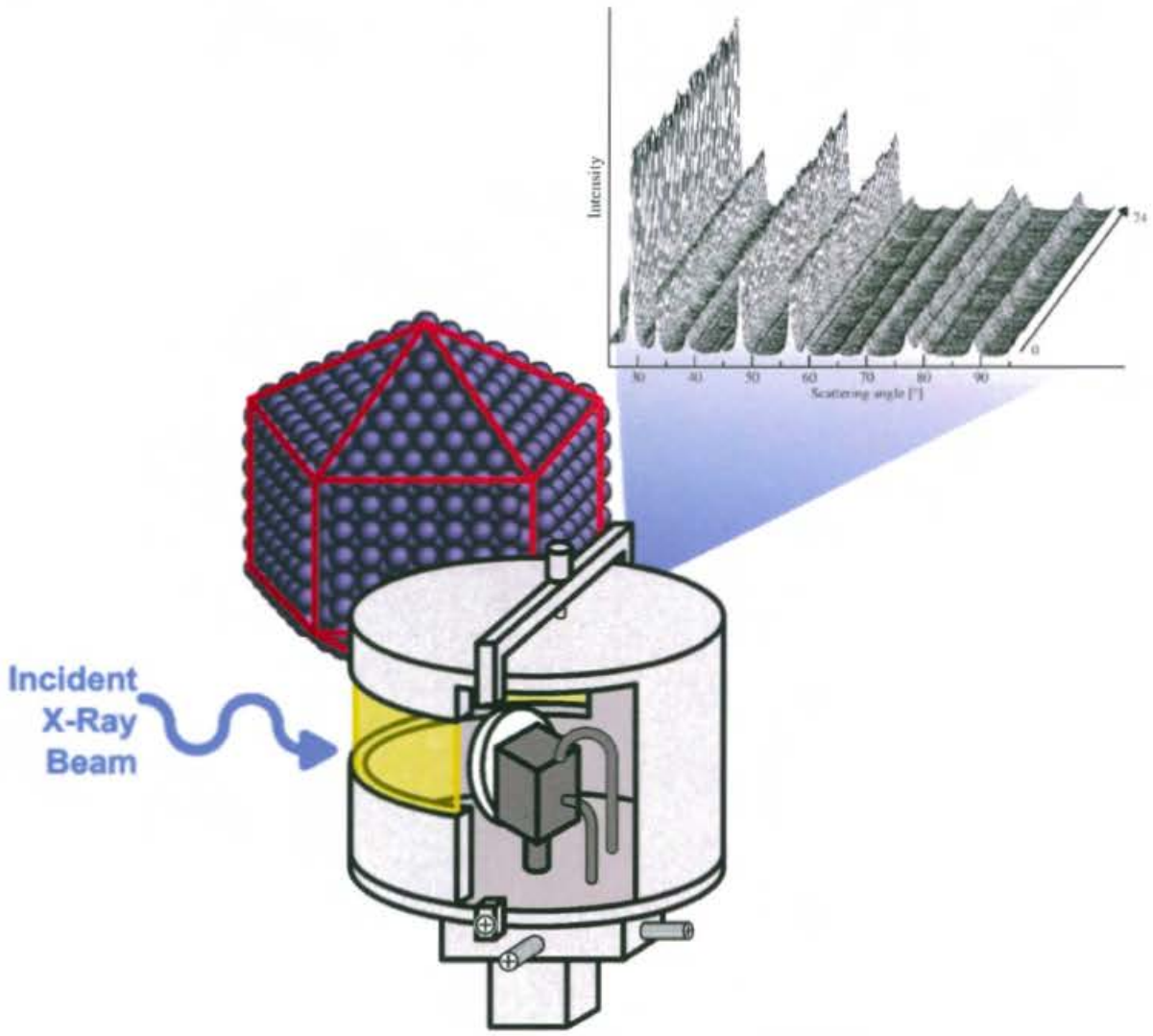

INSTITUTE OF PHYSICAL CHEMISTRY
POLISH ACADEMY OF SCIENCES

PhD Thesis

Structure dynamics of heterogeneous catalysts based on nanocrystalline gold in oxidation-reduction (REDOX) reactions

Maciej Zieliński, MSc. Eng.

Supervisor:
Zbigniew Kaszkur, PhD., DSc., Assoc. Prof. IPC PAS

Doctoral dissertation prepared within International Doctoral Studies
of the Institute of Physical Chemistry Polish Academy of Sciences
Kasprzaka 44/52, 01–224 Warszawa, Poland

July 2019
WARSZAWA

This research and author of this Thesis have been financially supported by:

- National Science Centre of Poland
  within the framework of OPUS 7 grant, no.: 2014/13/B/ST4/04619,
  and ETIUDA 5 scholarship, no. 2017/24/T/ST4/00194;
- German Academic Exchange Service (Deutscher Akademischer Austauschdienst, DAAD) with Forschungsstipendien – Kurzstipendien 2017 scholarship, agreement no. (PKZ): 91676919.

in-operando Transmission Electron Microscopy (TEM) studies were performed in close cooperation with Operando Electron Microscopy Group at the Fritz-Haber Institute of the Max-Planck Society, Faradayweg 4, 14195, Berlin, Germany.

Part of the *ex-situ* (TEM) examinations were performed thanks to access to the electron microscope provided by the Advanced Electron Microscopy and Nanostructures Group being part of Quantum Materials and Phenomena Laboratory, 10 rue Alice Domon et Leonie Duquet, F-75205, Paris, France, which is a joint research unit of University Paris Diderot and French National Centre for Scientific Research (CNRS).

The author of this thesis is deeply grateful for the engagement in this research.

Dedicated to my Wife

Her patience
and all kinds of support
were priceless,

who made this work possible.

Structure dynamics of heterogeneous catalysts based on nanocrystalline gold in oxidation-reduction (REDOX) reactions

Maciej Zieliński
Supervisor: Zbigniew Kaszkur, PhD., DSc., Assoc. Prof. IPC PAS

Introduction

The **main scope** of this research was to **study the dynamic structure changes of the surface of heterogeneous** catalysts containing supported nanocrystalline gold as their active component. Two model reactions were selected: stoichiometric oxidation of carbon monoxide (CO) by the molecular oxygen (O_2) (abbrev. sCOOX) and preferential oxidation of CO in the presence of H_2 (abbrev. PROX). Gold catalysts themselves are promising materials e.g. in the fuel cell industry for purification of hydrogen stream from CO, which contaminates the components of cells and decreases their efficiency.

The primary experimental technique used was the ***in-operando*** **Nanocrystalline X-Ray Diffraction (NXRD)** which was based on Powder X-Ray Diffraction (PXRD) coupled with Mass Spectrometry (MS) and a customised measurement strategy was applied. Furthermore, the ***in-operando*** **Transmission Electron Microscopy (TEM)** was also employed as a complementary technique. In this way, the research was focused specifically on **investigation of crystal structures evolution under working conditions of the catalysts**. Both experimental approaches were the world's newest methods able to address the question of the role of the heterogeneous catalyst surface in the chemical reaction mechanism.

Basic concepts

Catalysts facilitate chemical reactions to run under milder conditions or favour desired products if competing ones can be formed. It is the surface of the heterogenous solid catalyst that takes part in the reaction with gaseous reagents, so the gas molecules need first to adsorb on this surface. The assumed **hypothesis** suggested that **the interaction with adsorbents results in immediate perturbation of the initially relaxed structure of the surface**. PXRD and TEM are particularly suitable for detection of even little changes of the crystal lattice. The surface needs to adapt to the new electronic and energetic circumstances in order to dissipate the emerging energy excess. After the final products have been formed, these products desorb and the catalyst surface recovers its pristine configuration. The whole path is cyclically repeated, but the catalyst does not deteriorate in time.

In the case of nanocrystals, the surface constitutes a large fraction of the whole particle structure. Consequently, **any change occurring at the surface affects the bulk part of the particle as well**. Hence, tracking of the surface structure evolution was equally possible at the atomic level and through the averaged phenomena of X-Ray and electron diffraction.

Overview of the results

Three catalysts containing gold nanoparticles (AuNPs) deposited on different supports: cerium (IV) oxide (ceria, 9.4%$_{wt.}$ Au/CeO_2), silica (7.16%$_{wt.}$ Au/SiO_2) and carbon (20%$_{wt.}$ Au/C), were selected as the objects of interest for this research. The most remarkable results were obtained for **ceria decorated with AuNPs**. It was **the most efficient catalyst** reaching over 80% conversion of CO to CO_2 with high selectivity against water (H_2O) production (in PROX reaction). It was concluded that **ceria provided its extended surface for adsorption of CO and storage of activated oxygen moieties**. **AuNPs**, or their perimeter at the interphase with ceria, **were crucial for the CO_2 production** as pure CeO_2 remained inactive under the same reaction conditions. Moreover, **gold facilitated adsorption of reductive molecules (e.g. hydrogen, H_2) on ceria and, thus, induced the redistribution of oxygen vacancies inside the ceria nanocrystals**. Bare CeO_2 was unaffected by the hydrogen atmosphere at ~150°C, while in the presence of gold the structure of ceria slightly expanded. It corresponded to the appearance of higher number of Ce^{3+} ions in the CeO_{2-x} particle core.

The Au/SiO_2 and Au/C catalysts were observed to be much less active in the sCOOX and PROX reactions. The **reactivity of the silica-supported one strongly depended on the content of water vapour** in the gas atmosphere. The comparison of the metal-support interactions (MSI) between the reducible semiconducting CeO_2 and non-reducible insulating SiO_2 inspired conclusions on the reaction mechanism. **The Au/C catalyst served as the reference** of the catalytic activity of the bare gold nanocrystals.

The electron microscopy studies strongly implied that, although the imaging conditions were carefully chosen and did not influence the chemical activity results, the electron beam altered the irradiated sample electronic structure – additional part of Ce^{4+} ions in ceria were most probably reduced temporarily to Ce^{3+}. This phenomenon has to be considered in detail in the future.

Conclusions

This fundamental research showed that the *in-operando* NXRD and TEM techniques are powerful tools for investigation of the catalysts working mechanism. Thorough studies of three catalysts samples resulted in particularly interesting conclusions concerning the catalytic CO oxidation reaction mechanism and the challenges accompanying application of new research techniques.

Table of contents

1. Introduction

1.1. Basic concepts and background

This research focused on dynamic changes of the structure of solids influenced by interactions with the gas phase. The solid materials of interest were catalysts. The subject of the studies was the investigation of the surface interactions by tracking cyclic changes of the whole structure of the catalyst.

The phenomenon of *catalysis* is known for long. One of the first scientists who started to propagate the idea of *catalysis* was Swedish J. J. Berzelius in 1836. In general, catalysts facilitate chemical reaction to run under milder conditions or favour desired products if competitive compounds can be formed. It is possible, because the catalyst taking part in the reaction decreases the activation energy of selected reaction steps and, thus, directs the course of whole reaction. Although the catalyst must be involved in the reaction (otherwise its presence would not take any effect), it is not used, but is recovered, and can go through another reaction cycle. The role of the catalyst is to help formation of appropriate intermediate products and to release the desired products at the right moment.

The catalysts investigated in this work were solids, while the reagents were in the gaseous phase, hence they were the *heterogeneous* type of catalysts. Their active component were gold crystals of nanometric size. Three catalysts were studied – each was based on different support: cerium (IV) oxide, silicon (IV) dioxide and carbon. The first one will be referred to also as cerium dioxide, ceric oxide and ceria. The second will be frequently called “silica”. All supports played important role in the reaction mechanism, but their most basic task was to support gold nanocrystals and to separate them from each other.

The choice of the active component shall be shortly described. Gold which is the most noble metal is rather unreactive in the bulk state. Gold oxides are unstable compounds – the Gibbs enthalpy of formation of Au_2O_3 is +53.3 kJ · mol^{-1} [1] and it decomposes under ambient conditions. The melting temperature of gold, 1063°C, is relatively low. These two reasons, together with its amazing yellow colour, make gold a perfect material for jewellery production – it is easy to process and chemically stable for long time. The excellent electric current conductivity of gold allowed production of thin electrical connections resistant against corrosion.

The physical and chemical properties of gold differ substantially from its neighbours in the periodic table of elements. The relativistic effects are particularly noticeable in the case of gold. The electron shells are contracted. Consequently, the whole atom size is smaller and density of gold is assessed to gain about 20 % comparing with the general trend among similar elements. The reason for that is the high mass of the nucleus and the ratio of protons to neutron inside it. The electrons from the *1s* shell reach higher velocities which leads to the increase in their masses and stronger attraction to the nucleus. The electrons from higher shells are affected accordingly. The valence *5d* band is slightly destabilised [2] while the *s* and *p* bands are diffused [3]. Adsorption of gases on the surface of gold is very ineffective disabling gold to form stable bonds (chemisorption). Furthermore, physical adsorption is even weaker so that it is sometimes neglected at all [4].

The situation changes when the gold crystal size is decreased to nanometres. With the diminishing particle diameter several properties of bulk gold are totally altered [5]. The Au–Au bonds shorten. The average coordination number (CN) decreases, because the not-fully coordinated atoms at the surface become the more substantial fraction in the overall number of atoms building the particle. The partially coordinated surface atoms of gold generate some energy excess in the particle and, as a result, they become chemically active species and are eager to react. The chemical properties of gold nanocrystals are strongly dependent on the support used to prepare the catalyst: its basicity, reducibility, electric conductivity, charge transfer properties etc. Hence, the choice of supports cannot be random. Ceria is considered to be an easily reducible, semiconductive compound (band gap 3.19 eV [6]) with relatively high isoelectric point (~5) and huge oxygen storage capabilities [7, 8, 9]. Silica is also an oxide support, with isoelectric point ~2 [4] and highly insulating one [10, 11]. Carbon cannot supply oxygen and is believed not to affect chemically gold nanoparticles.

There were two test reactions selected for studies of the catalysts properties and working mechanisms:

a) stoichiometric oxidation of carbon monoxide (carbon (II) oxide, CO) with oxygen (abbreviated to sCOOX):

$$\mathbf{2\,CO + O_2 \rightarrow 2\,CO_2} \qquad (1)$$

b) preferential oxidation (PROX) of carbon monoxide in the presence of H_2 when H_2O formation is a competitive reaction.

Conversion of CO to CO_2 is a simple well-understood reaction, so the efforts could be focused on the investigation of the catalysts themselves. sCOOX is a highly exothermic reaction, $\Delta H^{298K} = -283\ kJ \cdot mol_{co}^{-1}$ [12], first carried out with the aid of the gold catalyst by Haruta in 1987 [13]. Kinetics of this reaction, when performed by means of catalysis, is a complex function of many parameters, but it is believed that the reaction rate is 0^{th} order with respect to CO and O_2 when their pressures are above 4 and 10 Torr or the content above 0.5 % and 1 $\%_{vol}$, respectively [14]. Apart from being a very convenient test reaction, CO oxidation is employed in industrial processes, like exhaust gases purification as well as in the developing branch of fuel cells. Catalysts used for hydrogen dissociation are very sensitive to CO contamination in the hydrogen stream (hence PROX reaction is studied) [15, 16].

1.2. Nanocrystalline gold

Nanocrystalline gold supported on an appropriate material is able to yield high selective conversion of CO to CO_2. The already mentioned strong dependence of gold catalytic activity on the used support suggests Mars–van Krevelen reaction mechanism [17] and there is plentiful evidence supporting this idea in the literature [18, 19, 20]. The Mars–van Krevelen mechanism applies to a two-molecule reaction. One of the molecules adsorbs on the metal nanocrystal and the other on the surface of the support, but close to the interface between them. Then the activated molecules recombine to form products. In such case, the support plays a significant role in the reaction mechanism and, thus, determine the selectivity and the overall performance of the catalyst.

Some mechanisms addressing the observed nanocrystalline gold catalytic activity have been already described. The issue that draws attention is the lack of thorough explanation of active role and behaviour of the catalyst surface, while high surface area is regarded as crucial for high selectivity and yield of the reaction. The properties are usually correlated to nanometric size of gold crystals and sometimes to interaction between gold and its support. The reported critical features include:

a) the gold nanocrystals huge surface to volume ratio [21];
b) the presence of the large number of low–coordinated Au atoms that build the crystal walls and are located in the corners and on the edges, where the adsorption is found to be stronger [22, 23, 24, 25, 26];
c) the presence of electrically charged nanocrystals due to the charge transfer occurring between the support and the metal crystals (MSI or PSI – for particles) or due to the ions bound to the crystals' surface (originating e.g. from gold salts used as precursors of the nanocrystals during the synthesis) [27, 28];
d) well–developed nanocrystal–support interface which serves as a preferential active site of the catalyst [2, 29];
e) quantum effects of size, that can lead even to the loss of metallic properties of sufficiently small Au particles [30, 31].

It is significant that, apart from quantum size effects, other features are not exclusively specific to nanocrystals. Here originates the reason why it is worth to focus on the surface itself and study interaction between the catalyst and reaction environment.

To start with, the expected experimental results should be evaluated. The crystal structure of nanomaterials, although resembles the structure of the bulk, differs significantly from the big crystals, because of the presence of the large surface, which can be neglected in other cases. The surface of the crystal is sometimes approached to as the natural defect of all grains accumulating energy. The surface energy excess has to be dissipated and the inner part of the nanocrystal structure is the only recipient of this energy. Surface relaxation of metals leads to shrinkage of the nanocrystals. As a result, the Apparent Lattice Parameter (ALP) [32], as the experimentally observed elementary cell dimension is frequently called, is decreased and this change is detectable [33]. It is a general observation that ALP of metals becomes smaller with the decreasing size, e.g. [5, 34].

The relaxed state of the surface is disturbed during interactions with adsorbates that come close enough to donate their electron cloud or accept the electron cloud from the surface. In catalysis, the reaction mechanism usually involved the, so called, activation step which requires weakening of the molecular bond in the adsorbed molecule. Heterogeneous catalyst act through its surface, so the activation or excitation of the adsorbate will inevitably affect the surface electronic and energetic state. The catalyst particles need to adapt to the new circumstances, thus yielding a change of the whole structure, similarly as it was in the case of surface energy excess relaxation caused by the limited size of the crystal grain. After the adsorbed reaction reagents recombine to products and these desorb, the surface and the whole structure relax again in order to recover its initial state. This oscillating structural behaviour is the essential phenomenon studied in the *in-operando* PXRD experiment that is specially designed for examination of the sample under working conditions.

1.3. *in-operando* Powder X-Ray Diffraction

X-Ray radiation is the electromagnetic wave of length λ between 0.01 nm and 10 nm. The corresponding photon energies are in the range approx. 125 – 0.125 keV (as energy is inversely proportional to wavelength). X-Rays interact with matter, essentially with electrons, either elastically (X-Rays energy is preserved) or inelastically (loss of X-Rays energy occurs). The latter type of interactions can be observed as Compton scattering (energy is transferred to the electron thus increasing its momentum) or fluorescence, which has been covered in Section 1.8.

1.3.1. Elastic scattering of X-Rays

Elastic interaction of X-Rays with electrons cause the electrons to oscillate with the same frequency as the frequency of the X-Ray waves. Therefore, each scattering object becomes the point source of a secondary X-Ray wave. This phenomenon is called Rayleigh scattering. An ordered array of scattering objects emits waves that interfere constructively with each other creating waves propagating only at specific angles with regard to the plane of scatterers. Interference in other directions is destructive and the waves are quenched.

This special kind of scattering is called diffraction. Laue equations relate the incident wave with the diffracted ones [35]. Imagine a periodic lattice of scattering objects. Let these objects be located in space so that their positions can be obtained by integer combination of primitive vectors – $\vec{a}$, $\vec{b}$, $\vec{c}$ – describing the lattice unit cell. If the incident wave vector is $|\overrightarrow{s_i}| = \frac{1}{\lambda}$ and the diffracted wave vector is $\overrightarrow{s_d}$ (with the same magnitude $\frac{1}{\lambda}$), the scattering vector $\Delta\vec{s} = \overrightarrow{s_d} - \overrightarrow{s_i}$ must satisfy the following conditions:

$$\vec{a} \cdot \Delta\vec{s} = h \tag{2}$$

$$\vec{b} \cdot \Delta\vec{s} = k \tag{3}$$

$$\vec{c} \cdot \Delta\vec{s} = l \tag{4}$$

where *h, k, l* must be integer numbers. There is an infinite number of *h, k, l* sets that fulfil the equations 2 – 4 The interpretation of these numbers is that they describe the three nodes of the periodic lattice defining a plane of scattering objects from which the incident wave seems to be simply reflected as light does from the mirror. The descriptors of this plane, thus also the *h, k, l* numbers, are called Miller indices. If these *h, k, l* sets are plotted in 3D space, the, so called, reciprocal lattice is formed. The reciprocal lattice (or space) is set on reciprocal vectors $\vec{a}^*$, $\vec{b}^*$, $\vec{c}^*$. The first reciprocal vector is defined according to equation 5 and the rest are defined analogously. The name "reciprocal" reflects well the general concept of this space where distances are measured in inverse length units (e.g. nm^{-1}) and the sizes of objects are inverted: if something is big in the real world, it is small in the reciprocal space; something long turns to something short; a plane becomes a point etc.

$$\vec{a}^* = \frac{\vec{b}\times\vec{c}}{V} = \frac{\vec{b}\times\vec{c}}{(\vec{a}\times\vec{b})\cdot\vec{c}} \tag{5}$$

The special case of Laue equations is the Bragg condition [35], sometimes called – from historical point of view more appropriately – Braggs' law as it was proposed by Lawrence Bragg and his father William Henry Bragg. It applies especially to diffraction on crystals. The crystal lattice is certainly an ordered array of scattering objects – atoms or ions. Crystal structure is periodical and it has translational symmetry. The basic building block is the elementary cell (also "unit cell") which contain all symmetry operations in it and the whole crystal structure can be reproduced just by replication of the elementary cell. Distance between atoms and the elementary cell dimensions are in the range of a few to several angstroms, so X-Ray radiation produced e.g. by electron bombardment of copper ($\lambda_{Cu\ K\alpha 1}$ = 1.54056 Å), is perfect for studies of crystalline matter.

The Bragg condition (equation 6) states that a set of equally spaced planes of atoms arranged in the same way irradiated by the incoming radiation at the θ angle will yield the 1st order constructive interference of diffracted waves at the θ angle with respect to the plane (and at the 2θ angle regarding the incident wave propagation direction).

$$n\,\lambda = 2\,d\sin\theta \tag{6}$$

where:

λ – wavelength of X-Rays;
d – interplanar spacing;
θ – incident and diffraction angle with respect to the plane surface;
n – integer number referred to as the "order of diffraction".

The distance d between the planes in the crystal correlates with the dimensions and geometry of the elementary cell, and the arrangement of atoms inside the cell:

$$\frac{1}{d_{hkl}^2} = (h\vec{a}^* + k\vec{b}^* + l\vec{c}^*)\cdot(h\vec{a}^* + k\vec{b}^* + l\vec{c}^*) \tag{7}$$

Equation 7 reduces for the face-centred cubic (FCC) system ($Fm\bar{3}m$ space group no. 225) of gold and cerium (IV) oxide equation 8, because $a = b = c$ and α, β, γ angles between unit cell edges equal all to 90°:

$$\frac{1}{d_{hkl}^2} = \frac{h^2+k^2+l^2}{a^2} \tag{8}$$

The same (*h k l*) plane appears in each unit cell and spreads far outside the volume of the particular cell, so it is also present in some other cells. Such set of (*h k l*) planes cross the *a*, *b* and *c* edges of each unit cell so that these edges are divided in *h*, *k* and *l* sections, respectively.

1.3.2. Powder diffraction pattern

A diffraction pattern (DP) is the distribution of the scattered intensity over the projection of the reciprocal space recorded by the detector. The scattering angle 2θ in the real experiment is limited to less than 180° being the maximum angle between the incident and scattered waves. 2θ = 180° scattering angle would mean perfect back scattering heading precisely the source of X-Rays. Hence, from the crystal irradiated by the incident X-Ray beam only the limited number of diffracted beams, traditionally called also "reflections", can be acquired. This limit is set by the Ewald sphere [35]. It is a sphere in

the reciprocal space and it has the radius of $\frac{1}{\lambda}$, so the size of Ewald sphere is determined by the wavelength of the incident X-Ray beam. Only the reflections originating from (*h k l*) planes represented by the spots inside the sphere can be experimentally observed.

Diffraction from a single crystal results in a discrete diffraction pattern containing spots. A polycrystalline powder sample consists of huge number of very small crystals – of micrometric or even nanometric size. Each of the illuminated crystals diffracts on its own and, thus, contribute to the DP formation. The Bragg law has to be obeyed, so each of the diffraction crystal produces a reflection according to its orientation in space with respect to the incoming beam. The discrete array of spots changes into the set of rings all centred around one point – the trace of the incident beam (although this spot is rarely experimentally recorded, because of high intensity of this beam, quick saturation of detector and potential risk of detectors damage). These rings actually represent the cross section of the surface of the detector with the Debye–Scherrer diffraction cone formed by all beams diffracted from appropriately oriented crystals in the powder sample.

Depending on whether a 2D surface detector or a 1D point or strip detector is used, the raw diffraction pattern will be a 3D appropriately scaled image of the Debye–Scherrer rings and their intensities or a 2D plot of the scattered beam intensity against the scattering angle. In the former case, the pattern is azimuthally averaged to also obtain the intensity profile as a function of the scattering angle.

The way X-Rays diffract on the crystalline powder sample and, consequently, the crystal structure of the sample are represented in the DP as peaks on the intensity profile. The information about the crystal structure of the sample is hidden in the diffraction peaks positions, their relative area (integrated intensity) and their shape (particularly Full Width at Half Maximum, FWHM, and peak's asymmetry with respect to the peak's top are useful parameters).

The *in-operando* studies of crystal structure dynamics are based on tracking changes of the parameters describing diffraction peaks under the set environment conditions – in the case of this research the temperature of the sample and the composition of the gas atmosphere were controlled. Because of the nanocrystalline character of the catalysts (both the active component, gold nanoparticles, and the supports), the diffraction peaks were substantially broadened, i.e. their FWHM was much higher than the device–related broadening of ~0.1°, and slightly asymmetric. These features indicated a broad distribution of elementary cell dimensions and interplanar spacings. The variation of these quantities resulted from differences in the surface relaxation of crystals of different size and, of course, were influenced by the provided gas environment. Therefore, the suitable term to describe the general observations is the Apparent Lattice Parameter (ALP) proposed by Palosz [32]. For nanocrystals the values of ALP determined from different reflections can differ as Kaszkur showed on the model DP computed following the Debye summation formula (equation 30 on page 49) [36].

As can be concluded from equations 6 and 8 (page 17), for the FCC structure, the position of each and every diffraction peak (i.e. the scattering angle for which the highest intensity is observed) can be recalculated to the apparent interplanar distance and then to ALP. The ALP values result from statistical analysis of a series of reflection measurements and standard deviation of these values corresponds to the precision of establishing the ALP (not to absolute accuracy). The relative changes of the ALP originating from the real

changes in the crystal structure are rather insensitive to systematic diffractometer errors, because the errors are repeatable and affect each collected diffraction pattern in the same way. Thus, the ALP values can be used to monitor the evolution of the crystal structure under *in-operando* conditions. The subject of this research was to study surface phenomena, so it is a crucial aspect to establish how the changes occurring at the surface of the nanocrystals affect the parameters describing the diffraction peaks, especially the ALP.

1.4. Contribution of nanocrystal's surface and core to scattering of X–Rays

A simple theoretical experiment was performed to show the contribution of the surface and the core of the nanocrystal to the diffraction pattern profile. The model nanoparticle was the ideal cuboctahedron made of 1415 atoms of palladium out of which the outer layers containing the total of 708 atoms were considered as the surface single-layer of the nanocrystal (also called "its shell") and the remaining 707 constituted the core. In both parts the Pd atoms arrangement agreed with the FCC structure.

Two models were built. In the first one, the core was based on an FCC unit cell with a_{core} = 3.90 Å, while the surface part had the lattice parameter a_{shell} = 3.89 Å. The second model had inversed core-shell properties. Both models were constructed in the Cluster program [37] described in detail in Section 2.6. The interatomic interactions in the core and the shell (surface) followed the Sutton-Chen n-body potential approach [38]. The only difference in potentials describing each part of the nanocrystals was the elementary

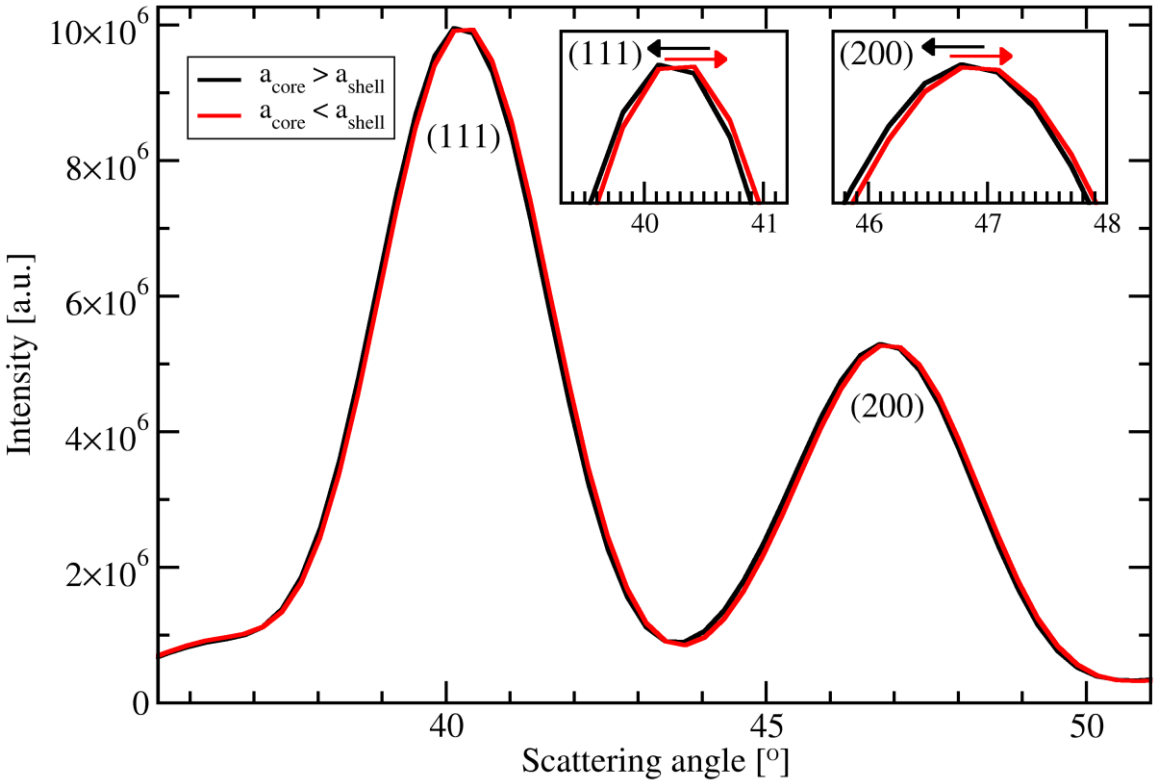

Fig. 1. The diffraction patterns of the relaxed (energetically minimised) cuboctahedral core–shell nanocrystals containing 1415 Pd atoms simulated in the Cluster program (see Section 2.6). The black curve represents nanoparticles, in which the core was based on 707 Pd atoms ordered in the FCC structure with unit cell parameter a = 3.90 Å, while the shell (corresponding to the surface layers of the particles) was made of 708 FCC-structured Pd atoms with a = 3.89 Å. The red curve represents nanocrystals with inverted core-shell properties.

cell constant a, as mentioned earlier. The interaction potential between Pd_{core} - Pd_{shell} corresponded to the reference palladium crystal structure (a = 3.89 Å). The crystal structures of both models were relaxed, i.e. energetically minimised.

The calculated diffraction patterns (Fig. 1) showed that the diffraction peaks were shifted to lower or higher scattering angles following the bigger ($a_{core} > a_{shell}$) or smaller ($a_{core} < a_{shell}$) lattice parameter of the core than.

This example clearly showed that the bulk part of the crystals influences more the diffracted intensity profile than the surface, although the numbers of scattering objects in the core and the shell were the same. Hence, the surface phenomena must involve deeper parts of the nanocrystal structure to make the effect visible in the experimental diffraction pattern. Similarly, the redistribution of the defects, initially formed on the surface, towards the inner parts of the particle will take bigger effect on the DP than accumulation of these defects near the surface.

The real case of the dependence of the diffraction peak position on the properties of the nanoparticle core was presented by Kaszkur in his studies of Pd-Ag alloyed nanocrystals [39]. When exposed to CO atmosphere, Pd atoms occupied the surface and the particle core was enriched with silver. The result was the shift of the diffraction peak to lower scattering angles, so it resembled more the scattering from pure silver. Under inert helium (He) environment the segregation was inverted and the surface consisted mostly of silver. Hence, the reflection moves to higher scattering angles because of the Pd-rich core. The phenomenon has been illustrated in Fig. 2.

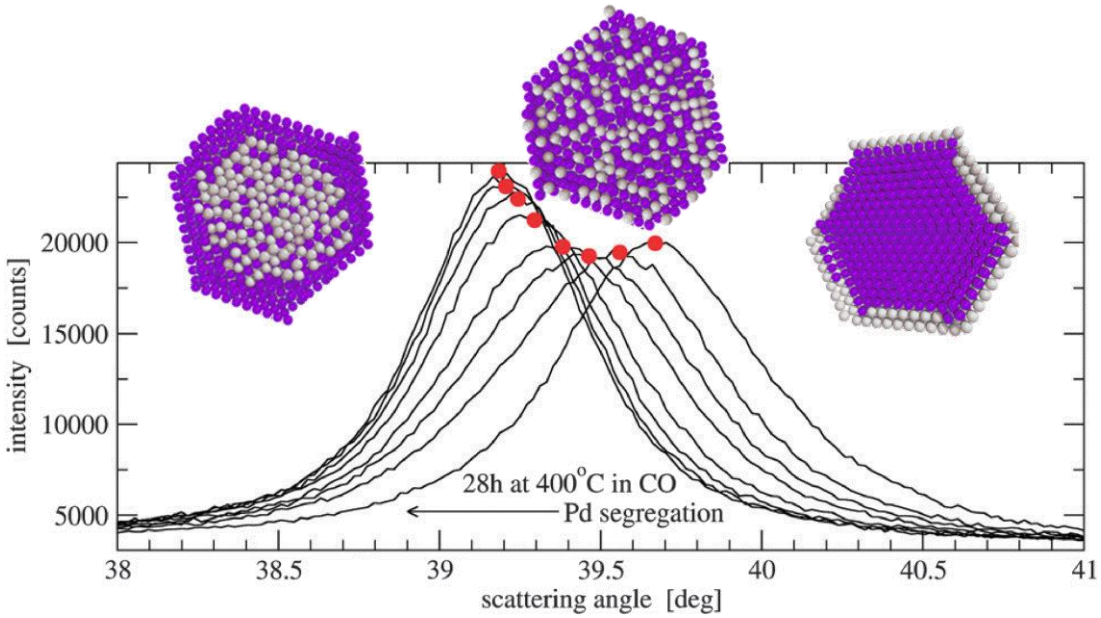

Fig. 2. The evolution of the (1 1 1) diffraction peak of the Pd-Ag alloyed nanoparticles during Pd segregation in the CO gas atmosphere. Initially, the sample was kept under helium.

The properties of the core of a single-domain FCC-structured nanocrystal are not the only factors influencing the intensity profile in the diffraction pattern. Metal nanoparticles can also crystallize as Multiply Twinned Particles (MTP). Out of all available MTPs shapes, the ones containing 5-fold symmetry axes are of special interest of the scientific community. They are frequently found in different nanometallic samples. Their structure and properties are extensively studied [40, 41, 42, 43, 44, 45]. Section 1.5 covers the topic of the structure and diffraction of X-Rays on MTPs.

1.5. Minimum energy shape of gold clusters and nanocrystals

The natural tendency of solid materials is to minimise the surface energy of its particles, crystals and clusters. For metals which have FCC crystal structure a typical low energy cluster shapes considered in literature are cuboctahedron and icosahedron. The cuboctahedra are formed through surrounding a single central atom by consecutive shells of closest neighbours according to FCC lattice symmetry.

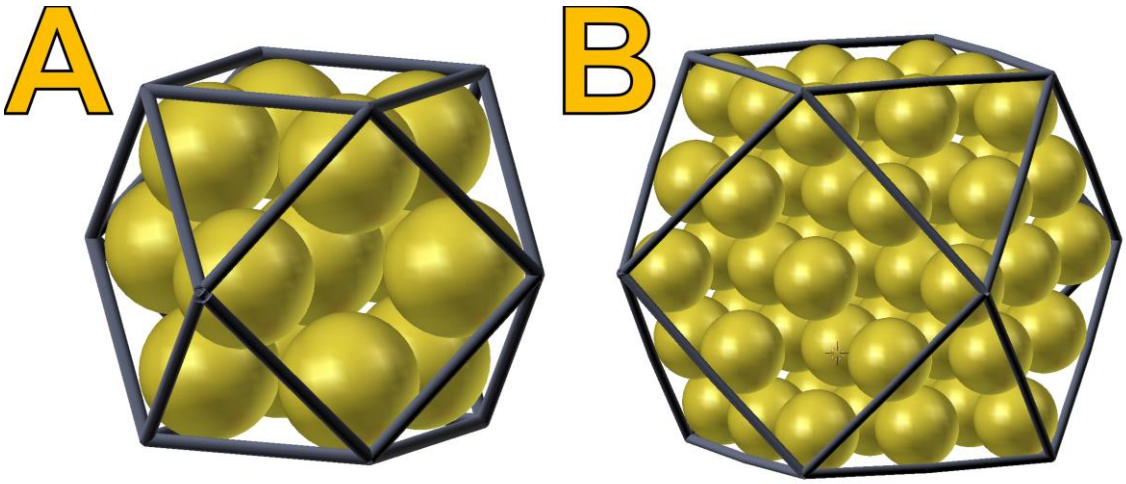

Fig. 3. The models atomic arrangement in 2 smallest FCC cuboctahedral gold nanocrystals containing 13 (A) and 55 (B) atoms.

Fig. 3.A and B show atomic arrangement for gold cuboctahedra consisting of 13 and 55 atoms, respectively. They form a characteristic shape of a cube with cut-off corners. The energy per atom decreases with the growing size of cuboctahedron (from $-3.205\frac{\mathrm{eV}}{\mathrm{atom}}$ for a 13-atom, then $-3.428\frac{\mathrm{eV}}{\mathrm{atom}}$ for 55-atom, to $-3.780\frac{\mathrm{eV}}{\mathrm{atom}}$ for bulk Au following the Sutton–Chen n–body potential scheme [38]. The total numbers of atoms in series of cubooctahedra form a sequence of so called “magic numbers”, i.e.: 13, 55, 147, 309, 561, 923 and so on.

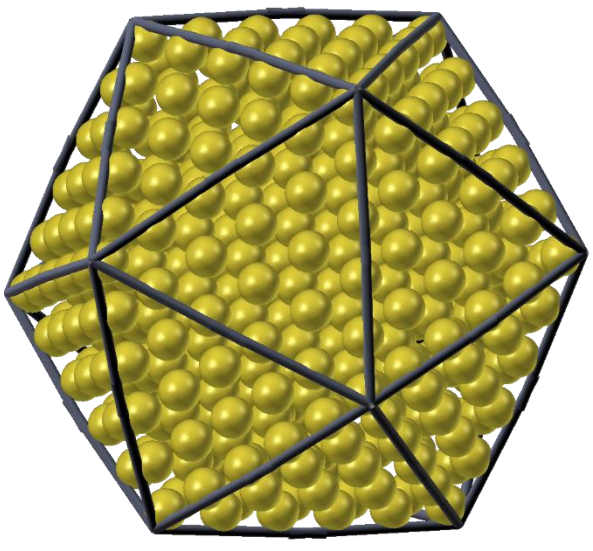

Fig. 4. The model of a 561-atom icosahedral gold nanoparticle.

Another considered arrangement of atoms that can be advantageous in small clusters is when they form an icosahedral shape (Fig. 4). Here the consecutive shells of neighbouring atoms contain the same number of atoms but they are slightly displaced. It leads to some atoms being a centre of 5-fold point symmetry. This arrangement contradicts full translation symmetry so icosahedra are not the fragments of a periodic lattice. The energy per atom is for most of metals more favourable if their particles have icosahedral shape ($-3.228\frac{\mathrm{eV}}{\mathrm{atom}}$ for a 13-atom AuNP, $-3.437\frac{\mathrm{eV}}{\mathrm{atom}}$ for a 55-atom AuNP, $-3.553\frac{\mathrm{eV}}{\mathrm{atom}}$ for a 147-atom AuNP). The cluster's icosahedral shape is a one of Platonic solids consisting of 20 triangular faces with 12 vertices laying on 5-fold symmetry axes.

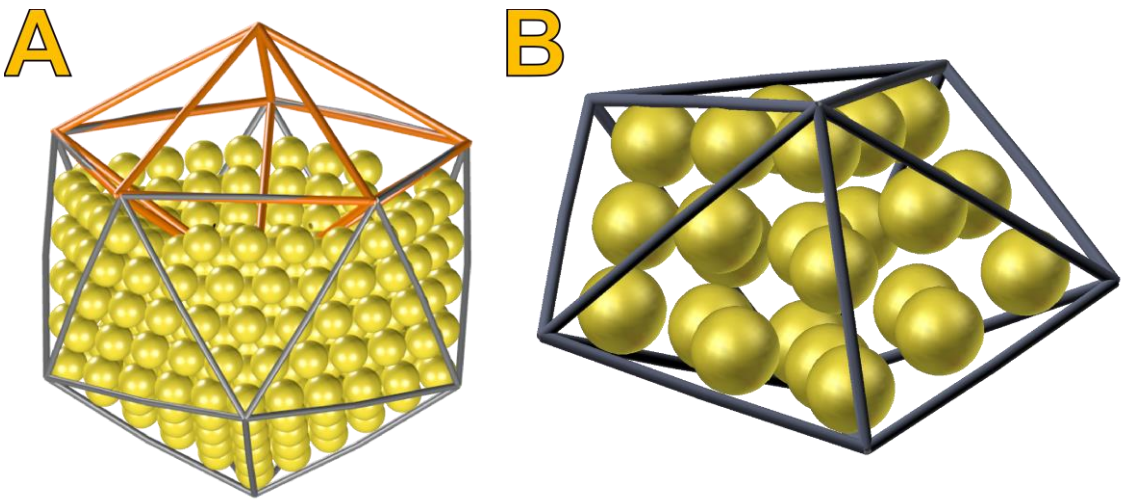

Fig. 5. The visualisation a decahedron (B) found inside the icosahedron (A).

It is possible to derive from the icosahedron one more form of the energetically advantageous atoms packing. To obtain all atomic positions within the solid one can plane cut icosahedron perpendicularly to all 5-fold symmetry axes, as shown in Fig. 5, subsequently relax with respect to energy the resulting cluster and, finally, obtain a decahedron. It consists of 10 faces formed from 5 triangular front faces surrounding vertex of 5-fold symmetry and completing the solid 5 triangular back faces surrounding the opposite vertex on the same 5-fold symmetry axis. The simplest decahedral cluster contains 7 atoms. The next decahedra consist of 23 (Fig. 5.B), 54, 105, … atoms with energy per atom decreasing in sequence: $-3.099\frac{\mathrm{eV}}{\mathrm{atom}}$ for a 7-atom, $-3.316\frac{\mathrm{eV}}{\mathrm{atom}}$ for a 23-atom, $-3.431\frac{\mathrm{eV}}{\mathrm{atom}}$ for a 54-atom and $-3.499\frac{\mathrm{eV}}{\mathrm{atom}}$ for a 105-atom nanoparticle. Within the used potential scheme, the decahedral arrangement is equally advantageous for packing as icosahedral one.

As is shown in Fig. 6, the powder diffraction pattern (DP) originating from decahedron differs substantially from that calculated for icosahedral and less for cuboctahedral shape of cluster. The series of patterns shown in Fig. 6 illustrate the patterns' evolution with growing size of the respective clusters. The patterns were calculated following Debye summation formula with use of the program Cluster [37]. It is clear that the patterns are easily distinguishable on the basis of the presence of typical FCC diffraction peaks: 1 1 1, 2 0 0, 2 2 0, 3 1 1, 2 2 2, etc., and using a ratio of amplitudes of 2 0 0 to 1 1 1 peaks. By analogy to their 2θ scattering angle, the peaks from icosahedron and decahedron clusters are also referred to following the Miller indices for FCC structure. For regular FCC

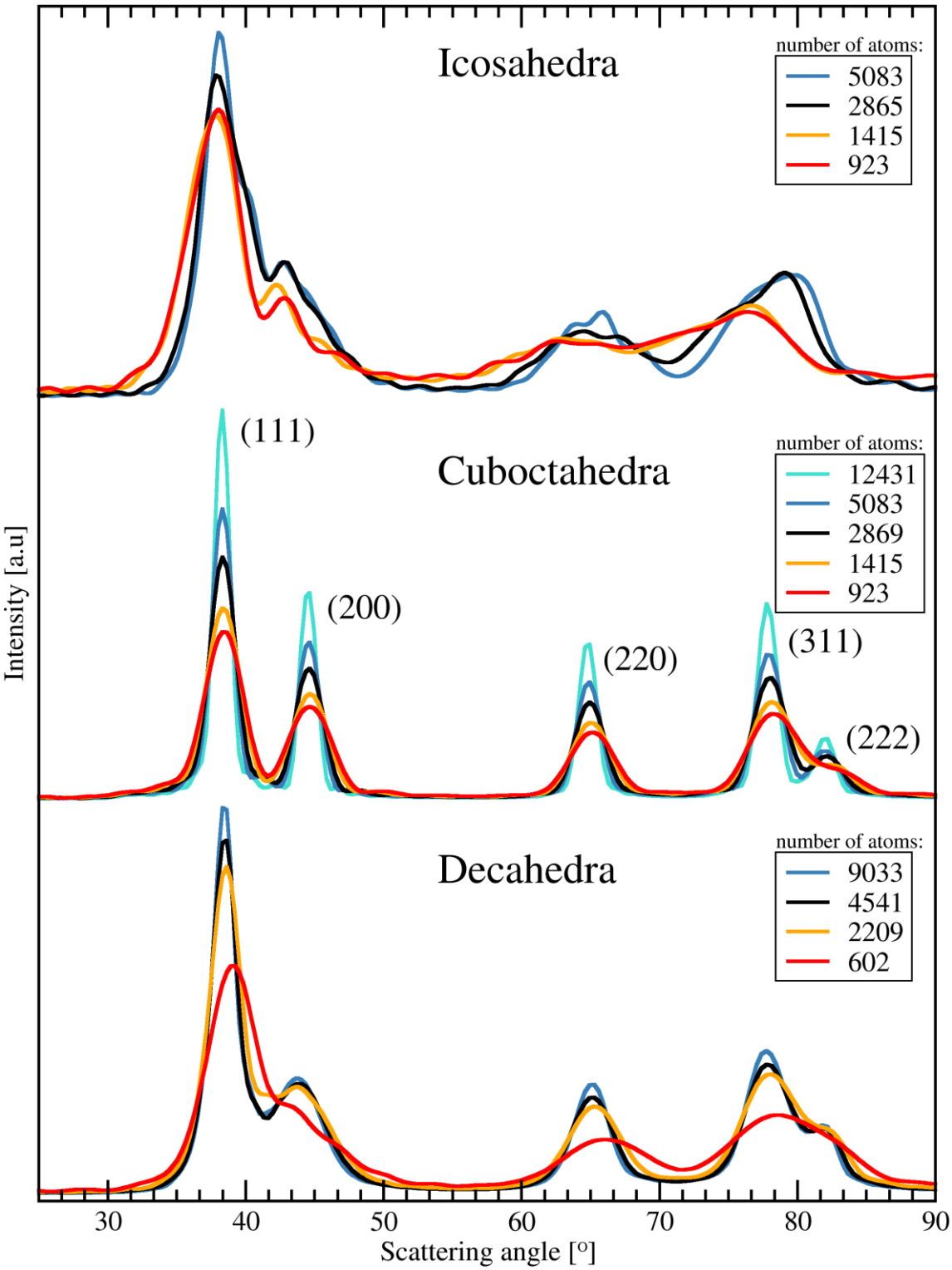

Fig. 6. The series of diffraction patterns (simulated with Cluster program [37]) of icosahedral, cuboctahedral and decahedral gold nanocrystals of varying number of atoms building the crystal lattice. The vertical axis is the intensity divided by the number of atoms in the model.

structure the ratio of 2 0 0 to 1 1 1 the peaks' amplitudes is close to 0.6 whereas for the decahedral clusters it can easily approach 0.2.

What is also worth to notice, is how intensity evolves with total number of atoms in the cluster. It is evident that the intensity from cubooctahedra small clusters grows quicker

with the number of atoms (N) than for icosahedra. For the same elemental content, cubooctahedra are better detectable by X-Ray diffraction. Model icosahedra give diffraction patterns much less resembling regular FCC patterns. The difference is best visible in much lower 2 0 0 peak height than for FCC, as well as in the intensity profile hardly separable into regular peaks. The diffraction patterns of decahedra more closely follow the FCC case. Though, the 2 0 0 peak height is still much lower and there is marked intensity in between 1 1 1 and 2 0 0 peaks expressed by the right hand side asymmetry of the 1 1 1 and the left-hand side asymmetry of the 2 0 0 reflection.

1.6. Analysis of diffraction patterns of gold nanoparticles containing the fraction of aperiodic crystals

In the previous Section 1.5 the changes observed in the diffraction patterns (DPs) of gold nanoparticles (AuNPs) due to the change of their shape, size and ordering of the atomic lattice have been discussed. A quantifiable measure of the magnitude of these modifications is necessary to support data analysis and drawing conclusions. The Debye-Waller factor estimation and the Williamson-Hall peak broadening analysis seem to be the suitable and simple tools to describe in general the deviations of the structure of the studied materials from the reference ideal crystal lattice.

A very important difference distinguishing DPs of FCC-structured cuboctahedra from evincing 5-fold symmetry icosahedra and decahedra was the peaks relative intensity or height. The decay of the intensity of reflections characteristic for a given crystallographic phase takes its origin from several factors:

- the value of the structure factor of the crystal phase for a given family of crystallographic planes – structure factor (equation 9) corresponds to the amplitude of the scattered wave detected at the certain 2θ position as the intensity of radiation;

$$F_{hkl} = \sum_x \sum_y \sum_z f_n \cdot e^{2\pi\, i\, (h\cdot x + k\cdot y + l\cdot z)} \tag{9}$$

where:
F_{hkl} – structure factor for a given (*hkl*) plane;
f_n – atomic scattering factor;
x, y, z – fractional coordinates of an atom *n* position.

- the temperature oscillations and/or the structure disorder which can be both described by Debye-Waller factor corresponding to the mean displacement of the atoms from lattice nodes;
- multiplicity (*M*) which indicates how many crystallographically equal planes are present in the structure;
- polarisation of the scattered wave which takes into account the unpolarised wave spectrum of the X–Ray tube and the fact that the amplitude of a diffracted wave is decreased in the diffraction plane (equation 10);

$$P(\theta) = \frac{1}{2}(1 + \cos^2 2\theta) \tag{10}$$

where:
$P(\theta)$ – polarisation factor;
θ – scattering angle.

- Lorentz factor (equation 11) which results from:
    a) finite aperture (slit) of the detector and changing semi-angle of the Debye-Scherrer cones (apparatus contribution),
    b) little tolerance of the Braggs' condition to misorientation of actively scattering crystal (geometry contribution),
    c) number of crystals oriented near the Bragg angle varying with the 2θ angle.

$$L \sim \frac{1}{\sin^2\theta \cos\theta} \tag{11}$$

where:
L – Lorentz factor;
θ – scattering angle.

1.6.1. The Debye-Waller factor

Apart from the second contribution, the others depend solely on the crystal structure type and the geometry of the diffractometer. The temperature has usually uniform effect on all reflection and the total acquired intensity of diffracted waves decreases. However, the disturbed ratios of the peaks intensities would suggest the deviations occurring in the ordering of atoms in the lattice. Icosahedral and decahedral crystals lack the long-range ordering corresponding to the FCC structure. Thus, the estimation of the Debye-Waller factor may be useful advice in the investigation of the AuNPs shape.

The Debye-Waller (D-W) factor modifies the structure factor F_{hkl} in the following way:

$$F_{hkl\,T} = F_{hkl} \cdot e^{-\frac{B\sin^2\theta}{\lambda^2}} \tag{12}$$

where:
$F_{hkl\,T}$ – the real structure factor affected by temperature oscillations or structure disorder;
F_{hkl} – reference structure factor;
θ – scattering angle;
λ – X-Ray wavelength;
B – D-W factor defined as: $B = 8\pi^2 < u^2 >$;
$< u^2 >$ – mean square displacement of atoms from the lattice nodes.

In order to calculate the Debye-Waller factor from the experimental diffractogram, the recorded DP intensity has to be corrected for all effects mentioned above:

$$I_{0\,hkl} \cdot e^{-\frac{B\sin^2\theta}{\lambda^2}} = \frac{I_{exp\ hkl}}{M \cdot P \cdot L \cdot F_{hkl}^2} \tag{13}$$

where:
$I_{0\,hkl}$ – real intensity of the diffracted wave;
$I_{exp\,hkl}$ – experimentally observed intensity of the diffracted wave;

Hence, it is possible to obtain the mean square displacement of atoms from the lattice nodes by applying the natural logarithm to the equation 13 and recalculate the *B* (D-W factor) to $<u^2>$ from the following correlation:

$$-\ln\left(\frac{I_{exp\ hkl}}{M\cdot P\cdot L\cdot F_{hkl}^2}\right)\sim B\left(\frac{\sin\theta}{\lambda}\right)^2 \tag{14}$$

The high value of $<u^2>$ may be indication of lattice disorder. Furthermore, the analysis of the distribution of points on the plot obtained using the equation 14 facilitates the identification of diffraction peaks which deviates the most from their predicted intensities within the assumed model, for instance FCC structure. The reason for these discrepancies may be the presence of Multiply Twinned Particles (MTPs) in the studied sample.

1.6.2. The Williamson-Hall approach

The primary scope of the analysis following the Williamson-Hall (W-H) scheme [46] is to differentiate between the contributions to the diffraction peak broadening originating from the size of the crystals in the investigated sample and the strains potentially present in the atomic lattice. If no strain is detected, still the average volume weighted size of the crystal domains can be assessed.

The W-H approach is based on several assumptions which frequently are not fulfilled in the case on examined material. Ideally, the broadening of the symmetric peaks caused by the size of the crystals and the strain found inside them should have the Lorentzian character. Moreover, the strain, if present, should be constant over sufficiently large range of distances. Also, the strain is required to be isotropic. Even if some of the approximations are slightly violated, the W-H approach can still show general tendencies useful in the assessment of the sample properties.

The more accurate analysis method was proposed by Warren and Averbach [47, 48], although its application in this research was found difficult. The general applicability of this method to the analysis of diffraction patterns from nanocrystals has been already evaluated by Kaszkur [49].The method proposed by us [33] requires usage of Voigt functions for the description of the peak shape. The Voigt functions used during data analysis in this research, as it has been described in Chapter 2 of this Thesis, did not have any constrains on the fitting parameters. Thus, the contribution of Gaussian and Lorentzian part to the Voigt function profile were to some extent random and did not correlate well-enough among different peaks. However, the overall peak shapes and FWHMs were described with the expected and satisfactory accuracy with the aid of XVoigt functions (see Section 2.5.4).

$$\beta_{tot}=\beta_D+\beta_\epsilon=\frac{K\cdot\lambda}{D\cdot\cos\theta}+C\cdot\epsilon\cdot\tan\theta \tag{15}$$

where:

β_{tot} – total broadening of the peak;
β_D – crystal size-related contribution to total broadening of the peak;
β_ϵ – strain-related contribution to total broadening of the peak;
D – volume-weighted average size of crystals;
ϵ – strain factor;
θ, λ – scattering angle and X-Rays wavelength;
K, C – apparatus and experimental constants;

The Williamson-Hall scheme defines the size (β_D) and strain (β_ϵ) broadening of the peak in a simplified way (equation 15). If they are both present in the material, their combined effect should be evaluated by their convolution, but W-H approximation allows to apply a classic sum. Multiplication of both sides of the equation 15 by $\cos\theta$ yields:

$$\beta_{tot}\cos\theta = \frac{K\cdot\lambda}{D} + C\cdot\epsilon\cdot\sin\theta \qquad (16)$$

which is actually a linear dependence of $\beta_{tot}\cos\theta$ on $\sin\theta$ and can be presented on, so called, Williamson-Hall plot. From the slope of this correlation the strain factor can be obtained. Similarly, the volume-weighted average size of the crystals can be calculated from the value of the intercept with the vertical axis. If the $C\cdot\epsilon$ factor is close to zero, it assumed that the crystals are unstrained, and *D* can be still estimated.

The estimation of the Debye-Waller factor and Williamson-Hall method were used in this work as standard analysis procedures in order to assess the general diffraction behaviour of the studied catalysts.

1.7. Transmission Electron Microscopy

Electron Microscopy (EM) utilises the wave nature of electrons and their wave interactions with matter. Transmission microscope (TEM) accelerates the beam of electrons emitted from the gun in the electric field of a few hundred kV (typically 120 - 1250 kV), because only electrons of high enough energy can be transmitted through the specimen. In this way, the inner structure of the studied sample can be examined, while only surface morphology features and its composition are accessible if a-few-tens keV electron are used. The different kinds of interactions with matter are classified as those when the energy of the electrons is preserved – elastic phenomena – and those which result in partial or total loss of the energy – inelastic phenomena. In most cases, the probability that a certain interaction will take place depends on the orientation of the studied object (or its part) with respect to the electron wave propagation direction. This 3D probability distribution is called crosssection. Out of various interactions between the electron beam and the sample, those used for this research have been described here in particular: TEM image formation, diffraction of electrons (ED) and selected electron spectroscopies.

Hardware [50]

To start with, the construction of TEM will be shortly described. Electron gun is believed to be one of the most powerful source available for research in terms of the energy flux [50]. There are two main technologies of producing electron beams [51]: through thermoemission and field-induced emisison. The former approach uses an LaB_6 prism crystal mounted on the heated tungsten (W) wire. Emission of electron from the crystal is a function of this crystal's temperature. In the field emission gun (FEG) the electrons are extracted from the emitter with a strong electric field. There are two types of FEGs available in the microscopes: Schotky type or with cold cathode (cold-FEG, CFEG).

The Schottky effect is observed when the potential barrier to expel electrons from the material is decreased in a strong electric field. Thus, the thermoemission from a tungsten tip can occur at lower temperature, which is important in terms of the energy spread of

the emitted electrons and the gun brightness. However, the beam emission current from the gun is lower than using thermoemission.

In the cold cathode FEG the electron emission is possible from the tungsten tip kept at room temperature by tunnelling the potential barrier thanks to strong electric field applied. CFEG offer the highest energy resolution and coherence. The disadvantage of the low tip temperature is that it is vulnerable to contamination and requires frequent cleaning every few hours (higher current is temporarily applied). Hence, the beam current is likely to fluctuate in time.

The first focusing lens in the optical path of the electron beam is the Wenelt cylinder, which is the sole electrostatic lens in the microscope. Then the electrons are accelerated in the linac (linear accelerator) to the desired energy (in this research it was 200 kV or 300 kV) and enter the condenser lens system. Condenser lenses' role is to form the beam (called also "probe") which will directly illuminate the sample. Particularly, a focused beam is necessary to obtain magnified real images or perform spectroscopy studies while parallel beam is suitable for ED patterns (EDP) acquisition. Between the condenser system and the sample usually there is a, so called, pre-specimen shutter which blanks the beam by redirecting it to the side and preventing the sample against irradiation with electrons. The shutter is used on demand to save sensitive samples from beam damage caused by prolonged exposure to electron radiation.

Below the sample the objective lens system is located. Its operation depends on the working mode: the imaging mode (spectroscopic studies are also performed in this mode) or diffraction mode. The role of the objective lens or lenses is to redirect chosen transmitted electrons to the optical path of the microscope, as in the finally formed image all transmitted beams should be recorded (ED mode) or only a real magnified image (alternatively appropriate spectrum). The objective system contains the objective aperture which is controlled by the microscope's operator and additionally limits the passing electrons only to those which were transmitted through the sample under the specified semi-angle.

Before entering the intermediate lens system, the Selected Area (SA) aperture can be inserted in the beam path. It is used to limit the area in the sample from which the signal is effectively acquired. The intermediate lenses are responsible for actual magnification of the real images or simulating different camera-to-sample distances (which affect the resolution of the EDPs).

Finally, the observed image (i.e. a real magnified image of the sample or diffraction pattern from the certain area of the sample) is formed by the projection lens on the fluorescent screen or the camera matrix. The process described above discarded aberrations of electromagnetic lenses used in TEM. The presence of aberrations being the result of imperfections of those lenses limits the resolution of TEM, also in the scanning mode (STEM). Modern TEMs utilise aberrations correctors that account for spherical aberration (change of lens's focal plane of beams that bends further from the lens's axis) of the projection system below the specimen (so called "image correctors") and condenser system above the specimen ("probe correctors).

The microscope can also be equipped with the Electron Energy Loss Spectrometer (EELS), accessible after the screen and the camera are lifted. The EELS appendix can

differentiate the electron energies (decreased by inelastic interactions with the atoms or the ions in the sample) taking advantage of how the electrons of different energies pass through the electric field.

TEM imaging [50]

The contrast observed in TEM images is the result of how the incident beam has been scattered by the specimen. The electron wave is characterised by its amplitude and phase, and both of them change after the beam passes through the sample, thus yielding contrast in the image. Although both amplitude and phase contrast contribute to virtually all images obtained in the TEM, usually such imaging conditions are chosen that one type of contrast dominates in image formation.

Amplitude contrast

First, the amplitude contrast will be described. It is observed in TEM as well as in STEM images. There are two principal types: mass-thickness and diffraction contrast. The former one originates from Rutherford scattering (incoherent elastic scattering) of electrons. The cross section for this phenomenon strongly depends on the atomic number (Z), so on the mass or density as well, and the thickness in the direction of the incident beam. As the Rutherford scattering occurs at low angles, imaging based on the beams from the small cone around the central beam is dominated by the mass-thickness contrast. Additionally, at very high angles, where Bragg reflections are so weak that no longer observed, some low-intensity scattered beams can be acquired. This high-angle scattering is also called the Z-contrast, because it depends on the atomic number (Z) only. It delivers the element-specific information about the sample and it can be obtained with atomic resolution if dark field scanning TEM (DSTEM) mode is used. Mass-thickness contrast is most important for non-crystalline samples (like silica or carbon support-containing catalysts) and sample containing phases differing in the atomic number.

Diffraction contrast

Diffraction contrast can be observed due to coherent elastic scattering occurring at Bragg angles, so it contains information about the orientation of a crystalline sample. Best images are obtained when the sample is illuminated with the parallel beam (convergence angle should be as small as possible), because the diffracted beams are well-focused and their intensities are not diffused. There are two ways to make the diffraction contrast dominating in the image formation:

a) the sample needs to be tilted so that a chosen ($h\ k\ l$) plane will be oriented exactly at the Bragg angle with respect to the incident beam and, thus, will be strongly excited;
b) only one diffracted or central beam will be selected by the objective aperture to create an image.

In the first case, two beams – namely: the excited one and incident – will be the strongest in the diffraction pattern and only those two should be collected by the objective aperture. Diffraction contrast based on two-beam conditions is very useful for imaging of various defects in single crystal samples, but has limited application for studies of powder samples of nanocrystalline catalysts.

The latter opportunity opens the possibility to create bright field (BF) or dark field (DF) images – depending on whether the central or one of the diffracted beams will pass through the objective aperture. Those images will be compatible to each other (when the same area of the sample is illuminated) and will clearly show the crystalline character of the sample. Selection of different reflections allows to distinguish crystal phases present in the sample while the central beam will carry the information about the amorphous part of the sample and its absoprtion. This imaging approach can efficiently enhance imaging of metal particles on non-crystalline supports and imaging of catalysts containing much differing crystal phases.

Phase contrast

Phase-contrast images are formed whenever more than one beam contributes to the formation of that image. Although phase contrast is experienced in most TEM images even at relatively low magnifications (e.g.: moire patterns, Fresnel contrast at defects), it is mostly associated with high resolution TEM (HRTEM). Mechanism of such contrast originates from the differences in the phases of electron waves after they have been scattered by the specimen. Many factors influence the final image: variable thickness of the sample, its orientation and its scattering factor. Also the varying objective lens astigmatism and focus affect what is visible in the image. The sensitivity of phases of electron waves to any changes is essential for imaging with atomic resolution.

The intensity of a scattered electron wave is a sinusoidal oscillation in the perpendicular plane to the diffraction vector (which is also perpendicular to the diffracting (*h k l*) plane). The periodicity of bright and dark fringes appearing in the image, as a result of interference of the scattered beam with the incident one, varies for different magnitudes of diffraction vector. Although the fringes period (reciprocal to the magnitude of diffraction vector) equals to the lattice planes spacing, the location of fringes in the image do not necessarily reflect the location of crystal planes in the sample. The reason for that is the variation of the excitation error (deviation parameter) used for description of the lack of precise fulfilment of the Bragg condition by the diffracting planes while still reflections from them are observed in the DP – the observed fringes will shift according to the excitation error and differences in the sample thickness as well.

If the incident beam is oriented along a low-index zone axis of the crystal (or vice versa – the crystal zone axis has already been oriented parallel to the incident beam and the microscope's optic axis), the fringes in the image will run in directions corresponding to the diffraction vectors (i.e. reflections seen in the DP). Thus, a net of spots can be observed in the image and they correspond to the projection of the crystal structure along this zone axis, but they have no direct relationship to the positions of atoms in the studied crystal. Such an image is formed because of interference of many beams: scattered and incident (all that passed though the objective aperture, if used) and it is called "on-axis lattice-fringe imaging".

The phase-contrast images were exploited both in the *ex-situ* and *in-operando* high resolution TEM (and STEM) studies as in these images it was possible to investigate crystals of nanometric size containing 5-fold symmetry axes.

Electron diffraction [50]

There are many types of diffraction techniques available in the TEM microscopes. In this research only the basic parallel-beam diffraction patterns (DPs) were acquired and, hence, will be introduced here. Elastic diffraction of electrons (ED) meets the same rules as diffraction of X-Rays – the Bragg condition has to be obeyed (at least approximately as the materials of interest are nanocrystals and the instrument is not perfect). The big advantage of ED over imaging techniques is that the precision of measurement of interplanar distances is better, but the structural information about nanocrystals is averaged over all that contributed to the EDP.

Irradiation of the specimen with a parallel beam is crucial for accurate studies. Convergent or divergent incident beam causes broadening of diffraction spots or rings, because the incident angle varies across the sample. Due to the lack of any appropriate focusing geometry for diffraction in the microscope, scattered waves travel through the optic system in different ways and form a distorted image. Parallel incident electron beam ensures that the diffraction pattern is sharpest possible and presents properly the reciprocal space of the investigated area of the sample.

Diffraction of electrons, like X-Rays, relies on absorption of waves and secondary emission. Emission from an ordered network of scattering objects yields constructive interference of emitted waves only at special angles (ED occurs at a few tens of miliradians, mrad) while destructive interference is observed at other angles. Emitted waves become planar, like the incident wave, at sufficiently large distances, hence ED is called far-field or Fraunhofer diffraction. Only then they can be focused by the microscope's optic system properly.

Diffraction patterns recorded from many nanocrystals in the field of view result in ring-like shapes rather than an ordered array of just a few spots in the image. The observed in this research Debye-Scherrer rings were actually still discrete, because the amount of material, thus scattering nanocrystals, was limited. However, after application of correction for ellipticity (projection system astigmatism), EDPs were azimuthally averaged to obtain 2D profiles of intensity as a function of scattering angle. Such form of diffraction data was more convenient for analysis.

1.8. X-Ray Fluorescence (XRF) Spectrometry

Brief theory of XRF [52, 53, 54]

X-Ray fluorescence (XRF) is the phenomenon of emission of secondary (i.e. fluorescent) X-Ray radiation by atoms in the sample which was exposed to high energy X-Rays produced by other source, usually X-Ray tube or synchrotron radiation. Exciting of the sample with different energy source constitutes other types of X-Ray emission spectroscopies. The emission spectrum contains discrete energies characteristic for a certain chemical element. Chemical composition of the studied material is qualitatively determined by measuring the emitted wave lengths (of energies) and quantitatively by measuring their intensity. On the spectrum (intensity plotted as a function of radiation energy), they form narrow peaks, thus are referred to as "lines". XRF spectrometry is an easy-to-use non-invasive technique. The analysed materials can be liquids or solids, crystalline or disordered, and, in principle, gases (however their examination is

challenging). This makes the XRF spectrometry a versatile tool for the chemical composition analysis.

In the classical approach to atom model, the nucleus built from protons and neutrons is surrounded by electrons. Electrons have quantified energy, so they occupy only certain orbitals that are grouped in shells labelled with consecutive alphabet letters starting from "K". The energy levels available for electrons depend on the nucleus composition (i.e. number of protons and neutrons). In other words, these energy levels are chemical element-dependent and characteristic for this element. Electrons occupying higher orbitals and shells have higher energy.

The electrons can be expelled from the atom when the atom is subjected to high energy X-Ray. The incoming photon will be absorbed by the electron if this photon poses high enough energy to overcome the bind of the electron in the atom. In this way, a hole (sometimes called "initial vacancy") is produced in one of the atomic electron shells and the atom becomes excited which is an unstable state. The recovery to the ground state requires one of the more energetic electrons present on further shells to be transferred to the created vacancy. The energy difference between the electron energy levels is compensated by emission of photon.

The electron energy levels are very specific for each element. Hence, the emitted photons have characteristic wave length and only those which are from 0.01 to 10 nm (X-Ray range of radiation) are of interest of this technique. The observed spectral lines can be used for identification of elements in the studied sample. In XRF spectrometry, lines are frequently labelled using Siegbahn notation, which describes between which orbitals in the atom the electron was allowed to transfer. A simplified example: $K_{\alpha 1}$ line means that the electron from the K shell was ionised and vacancy was filled by the electron (from the L shell occupying the energetically highest orbital) accompanied by emission of the most intense X-Ray radiation – "α1" symbol.

XRF equipment

XRF spectrometers can be equipped with energy or wavelength dispersive detecting systems, abbreviated to EDXRF and WDXRF respectively. The spectrometer used in this research was an EDXRF one. It had a solid state multichannel detector capable of measuring simultaneously the whole energy spectrum coming from the sample up to the energy of the rhodium lamp (30 keV). Measurement of characteristic lines of sodium (Na) to uranium (U) was possible. Elements with atomic number $Z < 11$ have very low florescence yield and their characteristic radiation is strongly absorbed by air. The spectrometer utilised the simplest 2D optics arrangement, i.e. the X-Ray lamp, the sample and the detector form one plane with the exciting and fluorescent radiation path. In this geometry, the sample was directly irradiated by the lamp and the detector collected the fluorescent photons. Although the intensity of acquired X-Rays was very high, the drawback was that the lines from the target of the lamp (rhodium), traces from spectrometer's building materials as well as occasional diffraction lines appeared in the resulting spectrum and had to be taken into account during analysis.

2. Experimental and methodology section

2.1. Synthesis of 9.4%$_{wt.}$ Au/CeO_2 catalyst

The synthesis of 9.4%$_{wt.}$ Au/CeO_2 catalyst (composition assessed by XRF measurements, refer to results on page 63) was inspired by M. Haruta recipe [4] and my MSc Thesis [55] modified by the introduction of the final reduction step with $NaBH_4$.

The following reagents and materials were used during the synthesis process: cerium dioxide (CeO_2, Austranal Praeparate), hydrogen tetrachloroaurate(III) trihydrate ($HAuCl_4 \cdot 3\,H_2O$, 99.9%, Alfa Aesar), sodium borohydride ($NaBH_4$, 99%, Sigma-Aldrich), sodium hydroxide (NaOH, ppa, Chempur) and double-distilled water (also referred to as redistilled water).

20 ml 0.0254 M (0.82%$_{wt.}$) of tetrachloroauric acid solution diluted with 330 ml of redistilled water was vigorously stirred at 500 rpm in darkness. Under constantly monitored pH value which never exceed pH = 11, it was alkalized dropwise with 51 ml of 0.05M $NaOH_{aq}$ and was left overnight under stirring. The initially yellow solution turned into transparent. This indicated the tetrahydroxyaurate ($Au(OH)_4^-$) complex was formed successfully. Then, 900 mg of CeO_2 which was suspended in 50 ml of redistilled water via ultrasonication aided by mechanical stirring was added to the tetrahydroxyaurate complex solution. The mixture was further stirred for 2 h at 80-85°C. After cooling the mixture down to 0°C, 58 mg of $NaBH_4$, dissolved in 20 ml of 0.1M $NaOH_{aq}$, was added dropwise. It resulted in immediate colour change into purple. The mixture was subsequently stirred for another 12 h in room temperature. Then, the catalyst was filtered and rinsed 15 times with redistilled water until no chlorine anions were detected. It was finally dried overnight under vacuum in 40°C. A ready-for-use catalyst was stored in darkness in a desiccator.

2.2. Synthesis of 20%$_{wt.}$ Au/C catalyst

The 20%$_{wt.}$ Au/C catalyst synthesis recipe originates from J. Turkevich method [56] appropriately modified according to K. C. Grabar [57]. This particular method, which allowed to obtain stable gold colloids with gold crystals of the mean size around 5 nm, was successfully applied to the synthesis of gold based catalysts by N. Kristian et al. [58] and E. Frota [59].

The following reagents and materials were used during the synthesis process: carbon Vulcan XC 72 (Cabot Corporation), hydrogen tetrachloroaurate(III) trihydrate ($HAuCl_4 \cdot 3\,H_2O$, 99.9%, Alfa Aesar), sodium borohydride ($NaBH_4$, 99%, Sigma-Aldrich), trisodium citrate dihydrate ($Na_3C_6H_5O_7$, ppa, Chempur), propan-2-ol (ppa, Stanlab) and double-distilled (redistilled) water.

In order to prepare 500 mg of the catalyst, 400 mg of carbon was suspended (ultrasonication aided by mechanical stirring) in 85 ml mixture of propan-2-ol and water (volume ratio 3:1). 20 ml of 0.82%$_{wt.}$ (0.0254 M) tetrachloroaurate solution was diluted under vigorous stirring (~600 rpm) at room temperature with 1725 ml of water and then 17 ml of 4%$_{wt.}$ trisodium citrate solution was added. In a separate beaker a reducing agent solution was prepared. It consisted of sodium borohydride (15 mg) dissolved in 4%$_{wt.}$ aqueous trisodium citrate (17 ml). Addition of the reducing agent solution to

citrate-protected tetrachloroaurate resulted in immediate colour change to deep red which is characteristic for gold colloids containing approx. 5 nm particles. After 5 minutes, the carbon suspension was purged into the red gold colloid. The mixture was stirred for 48 h in darkness. Then, it was filtered and rinsed with water until no chloride anions were detected. Finally, the catalyst was dried overnight under vacuum in temperatures not exceeding 40°C. A ready-for-use catalyst was stored in darkness in a desiccator.

2.3. Synthesis of 7.16%$_{wt.}$ Au/SiO_2 catalyst

The 7.16%$_{wt.}$ Au/SiO_2 catalyst (composition assessed by XRF measurements, refer to results on page 63) synthesis recipe was based on the idea of Y. L. Lam and M. Boudart [60] which was applied so that only gold containing catalyst was obtained (originally Au-Pd alloyed catalyst's active phase was obtained). Gold precursor was prepared according to original B. P. Block and J. C. Bailar [61] which was re–examined by W. J. Louw and W. Robb [62] and optimised by K. Kitada [63].

The following reagents and materials were used during the synthesis process: hydrogen tetrachloroaurate(III) trihydrate ($HAuCl_4 \cdot 3\,H_2O$, 99.9%, Alfa Aesar), 1,2-ethylenediamine ($H_2NCH_2CH_2NH_2$, will be abbreviated by "en", ≥99.5%, Roth), silica ($SiO_{2\ silica}$, Davison 62), diethyl ether ($(CH_3CH_2)_2O$, will be abbreviated by "Et_2O", ppa, Chempur), propan-2-ol (ppa, Stanlab), 25% ammonia solution ($NH_{3\ aq}$, ppa, POCH) and double-distilled (redistilled) water.

2.3.1. Gold precursor – di(ethylenediamine)gold chloride ($Au(H_2N(CH_2)_2NH_2)_2Cl_3$ = $Au(en)_2Cl_3$)

Solutions of 1 g of hydrogen tetrachloroaurate(III) trihydrate in 10 ml of diethyl ether and 1 ml of 1,2-ethylenediamine in 5 ml of Et_2O were mixed. A gummy yellow precipitate was formed. Following 30 min of refluxing, the solvent was evaporated under diminished pressure. An orange solution of the product was obtained after addition of approx. 10 ml of water. Following addition of approx. 90 ml of propan-2-ol a yellowish precipitate was formed and subsequently filtered. Crystallization from water and propan-2-ol mixture was repeated resulting in white powder which was dried overnight under vacuum at 40°C. Recrystallization was applied every time before using the gold complex in catalyst's synthesis.

2.3.2. Au/SiO2 catalyst

All of the steps were performed in darkness. In order to prepare 1000 mg of the catalyst, 900 mg of $SiO_{2\ silica}$ was suspended in 0.4 ml of 25% ammonia solution diluted with 50 ml of water resulting in pH~11. The mixture was stirred at 500 rpm. 215 mg of fresh di(ethylenediamine)gold chloride dissolved in 50 ml of water (transparent solution) was added dropwise to silica suspension. The slurry was heated up to 70°C. Following 1 h when the temperature never dropped below 68°C, the mixture, which turned into yellow, was filtered under diminished pressure, rinsed 10 times with water and dried overnight under vacuum. A yellow powder was obtained.

Before performing any experiments, the catalyst was activated in 20 ml/min flow of hydrogen for 80 min in 50°C, then 160 min in 100°C and finally 400 min in 150°C. The activation procedure aimed at reducing the gold cation complex anchored to SiO_2 surface

to gold particles closely bound with the support surface. At the same time, the 1,2-ethylenediamine ligand was released as possibly free ammonia (NH_3) and ethane (C_2H_6).

2.4. Reaction setups for the chemical performance tests of the catalysts

2.4.1. U-shaped glass reactor with thin layer fixed bed

Catalytic activity of synthesised sample was first evaluated in a glass (borosilicate glass) flow reactor. The results obtained there were later used as a reference during analysis of data collected with the *in-situ* PXRD-MS setup (refer to Section 2.5). The gas sequence and temperature settings were fully controlled by the computer script. Thus, it was later feasible to reproduce with high accuracy the measurement conditions while the studies of the structure dynamics of the catalysts were carried out. Furthermore, thanks to automatic on-line data collection, results were readily correlated in time.

The setup consisted of a U-shaped glass reactor, Fig. 7, with a porous sintered glass disk where a thin (~1 mm) catalyst bed was formed. The design of this non-fluidized bed reactor provided uniform flow of gas through the bed and thus uniform performance of the whole loaded sample. Therefore, model of a differential Plug Flow Reactor (PFR) could be assumed.

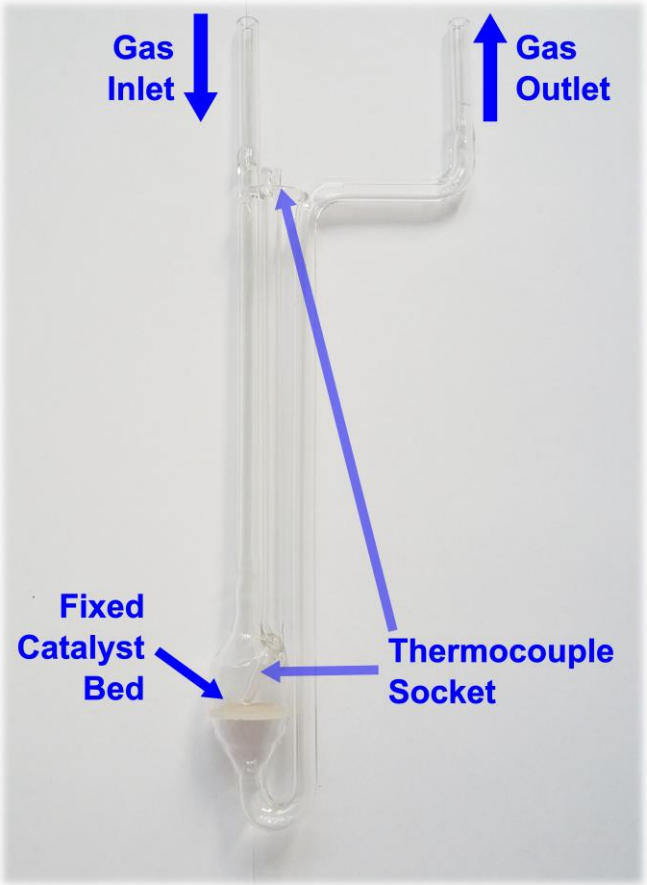

Fig. 7. The photograph of the U-shaped glass reactor used for the chemical performance test of the catalyst.

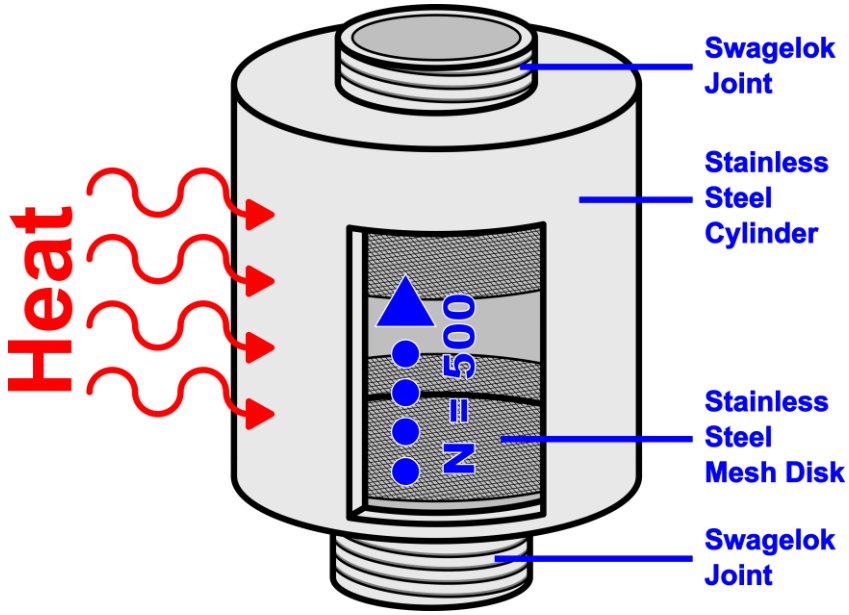

Fig. 8. The cross-section model of the nickel carbonyl ($Ni(CO)_4$) trap used in order to prevent the catalyst against contamination with nickel. The cylinder was filled with ~500 steel mesh disks and heated to ≥200°C.

The reactor was heated by a tube furnace controlled by its inner thermocouple. Another thermocouple indicated the temperature of the catalyst bed. Some deviations between the temperatures of the furnace and the catalyst bed were experienced, so any references are always made to the temperature of the sample. At the inlet of the reactor there was a nickel carbonyl ($Ni(CO)_4$) trap (abbrev. Ni-Trap, Fig. 8) made of stainless steel cylinder tightly filled with steel mesh, which improved heat transfer. It was heated up to 200°C or more in order to decompose $Ni(CO)_4$ and to avoid catalyst poisoning of the catalyst by the nickel deposits as well as to avoid the possible influence of chemical properties of nickel on the monitored chemical performance of the studied sample. All parts of the setup, between the Ni-Trap and inlet of the mass spectrometer (MS), which were placed outside the tube furnace, were heated by a heating mantel. Its major role was to prevent condensation of any vapours (e.g. H_2O which might be a side product) in the tubes before the gas stream reached the MS inlet and the vapour condenser afterwards. Formation of droplets could be harmful for the MS ionisation, for the quadrupole chambers or for the turbomolecular pump and could cause undesirable spikes on MS spectra being the result of oversaturation of Faraday cup or Secondary Electron Multiplier (SEM) detectors. For MS working conditions refer to Section 2.5.1.

Gas stream was supplied from a separate vacuum–gas system, which was used as a source of gas for other experimental setups as well. Refer to page 38 and Fig. 9 for detailed description of its design. Briefly, the vacuum-gas system allowed supply of the setup with a gas stream of desired composition, which was adjusted by two mass flow controllers (MFC). MFCs were connected to two ducts which allowed to choose the proper gas from the pressurised bottle. Ducts were evacuated 3 times when a change of gas was needed. This allowed a quick and efficient gas exchange.

2.4.2. Reactor with SiC-diluted catalyst bed

One catalyst, 9.4%$_{wt.}$ Au/CeO_2, underwent additional thorough investigation of its chemical properties, as it appeared to be the most promising candidate for efficient CO oxidation. On that basis this sample was also selected for *in-operando* transmission electron microscopy (TEM) research (Section 3.5).

This experiment was carried out by Fritz-Haber Institute (FHI), Max-Planck Society, Berlin, Germany, with their in-house built station designed solely for CO oxidation reaction. A reactor with the catalyst bed formed between two glass wool plugs was the primary part of the apparatus. The sample was mixed with SiC to dilute it and enlarge the volume. The reactor was connected to the gas supply system based on the Bronkhorst® automated MFCs and the pressurised bottles. The temperature was maintained by a heating chamber controlled by an Eurotherm™ controller with a thermocouple. The chemical output was measured with Emerson® Rosemount™ X-STREAM 4-channel continuous gas analyser.

Before the main part of research, the sample was conditioned at 200°C in synthetic air-like atmosphere (80%$_{vol.}$ He + 20%$_{vol.}$ O_2) overnight.

There were two gas mixtures used during this experiment. Helium constituted 90%$_{vol.}$ of the gas stream. The remaining 10%$_{vol.}$ was either: the FHI standard mixture with 20-fold excess of oxygen over carbon monoxide, 1 : 10 (by volume) CO : O_2; or 2 :1 (by volume) CO : O_2 mixture, which reflected the ratio used in *in-operando* PXRD-MS studies.

2.5. *in-operando* PXRD-MS technique

The experimental setup (Fig. 9) for *in-operando* Powder X-Ray Diffraction coupled with Mass Spectrometry (PXRD-MS) was designed to mimic the working conditions of a chemical reactor while allowing investigation of dynamic (and possibly cyclic) evolution of crystal structure of powder sample. A customized in-house built measurement chamber is the crucial part of a bigger system. Equipment, together with data acquisition and analysis methodology, is referred to as *in-operando* Nanocrystalline X-Ray Diffraction (NXRD).

The apparatus consisted of 6 main parts:

1) vacuum-gas supply unit;
2) liquid vapour saturator;
3) $Ni(CO)_4$ trap (“Ni-Trap”);
4) measurement chamber mounted on the goniometer in the diffractometer;
5) mass spectrometer (MS);
6) vapour condenser (embedded in the exhaust system).

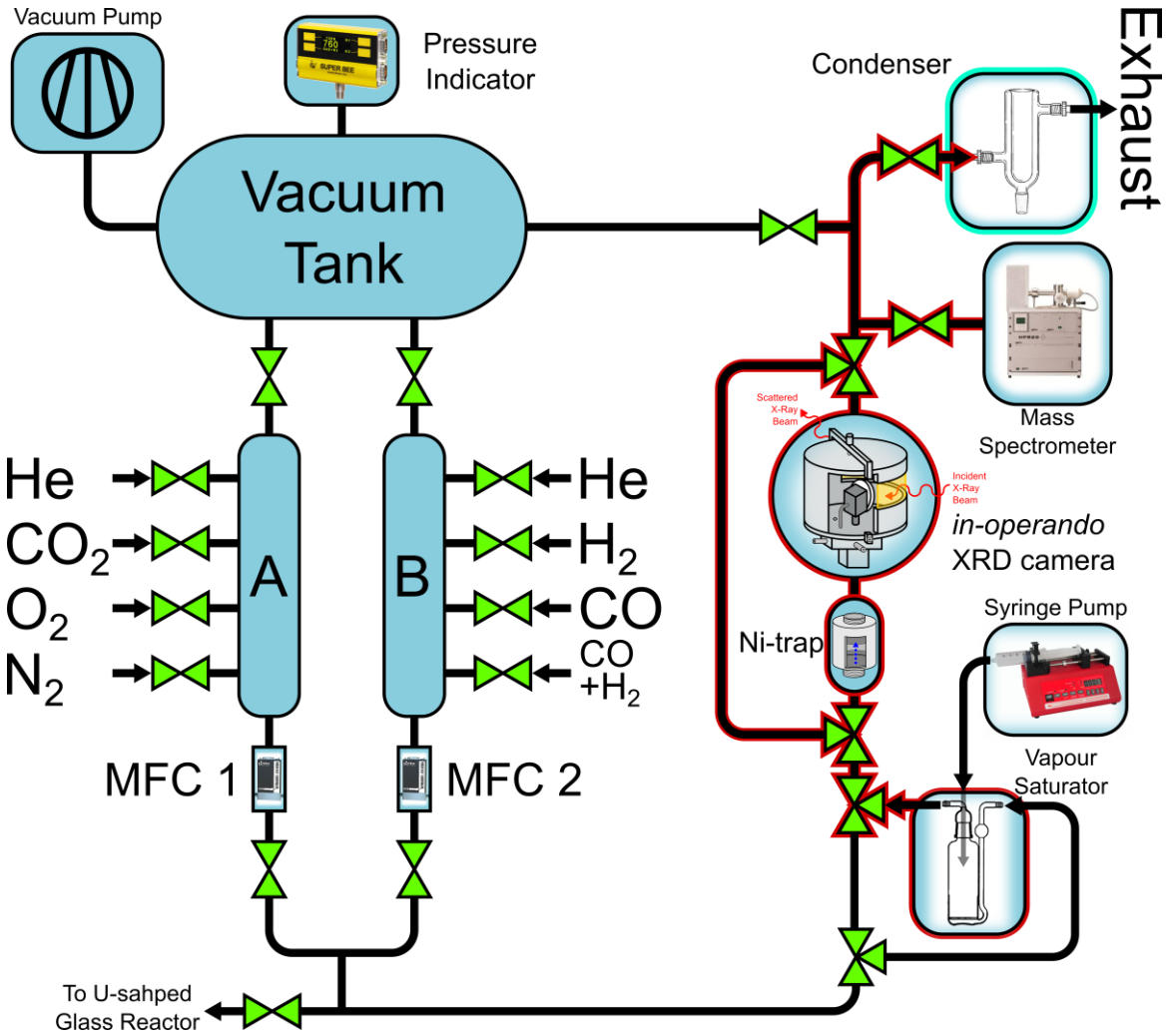

Fig. 9. Diagram of the experimental setup for *in-operando* Powder X-Ray Diffraction coupled with Mass Spectrometry (PXRD-MS) studies. The installation was also used for the chemical tests in the U-shaped glass reactor. MFC ≡ Mass Flow Controller; A, D ≡ gas ducts A and B.

2.5.1. Experimental setup – general equipment specification

Tubing and manual valves were the Swagelok stainless steel parts. The vacuum-gas supply unit was equipped with an oil pump, pressurised gas bottles, pressure gauges by InstuTech Inc., electromagnetic on/off valves by REG-ADA and MKS® mass flow controllers (MFC). MFCs were calibrated using a bubble meter of 5 ml or 10 ml volume. Apart from gas bottles, all parts are operated automatically by the computer script according to the programmed sequence. Data was stored on a network attached storage (NAS).

Pressurised gas bottles contained following substances:

- helium, He, 99.999%, Multax;
- hydrogen, H_2, 99.999%, Multax;
- carbon monoxide, CO, 99,997%, Linde Gas;
- oxygen, O_2, 99.999%, Multax;
- carbon dioxide, CO_2, 99.8%, Linde Gas;
- synthetic gas, mixture CO : H_2 1 : 2 by volume, prepared on-site;
- nitrogen, 99.999%; Multax.

Vapour saturator (liquid evaporator) consisted of a U-shaped borosilicate glass tube with a sintered porous glass diaphragm in the evaporation zone. Glass tube was covered with a heating mantle. Selected liquid was provided to the saturator by a syringe pump (NE 4000, New Era Pump Systems Inc.) through a needle and a septum.

A Siemens D5000 X-Ray diffractometer arranged in Bragg-Brentano θ-2θ geometry was used for structure studies. It was equipped with a PANalytical® Cu lamp operating at 40 kV and 40 mA ($K_{\alpha1}$ = 1.54056 Å, $K_{\alpha2}$ = 1.54439 Å, 99.5% of K_{β} radiation was blocked by a 10-20 μm nickel filter mounted at the detector side) and a Bruker® LynxEye strip detector with 192 stripes (energy resolution ~20% FWHM of Cu-radiation) covering 4.0512° of 2θ range at 220 mm goniometer radius. The detector had a 8 mm anti-scatter slit, 2.5° Soller slits and moved continuously and the analytical signal was integrated appropriately. Diffraction patterns were collected with $0.02° \cdot s^{-1}$ speed. The X-Ray beam was limited by a pair of 1 mm and 2 mm fixed divergence and anti-scatter slits, respectively, as well as by 5° Soller slits. Such geometry aimed at highest diffraction peaks intensity, while the resolution plays a less important role in the studies of nanomaterials due to their intrinsic large peaks broadening.

A quadrupole mass spectrometer HPR-20 from Hiden Analytical Ltd. had the Faraday cap and the Secondary Electron Multiplier (SEM) detectors. The ion masses up to 200 amu could be detected. Total operating range of ion current was from 10^{-13} to 10^{-5} Torr. Electroionisation was performed at 70 V and SEM accelerating voltage was 975 V. MS was able to probe 1 atm gas stream due to capillary sampling and Pt membrane (aperture) limiting access to open ionisation chamber. The yttria coated iridium (YO_x–Ir) filament was resistant to air inrushes and had lower emission temperature what results in its weak interactions with residual gases.

Glass vapour condenser ("cold finger" type) used a static coolant (usually "dry ice" – solid CO_2 – in acetone) and was cleaned after every experiment. Similarly to the chemical reaction setup, tubes between the vapour saturator and the condenser, including the measurement chamber and the MS inlet, were heated by the heating mantel (marked as red contour in Fig. 9).

Temperature values were monitored and adjusted by the Lumel RE15 controllers working with the K-type thermocouples. The offset for each thermocouple was calibrated using ice bath and a laboratory thermometer.

2.5.2. Experimental setup – *in-operando* PXRD chamber

The *in–operando* PXRD measurement chamber (Fig. 10) was the heart of the whole setup. All of the interesting physical and chemical phenomena originated from the properties of the studied sample, which is hidden inside this volume. The chamber was an in-house built 2-part assembly connected to vacuum-gas supply and analysis system, mounted on the goniometer in the X-Ray diffractometer. In spite of the differential Plug Flow Reactor (PFR) used for the chemical tests (Section 2.4), the chamber acted as a Continuous Stirred Tank Reactor (CSTR) with additional assumption of perfect (ideal) mixing of the reagents and products (CISTR model).

The removable aluminium cap had a Kapton™ window which allowed for crystal structure studies by means of XRD. There was a Viton™ gasket fitted between the cap and basement to ensure air-tight closing.

The basement was a stainless steel plate with several other parts and fittings soldered to it. The most important piece was the heating block which acted also as the sample holder and outlet for the gases from the chamber. Catalyst sample was spread onto and pressed into a sintered porous glass plate, and formed a thin layer on the plate.

The glass disk was mounted on the heating block so that it covered the gas outlet which was embedded in the block. Right next to the chamber's outlet there was the inlet to the MS probing capillary via 3-way connector. Due to such arrangement, all alternations in the gas stream composition could be instantly detected by MS.

Before the chamber's inlet, there was a Ni-Trap. Identically to chemical reaction setup, it was heated to at least 200°C and it prevented catalyst poisoning by decomposing $Ni(CO)_4$.

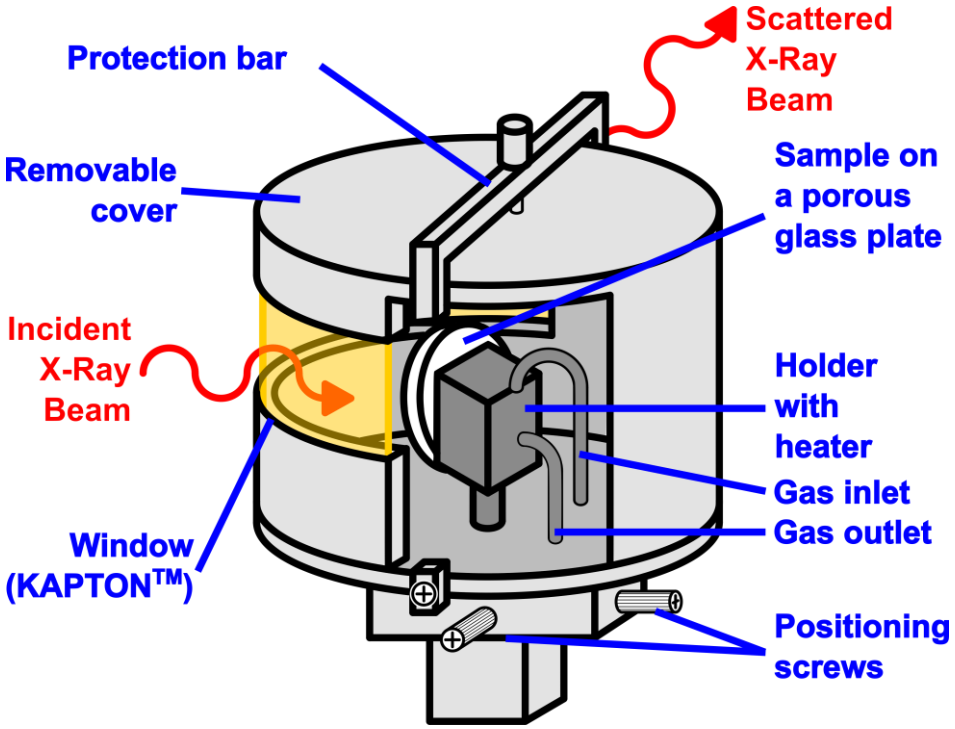

Fig. 10. The cross–section model of the *in–operando* PXRD measurement chamber (sometimes also called "camera"). The removable cover secured by the protection bar allowed to mount the sample inside the chamber. The inlet gas stream was supplied at the back of the heating block in order to enhance good mixing and pre–heating of reagents prior they reached the catalyst surface.

2.5.3. Measurements strategy

Sample preparation started from its milling in the mortar to obtain fine-grinded material and to facilitate sample deposition on the sintered porous glass plate (see Section 2.5.2). Additionally, an aliquot of polycrystalline quartz was mixed with the sample. Quartz ($SiO_{2\ quartz}$) played a double role. It was used as an internal reference material to calculate corrections for systematic errors (especially specimen off-axis displacement) and as an internal probe of the temperature of the catalyst (details on temperature dependence of

quartz structure are described in Section 2.5.5). Quartz diffraction peak positions (quick quartz structure refinement) were also utilized during initial alignment of the chamber with the available positioning screws, which aimed at bringing the surface of the sample as precisely as possible to the goniometer rotation axis and centre of the area illuminated by X-Ray beam. Usually it was achieved with accuracy greater than 0.5 mm.

After the chamber basement with the sample holder had been aligned, the cell was tight-closed with the cap. Air was evacuated by purging the chamber with helium at room temperature. MS spectra were checked for any leakages.

If it was necessary (as in the case of e.g. Au/SiO_2), the catalyst activation and conditioning were performed *in-situ* inside the chamber prior to the main part of the experiment.

Common conditions were applied to all samples during PXRD-MS studies and all important experimental parameters describing them were thoroughly logged, i.e.:

- pressure,
- temperature,
- gas mixtures sequence,
- inlet gas stream composition,
- data collection procedure.

Pressure was not controlled, only monitored in case any abnormalities might appear. The experimental setup exhaust was opened to atmosphere and ended with a convergent tube only. No back diffusion of air was detected thanks to several-meter-long exhaust tube, which assured possible air contamination level below the detection limit (i.e. below a few particles per billion, ppb, according to SEM detector of MS).

During the main part of each experiment the temperature of the heating block and chamber chassis were kept at 150°C ± 0.1°C (apart from short periods of rapid gas exchange which, due to varying heat capacity of gases, caused a few degree vanishing alternations of the temperature). There were several reasons for deciding on this temperature. The Au/CeO_2 catalyst was found to reach ~100% conversion of CO to CO_2 already slightly above 80°C (for exact results please refer to Sections 3.2.2 and 3.2.5). If any water is formed in competition with CO oxidation when hydrogen was added to the gas mixture, the setup was required to stay at least at 100°C to avoid H_2O condensation. Finally, $Ni(CO)_4$ can hardly form above 150°C [64]. In account for stainless steel basement of the measurement cell, 150°C temperature was selected as the lowest that provided reliable chemical and structure dynamics results (foreseen difficulties included: catalytic properties of deposited Ni atoms or particles and possible formation of Au-Ni alloy, core-shell structure or intermetallic compound).

The gas sequence was designed so that it enabled investigation of physical and/or chemical adsorption of gases on the catalyst's surface as well as phenomena accompanying the stoichiometric CO oxidation (abbrev.: sCOOX) or its preferential oxidation in the H_2-rich stream (abbrev. PROX). For PROX, an unstoichiometric ratio of CO and O_2 was used (2-fold excess of oxygen. $CO : O_2 = 1 : 1$ by volume) to check readily the catalysts' selectivity. It was assumed that the relaxed and adsorbate-free surface would be observed during sample exposure to pure He. The structure of the catalyst under He after initial air evacuation was considered as an absolute reference (in

case any persistent changes were observed while the experiment progressed). Helium was used also for cleaning the surface from the current adsobate before exposure to a new one was performed. Exposure to CO_2 being the product of CO oxidation was moved to the end of the sequence in order not to influence the sample prior CO_2 was formed by itself, in case any strong interaction would take place. The resulting sequence was as it has been presented in Fig. 11.

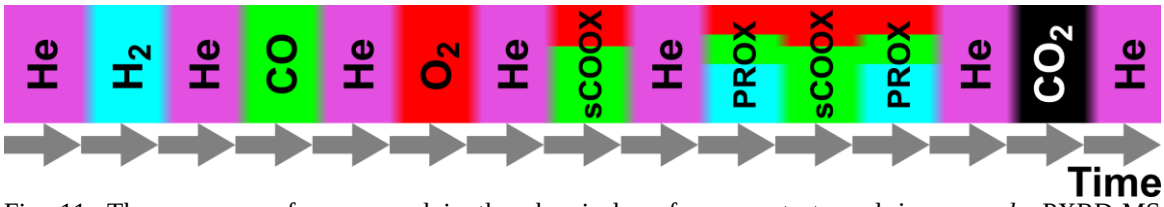

Fig. 11. The sequence of gases used in the chemical performance tests and *in-opernado* PXRD-MS experiments.

Acquisition of each X-Ray diffraction pattern (DP) was the most time-consuming part of each experiment. Depending on the catalyst support, the 2θ angle range was ~50-70° wide, which resulted in time of signal collection from ~40 to ~60 min. Furthermore, the whole experiment took at least 1 week, but as much as 2 or 3 weeks were needed if the measurement statistics had to be improved. That is why the experiment time scale was based on DP acquisition time. In this way, each peak on the DP represented averaged structure at the same physi-chemical state.

2.5.4. Data analysis procedures – tracing of diffraction peaks' positions

Outlet gas composition and parameters of chemical performance of the catalysts

MS spectra, temperature and gas flows logs were collected and stored in separate files. Every kind of data was further divided into smaller files labelled appropriately. The file index corresponded to the index of currently acquired DP. This data management system allowed easy correlating the results in time. The ease of analysis of any observed changes was greatly improved in this way. Data did not need any corrections since the instruments had been calibrated before conducting the experiments.

$$\eta_{CO\rightarrow CO_2} = \frac{I_{CO_2^+}}{I_{CO^+}+I_{CO_2^+}} \cdot 100\ \% \tag{17}$$

$$\eta_{O_2\rightarrow CO_2} = \frac{I_{CO_2^+}}{2I_{O_2^+}+I_{H_2O^+}+I_{CO_2^+}} \cdot 100\ \% \tag{18}$$

$$\eta_{O_2\rightarrow H_2O} = \frac{I_{H_2O^+}}{2I_{O_2^+}+I_{H_2O^+}+I_{CO_2^+}} \cdot 100\ \% \tag{19}$$

$$S_{CO_2} = \frac{I_{CO_2^+}}{I_{H_2O^+}+I_{CO_2^+}} \cdot 100\ \% \tag{20}$$

where:

$\eta_{A\rightarrow B}$ – yield of product B with respect to reagent A;
I_{X^+} – ion current of X^+ cation (MS data);
S_{CO_2} – selectivity towards CO_2.

Catalytic activity was monitored by two quantities: yield of CO to CO_2 conversion and selectivity to CO_2 (against H_2O production). Yields of CO_2 and H_2O production as well as selectivity towards CO_2, were calculated according to equations 17 – 20.

Crystallographic phase description

DPs were analysed in program Fityk [65] aided by my external script. The main scope of the script was to extract parameters describing all diffraction peaks visible in all DPs. Diffraction peak shape was approximated with a pair of analytical Voigt functions jointly referred to as XVoigt function. The Voigt function is a convolution of Gaussian and Lorentzian functions and its formula is as follows (according to R. J. Wells [66]):

$$Voigt\left(h, c, G, r_{L,G}\right) = \frac{h \cdot \int_{-\infty}^{+\infty} \frac{e^{-t^2}}{r_{L,G}^2 + \left(\frac{x-c}{G} - t\right)^2} dt}{\int_{-\infty}^{+\infty} \frac{e^{-t^2}}{r_{L,G}^2 + t^2} dt} \quad (21)$$

where:

h – peak's intensity;
c – peak's 2θ angle position;
G – variable proportional to width of Gaussian contribution;
$r_{L,G}$ – variable proportional to the ratio of Lorentzian and Gaussian FWHM.

The XVoigt function was used in order to automatically account for both Cu $K_{\alpha 1}$ and $K_{\alpha 2}$ radiation contributions to the peak shape. The following formula was used to create an XVoigt profile:

$$XVoigt\left(h, c, G, r_{L,G}\right) = Voigt_{K_{\alpha 1}}\left(h, c, G, r_{L,G}\right) + \\ + Voigt_{K_{\alpha 2}}\left(0.5 \cdot h\ , 2 \cdot \frac{180}{\pi} \cdot \operatorname{asin}\left(\frac{1.54439}{1.54056} \cdot \sin\left(\frac{c}{2} \cdot \frac{\pi}{180}\right)\right), G, r_{L,G}\right) \quad (22)$$

Quartz used was a very well polycrystalline material with narrow peaks (FWHM ~0.1°). Its peaks were analysed at first by my script. In this case, the background was estimated as a straight line, for each quartz peak separately, regardless of whether the particular quartz reflection was or not on a shoulder of a peak of CeO_2 or Au.

Background handling

Ceria was the only crystalline support used in catalysts syntheses (refer to its DP on Fig. 12). The background in the DPs of Au/CeO_2 samples was always smooth and it was possible to approximate it by a simple polyline. Points (2θ angle positions) defining the polyline were chosen empirically and were kept constant during processing of the whole DPs series. After subtraction of the background, reflections originating from ceria were fitted before those coming from gold. In the cases the CeO_2 and Au peaks overlapped each other, they were fitted simultaneously at the same time.

Both silica and carbon are the supports that are regarded as amorphous or strongly disordered. As a result of poor preservation of the long–range crystallographic order, scattering of X–Rays led to a few–degree broad and usually asymmetric bands. They strongly influenced the models fitted to the DPs. Thus, despite the difficulties in their analytical description, their contribution cannot be neglected. A handy approach was

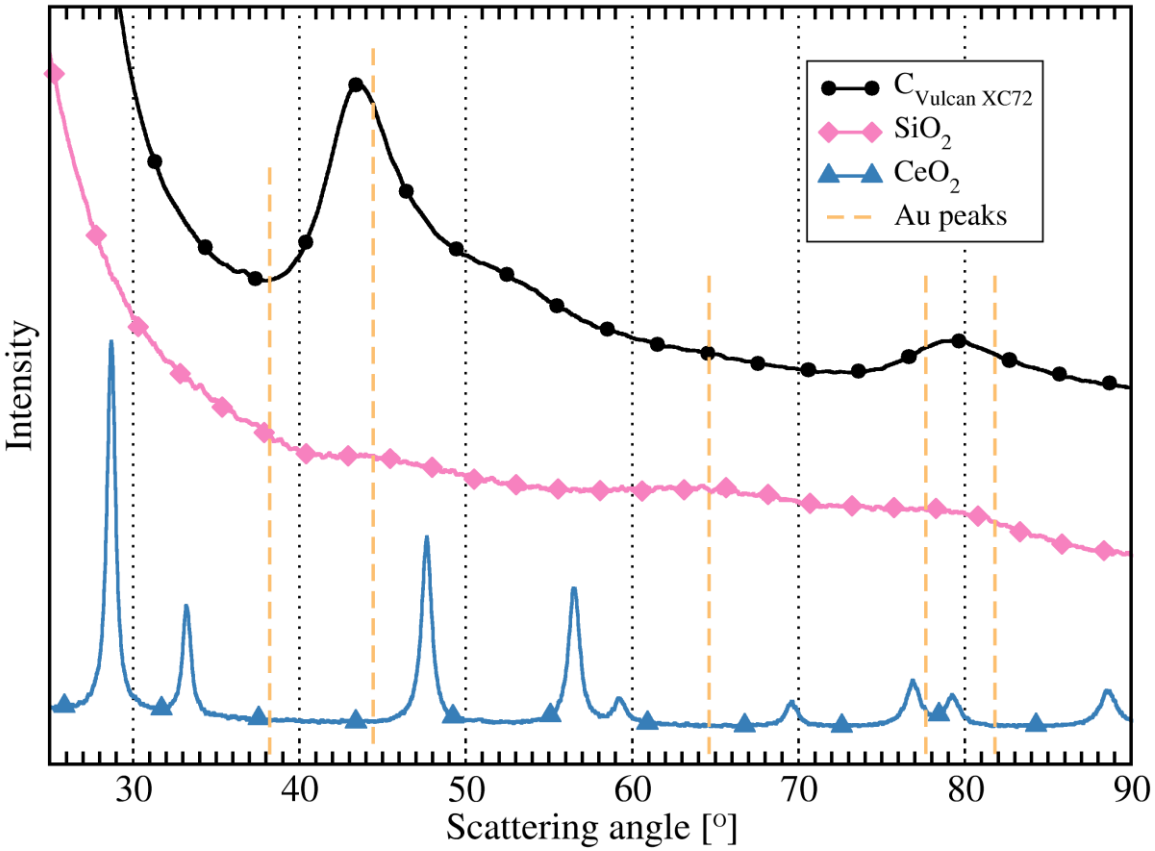

Fig. 12. The diffraction patterns of the supports: CeO_2, SiO_2 and $C_{Vulcan\ XC72}$, with marked gold peaks positions.

developed to handle the issue effectively. At first, it was assumed that the catalyst sample can be characterised by an average uniform coefficient of X–Ray absorption. Consequently, the total scattering of the powder sample was a scaled sum of contributing phases (however the intensity originating from the mixed Au–support distances was neglected):

$$I_{total}(\theta) = A(\theta) \cdot I_{Au}(\theta) + A(\theta) \cdot I_{support}(\theta) \tag{23}$$

where:

$I_{total}(\theta)$ – total observed experimental intensity;
$I_{Au}(\theta)$ – contribution originating from pure gold phase;
$I_{support}(\theta)$ – contribution originating from pure support phase;
$A(\theta)$ – average sample absorption coefficient.

Hence, the contribution of gold nanocrystals' phase to the DP could be extracted as:

$$A(\theta) \cdot \left(\frac{I_{Au}(\theta)}{I_{support}(\theta)} + 1 \right) = \frac{I_{total}(\theta)}{I_{support}(\theta)} \tag{24}$$

$$A(\theta) \cdot \frac{I_{Au}(\theta)}{I_{support}(\theta)} = \frac{I_{total}(\theta)}{I_{support}(\theta)} - A(\theta) \tag{25}$$

$$A(\theta) \cdot I_{Au}(\theta) = I_{total}(\theta) - A(\theta) \cdot I_{support}(\theta) \tag{26}$$

To sum up, the observed intensity of the catalyst's DP should be divided by the intensity of pure support DP. Then, $A(\theta)$, which corresponds to a smooth background between the Au peaks, is represented by a constant value or a line with a very mild slope ($A(\theta) = A_1 \cdot \theta + A_2$, where $A_1 \to 0$). It is subtracted from the remaining intensity profile. The last step is to multiply backwards the resulting scattering profile by the DP of raw support used at the beginning of the procedure. The resulting intensity dependence on 2θ represents the separated contribution of only gold phase, which can be then described by analytical approximation more easily. The whole procedure aimed at obtaining the average absorption coefficient, $A(\theta)$, which cannot be straightforwardly assessed.

The method described above was used only in the case of silica and carbon support, which scattered much more weakly than gold. This justifies the neglecting of any decay of intensity due to interaction and screening of the gold phase by the surrounding support. The effect that each step of the procedure took on a selected experimental DP of Au/SiO_2 can be examined in Fig. 13.

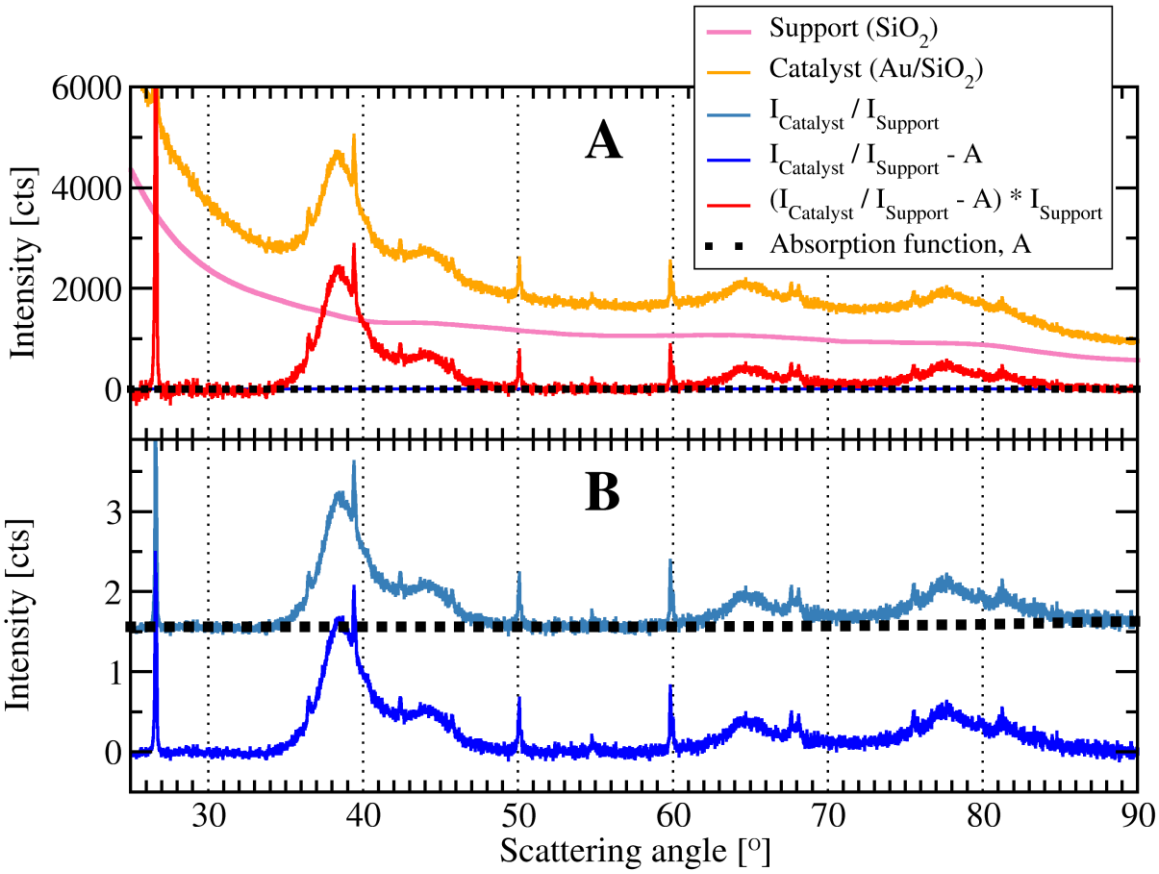

Fig. 13. The effects of the consecutive steps of the background handling method on the sample diffraction pattern of the Au/SiO_2 catalyst. The method is described on pages 43–45 and with equations 23–26.

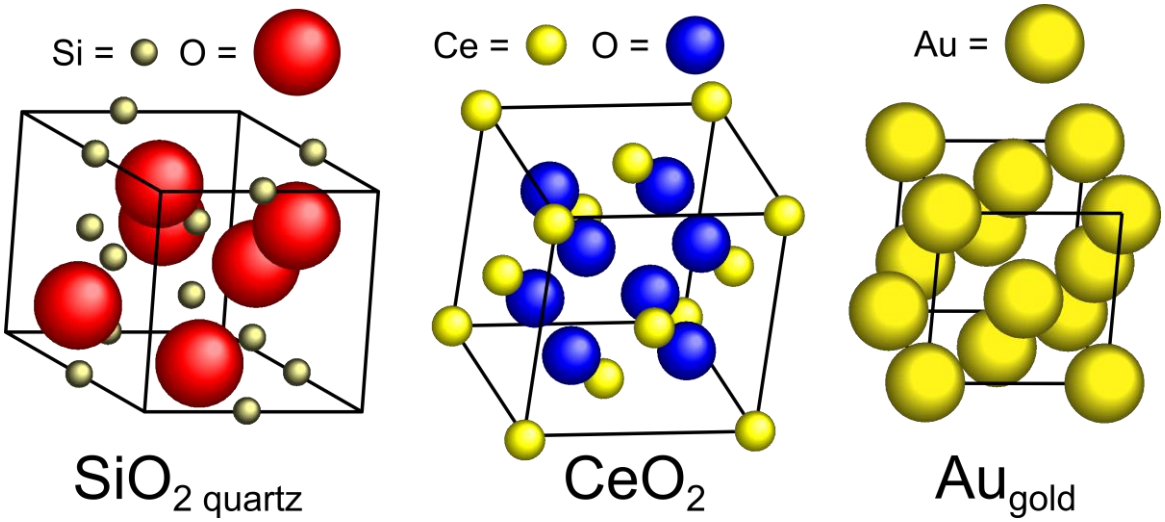

Fig. 14. The models of the crystal elementary cells of quartz ($SiO_{2\ quartz}$), cerium (IV) oxide (CeO_2) and gold (Au).

Systematic diffraction errors corrections and approach to temperature effects

The output of my script was a space–separated file listing fitted parameters of all analytical functions describing $SiO_{2\ quartz}$, Au and CeO_2 (if applicable) phases. The reflection positions corresponded to the Cu $K_{\alpha 1}$ radiation. Data were then loaded to MS® Office Excel program for further processing.

$$2\,\delta_{2\theta_{obs}} = 2 \cdot \frac{\Delta_R}{R} \cdot \cos\theta_{obs} \cdot \frac{180}{\pi} \tag{27}$$

where:

$2\delta_{2\theta_{obs}}$ – specimen displacement error in degrees 2θ;

R – goniometer radius;

Δ_R – specimen displacement from the goniometer rotation axis;

θ_{obs} – half of the experimentally observed scattering angle, $\frac{2\theta_{obs}}{2}$.

Quartz peaks were used to assess the specimen displacement error (SD error) and the actual temperature of the catalyst bed. Both values were obtained through refinement of quartz structure using least squares method. $SiO_{2\ quartz}$ crystal structure (Fig. 14) belongs to P 3_221 (D_3^6, no. 154) space group and it has lattice parameters $a = 4.9134$ Å and $c = 5.4042$ Å at $T = 25$°C [67]. Initial values of lattice constants were calculated with regard to the expected temperature and coefficient of thermal expansion (refer to next Section 2.5.5).

On the basis of quartz structure refinement, peak positions (or corresponding interplanar distances, d_{hkl}) of Au and CeO_2 (if applicable) were corrected for specimen displacement from the goniometer rotation axis. Any temperature effects due to exothermic CO oxidation reaction were also compensated and scaled to the temperature of the sample during the first exposure to helium (He). Temperature shift of scattering angle was adjusted according to:

$$d_{T_0} = \frac{d_{T_{obs}}}{CTE \cdot (T_{obs} - T_0) + 1} \quad (28)$$

where:

T_0 – catalyst temperature under He atmosphere;
T_{obs} – actual catalyst temperature under non–inert gas atmosphere;
d_{T_0} – distance between (hkl) planes in He atmosphere;
$d_{T_{obs}}$ – observed interplanar distance;
CTE – coefficient of thermal expansion.

Such processed data were the subject of interpretation of crystal structure dynamics induced by physi– and chemisorption, and chemical reaction carried out on the catalyst's surface.

2.5.5. Estimation of the coefficient of thermal expansion (CTE)

Values of coefficients of thermal expansion (CTE) for $SiO_{2\ quartz}$, Au and CeO_2 were established experimentally and corresponded well with the CTE range reported in the literature [68, 69].

In each case, the same *in–situ* PXRD-MS setup was used as for structure dynamics studies (Fig. 9). Powder sample was pressed onto the porous glass plate which was placed inside the measurement chamber with flow of He (20 ml · min^{-1}). Then the temperature was ramped according to the programmed sequence: 22°C (conditioned room temperature), 60°C, 120°C, 180°C, 230°C and 300°C.

For estimation of CTE for CeO_2 and Au, a 9.4% Au/CeO_2 catalyst was used. Quartz was also mixed with the catalyst in order to provide an internal standard for better systematic errors correction (thanks to peaks' FWHM ~0.1°C) and real specimen temperature.

Experimental DPs were processed using the script under the Fityk program described in Section 2.5.4. Next, the crystal structures of quartz, Au and CeO_2 were refined using least squares method. The lattice constants (or interplanar distances, d_{hkl}) were plotted against the temperature. It was possible to obtain CTE from this dependence following equation 29. The results are presented in Table 1.

$$\mathrm{CTE} = \frac{\tan \sphericalangle\left(d_{hkl} = f(T)\right)}{d_{0\ hkl}} \quad (29)$$

where:

$\tan \sphericalangle\left(d_{hkl} = f(T)\right)$ – slope of linear function fitted to d_{hkl} vs. T dependence;
$d_{0\ hkl}$ – interplanar distance measured at the lowest (room) T.

Table 1. Coefficients of thermal expansion (CTE) of quartz ($SiO_{2\ quartz}$), gold nanoparticles (AuNP) and cerium (IV) oxide (CeO_2).

Material (*hkl*)	$10^6 \cdot \mathrm{CTE}\ \left[\frac{\mathrm{m}}{\mathrm{m} \cdot \mathrm{K}}\right]$	Δ CTE [%]
$SiO_{2\ quartz}$ (100)	14.23	2.5
$SiO_{2\ quartz}$ (001)	7.97	3.7
AuNP	13.51	2.0
CeO_2	8.03	1.6

2.6. Simulations of powder diffraction patterns of model nanocrystals

Research focused on nanomaterials require special tools to analyse collected data. Sufficiently small objects usually cannot be described using theories that apply to bulk materials. Concerning X–Ray diffraction, the issues arise from the observation that the Braggs' law is not strictly obeyed [70]. Although clearly separated diffraction peaks appear in the diffraction pattern (DP) and they evidently correspond to a known crystal structure, large errors are obtained during the structure refinement. Hence, the analysis should account for phenomena accompanying the objects of very small size.

Because of lack of ready-to-use tools which would meet the expectations and needs of the research topic of nanocrystals structure dynamics, the group had decided to develop our own program – Cluster [37] – devoted to large-scale simulations of the structures of particles containing several thousand or tens of thousands metal atoms. The program was available as a fully working package and could be readily used in the research for this Thesis. On this basis, it was possible to predict observed experimental results and to provide support for the proposed explanations of these observations.

The Cluster program has an object–oriented code and graphical user interface (GUI). It allows to generate FCC-structured clusters (nanocrystals) of atoms:

- cuboctahedra;
- icosahedra;
- decahedra;
- spheroid;
- cylinder;
- hemisphere (also available with hexagonal close packed HCP structure);
- hemishell;
- cube.

Cuboctahedra, icosahedra and decahedra are created as "closed shell" crystals, i.e. each layer of atoms was fully occupied and the total number equalled consecutive magic numbers [71]. Icosahedra and decahedra preserve FCC ordering of atoms only in the limited range, because they contain 5–fold symmetry axes. All models can be further tailored using mirror and two mirror reflections, atoms can be deleted, added or selectively exchange for different ones.

The interactions between atoms in the modelled nanocrystal are described according to N-body potentials proposed by Sutton-Chen [38] and modified by Kaszkur for bimetallic systems [72]. The energy of the structure of a created model of a nanocrystal can be

minimised, which step is intended for relaxation of the strains and dissipation of the surface energy excess. The minimisation procedure is based on the Fletcher-Reeves conjugated gradient routine [73].

For such energetically optimised models of gold nanoparticles diffraction patterns could be calculated or the list of atoms positions could be exported and used for the TEM images simulation in the QSTEM program (refer to Section 2.9.4). Diffraction patterns profiles were obtained according to Debye summation formula 30 (sometimes called also "Debye scattering equation") [74, 35], which is a general equation for scattering from any ordered or disorder object.

$$I_{eu} = \sum_m \sum_n f_m f_n \frac{\sin kr_{mn}}{kr_{mn}} \qquad (30)$$

where:
I_{eu} – scattering intensity of the studied object (sample) in electron units (*eu*);
f_m, f_n – atomic scattering factor of atom "*m*" and "*n*";
r_{mn} – difference vector between the positions of atom "*m*" and "*n*" ($r_m - r_n$);
k – scattering vector $= \frac{4\pi \sin\theta}{\lambda}$; $\theta \equiv$ scattering angle; $\lambda \equiv$ wave length.

The intensity is the sum of the amplitude of scattering from different atoms and constitutes the average unmodified intensity from an array of atoms which takes all orientations in space. Worth of notice is the fact that only the magnitudes of r_{mn} between each and every pair of atoms are involved in the formula.

The theoretically calculated DPs, after rescaling, could be compared to the experimental profile and the dominant shape of the nanocrystals could be identified.

2.7. Fragmentation of gas molecules in the Mass Spectrometer

Both Mass Spectrometers (MS) mounted in the *in-operando* PXRD-MS and TEM-MS setups ionised the analysed gases probed from the outlet gas streams using electron bombardment (electron ionisation, EI). The quadrupole ion selector was set to let only positive ions (cations) to pass to the detectors. Because in the experiments only small molecules built from a few atoms were used or produced, fragmentation pathways included breaking molecular bonds, double ionisation of fragments and, rarely, addition of hydrogen ion. No isomerisation could occur. Hence, the MS spectra of molecules were very simple and consisted only from a couple of lines. The characteristic MS signals (*m/z* ratios) have been shown in Table 2.

Table 2. Fragmentation ions, their *m/z* ratio and relative ion current intensity (Int.) created by the electron ionisation (EI) in the mass spectrometer from selected gas molecules. Data sources: [75, 76].

Gas molecule	Ions								
H_2	Ion	H_2^+	H^+						
	m/z	2.0	1.0						
	Int.	9999	210						
He	Ion	He^+							
	m/z	4.0							
	Int.	9999							
H_2O	Ion	$^2H_2O^+$	$^2H^1HO$	H_2O^+	OH^+	O^+			
	m/z	20.0	19.0	18.0	17.0	16.0			
	Int.	30	50	9999	21222	90			
H_2O_2	Ion	$H_2O_2^+$	HO_2^+	OH^+	O^+				
	m/z	34.0	33.0	17.0	16.0				
	Int.	9999	87	198	20				
CO	Ion	$^{13}CO^+$	CO^+	O^+	C^+				
	m/z	29.0	28.0	16.0	12.0				
	Int.	120	9999	170	470				
N_2	Ion	$^{15}N^{14}N^+$	N_2^+	N^+					
	m/z	29.0	28.0	14.0					
	Int.	74	9999	1379					
O_2	Ion	O_2^+	O^+						
	m/z	32.0	16.0						
	Int.	9999	2180						
CO_2	Ion	$C^{18}O^{16}O^+$	$^{13}CO_2^+$	CO_2^+	$^{13}CO^+$	CO^+	CO_2^+	O^+	C^+
	m/z	46.0	45.0	44.0	29.0	28.0	22.0	16.0	12.0
	Int.	40	120	9999	10	981	190	961	871

2.8. X-Ray Fluorescence (XRF) Spectroscopy

Catalysts' compositions after syntheses were established by means of X–Ray Fluorescence Spectroscopy (XRF). PANalytical MiniPal 4 PW4025/00 energy dispersive spectrometer (EDXRF) was equipped with a rhodium lamp operating at the maximum voltage of 30 kV and a semiconductor Si–PIN detector. Optics was arranged in 2–dimensional (2D) geometry and sample was directly illuminated and excited by X–Rays. There was also provided a set of filters consisting of two Al foils (thin and thick), Mo

foil, Ag foil and empty filter slot. These filters were used during execution of the factory measurement program (Standardless® or Omnian® Analysis) in order to block bremsstrahlung, backscatter bulge, improve signal-to-noise ratio and promote intensity of low-energy peaks.

Powder samples were put into plastic containers, their bottoms made of Prolene 4™ 4 μm foil. The container was spun inside the holder to maintain collection of signal from the whole exposed sample area. The measurement time was always optimised individually, so that the detector working conditions were close to suggested by the manufacturer. Spectra were always acquired in the range from 0 to 30 keV.

Deconvolution of spectrum profile was done under PANalytical MiniPal software using its built–in interpreter of the results. Element characteristic lines were chosen from the library and their quantification was done according to inner algorithms and calibration files embedded in the program.

2.9. *ex-situ* TEM

2.9.1. Experimental setup

Basic *ex–situ* Transmission Electron Microscopy (TEM) examination was used for examination of sample morphology including:

- Au (and support if applicable) crystals size distribution;
- AuNPs dispersion on CeO_2 particles;
- Au–CeO_2 interface and crystal structures epitaxial relation;
- Au facets exposed to environment.

ex–situ TEM studies were conducted on two types of microscopes: FEI Titan Cubed 80-300 and JEOL JEM-ARM-200F. Their selected parameters were compared in Table 3.

Table 3. Comparison of capabilities of FEI Titan Cubed 80-300 and JEOL JEM-ARM-200F transmission electron microscopes.

Feature	FEI Titan Cubed 80-300	JEOL JEM-ARM-200F
Accelerating voltage [kV]	300	200
Relativistic electron wavelength [pm]	1.97	2.51
Type of electron gun	Schottky Field Emission Gun (FEG)	Cold FEG
Point resolution in transmission mode [pm]	90	110
Point resolution in scanning transmission mode [pm]	136	80

Both microscopes were equipped with the Energy Dispersive Spectrometers for analysis of elemental characteristic X radiation, so they were capable of analysis of sample composition. In the case of each sample and microscope, the highest available accelerating voltage was used. Illumination parameters (e.g. electron flux, gun spot size etc.) were adjusted according to current needs and sample behaviour under the beam, i.e. to avoid sample electrical charging, melting, decomposition and movement. Before conducting the imaging, the microscopes were aligned to maintain high brightness of their electron guns and to compensate aberrations of the magnetic lenses. The microscopes were controlled by their manufacturer softwares and cameras used for image acquisition were controlled by Gatan Digital Micrograph® which was later used for data analysis.

2.9.2. Specimen preparation

Powder samples of the catalysts were dispersed in H_2O using ultrasonic bath. Then TEM Cu grids (300 or 400 mesh) covered with amorphous holey or lacey carbon layer were immersed in catalysts' suspensions and left to dry on air. After the grid was mounted in the sample holder, it was pumped under ultra high vacuum (UHV) for at least 0.5 h, preferably overnight. No plasma cleaning was applied in order not to affect fragile AuNPs. Such prepared sample was ready to be inserted into the microscope's column and to be examined.

2.9.3. Data analysis

Collected high resolution (HR TEM) images were analysed using Gatan Digital Micrograph® software. The analysis procedure and steps varied according to the quantity to be obtained.

Gold crystal size distribution (CSD)

Gold crystals appeared to have the shapes close to spheres. Sometimes, particles exhibiting facets looking like the projection of cuboctahedron or characteristically "edge"–oriented icosahedron, or polyhedral shapes with visible 5-fold symmetry, like truncated decahedron, could be seen.

All these shapes, although they are highly symmetrical polyhedra, posed difficulties in defining a parameter which would describe their average outer sizes. To approach this problem, it was decided that each AuNP was circumscribed and the circumradius was regarded as the diameter of the particle.

Gathered values of circumradii were plotted as a histogram of CSD. Usually approx. 100 particles were analysed [77]. Since the potential errors originating from complicated shape of AuNPs had been identified in advance, the number of examined crystals was sometimes risen to approx. 500–1000.

Crystal structure determination

Crystal structure determination was based on identification of the structure projection exhibited by the particle. Further, it was possible to define the Miller *h k l* indices of the

facets which terminated the observed particle. If both structures of Au and CeO_2 were visible, the epitaxial relation of these structures could be described.

At least three parameters are vital to identify the structure projection: two interplanar spacings and an angle between those two sets of planes. These criteria are characteristic of a crystal structure which belongs to a certain space group, when the lattice parameters and distribution of the atoms in the elementary cell are known. When the measured values match to the theoretical ones (including system geometry), the projection can be considered as identified.

A set of planes is represented on the HR TEM image by a set of periodically altering stripes of high and low intensity. When two sets intercept each other, a pattern consisting of regularly distributed spots appear (e.g. Fig. 60). Interplanar distance is the width between two stripes (the former case) or rows of spots (the latter case). The required angle is the angle formed between two non–parallel rows of spots.

The same results can be obtained by using the (Fast) Fourier transformed (FT or FFT) HR TEM image. An image represents the real projection of the sample structure (real space image), while FT image reflects the reciprocal space corresponding to the periodic crystal structure visible in real space image. In reciprocal space, sets of planes from real space are represented by spots. While FT image is centrosymmetric, angles between these sets of planes are preserved and equal to those between the lines (zones) connecting the spots and the FT pattern centre. The distance of the spot from the FT pattern centre is inversely proportional to the interplanar distance in the real space, according to:

$$d\ [\mathrm{nm}] = \frac{1}{d^*\ [\mathrm{nm}^{-1}]} \tag{31}$$

where:
d – interplanar distance in real space, nanometres [nm];
d^* – interplanar distance in reciprocal space, inverse nanometres [nm^{-1}].

2.9.4. TEM image simulation

Simulations of the TEM images were particularly useful during analysis of the non-crystallographic particles containing 5–fold symmetry axis. The QSTEM program available from C. Koch was used to generate the theoretical images based on the provided structure model [78].

The program needed the structure model to work on. The QSTEM algorithm does not require the model to be an ordered atomic lattice with long–range periodicity preserved. Following the QSTEM manual, the appropriate configuration files were created. They contained: basic information about the model of a particle in vacuum (vectors describing the size of its volume, units of length, the total number of listed atoms and any additional parameters necessary for proper model handling and calculations); the positions of atoms in the Cartesian coordinate system (*x*, *y*, *z*), their element symbol and atomic masses. An example of such configuration file is presented in Fig. 15.

The structure models of cuboctahedral, decahedral and icosahedral gold nanoparticles were generated using the Cluster program, described in Section 2.6, with the aid of its built-in literature-based algorithms designed to output ideal “closed-shell” (i.e. each layer

of atoms was fully occupied) polyhedra of specific space symmetry. Atomic lattice of the cuboctahedral crystal was based on face-centred cubic (FCC) structure of gold. The decahedral and icosahedral particles were based on one or six 5–fold symmetry axes, respectively.

The QSTEM program relies on calculating at first the electron wave function after passing through the volume of the provided model. Then, the TEM image simulation is derived from the wave function. The calculation algorithm utilises the multislice approach which divide the model structure into slices of a given thickness along the electron wave propagation direction. The number of slices (or their thickness) is a variable and its value strongly influence the result of the calculations. Ideally, each slice should contain only one layer of atoms, i.e. atoms should not overlap each other within one slice. Accounting for the large number of atoms in a-few-nanometre nanoparticle which was rotated in space to exhibit preferred zone axis parallel to the direction of wave propagation, 0.15 Å slice thickness was chosen.

Other settings included:

- the resolution of the resulting wave image – it was kept as close as possible to 0.1 Å (dependent on the model size and its tilt in space);
- electron microscope (EM) beam energy – was set to the energy of the electron accelerated by 300 000 V;
- spherical aberration of EM lenses Cs = 0.001 mm;
- chromatic aberration of EM electron source, Cc = 0.001 mm;
- initial defocus (*dF*) of the image plane = –2 nm.

```
Number of particles = 49049
A = 1.0 Angstrom (basic length-scale)
H0(1,1) = 72.0 A  #
H0(1,2) = 0 A
H0(1,3) = 0 A
H0(2,1) = 0 A
H0(2,2) = 72.0 A   #
H0(2,3) = 0 A
H0(3,1) = 0 A
H0(3,2) = 0 A
H0(3,3) = 72.0 A #
.NO_VELOCITY.
entry_count = 3
197
Au
0.50000     0.50000     0.50000
0.50000     0.50000     0.52000
0.51458     0.48958     0.50896
…
```

Fig. 15. The beginning of a sample QSTEM configuration file which contains the structure model of a ~12 nm gold icosahedron. After the 3 first lines specifying *x*, *y*, *z* positions of Au atoms, there only another 49 046 sets of coordinates.

The obtained file with the wave function was uploaded to the TEM image simulation part of the QSTEM program, where the final theoretical micrograph was generated and as such was ready to be compared with the true image. The following settings were adjusted:

- EM accelerating voltage = 300 000 V;
- defocus (*dF*) = –2 nm;
- focal spread = 3 nm.

Such configuration allowed to obtain sharp images that could be compared with the experimentally collected data described in Section 3.4.

2.10. *in–operando* TEM

2.10.1. Experimental setup

In–operando TEM experiments under gaseous atmosphere were carried out using FEI Titan 60-300 microscope (operating at 300 kV accelerating voltage and equipped with Schottky FEG) and Protochips Atmosphere sample holder setup (see Fig. 16).

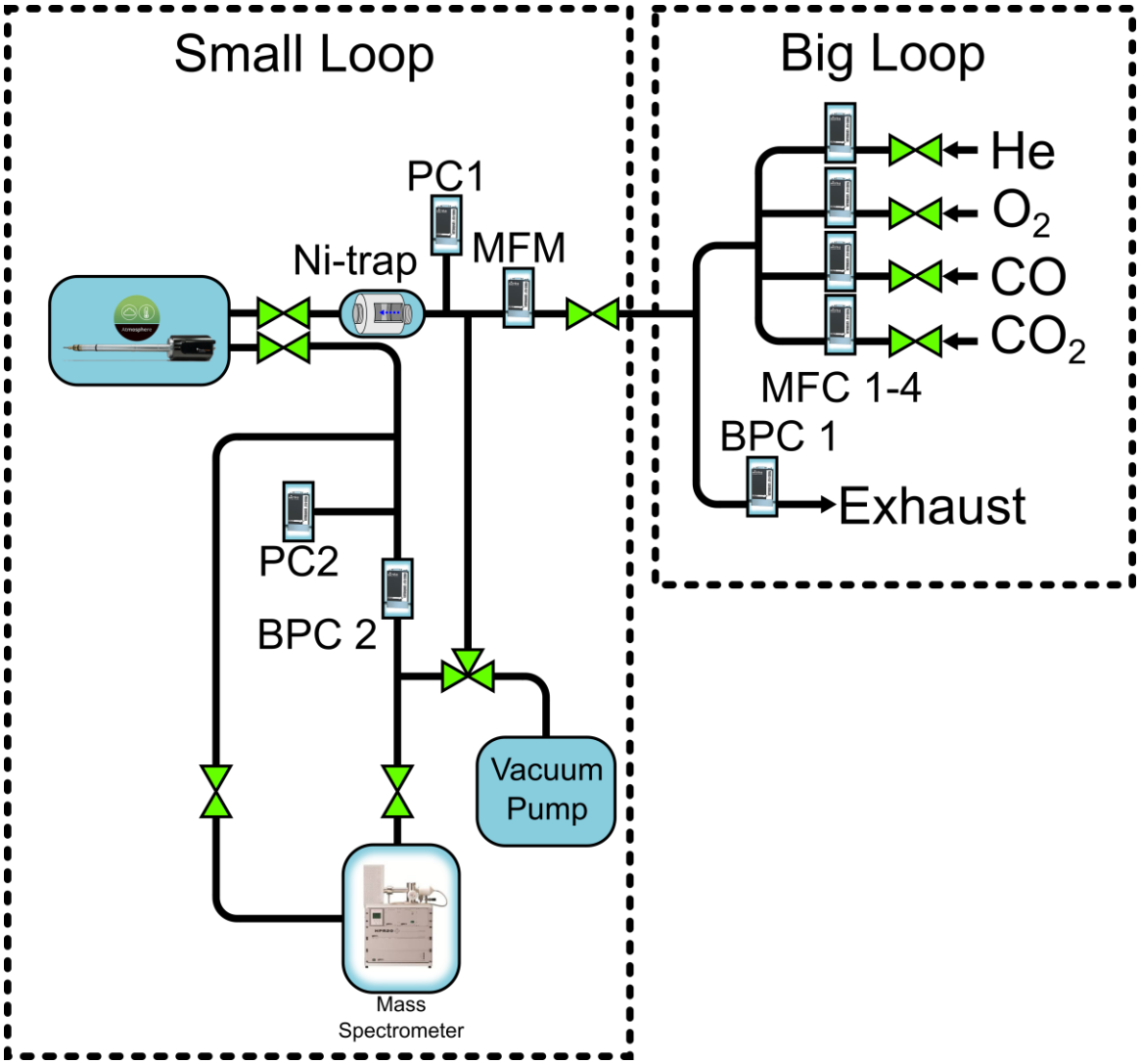

Fig. 16. The diagram of the *in–operando* TEM–MS experimental setup. The names "Small" and "Big loop" refer to the real length of the tubing used to construct the system. MFM ≡ mass flow meter; MFC ≡ mass flow controller; PC ≡ pressure indicator (main controlled parameter); BPC ≡ back pressure controller.

The sample holder was connected to the gas dosing and analysis system (called “small loop”) and further to the gas manifold (called “big loop”). Gas manifold was responsible for the composition of the gas stream. Pressurised bottles (provided by Westfalen AG) containing high purity He (99.999%), O_2 (99,999%), H_2 (99.99%) and CO (99.997%, in aluminium bottle) were connected to the Bronkhorst mass flow controllers (MFCs).

Main gas stream flow balanced at 100 ml · min^{-1} was partially redirected to the “small loop” through a leak valve. The inlet pressure on the sample holder was kept constant and was initially adjusted to value in 900 – 1000 mbar range. A $Ni(CO)_4$ trap (abbrev. to Ni-Trap, see Fig. 8, Fig. 16) was mounted just before the PEEK (polyether ether ketone) capillary (20 μm interior diameter) running directly to sample holder. Ni-Trap was heated to 200°C ± 0.5°C by a heating tape wrapped around the filter. The temperature was controlled by an in-house built PID temperature controller (based on the Eurotherm® unit) with automatically adjusted output power.

The outlet from the sample holder was evacuated through the Pfeiffer Prisma QMS 200 quadrupole mass spectrometer (MS). Pressure before the entrance to MS was maintained below 1 mbar, preferably even below 0.1 mbar.

Pressure inside the microreactor located at the Protochips Atmosphere sample holder tip was estimated to be the average of the inlet and outlet pressures as tubing was symmetric on both sides of the microreactor up to pressure indicators.

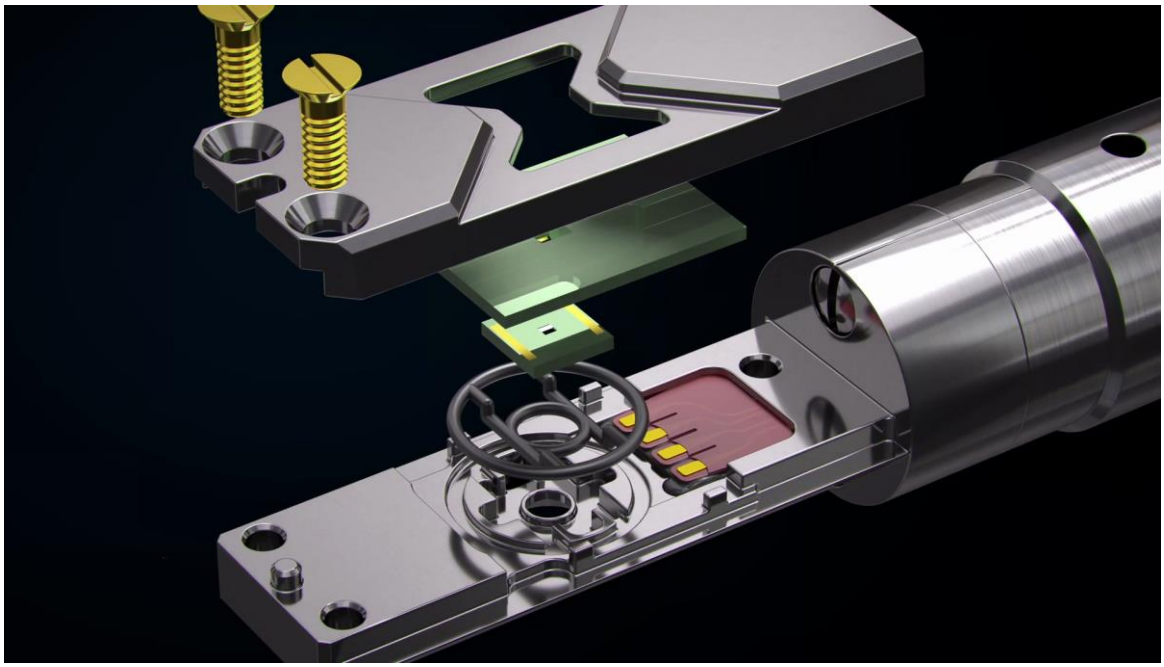

Fig. 17. The graphical visualization of the holder tip assembly containing the E–chips (two green plates) that constitute the microreactor. The gas chamber has been sealed against the microscope’s vacuum by a 2–part integrated gasket [79].

The microreactor was built of two, so called, E-chips made of silicon (Si) wafers sealed with two Viton™ O-rings (see Fig. 17). On the first E-chip there were: the ceramic SiC heater, its gold contacts and 6-9 holes in the middle of the heating zone. The second chip had a large hole that overlapped all holes of the first chip. Both E–chips were covered with amorphous 30 nm thick silicon nitride (SiN_x, unstoichiometric Si_3N_4). SiN_x acted as

windows closing the holes in Si wafers and separated the gas–containing interior of the microreactor from the UHV of the microscopes column (typically ~10^{-5} Pa).

2.10.2. Sample preparation

Powder sample of the catalyst was deposited on the heating zone of one of the chips. Catalyst was ultrasonically dispersed in H_2O and dropcasted on the surface of the wafer. The deposition process had to be monitored under the optical microscope, because the spacers separating both chips were only approx. 4 μm high (sample agglomerates could not be higher as the thin silicon nitride windows might break) and in the field of view of the electron beam there should be enough beam–transmittable material. Both E–chips and the rubber O–ring were kept in UHV chamber overnight before the TEM holder can be assembled. This step was crucial to avoid contamination occurring during imaging under the electron beam inside the microscope.

After the microreactor was assembled on the tip of the sample holder and it was proved to be leak tight it was inserted to the microscope's column. Then the air was evacuated from the microreactor by cyclic pumping and purging with helium 3 times. It was then left overnight at 200°C under "synthetic air" (O_2 : He = 1 : 4 by volume) to condition the sample and to desorb weakly bound contaminants before it would be exposed to highly energetic electron beam.

2.10.3. Microreactor pre-treatment and optimisation

Concentrated electron beam is likely to decompose carbon containing compounds (e.g.: carbohydrates). This results in contamination of the sample surface by deposition of usually amorphous carbon layer on it. This contamination shell poses problem with high resolution imaging of the crystal structure of the sample as the contrast on the image is lost due to extensive electron scattering on disordered phase. Therefore, it was necessary to determine the optimal CO : O_2 volumetric ratio and whether the gas stream should be diluted with inert He. It was foreseen that, because of different engineering design of the microreactor comparing to chemical glass reactor or PXRD chamber described earlier (see Sections 2.4 and 2.5.2), the experimental conditions, i.e. gas atmosphere composition and temperature, might vary from those used in other setups.

Optimisation of the reaction conditions was carried out by:

- varying CO, O_2 and He concentration in the gas stream feeding the "small loop";
- ramping the temperature from ambient to 600°C.

It was found that 9.4%$_{wt.}$ Au/CeO_2 catalyst was inactive at temperatures below 300°C. In addition, temperature of 200°C was chosen for preliminary investigation of sample in its inactive state while using the Protochips® holder. Sample was considered to be active at 400°C and this temperature was still much below the temperature of spontaneous CO ignition which is 605°C [80]. The highest CO_2 signal rise when approaching 400°C was found for stoichiometric CO : O_2 = 2 : 1 (by volume) gas composition without dilution with He (see Fig. 18). Helium was used as an inert gas and the catalyst under He atmosphere at 400°C served as reference state in comparison with its state when under reaction gas mixture CO was actively converted to CO_2.

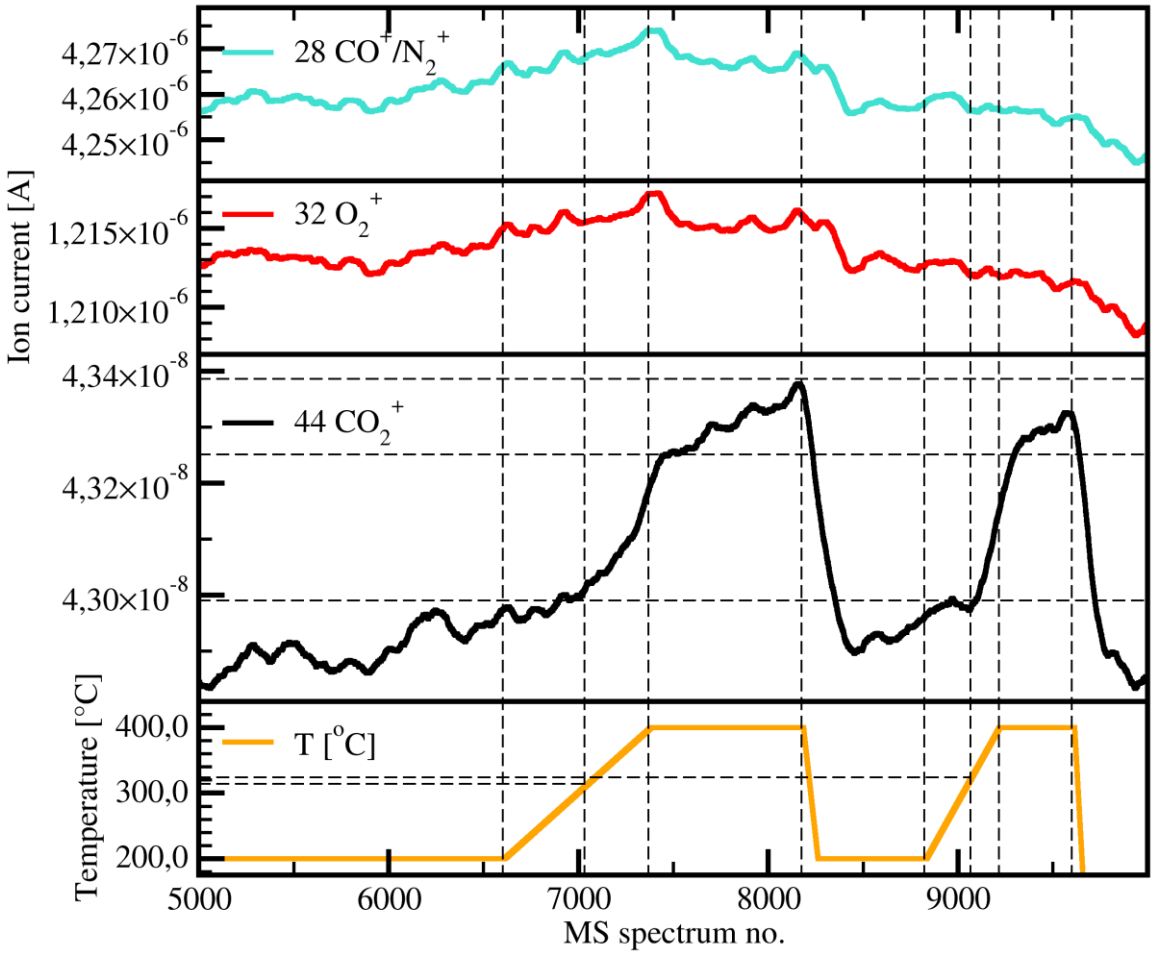

Fig. 18. The dependence of mass spectrometry (MS) signals (ratio of mass to the charge of an ion) 28 ≡ CO^+, 32 ≡ O_2^+ and 44 ≡ CO_2^+ on the temperature of the heater in the TEM microreactor fed with 20 μL · min^{-1} gas stream containing CO : O_2 = 2 : 1 (by volume). Here 2 cycles with different rate of heating are shown, 5 and 10°C · min^{-1} respectively. Accounting for the delay of MS indications, the activation temperature varies from 315 ± 5°C to 338 ± 10°C for cycle 1 and 2, respectively.

2.10.4. Beam influence evaluation

The electron beam available in the electron microscope, which can be used for sample imaging, diffraction and spectroscopic studies, is probably the source with the highest energy flux that a specimen can be directly exposed to [50]. Consequently, it was crucial to determine whether or not and to what extent the energy: heat, charge and kinetic energy; transferred to the sample influenced its state and the results obtained. Hence, the last step, before the main *in-operando* TEM studies could be performed, was to conduct the beam influence tests. Highly energetic electron beam interacts with the sample in several ways that can damage or severely alter the investigated material:

- transfers electric charge that can accumulate if it is not drained efficiently;
- heats up the sample by absorbing part of the incident beam;
- transfers energy as a result of inelastic scattering phenomena that, among other implications, can destroy molecular (or atomic) bonds, induce crystal phase changes, recrystallisation or amorphisation;
- chemical reactions in the gas phase may be induced.

The simplest way to avoid undesired effects is to reduce appropriately the beam dose (expressed usually in e · nm^{-2} · s^{-1}) while maintaining sufficient electron flux to perform

research. Secondly, the specimen can be irradiated by the beam only during acquisition of images. In the meanwhile, when the camera reads out data or time to the next acquisition is counted down, the beam can be hidden behind the shutter or blanked away from the specimen, thus minimising the exposure time of the studied sample area to the beam.

Beam damage studies involved monitoring the same area of the sample (on E-chip window) during 3 hours, at 200°C, under the reaction gas atmosphere, using 1 000, 5 000, 10 000, 50 000, 100 000 and 1 000 000 $e \cdot nm^{-2} \cdot s^{-1}$ electron flux. It was found that the beam did not alter the course of chemical reactions (i.e. beam itself did not induce chemical reactions) and the catalyst sample was resistant even against high beam doses for sufficiently short period of time. Shortening of the sample exposition time to the beam was achieved with usage of the pre–specimen shutter, so the catalyst was illuminated only during image or diffraction pattern acquisition. Unfortunately, extensive constant electron irradiation when pre-specimen beam blanker was not used resulted mainly in recrystalisation of smallest fragile nanoparticles or in change of their orientation in space. Such case has been described in Section 3.5.3. The beam electron dose used during: low magnification imaging, high resolution imaging and electron diffraction patterns acquisition; was limited to ~30 000, ~200 000 and ~5 000 $\frac{e}{nm^2 \cdot s}$, respectively (except for the "high dose" studies, where it was ~870 000 $\frac{e}{nm^2 \cdot s}$). The other details concerning the measurement strategies have been described in the next Section 2.10.5.

2.10.5. Measurement details and settings

Having done all preparation steps, the real space imaging (true magnified imaging) and electron diffraction (reciprocal space projection) studies could be carried out. Low magnification (Low–MAG) imaging gave insight into any possible sample morphology changes occurring at nanometre scale. High resolution (Hi-Res) imaging allowed to examine evolution of individual particles, preferably also changes happening to their atomic lattices. Electron diffraction patterns (EDP) reflected well crystal structure changes which can be spotted only with sub-Angstrom resolution. In all modes, catalyst sample was exposed to pure He and to $CO : O_2$ (2 : 1, by volume) gas mixture at 400°C. Simultaneously, MS spectra of the gas stream coming out from the microreactor were recorded to ensure that the active state of the catalyst was studied. The details on the measurement settings are shown in Table 4.

Under each of the experimental conditions, a series of 360 images or 2D EDP was recorded with time interval of 10 s. Helium atmosphere was used as a reference atmosphere, where the catalyst was free from surface adsorbates and crystal structures (gold and support) were relaxed.

Table 4. The measurement settings for low magnification (Low-MAG) and high resolution (Hi–Res) imaging, and electron diffraction patterns (EDP) series acquisition: technical parameters, gas stream composition (volume ratio) and microreactor's heater temperature.

	Low-MAG Imaging		**Hi-Res Imaging**		**EDP acquisition**	
Magnification	× 61 000		× 380 000		–	
Objective aperture	50 μm		none		–	
Camera length	–		–		245 mm	
Selected area aperture	–		–		40 μm	
Exposure time	2.0 s		2.0 s		2.0 s	
Image/pattern rec. interval	10.0 s		10.0 s		10.0 s	
Beam dose	~30 000 $\frac{e}{nm^2 \cdot s}$		~200 000 $\frac{e}{nm^2 \cdot s}$		~5 000 $\frac{e}{nm^2 \cdot s}$	
	He	2 CO + O_2	He	2 CO + O_2	He	2 CO + O_2
400°C						

2.10.6. Data analysis – image series

Images from each series were thoroughly examined and compared under Gatan Digital Micrograph® program in order to notice any morphological or structural changes of the sample or differences in contrast of visible particles. Images taken before and after EDP series acquisition were also analysed to check that the studied sample area did not evolve.

With help of ImageJ [81] or Fiji [82], images from each series were cropped appropriately and converted to a movie according to the time stamp of each image file. Such a way of data presentation allows to spot differences between images more easily.

2.10.7. Data analysis – EDPs series

At first, EDPs were examined in the same way as real space images (see Section 2.10.6). After proving that EDP series was stable in time, 1 pattern recorded every 10 minutes (7 patterns in total) was selected for further processing. Gatan Digital Micrograph with PASAD plugin [83] and Fityk [65] were used to extract the information about catalyst crystal structure from 2D diffraction patterns.

The shade of beam stop was always visible on EDP. It was precisely cropped with tool available as a part of PASAD plugin, which refined exact shape on the basis of the pixel intensity profile near the edge of the beam stop shade. Next, the coordinates of pattern's centre (position of the incident beam) was roughly assessed assuming that traces of Debye-Scherrer cones are ideal rings. Then, refinement of the centre position and ellipticity parameters (ratio of the radii of the ellipsis, called "distortion", and how it is rotated with respect to the image vertical direction) of actually non-ideal Debye-Scherrer

rings was needed. To achieve it, it was necessary to remove the central part of the pattern up to ~ 5 nm^{-1}. PASAD plugin took into account the most intense ring, which was usually one of the first rings corresponding to large interplanar spacings. These rings hed small diameters, so ellipticity assessment was subjected to errors and deviateed from the true values. By removing a few rings representing electrons scattered at low angles, PASAD plugin was forced to work on further rings and the quality of its calculation results was greatly improved (e.g.: ellipticity parameters were much more consistent among patterns selected from one series).

Next, the incident beam position and ellipticity corrections were copied to the raw image with cropped beam stop shade. There were doubts if the azimuthal averaging of the whole image handled properly the complicated shape left after the beam stop. As the EDP is centrosymmetric and the high-enough overall number of crystals scattered the electrons, it was allowed to average azimuthally only one half of the 2D EDP, which was proved to be performed correctly by the PASAD plugin. The summary on data processing utilizing the PASAD plugin and Gatan Digital Micrograph has been visualised in Fig. 19.

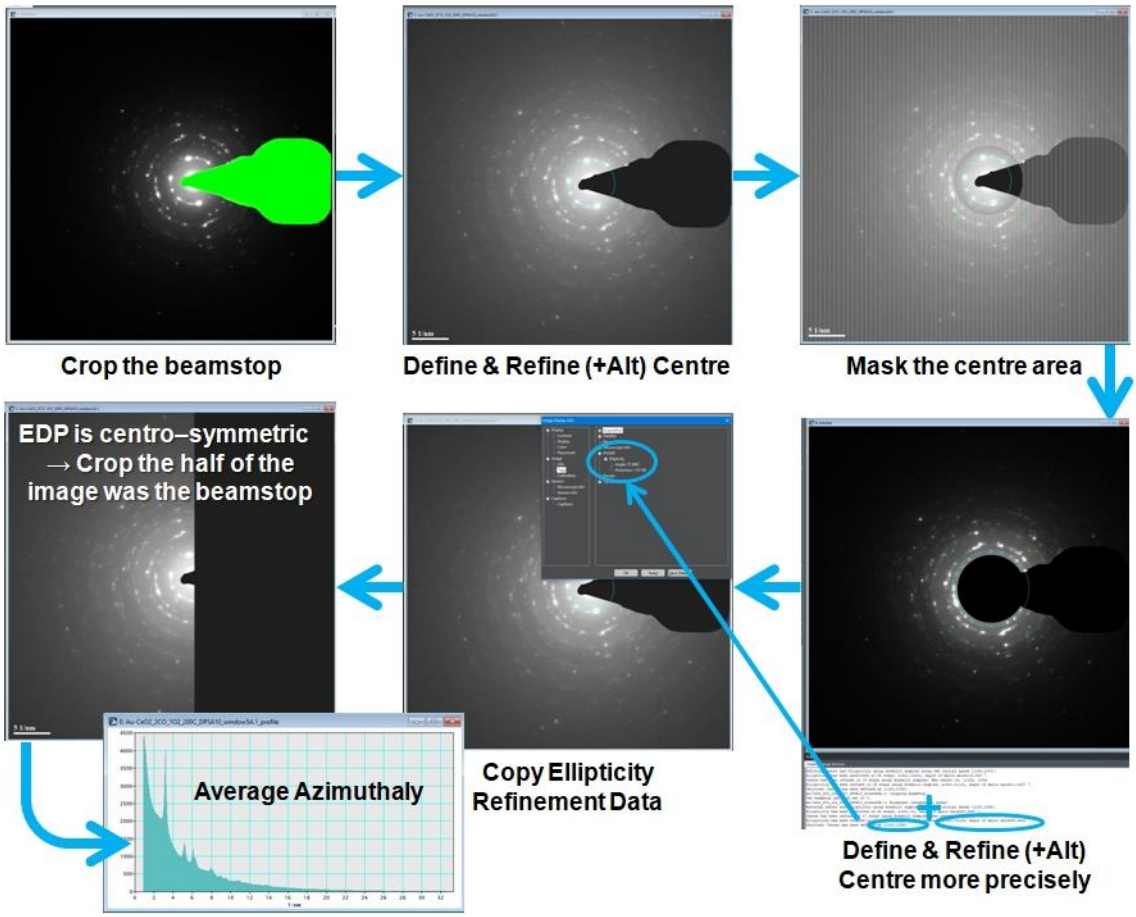

Fig. 19. The overview of the electron diffraction data processing procedure utilizing the PASAD plugin [83] and the Gatan® Digital Micrograph program.

The resulting 1D electron diffraction plot of intensity against scattering vector k [nm^{-1}] was saved as an XY text file and imported to Fityk program. Before fitting a model with Voigt analytic functions, background had to be subtracted. As background profile, the EDP of an empty SiN_x window was used. It was simply scaled to the catalyst EDP with an appropriate multiplication factor and then subtracted from it. In the next step, Voigt functions were fitted to the residual diffraction pattern. Here, one Voigt function per one

diffraction peak was sufficient to describe the experimental peak profile. Wave length of an electron accelerated with 300 kV equals precisely to 1.97 pm and the energy spread due to electron gun properties is negligible in this case. The parameters of Voigt functions contributing to the fitted model of the catalyst crystal structure were listed to a space-separated file and were ready for interpretation of crystal structure dynamics induced on the catalyst's surface.

3. Results and discussion

3.1. Catalysts' composition

The composition of each catalyst was checked after the synthesis to ensure that the desired gold loading on the support had been achieved and no impurities had been introduced. Samples after *in–operando* PXRD–MS experiments were also examined mainly towards confirmation of the Ni-Trap good performance.

As a rule, all catalysts were investigated by X-Ray fluorescence (XRF) spectroscopy (see results listed in Table 7). This was a suitable tool for identification of elements starting from sodium (Na), i.e. which atomic number *Z* is higher than 11 and core electron binding energy is above 1 keV. In the case of carbon supported catalyst, the characteristic lines of carbon were below the energy detection limit of the used spectrometer. This low-energy radiation was absorbed and scattered in air (which also consisted of carbon containing compounds) and deconvolution of the spectrum required advanced background and precise inter-element corrections. Therefore, XRF technique served in the case of Au/C catalyst investigation only for the determination of the possible presence of any impurities.

XRF spectra were all affected by signals coming from the interior of the apparatus. The elements whose characteristic fluorescent lines usually appeared in the spectra have been listed in Table 5. These elements were present in the materials the inner parts of the spectrometer had been made of.

Table 5. Characteristic X–Ray emission energies of elements commonly appearing in the XRF spectra. The se signal originate from the fluorescence of inner parts of the XRF spectrometer.

Element		Characteristic X-Ray emission energy [keV]	
Name	Symbol	K_α	K_β
argon	Ar	2.957	3.190
iron	Fe	6.398	7.057
cobalt	Co	6.924	7.648
nickel	Ni	7.471	8.263
copper	Cu	8.040	8.904

In each *in-operando* PXRD–MS, catalysts are pressed onto a porous glass plate. After dismounting from the diffractometer, they were analysed by means of XRF as such, together with the glass plate. Consequently, lines of elements listed in Table 6 were frequently found in the spectra of examined samples. They originated from the composition of the porous glass plates supporting the samples in the PXRD chamber.

Table 6. Characteristic X–Ray emission energies of additional elements (with respect to Table 5) commonly appearing in the XRF spectra of the samples after the *in-operando* PXRD-MS experiments.

Element		Characteristic X-Ray emission energy [keV]			
Name	Symbol	K_α	K_β	L_α	L_β
aluminium	Al	1.486	–	–	–
silicon	Si	1.739	1.836	–	–
calcium	Ca	3.690	4.012	–	–
titanium	Ti	4.508	4.931	–	–
zirconium	Zr	15.744	17.665	2.042	2.124

Commonly, all additional lines originating from the spectrometer inner parts had very small intensity. Thus, after quantification, their concentration stayed within the error level of the technique, i.e. below 1%$_{at.}$. Elements originating from diffractometer sample holder parts (glass plate) were easy to distinguish as they had low atomic mass. The composition of the catalyst after the *in-operando* PXRD-MS experiments was unchanged,

Table 7. Results of XRF analyses of catalysts after their syntheses. The last row of the table presents Au loading (%$_{wt.}$) with respect to the mass of the catalyst. For Au/C catalyst Au loading was assumed to meet the expected value.

	Concentration [%$_{at.}$]		
Element	Au/CeO_2	Au/SiO_2	Au/C
Al	-	1.20	-
Si	-	82.96	-
S	-	-	1.84
Cl	-	0.01	-
Ar	-	1.86	2.00
Ca	-	0.09	0.15
Ti	-	0.05	-
Fe	-	0.06	0.43
Ni	-	0.01	0.03
Cu	0.08	0.06	0.16
Ce	88.63	-	-
Au	11.29	13.70	95.40
Au Loading	9.4 %$_{wt.}$	7.2% $_{wt.}$	20.0% $_{wt.}$

3.2. Catalytic properties assessment

For chemical performance tests, two sets of experiments were performed. They both involved studies using plug flow types of reactors (PFR). The setups have been described in Sections 2.4.1 and 2.4.2. The main part of each system was the U-shaped reactor with fixed catalyst bed. Construction details on those two apparatus configurations are briefly summarised below.

In one case, the setup required a thin, ~1 mm, layer of powder formed on the porous sintered glass plate inside the glass reactor. Gas stream was supplied form the same manifold which was used for *in-operando* PXRD–MS studies. The outgoing stream was analysed by mass spectrometer. Results from experiments which utilised this apparatus have been described in Sections 3.2.1 – 3.2.4.

In the other system, the catalyst sample was mixed with silicon carbide (SiC) and thus diluted. The reactor was connected to the gas supply system based on MFCs and pressurised bottles. The chemical output was measured with Emerson® X-STREAM continuous gas analyser. Only the most promising 9.4%$_{wt.}$ Au/CeO_2 catalyst was investigated in this way and the results have been shown in Section 3.2.5.

Conducted experiments aimed, first, at testing whether the apparatus as a whole was sufficiently inert and would not violate chemical result analysis, secondly, at evaluation of catalytic properties of all 3 catalysts (Au/CeO_2, Au/ SiO_2, Au/C) before carrying out experiments in our customized in-house built PXRD vacuum-gas chamber.

Each of the 3 studied catalysts proved to be stable for long enough time spent on stream. Thus, they were suitable for *in-operando* PXRD–MS studies, which were time consuming due to diffraction patterns acquisition duration.

3.2.1. Performance of the empty glass reactor with thin layer specimen bed

An empty clean glass reactor was connected to the vacuum-gas system. The programmed gas sequence (see Fig. 11) was the same as used later during tests of the catalysts. Temperature was set to 160°C as it was the highest temperature ever used in conducted experiments (at least 100°C was required to avoid H_2O condensation and, in PXRD chamber, 150°C temperature prevented any extra $Ni(CO)_4$ formation behind the Ni-Trap). The results of the empty reactor performance are presented in Fig. 20 and Table 8.

Firstly, there are only traces of CO_2 production during stoichiometric and preferential CO oxidation (abbr. sCOOX and PROX, respectively). Very low ion currents (i.e. $< 2.0 \cdot 10^{-7}$) are not measured properly by the Faraday MS detector, so values reported by SEM detector were taken into consideration. Generally, the yields of CO_2 or H_2O production never exceed 1%.

These negligible amounts of the main product (CO_2) of both reactions and PROX reaction side product (H_2O) could be the consequence of very limited, but still visible, chemical activity of Ni-Trap, which had been made of stainless steel and was heated up over 200°C. Commercially available iron oxide-based catalyst for High Temperature (Water-Gas) Shift (HT–WGS, or shortly HTS) reaction (CO conversion with H_2O steam) start to operate at approx. 250°C [84]. Swagelok® steel contains iron (Fe), chromium (Cr), nickel

(Ni) and molybdenum (Mo). All these elements form oxides easily and Ni-Trap could be slightly oxidised on the surface. This thin oxide layer might be reduced by hydrogen. Furthermore, H_2 diffuses through steel, which is a slow reversible process (yet hydrogen is distributed in pressurised steel bottles), so this might be the reason why some infinitesimally small amounts of H_2O and H_2O_2 (hydrogen peroxide) are detected in pure oxygen atmosphere.

Further, the suggested explanation fits also to PROX-sCOOX-PROX gas sequence. However, the comparably high H_2O^+ signal level under carbon dioxide atmosphere is believed to be the consequence of low purity CO_2 (only 99.8%, ref to Section 2.5.1) supplied from the pressurised bottle.

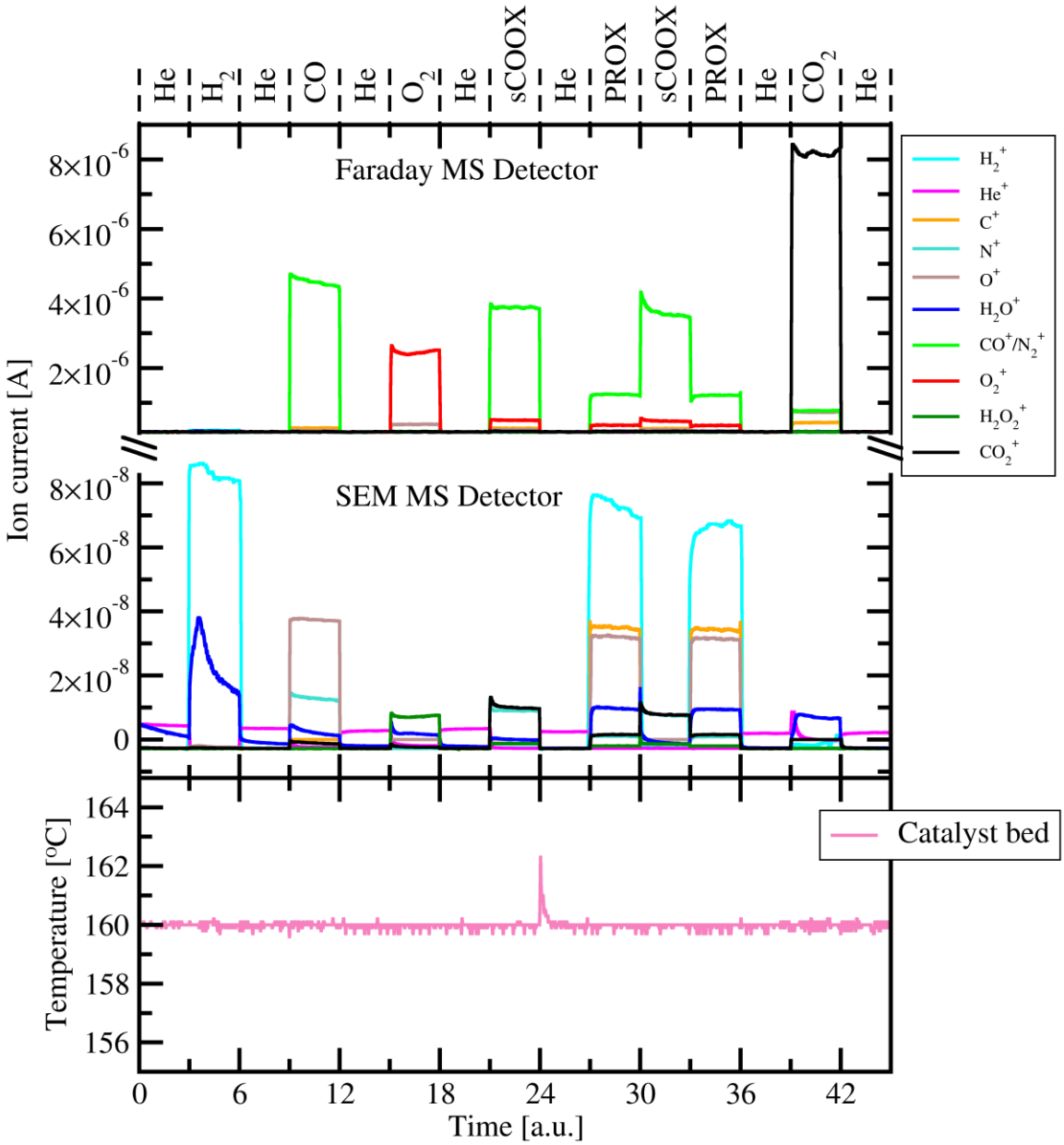

Fig. 20. Outlet gas composition analysis by mass spectrometry (MS) of the stream leaving the empty glass reactor and the actual temperature of the empty specimen bed. MS signals corresponding to relevant cations are shown. Data are plotted against time normalized to time required by the experimental computer script to collect 30 data points in each log file (approx. 30 minutes). sCOOX ≡ stoichiometric CO oxidation; PROX ≡ preferential oxidation (of CO).

Any traces of impurities (nitrogen, water, CO_2, etc.) must originate from the inside of the setup, because under helium (all exposure starting from 12 – 15 time units in Fig. 20) the whole system proved to be air–tight. During first two exposures to He, the $\frac{m}{z} = 18\ amu$ signal seemed to be generated by the residual water flushed out gradually from the setup as it was vented by air after every experiment.

Table 8. Outlet gas composition and reaction yields analysis for the empty glass reactor. sCOOX ≡ stoichiometric CO oxidation; PROX ≡ preferential oxidation (of CO).

Compound	Ion current [$\times 10^{-6}$ A]		$\eta_{\rightarrow CO_2}$ [%]		$\eta_{\rightarrow H_2O}$ [%]	
	sCOOX	PROX	sCOOX	PROX	sCOOX	PROX
CO	3.50	1.24	0.15	0.09	-	-
O_2	0.475	0.35	0.55	0.15	0.00	1.49
CO_2	0.0076	0.0015	-	-	-	-
H_2O	0.00	0.0099	-	-	-	-

3.2.2. Performance of Au/CeO_2 catalyst

212 mg of 9.4%$_{wt.}$ Au/CeO_2 was loaded to the glass reactor in which the temperature was set to 125°C. The catalytic activity in stoichiometric and selective (preferential) CO oxidation was studied under programmed sequence of gases. The chemical performance results have been presented in Fig. 21 and Table 9.

At the beginning a small amount of water was released from the sample under helium, which reflected the temperature ramp during this first stage of experiment. Then the H_2O^+ signal rose again when hydrogen was introduced, similarly to the case of the empty reactor (Section 3.2.1), so most probably it could be again attributed to the modest chemical activity of Ni–Trap connected with reduction of stainless steel surface oxides. The water signal increase during exposure to oxygen is also likely to be bound to hydrogen accumulated in Ni-Trap chassis.

Traces of CO_2 detected while the reactor was purged with carbon monoxide, are believed to reflect the observations made for pure cerium dioxide studied in the PXRD chamber (see Section 3.3.2). Unlike the case of the empty glass reactor or empty chamber, slight CO_2 production, catalysed by CeO_2, was also noticed.

Under studied conditions, pure CeO_2 proved to be rather inactive in CO oxidation. On the contrary, Au/CeO_2 catalyst reached full conversion of oxygen to carbon dioxide in both sCOOX and PROX reactions. The CO traces left in the stream could originate from little error in calibration of the two MFCs used in the vacuum-gas manifold. In PROX reaction, O_2 was partially consumed to produce water, what was a negligible effect in sCOOX.

Due to the fact that:

- CO oxidation is a highly exothermic reaction ($\Delta H^{298K} = -283\ \mathrm{kJ \cdot mol^{-1}}$ [12]);
- the catalyst with relatively high loading was used (9.4%$_{wt.}$ is a 3 – 100 fold excess comparing to literature reports, e.g. [85]),

the undesired phenomenon called "catalyst *light-off*" [86] was always observed in the case of Au/CeO_2. Here, in the glass reactor during first sCOOX exposure (14 – 22 time units in Fig. 21), the thermocouple initially reported the temperature as high as 193°C of the catalyst bed which led to furnace power cut-out because of detected overheating. Nevertheless, the reaction was able to maintain the temperature of the bed at ~172°C while the furnace power was sufficient to keep only 115 – 120°C. Similarly in PROX (24 – 26 time units in Fig. 21), the temperature increased to 167°C at first and stabilised at 154°C right after.

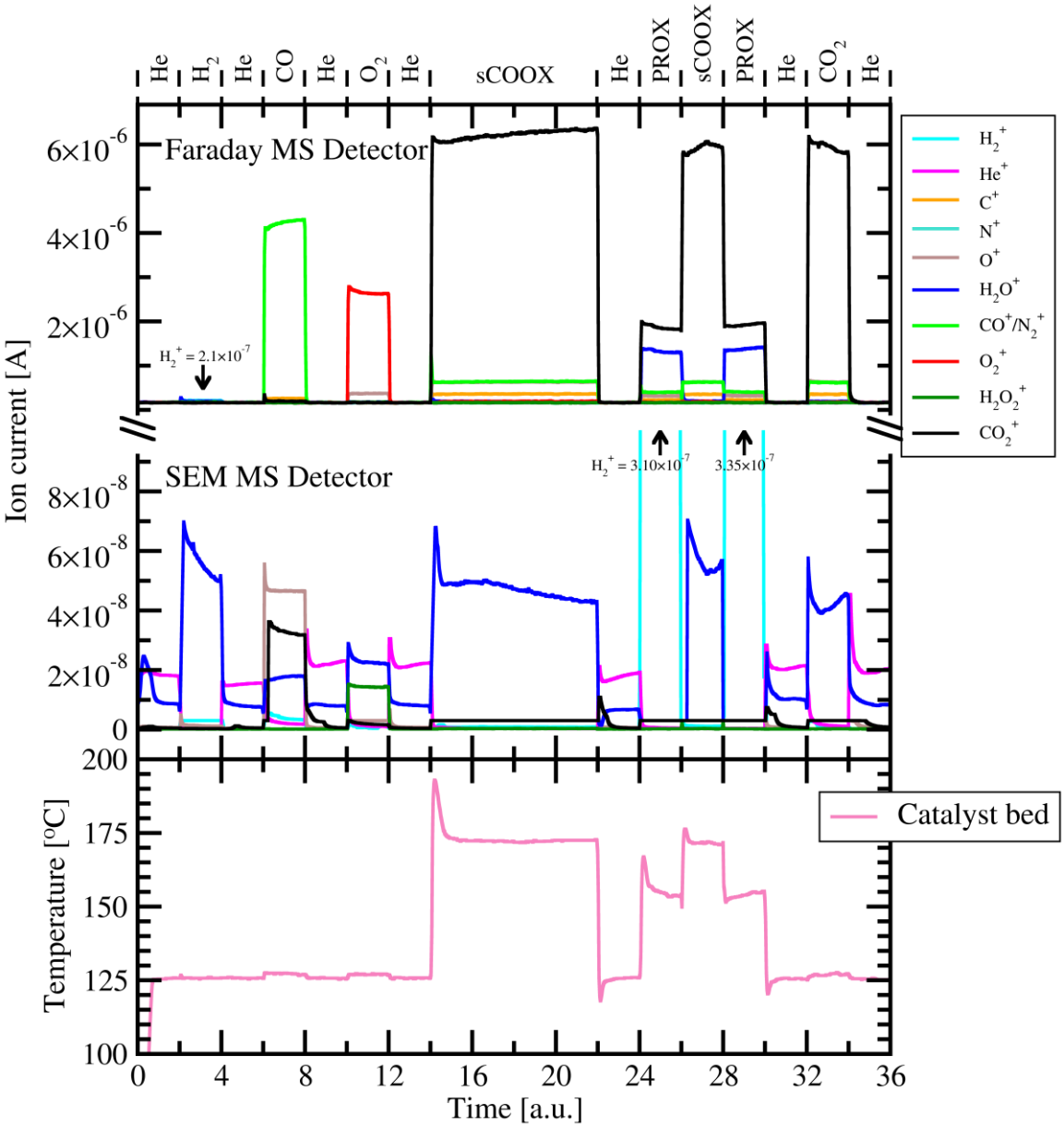

Fig. 21. Mass spectrometry (MS) analysis of composition of the gas stream leaving the glass reactor loaded with 9.4%$_{wt.}$ Au/CeO_2 and the actual temperature of the specimen bed. MS signals corresponding to relevant cations are shown. Data are plotted against time normalized to time required by the experimental computer script to collect 30 data points in each log file (approx. 30 minutes). sCOOX ≡ stoichiometric CO oxidation; PROX ≡ preferential oxidation (of CO).

Bearing in mind, that light-off may happen also in the PXRD chamber, crystalline quartz was always added to the specimen for the *in-operando* PXRD-MS studies. It served as a reference material necessary for compensation of thermal expansion of crystal structures.

Table 9. Outlet gas composition and reaction yields analysis for the sCOOX and PROX reaction performed on 9.4%$_{wt.}$ Au/CeO_2 catalyst. sCOOX ≡ stoichiometric CO oxidation; PROX ≡ preferential oxidation (of CO).

Compound	Ion current [$\times 10^{-6}$ A]		$\eta_{\rightarrow CO_2}$ [%]		$\eta_{\rightarrow H_2O}$ [%]	
	sCOOX	PROX	sCOOX	PROX	sCOOX	PROX
CO	0.63	0.39	87.6	77.2	-	-
O_2	0.00	0.00	98.9	47.9	1.2	52.1
CO_2	6.20	1.85	-	-	-	-
H_2O	0.05	1.30	-	-	-	-
Selectivity to CO_2, S_{CO_2} [%]:				47.9		

3.2.3. Performance of Au/SiO_2 catalyst

89 mg of 7.16%$_{wt.}$ Au/SiO_2 was loaded to the glass reactor. After the air was flushed out from the reactor with helium, the activation procedure was applied. This activation

Table 10. Outlet gas composition and reaction yield analysis for the sCOOX and PROX reactions performed on 7.16%$_{wt.}$ Au/SiO_2 catalyst at 110°C and 160°C. sCOOX ≡ stoichiometric CO oxidation; PROX ≡ preferential oxidation (of CO).

$T = 110°C$						
Compound	Ion current [$\times 10^{-6}$ A]		$\eta_{\rightarrow CO_2}$ [%]		$\eta_{\rightarrow H_2O}$ [%]	
	sCOOX	PROX	sCOOX	PROX	sCOOX	PROX
CO	1.15	0.52	0.40	0.29	-	-
O_2	0.55	0.43	0.41	0.16	0.58	3.02
CO_2	0.0065	0.025	-	-	-	-
H_2O	0.006	0.0021	-	-	-	-
Selectivity to CO_2, S_{CO_2} [%]:				5.15		
$T = 160°C$						
Compound	Ion current [$\times 10^{-6}$ A]		$\eta_{\rightarrow CO_2}$ [%]		$\eta_{\rightarrow H_2O}$ [%]	
	sCOOX	PROX	sCOOX	PROX	sCOOX	PROX
CO	1.1	0.43	22.6	40.8	-	-
O_2	0.52	0.26	20.0	22.2	0.6	37.9
CO_2	0.43	0.43	-	-	-	-
H_2O	0.0088	0.47	-	-	-	-
Selectivity to CO_2, S_{CO_2} [%]:				36.9		

procedure has been described in Section 2.3.2, however the last step (conditioning under the hydrogen) was slightly modified – it was performed at 180°C. Initially, the catalytic activity was studied at the temperature 110°C with the same gas reaction mixture as for other experiments. As no desired chemical activity was found, it was decided to carry out the temperature ramp under PROX reaction conditions. Then sCOOX was checked too. MS results together with the temperature profile have been shown in Fig. 22.

At the beginning, during catalyst exposures to H_2, CO and O_2, as well as later during exposure to pure CO_2, only traces of water released from the specimen were detected. Under sCOOX reaction conditions (time period between 14 – 18 and 26 – 30 time units in Fig. 22) tiny amounts of CO_2 and H_2O were visible on SEM detector. Comparing with atmosphere for PROX reaction, H_2O level increased approx. 3 times, however the signal still remained negligible.

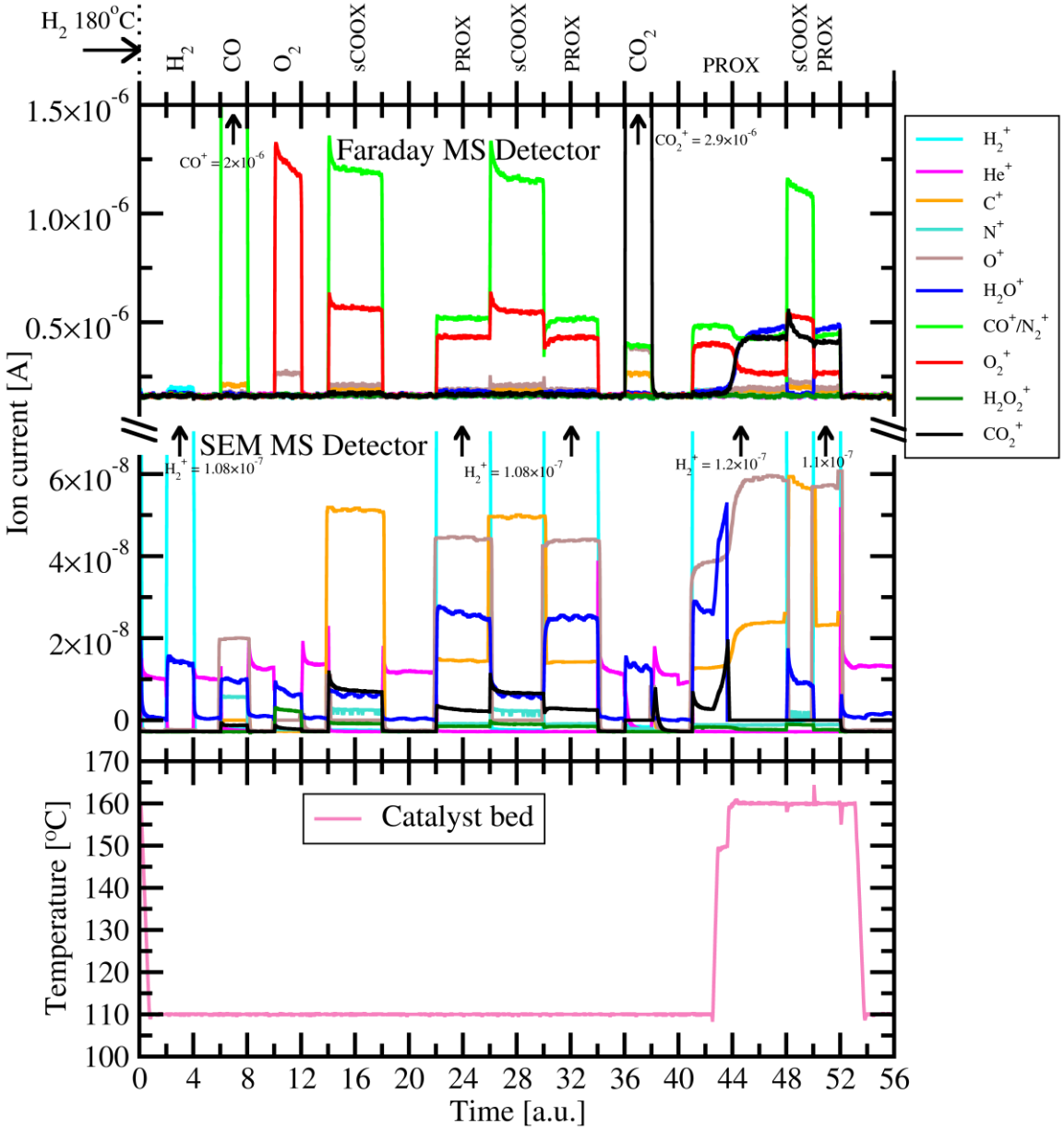

Fig. 22. Mass spectrometry (MS) analysis of composition of the gas stream leaving the glass reactor loaded with 7.16%$_{wt.}$ Au/SiO_2 and the actual temperature of the specimen bed. MS signals corresponding to relevant cations are shown. Data are plotted against time normalized to time required by the experimental computer script to collect 30 data points in each log file (approx. 30 minutes). sCOOX ≡ stoichiometric CO oxidation; PROX ≡ preferential oxidation (of CO).

Because of the lack of catalytic activity of the Au/SiO_2 catalyst at 110°C in CO oxidation, the temperature was ramped to, first, 150°C and then, when it occurred not to be enough, further up to 160°C, which already exceeded the common temperature setting of 150°C used later in PXRD chamber. The temperature seriously affected the chemical performance of the system, which was kept under PROX reaction conditions, and CO_2 production became significant. Conversion was still far from 100% and selectivity was poor, approx. 50%. Details on the chemical properties of 7.16 $\%_{wt.}$ Au/SiO_2 catalyst are presented in Table 10.

3.2.4. Performance of Au/C catalyst

44 mg of 20$\%_{wt.}$ Au/C was loaded to the glass reactor. The air-evacuated reactor was heated initially to approx. 125°C. Eventually, the temperature was ramped further up to almost160°C. Even though the temperature was increased above 150°C, no significant activity towards CO oxidation was obtained. MS results together with the temperature profile are shown in Fig. 23 and Table 11.

At all stages of the experiment, little amounts of water were always released from the sample. H_2O concentration increased under PROX reaction conditions and additional rise was found when the temperature reached 145°C and 155°C. Comparatively, the CO_2

Table 11. Outlet gas composition and reaction yield analysis for the sCOOX and PROX reactions performed on 20$\%_{wt.}$ Au/C catalyst at 110°C and 160°C. sCOOX ≡ stoichiometric CO oxidation; PROX ≡ preferential oxidation (of CO).

$T = 125°C$						
Compound	Ion current [$\times 10^{-6}$ A]		$\eta_{\rightarrow CO_2}$ [%]		$\eta_{\rightarrow H_2O}$ [%]	
	sCOOX	PROX	sCOOX	PROX	sCOOX	PROX
CO	2.5	0.96	6.2	14.6	-	-
O_2	1.1	0.78	6.2	8.2	7.6	12.1
CO_2	0.23	0.23	-	-	-	-
H_2O	0.18	0.22	-	-	-	-
Selectivity to CO_2, S_{CO_2} [%]:			40.3			
$T = 155°C$						
Compound	Ion current [$\times 10^{-6}$ A]		$\eta_{\rightarrow CO_2}$ [%]		$\eta_{\rightarrow H_2O}$ [%]	
	PROX		PROX		PROX	
CO	0.95		15.6			
O_2	0.73		8.6		17.2	
CO_2	0.25					
H_2O	0.32					
Selectivity to CO_2, S_{CO_2} [%]:			33.4			

signal did not change upon the temperature increase. It was then impossible to judge, whether the additional amount of water originated from the hydrogen oxidation or it was the result of H_2O desorption from the specimen induced by higher temperature. CO_2 was produced with low yield regardless of the temperature of the reaction or the presence of hydrogen.

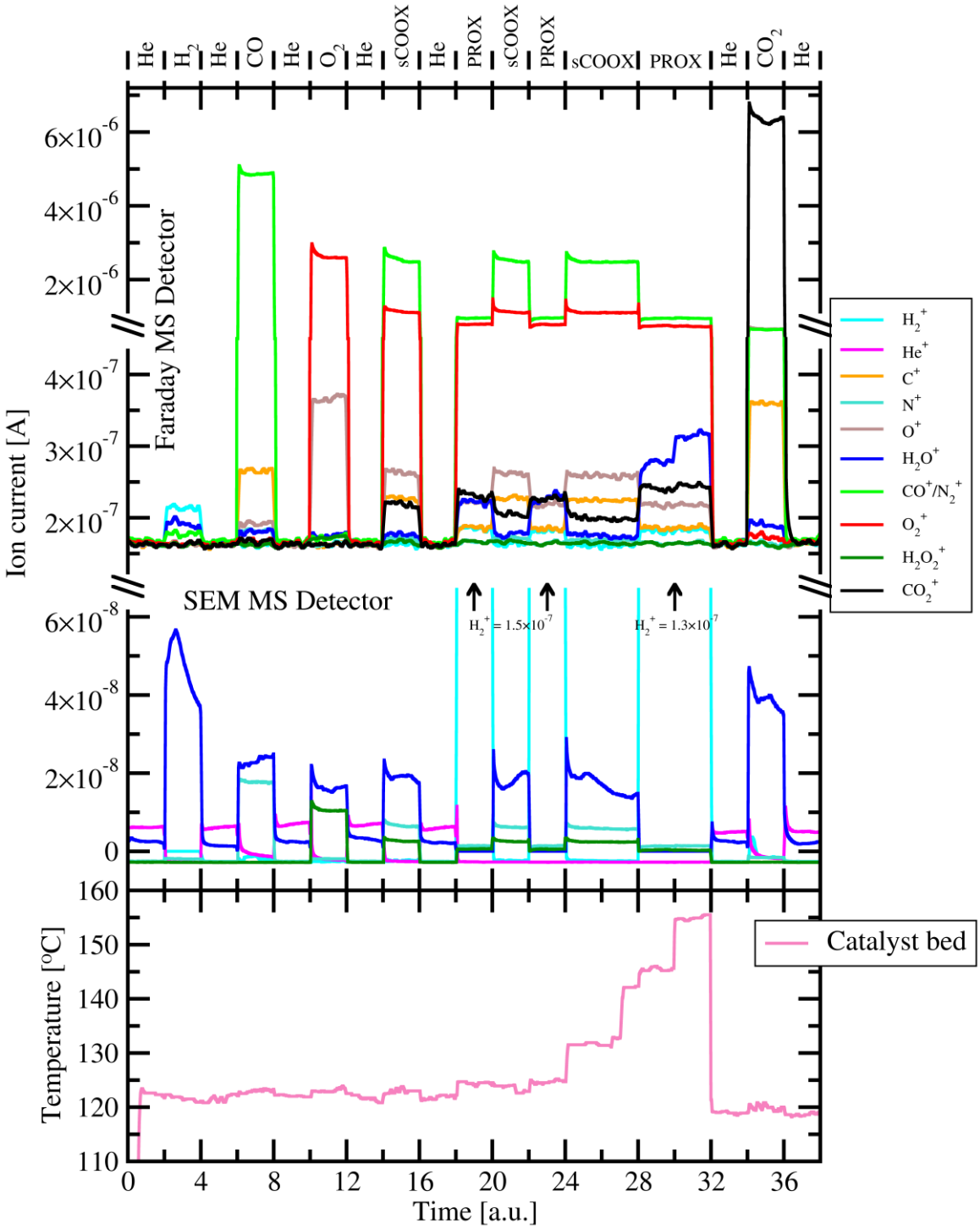

Fig. 23. Mass spectrometry (MS) analysis of composition of the gas stream leaving the glass reactor loaded with 20%$_{wt.}$ Au/C and the actual temperature of the specimen bed. MS signals corresponding to relevant cations are shown. Data are plotted against time normalized to time required by the experimental computer script to collect 30 data points in each log file (approx. 30 minutes). sCOOX ≡ stoichiometric CO oxidation; PROX ≡ preferential oxidation (of CO).

3.2.5. Performance of Au/CeO_2-SiC specimen

There were 2 gas stream compositions examined. In both cases, helium constituted 90%$_{vol.}$ of the stream. The remaining 10%$_{vol.}$ were: CO : O_2 = 1 : 10 or CO : O_2 = 2 :1 (by volume). Percentage of CO conversion to CO_2 was monitored as a function of temperature and both quantities were plotted against time to visualise the correlation (see Fig. 24 and Fig. 25).

Under excess of oxygen, full conversion was reached at approx. 125°C or 130°C, during first and second run respectively. When the stoichiometric CO : O_2 gas mixture was used, nearly quantitative CO oxidation was observed at approx. 160°C (average from 3 runs), which is by ~30°C higher than in the case of 20-fold O_2 excess.

This shift of maximum performance conditions may be the consequence of the experimental procedure. It involved application of temperature profile up to ~230°C. The catalyst proved to be stable even at high temperature while maintaining highest CO_2 production rate. However, it cannot be excluded, that in much longer perspective, deactivation of the catalyst might become visible. At the temperatures exceeding 200°C it is possible that gold nanoparticles (AuNP) sinter slowly. Further, they may gradually become less active and/or require more energy to be supplied to the system to overcome the reaction barrier, which is believed to be higher on the surface of bigger particles.

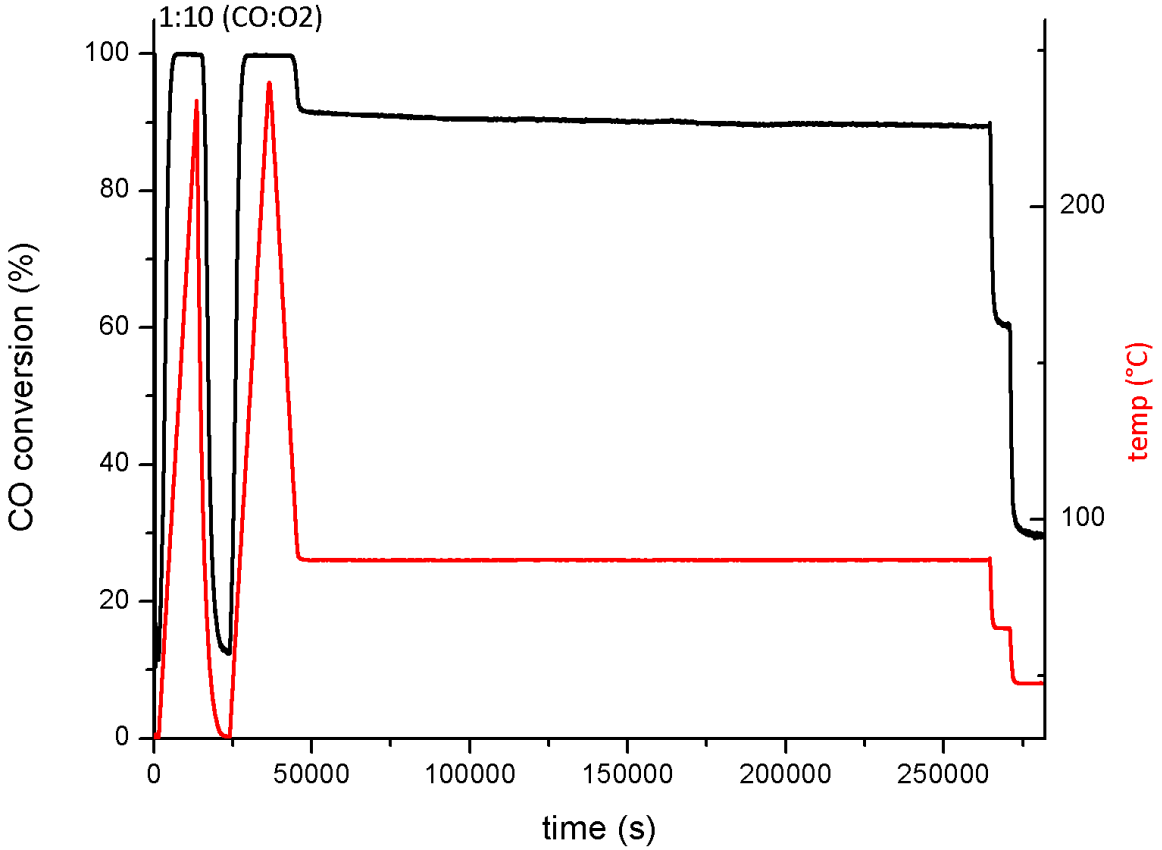

Fig. 24. The plot of the CO conversion to CO_2 by the 9.4%$_{wt.}$ Au/CeO_2 catalyst as a function of temperature and time. The feeding stream contained the CO : O_2 ratio 1 : 10.

The catalyst remained marginally active even at room temperature, as CO conversion never went down to absolute 0.00 %, which is not the case for empty reactor filled only

with SiC. Moreover, CO_2 production always increased after the temperature started to rise. Good indication of the catalyst's activity is the temperature of 50% conversion to the desired product, which in the case of 9.4%$_{wt.}$ Au/CeO_2 catalyst is ~85°C. Thus, this material could be easily tuned using only temperature in order to reach the desired performance in CO oxidation.

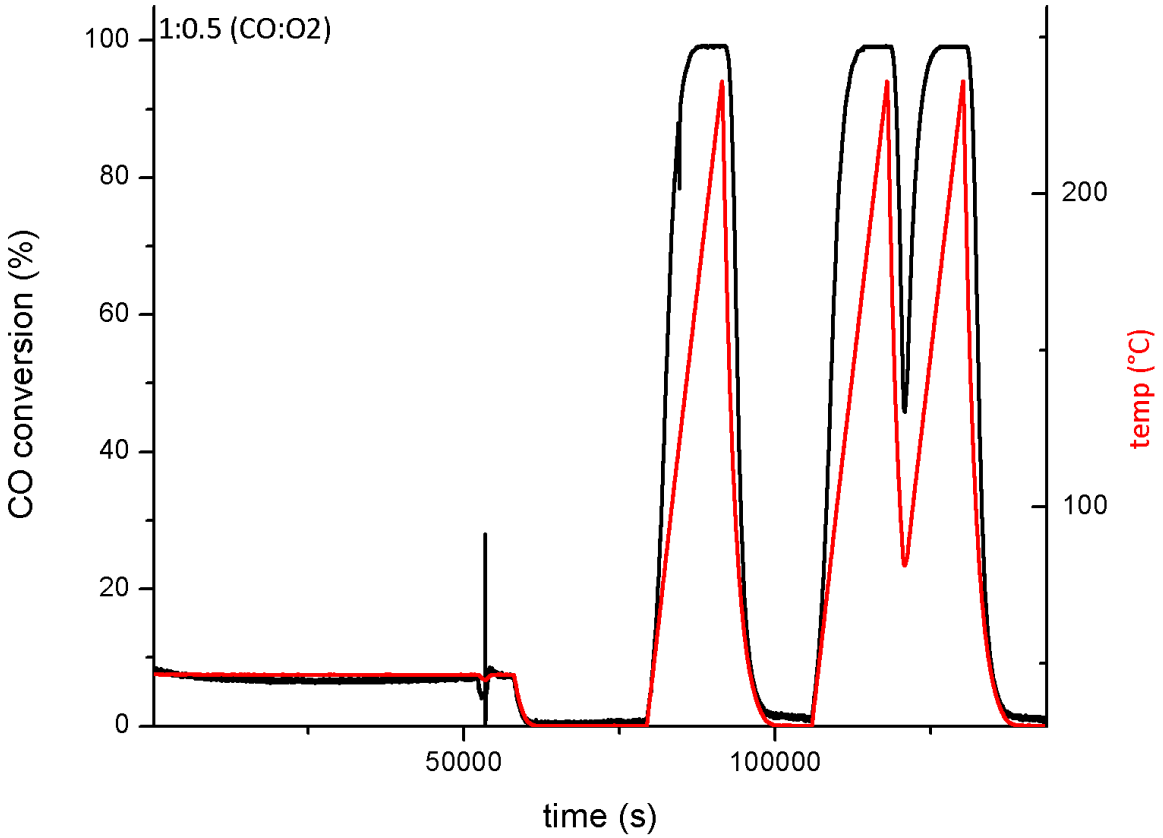

Fig. 25. The plot of the CO conversion to CO_2 by the 9.4%$_{wt.}$ Au/CeO_2 catalyst as a function of temperature and time. The feeding stream contained the CO : O_2 ratio 2 : 1.

3.2.6. Conclusions from the chemical performance studies

Thorough studies of catalytic activity of all 3 catalysts clearly pointed to strong dependence on their chemical properties and the used support. It is expected, that the size of the gold nanoparticles (AuNP) plays an important role too, although it was not examined in the conducted experiments. As it has been shown later, the AuNPs were smaller than 15 nm in each catalyst, with significant or sometimes even dominant fraction of the NPs of the size below 5 nm NPs.

Au/CeO_2 was found to be the most active in CO oxidation. The synergic mutual enhancement effect of gold and ceria was evident, as pure cerium (IV) oxide did not exhibit significant CO oxidation properties (refer to Section 3.3.2). The stable performance facilitated further research by means of X-Ray diffraction. This catalyst could reach full conversion of CO to CO_2 within the temperature range of 120 – 160°C. Unfortunately, high catalytic activity resulted also in the *light-off* phenomenon, which implied the requirement to correct the structure data for the temperature effects. On the other hand, the self-heating, that can be controlled, creates opportunities for optimisation of reaction conditions, as less external heat can be supplied to the system, thus improving cost-effectiveness of an industrial scale process. One more weak point of Au/CeO_2

catalyst was found, that is its moderate selectivity towards CO_2 when H_2 was mixed to the stream.

Next, 7.16% Au/ SiO_2 catalyst was found poorly selective and achieved low yield with respect to CO_2 production. In the case of this sample, the *light-off* phenomenon appeared as well. Most probably, it directly influenced the step increase in CO_2 when temperature was changed by only 10°C from 145°C to 155°C. The catalyst did not experience deacivation, which was a very desired feature in *in-operando* PXRD studies.

Lastly, the Au/C system was regarded as a reference of how bare AuNPs perform in CO oxidation. No noticeable activity in CO_2 production was spotted, independently of the applied temperature. Even successfully synthesised high loading of gold was not sufficient to improve the chemical output of this catalyst, however strong well–shaped XRD reflections were observed in diffraction patterns. The increase of H_2O^+ cation signal after the target temperature had been reached cannot be undoubtedly bound to either water release from the hotter sample or to H_2 oxidation.

3.3. *in–operando* PXRD-MS studies

In-operando Nanocrystalline X–Ray Diffraction (NXRD) is a technique and methodology designed precisely to study phenomena happening on the nanocrystal surface. Its crucial advantage is utilisation of powder X–Ray diffractiometer (PXRD) widely available in scientific institutions worldwide.

A powder sample is placed in the PXRD measurement chamber in its working conditions, including gas atmosphere composition (or vacuum) and temperature. Series of diffraction patterns (DPs) is acquired and correlated with chemical performance of the sample.

Phenomena taking place on the sample's surface are reflected in diffraction peak shapes and positions. Change of reflection scattering angle, intensity, profile width and asymmetry are the most important features the analysis focuses on.

3.3.1. Chemical performance of the empty PXRD chamber

An empty PXRD chamber (refer to Fig. 10) connected to the vacuum-gas manifold with clean sintered glass plate mounted in the sample holder was tested against its inertness using the programmed gas sequence (see Fig. 11). Temperature on the heating block was set to 160°C as it provided approx. 150°C at the sample. H_2O condensation and any extra $Ni(CO)_4$ formation behind the Ni-Trap were also prevented this way. The results of the PXRD chamber performance have been presented in Fig. 26 and Table 13.

Similarly to the empty glass reactor with thin layer specimen bed (results in Section 3.2.1), the chamber for *in-operando* PXRD studies showed negligible chemical activity. When examined in detail, the CO_2 and/or H_2O MS signals during exposures to sCOOX and PROX reaction conditions are slightly higher than those in the case of the empty glass reactor. Fortunately, this fact does not affect the general conclusion that the chamber itself can be treated as inert. As showed in forthcoming sections, there is clear evidence proving that chemical performance of an active catalyst can be monitored without perturbations.

These traces of CO_2 and H_2O should be attributed to the Ni-Trap heated to over 200°C and the chamber itself remaining at the temperature about 150°C. The Ni-trap and the chamber had been made of stainless steel and, additionally, chamber cap had been made of aluminium. These materials, as discussed earlier, could serve as, fortunately rather inefficient, catalysts for CO oxidation and H_2O production. The surface metal oxides might be reduced under such conditions as well.

Each introduction of new gas environment (look at the beginning of every 5th time unit in Fig. 26) was accompanied by a spike (up to ±3°C) on the temperature profile. They originated from differences of thermal conductivity and heat capacity (refer to Table 12) of the gases used during the experiment. Here, the thermal conductivity played the major role, as the gases either well or badly dissipated the heat from the heating block. The higher was the thermal conductivity of the gas, the more easily the heat was transferred to the environment from the block. Thus, introduction of He and H_2, and retraction of other gases, resulted in a slight drop of the temperature. During the gas atmosphere exchange, the temperature controller needed to adjust the heating power while the gas composition in the chamber changed quickly. PID algorithm of the controller did not allow it to work equally efficient during constant and varying gas environment. Therefore, the PID

Table 12. Comparison of heat conductivity and heat capacity of the gases used in the experiments [87].

Element	Thermal conductivity $\lambda\ \left[\frac{\mathrm{W}}{\mathrm{m}\cdot\mathrm{K}}\right]$	Molar heat capacity $C_p\ \left[\frac{\mathrm{J}}{\mathrm{mol}\cdot\mathrm{K}}\right]$
H_2	0.1850	28.836
He	0.1550	20.786
H_2O_{gas}	0.0288	37.470
CO	0.0250	29.141
O_2	0.0265	29.380
CO_2	0.0166	37.135

Table 13. Outlet gas composition and reaction yield analysis for the sCOOX and PROX reactions carried out in the empty PXRD chamber. sCOOX ≡ stoichiometric CO oxidation; PROX ≡ preferential oxidation (of CO).

Compound	Ion current [$\times 10^{-6}$ A]		$\eta_{\rightarrow CO_2}$ [%]		$\eta_{\rightarrow H_2O}$ [%]	
	sCOOX	PROX	sCOOX	PROX	sCOOX	PROX
CO	2.55	0.91	1.0	1.1	-	-
O_2	1.1	0.75	1.1	0.6	0.0	1.9
CO_2	0.035	0.014	-	-	-	-
H_2O	0.00	0.027	-	-	-	-

temperature controller, which relied on the indication of the thermocouple located in the heating block, was optimised to stabilise well the temperature (approx. ±0.1°C) after the gas exchange had been completed. These spikes were experienced in all experiments with the PXRD chamber and behaved always in the same manner.

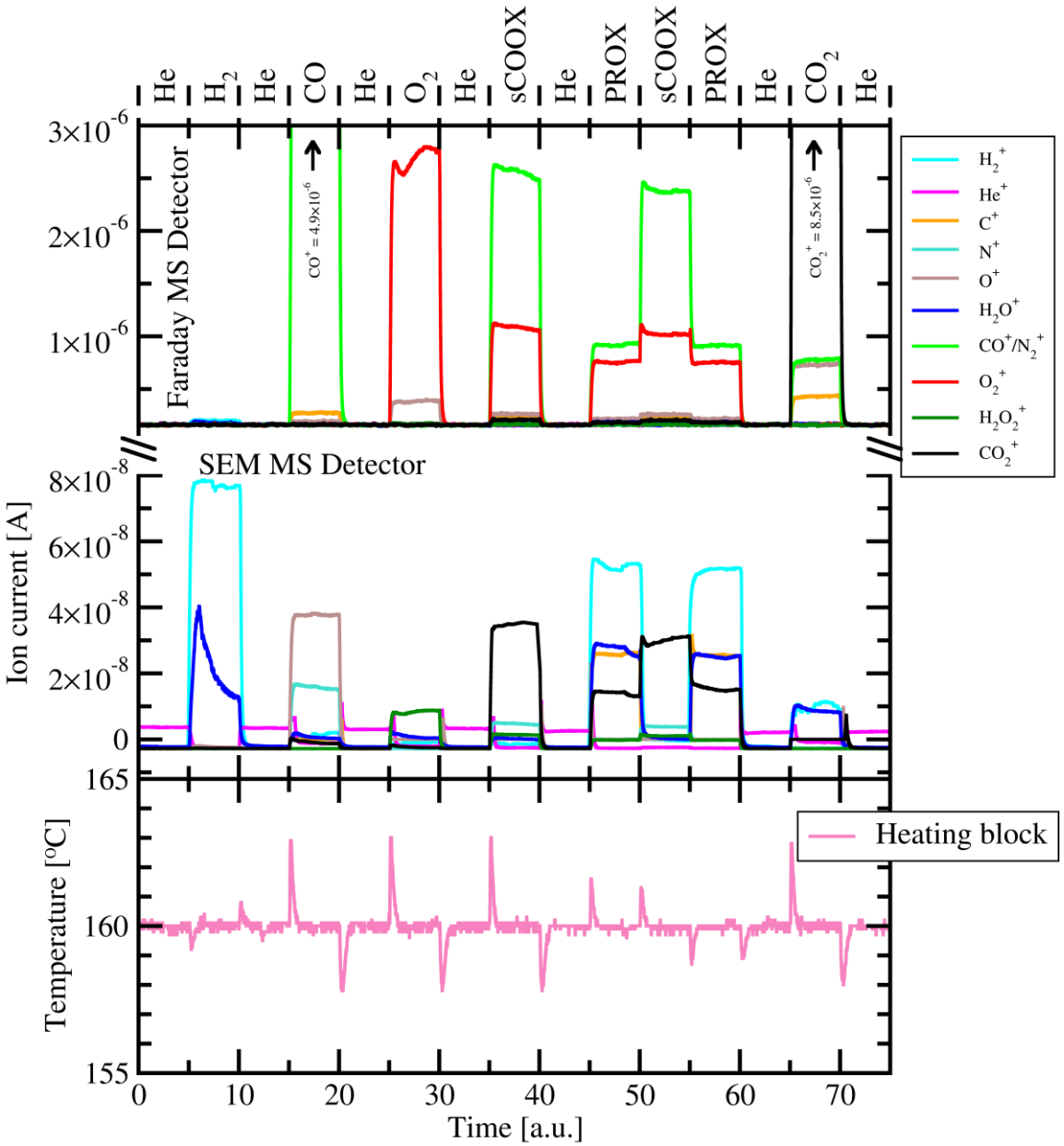

Fig. 26. Mass spectrometry (MS) analysis of composition of the gas stream leaving the empty PXRD chamber and the actual temperature of the specimen bed (clean sintered glass disk). MS signals corresponding to relevant cations are shown. Data are plotted against time normalized to time required by the experimental computer script to collect 30 data points in each log file (approx. 30 minutes). sCOOX ≡ stoichiometric CO oxidation; PROX ≡ preferential oxidation (of CO).

3.3.2. Pure CeO_2 – chemical performance and crystal structure dynamics

74 mg of pure cerium (IV) oxide powder, used for Au/CeO_2 catalyst synthesis, was pressed onto a clean sintered porous glass disk. It was then mounted inside the PXRD chamber on the heating block. After the air had been removed by purging with helium, the temperature was set to 120°C on the heating block. Examination with XRF showed that there were no traces of nickel found in the specimen after the experiment. The mean CeO_2 crystal size was 13.9 ± 1.5 nm according to Debye-Scherrer equation and DPs series statistics. A sample DP has been presented in Fig. 12 (page 44). The lack of chemical activity of CeO_2 has been presented in Fig. 28 and Table 14. Crystal structure dynamics induced by gas environment has been shown in Fig. 29 and summarised in Table 15.

The chemical activity of pure ceria, without gold supported on it, was negligible. Although the Ni-Trap worked at ~200°C, as usually, the MS signals of CO_2 and H_2O were extremely weak and even smaller comparing to the case of the empty chamber (see Section 3.3.1). Recalling chemical tests described e.g. in Section 3.2.5, the Au/CeO_2 catalyst showed much activity already in this temperature regime. Pure ceria usually requires higher temperature to exhibit any CO conversion to CO_2. For instance, Laguna et al. reported CeO_2 activity in CO oxidation observed from 225°C, but it increased slowly with the temperature, reaching only approx. 15 % at 300°C [88]. To conclude, bare CeO_2 is incapable of efficient oxidation of CO under conditions applied in the PXRD chamber.

Although ceria was not chemically active during the experiment, attention should be turned to its crystal structure response to provided gas environment. It was convenient to treat the structure under helium as the default state. After CeO_2 had been exposed to carbon monoxide, an immediate isotropic expansion in all crystallographic directions was noticed. It was not the case under hydrogen atmosphere, when only little deviations comparing to apparent lattice parameter (ALP) measured under helium were spotted. According to Brauer and Gingerich [89, 90], FCC structure of CeO_2 expands when the oxygen content is decreased and ceria become unstoichiometric oxide, CeO_{2-x}. Ceria lattice parameter "*a*" is proportional to the degree of unstoichiometry [91], represented by "x" in CeO_{2-x}, according to equation 32:

$$a_{CeO_{2-\mathrm{x}}} = a_{CeO_2,He} + 0.4612 \cdot \mathrm{x} \qquad (32)$$

where:

$a_{CeO_{2-\mathrm{x}}}$ – lattice constant of unstoichiometric CeO_{2-x};

$a_{CeO_2,He}$ – lattice constant of CeO_2 under helium;

x – measure of unstoichiometry in CeO_{2-x}, proportional to the fraction of created oxygen vacancies.

The expansion of CeO_{2-x} structure is attributed to the bigger Ce^{3+} cation radius than that of Ce^{4+}. It has been found that oxygen vacancy effective volume is smaller than oxygen anion [92, 93, 94, 95, 96, 97], so the difference of cerium cation radius is huge enough to compensate even this effect. Earlier, in 2000, Tsunekawa et al. [98] has also found that transformation from Ce^{4+} to Ce^{3+} reduces the electrostatic forces inside CeO_{2-x} clusters. Their size dependence on Apparent Lattice Parameter (ALP) agrees well with the change of valence shell of cerium ions ($I(\mathrm{Ce}^{3+})/\{\mathrm{I}(\mathrm{Ce}^{4+}) + \mathrm{I}(\mathrm{Ce}^{3+})\}$) as evaluated by the summed intensity ratio of X–Ray Photoelectron Spectroscopy (XPS) Ce $3d_{5/2}$ peaks.

It may be surprising, that, unlike CO, H_2 did not induce partial reduction of cerium dioxide, although such a result may be expected. H_2–TPR studies [99] done on pure CeO_2 showed its reduction occurring at temperature not lower than 649 K. Hydrogen molecule, by itself, is a stable molecule. Activation of this molecule in heterogeneous catalysis requires its chemisorption on the catalyst's surface, as physisorption, which is usually weak under moderately high temperatures (100 – 150°C), is not enough to enable reaction of H_2 with another molecule. On the contrary, CO is more eager to share its electrons located on the antibonding molecular orbital.

Exposure of ceria to oxygen does not bring much distraction to CeO_2 structure with respect to its state under helium. This is the result of nearly fully oxidised form of ceria stored under the air atmosphere or in the desiccator. Following Brauer and Gingerich [89], deep reduction of cerium (IV) dioxide to obtain unstoichiometric composition, e.g. down to $CeO_{1.7}$, requires harsh conditions, including high temperature ~800 – 900°C. Basically, the concentration of oxygen vacancies in the air-exposed CeO_2 structure is very low. In addition, exposure to pure oxygen cannot influence much the oxidation state of cerium dioxide.

On average, the CeO_2 lattice constant influenced by CO at 120°C increased by ~0.55 pm, so relatively by ~0.1%. This effect was statistically very well visible without doubts. It was also a reversible phenomenon as ceria structure contracted quickly after CO was replaced by He. A weak recall of this observation was noticeable under stoichiometric (sCOOX) and H_2-rich (PROX) CO oxidation reaction conditions. These times the expansion was not so much pronounced, most probably because of competition between CO and O_2 to occupy the cerium dioxide surface.

Further speaking, adsorption of carbon monoxide and oxygen on ceria surface are two opposite processes. Interaction with CO may yield following effects:

- generation of oxygen vacancies in the structure of CeO_2;
- binding of oxygen cations on ceria surface;
- donation of electrons by CO to the surface through creating bonds with surface oxygen moieties.

New oxygen vacancies were unlikely to be generated, because no CO_2 was produced. However, CO interacting with oxygen available on CeO_2 surface caused oxygen vacancies to be redistributed inside of the ceria structure. Normally, concentration of vacancies rises from the centre of a particle towards its surface (see Fig. 27). If oxygen was bound at the surface by carbon monoxide, the vacancies would move to the bulk part of the particle. Reduction of ceria is known to start at the surface and then propagates towards the particle's interior through redistribution of oxygen vacancies – such a mechanism was proposed by Binet et al. [100] for reduction of CeO_2 beginning at 200°C. Binding of oxygen species of the ceria surface by carbon monoxide only speeds up the process and facilitates it to occur at the lower temperatures.

Apparent lattice parameter (ALP) reflects the average distances between the atoms in the particles. The interior of the nanoparticle has the biggest impact on the ALP value (as discussed in Section 1.4), thus it is necessary that the surface phenomena influence the state of the deep atomic layers. Only then the surface interactions are detectable with X-Ray diffraction. The experimental ALP shifts, due to the redistribution of O^{2-} to the surface of ceria (where oxygen was bound by CO) and counter-redistribution of oxygen

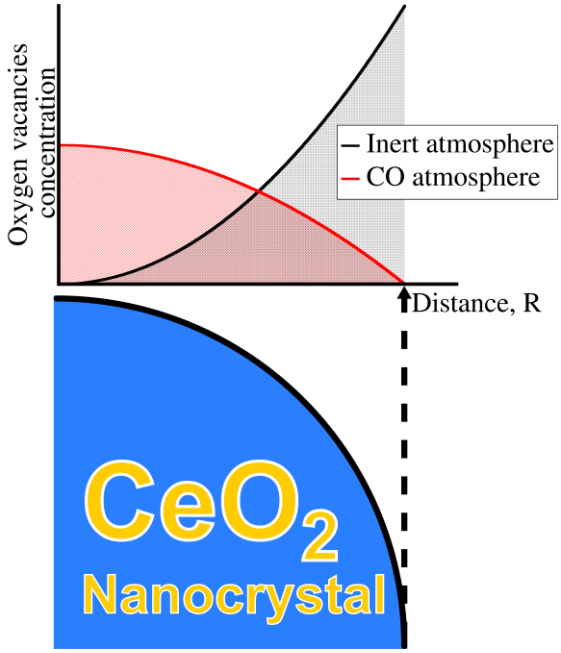

Fig. 27. The schematic illustration of the redistribution of the oxygen vacancies inside a CeO_2 nanocrystal exposed to an inert atmosphere and compared to exposure to CO.

vacancies towards the bulk of the particle, suggest, when equation 32 is applied, that ceria is reduced by 0.6 % under CO atmosphere, which seems to be the value in line with the data concerning oxygen extraction under reducing atmosphere for high surface area CeO_2 [101] – generally close to 0 % at 200°C.

It is worth to notice, that in a 14–nm nanocrystal which has got a roundish shape (e.g. is cuboctahedral) approx. 10–11 % of all the atoms are on the surface. Even if the whole partial reduction is assigned only to oxygen involved in the interactions with CO on the particle surface, it is clear that the CO coverage of the surface equals to about 6 %. In addition, this should be regarded as the limit of CO influence on pure CeO_2 under applied experimental conditions (pressure of CO and temperature of the specimen).

On the contrary to carbon monoxide, the free gaseous oxygen molecules fill vacancies available on ceria particles' surface and, consequently, should create active oxygen moieties available to bind CO. This, however, did not lead to formation of CO_2 on pure ceria, so it seems that oxygen molecules are not dissociated on ceria surface, but only occupy exposed sites. Even if the molecular bond between the oxygen atoms in O_2 is weakened, it is not weak enough to allow recombination with CO to CO_2.

Analysis of the ceria structure exposed to sCOOX and PROX conditions revealed only very slight increase of ALP. The competition between CO and O_2 to adsorb on the surface has to be very dynamic and therefore only little structural change in favour of CO adsorption was visible. Presence of hydrogen did not introduce additional distraction to the system. Comparably to CO oxidation reaction conditions little expansion can be noticed under pure CO_2 atmosphere.

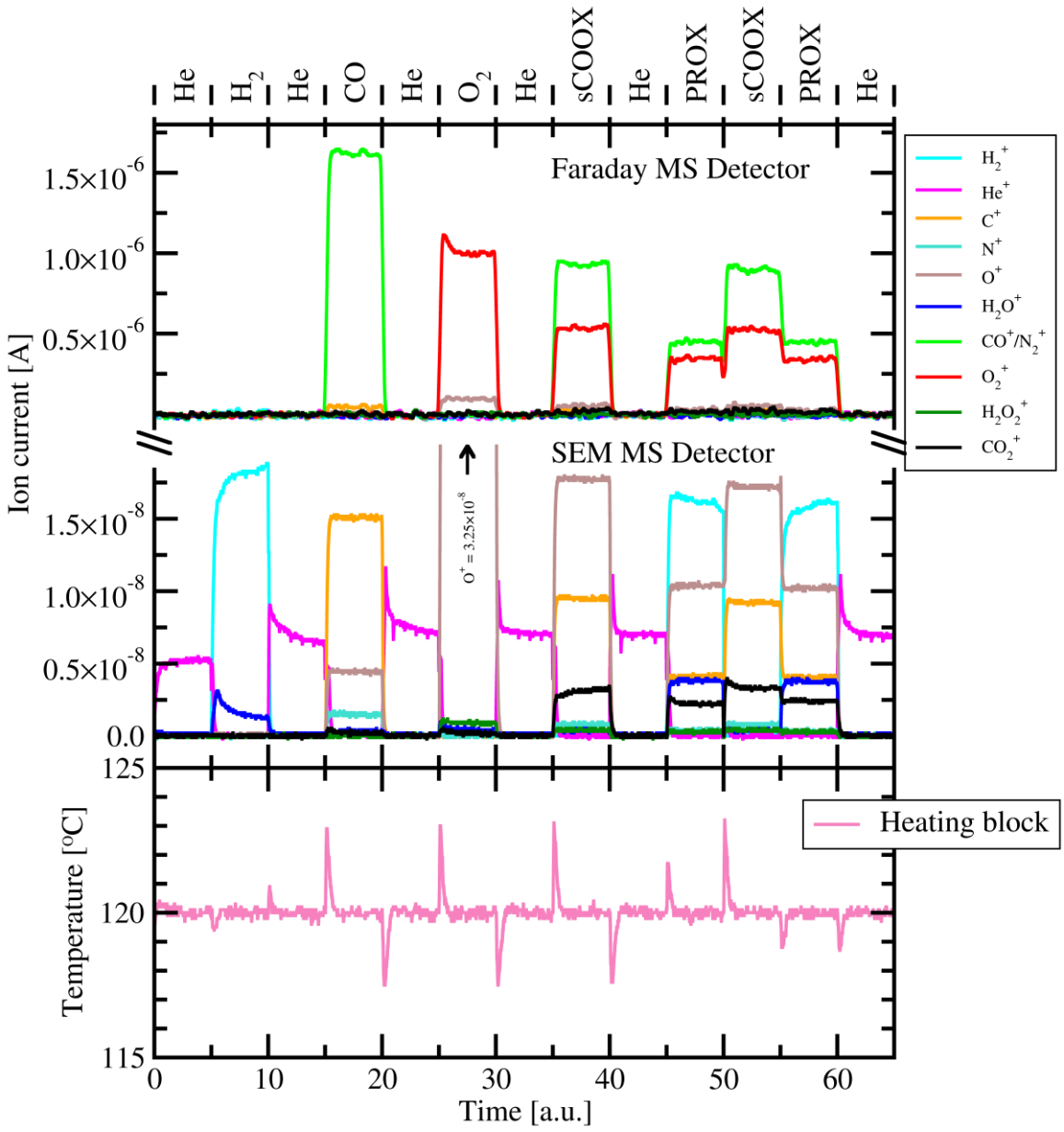

Fig. 28. Mass spectrometry (MS) analysis of composition of the gas stream leaving the PXRD chamber with CeO_2 pressed onto sintered glass disk and the actual temperature of the specimen bed. MS signals corresponding to relevant cations are shown. Data are plotted against time normalized to time required to acquire one diffraction pattern (DP; approx. 42 min). sCOOX ≡ stoichiometric CO oxidation; PROX ≡ preferential oxidation (of CO).

Table 14. Outlet gas composition and reaction yield analysis for the sCOOX and PROX reactions carried out on CeO_2 in the PXRD chamber. sCOOX ≡ stoichiometric CO oxidation; PROX ≡ preferential oxidation (of CO).

Compound	Ion current [× 10^{-6} A]		$\eta_{\rightarrow CO_2}$ [%]		$\eta_{\rightarrow H_2O}$ [%]	
	sCOOX	PROX	sCOOX	PROX	sCOOX	PROX
CO	0.93	0.45	0.25	0.35	-	-
O_2	0.53	0.35	0.21	0.22	0.00	0.58
CO_2	0.0032	0.0022	-	-	-	-
H_2O	0.00	0.0038	-	-	-	-

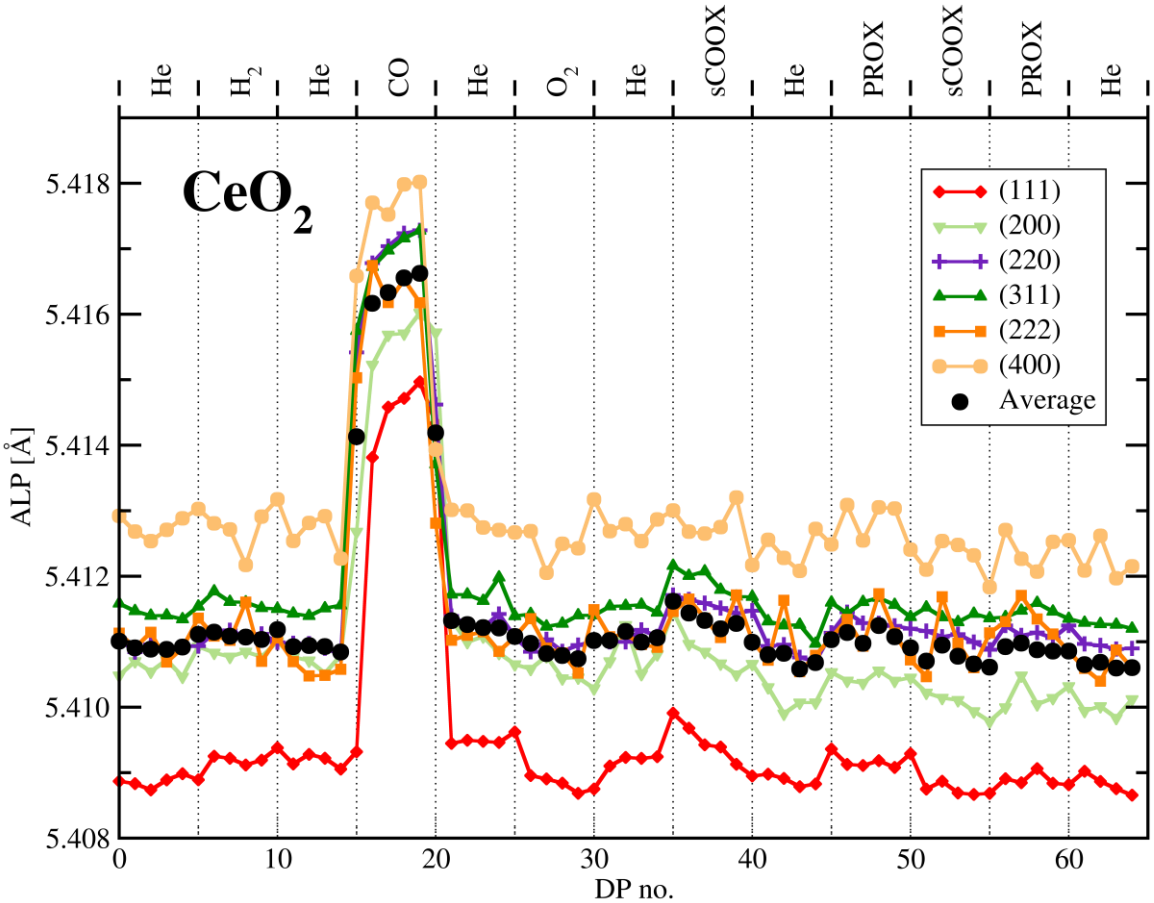

Fig. 29. Apparent Lattice Parameter (ALP) of CeO_2 calculated from the position (scattering angle 2θ) of each diffraction peak is plotted against the index of the diffraction pattern (DP) in the series of DPs. Acquisition of one DP takes ~42 min. Gas sequence is shown above the graph. sCOOX ≡ stoichiometric CO oxidation; PROX ≡ preferential oxidation (of CO).

Table 15. Crystal structure dynamics as a function of gas atmosphere. For each gas atmosphere composition the average apparent lattice parameter (ALP) is calculated. sCOOX ≡ stoichiometric CO oxidation; PROX ≡ preferential oxidation (of CO).

Gas atmosphere	DP range	ALP [Å]	Std. Dev. [$\times 10^{-6}$ Å]
He	0 – 4	5.410897	17
H_2	5 – 9	5.411083	47
He	10 – 14	5.410907	44
CO	15 – 19	5.416418	210
He	20 – 24	5.411251	52
O_2	25 – 29	5.410830	102
He	30 – 34	5.411056	72
sCOOX	35 – 39	5.411308	101
He	40 – 44	5.410721	111
PROX	45 – 49	5.411109	114
sCOOX	50 – 54	5.410771	127
PROX	55 – 59	5.410908	55
He	60 – 64	5.410633	41

3.3.3. Au/CeO_2 – structure dynamics and chemistry

9.4%$_{wt.}$ Au/CeO_2 catalyst supported on a sintered porous glass plate was loaded into the PXRD chamber. The temperature on the heating block was set to 160°C. The catalyst was found to be very active in CO oxidation. MS data are shown in Fig. 30 and Table 16. The volume weighted mean size of CeO_2 crystals was 20.0 ± 3.6 nm and Au crystals was 13.7 ± 0.8 nm as estimated using Williamson-Hall approach (see appropriate subsection "Structure analysis – stress and strain"). Crystal structure dynamics of the support and gold phase are presented in Fig. 32 and Fig. 33, and Table 17 and Table 18. TEM *ex–situ* characterisation of gold particles reveals the particles' size distribution agreeing with the above volume–weighted average value with significant fraction of small crystals (< 5 nm, please refer to Section 3.4.1).

Chemical performance

First, the chemical properties of the catalyst will be briefly discussed. Similarly to the results from Sections 3.2.2 and 3.2.5, the catalyst occurred to be highly active in CO oxidation. CO_2 production rate was close to full conversion of CO to CO_2 under both stoichiometric (sCOOX) and H_2-rich (PROX) reaction conditions. The significance of this result is even more pronounced if differences in the types of reactors used here and earlier are considered. The PXRD chamber works more as Continuous Stirred Tank Reactor (CSTR), rather than ideal Plug Flow Reactor (PFR) used for initial chemical

tests. In the field of heterogeneous catalysis, PFR is more convenient to use in a production plant and usually allows to reach higher production yields. Higher efficiency of PFR originates from the fact, that the reagents in the stream move in one common direction, so products desorbing from the catalyst do not mix with fresh reagents and do not compete in adsorption again. 9.4%$_{wt.}$ Au/CeO_2 catalyst was indeed efficient enough to reach excellent chemical output within the given residence time of reagents in the chamber.

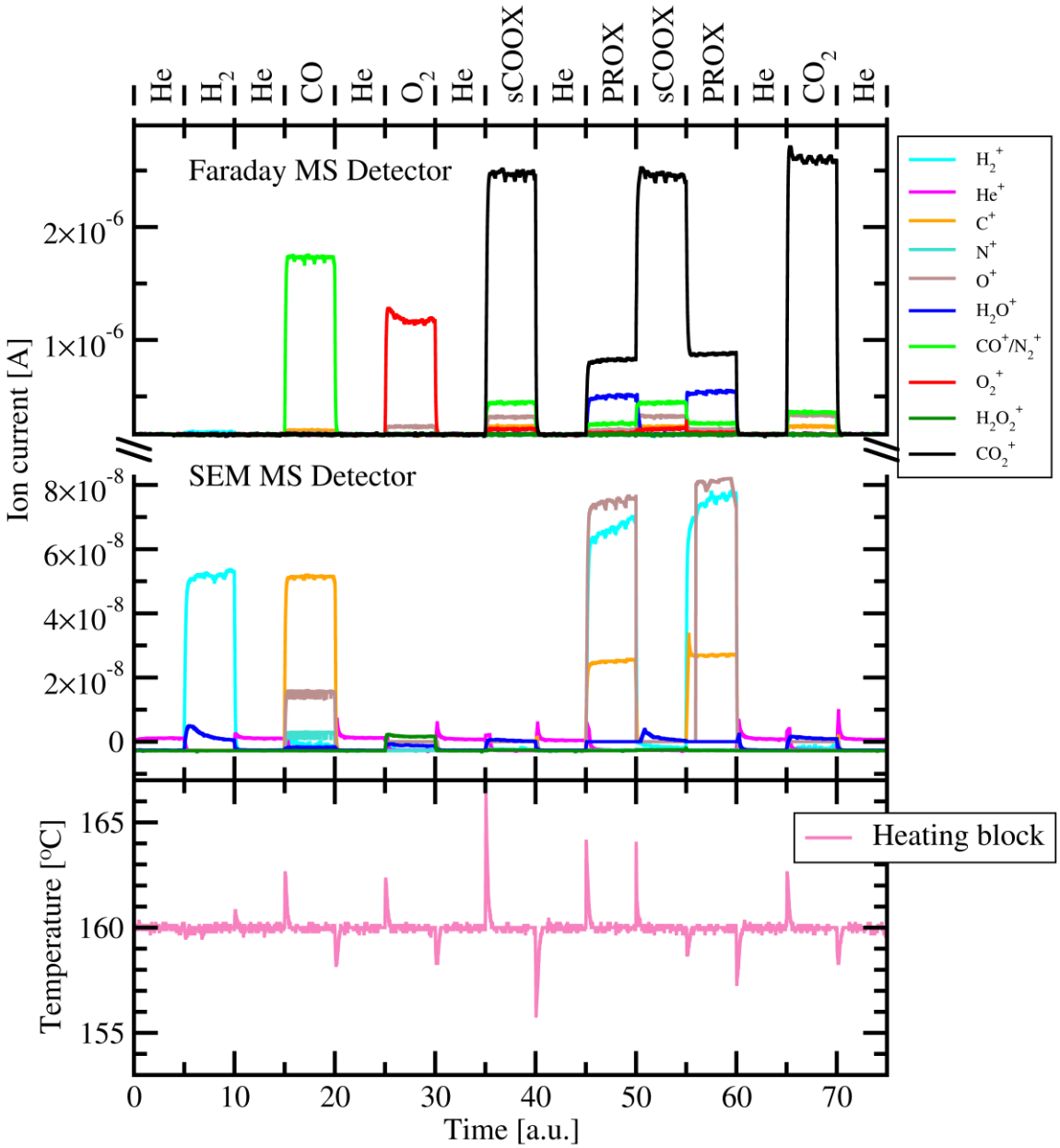

Fig. 30. Mass spectrometry (MS) analysis of composition of the gas stream leaving the PXRD chamber with 9.4%$_{wt.}$ Au/CeO_2 and the actual temperature of the heating block. MS signals corresponding to relevant cations are shown. Data are plotted against time normalized to time required to acquire one diffraction pattern (DP; approx. 42 min). sCOOX ≡ stoichiometric CO oxidation; PROX ≡ preferential oxidation (of CO).

The high activity of the catalyst was accompanied by the *light-off* phenomenon [86] as well as it was revealed in the glass reactor. Fig. 46 shows the specimen's bed temperature established on the basis of thermal expansion of "a" crystal lattice constant of quartz,

which was mixed with the sample. Generally, throughout the experiment, temperature alternations were mainly the consequence of different heat conductivity coefficients of gases (refer to the Table 12) currently feeding the chamber. However, during sCOOX and PROX reactions, the specimen bed was heated up by approx. ~100°C and ~40°C, respectively. Despite the fact that the catalyst reached 100% yield of CO_2 production at approx. 160°C (refer to Section 3.2.5), the observed temperature increase could further boost the chemical performance of the catalyst or be responsible for lower heat uptake of the system from the heating block. Temperature raise was also reflected in changes of CeO_2 and Au structures, because they simply underwent thermally induced expansion.

Table 16. Outlet gas composition and reaction yields analysis for the sCOOX and PROX reactions carried out on 9.4%$_{wt.}$ Au/CeO_2 catalyst in the PXRD chamber. sCOOX ≡ stoichiometric CO oxidation; PROX ≡ preferential oxidation (of CO).

Compound	Ion current [× 10^{-6} A]		$\eta_{\rightarrow CO_2}$ [%]		$\eta_{\rightarrow H_2O}$ [%]	
	sCOOX	PROX	sCOOX	PROX	sCOOX	PROX
CO	0.44	0.25	79.9	70.3	-	-
O_2	0.00	0.00	100.0	51.8	0.0	48.2
CO_2	2.45	0.83	-	-	-	-
H_2O	0.00	0.50	-	-	-	-
Selectivity to CO_2, S_{CO_2} [%]:				51.8		

Structure analysis – lattice constant

In the analysis of the evolution of CeO_2 and Au crystal structures, their thermal expansion was accounted for by recalculation, with the aid of thermal expansion coefficient (reported in Section 2.5.5), of the lattice parameters back to the values they would have at the initial temperature of the sample under helium (diffraction patterns 0 – 5 in Fig. 34).

The most evident structural response to the gas environment was noticed under hydrogen atmosphere. Ceria elementary cell expanded by 0.88 pm when it acted as the support in the Au/CeO_2 catalyst, unlike when it was a pure phase (see Section 3.3.2). This is a solid evidence testifying that strong metal-support interaction (SMSI) occurred between cerium dioxide and gold deposited on it. According to e.g. the results of H_2-TPR (Temperature Programmed Reduction) published in 2015 by Li, Wang, Cardenas–Lizana and Keane [102], the reduction of pure CeO_2 with hydrogen has two steps at 742 K and 1148 K assigned to reduction of surface layer first and then the bulk of ceria to Ce_2O_3. Behaviour of pure cerium (IV) oxide was compared to ceria with gold deposited on it (AuNPs size was estimated by TEM as very low, below 5 nm). It was discovered that a broad reduction band appeared with maximum just at 420 K (i.e. 147°C). Hydrogen consumption exceeded the amount needed for Au precursor reduction, but was insufficient for full reduction of ceria. Hence, partial reduction of CeO_2 (to CeO_{2-x}) was concluded as also reported earlier by Andreeva and co-workers [103, 104] or Centeno et al. [105]. The temperature 160°C used here in *in-operando* PXRD experiment belongs to the same regime.

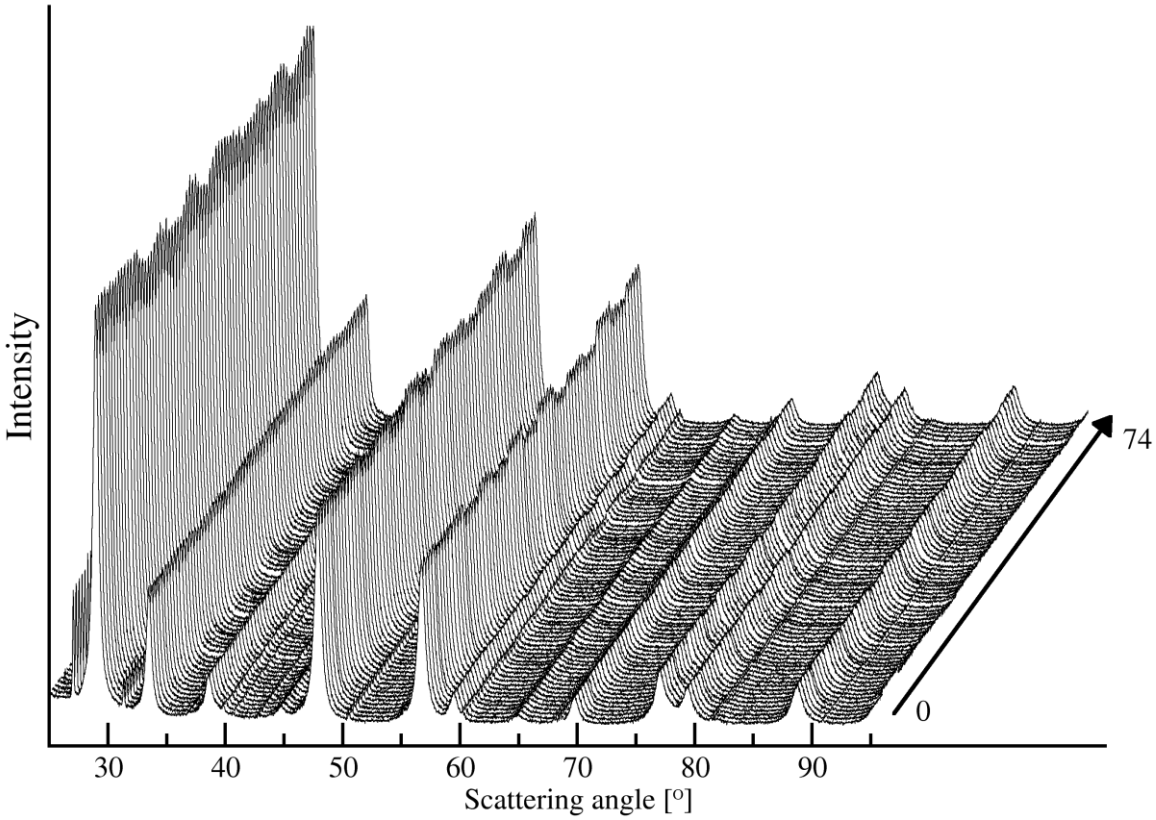

Fig. 31. The overview on the 75 collected diffraction patterns of the 9.4%$_{wt.}$ Au/CeO_2 during the *in-operando* PXRD-MS experiment.

Bearing in mind the lack of any intense ALP change of pure CeO_2, the case of the catalyst must rely on hydrogen molecule activation. Because the only new component in the system were AuNPs, it's a clear indication of interaction of H_2 with gold. This noble metal is known to be a great selective catalyst in hydrogenation of unsaturated organic compounds [55, 106, 107, 108, 109]. It has been also found already that admetals, like Cu and Au, aid generation of oxygen vacancies in ceria [110]. Here, gold helped to partially reduce ceria. The overall degree of reduction was obviously low and no new phase appearance (e.g. Ce_2O_3) was noticed. Following the equation (# - presented in Section 3.3.2) from Section 3.3.2, the calculated oxygen content regarding the 0.88 pm lattice expansion corresponded to $CeO_{1.981}$, so ceria was reduced by almost 1 %.

Most probably, hydrogen molecule activation took place at the interface of CeO_2 and AuNPs, precisely on the perimeter of gold particles. Such a mechanism was proposed on the basis of deep investigation of Au/TiO_2 system by infrared (IR) spectroscopy [111]. It was concluded that the activation energy of H_2 molecule dissociation to form Ti–OOH and Ti–OH species is in the range of 0.16–0.25 eV.At the same time, gold structure was not visibly affected by H_2 atmosphere. An important observation was also the reversible behaviour of this H_2-induced expansion of ceria – immediately after hydrogen was replaced by helium, CeO_2 structure contracted to its initial state. It is then hard to state that H_2 was dissociated to atoms or radicals, which in the next step reacted with surface oxygen moieties available on ceric oxide. Such a way of chemisorption might be expected to be more persistent and not to disappear so quickly after gas environment exchange. Finally, it was concluded that H_2 molecule was coordinated as whole molecule without division by surface oxygen of ceria. It is now an open question for spectroscopic studies how the conformation of this adsorbate looks like. The mechanism of CeO_2 structure

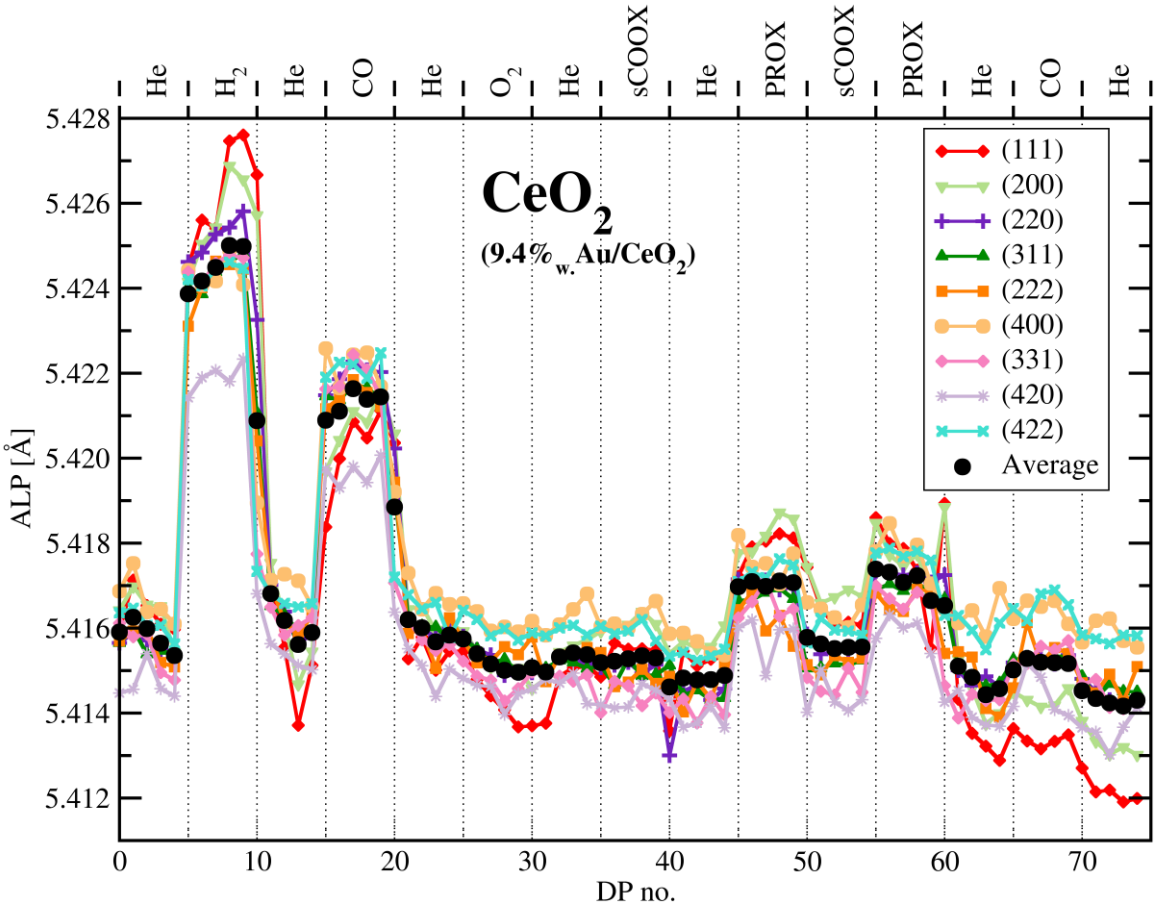

Fig. 32. Temperature-corrected apparent lattice parameter (ALP) of CeO_2 (the support of 9.4%$_{wt.}$ Au/ CeO_2 catalyst) calculated from the position (scattering angle 2θ) of each diffraction peak is plotted against the index of the diffraction pattern (DP) in the series of DPs. Acquisition of one DP takes ~42 min. Gas sequence is shown above the graph. sCOOX ≡ stoichiometric CO oxidation; PROX ≡ preferential oxidation (of CO).

expansion, from the cerium dioxide nanocrystals' point of view, should be identical to the one described in Section 3.3.2 for CO influence on ceria. H_2 interaction with oxygen on the surface bound the latter on Au particles' perimeter, thus increasing the concentration of vacancies in deeper layers of the particles. How far from a gold particle hydrogen molecules can influence the ceria surface remained a puzzle, but even a few tens of angstroms (up to 30 Å) range is possible [112] as enhanced diffusion of Ce and O on the CeO_2 surface under reducing gas atmosphere has been already reported [97, 113].

This mechanism was again responsible for CeO_2 structure behaviour under CO. Under these conditions there was no difference between the observation of the catalyst and pure ceria. The catalyst's support expanded exactly by 0.55 pm, which is much less than 0.88 pm experienced under hydrogen. Furthermore, gold reflections were not influenced by carbon monoxide.

The lack of global statistically proven shift of gold diffraction peaks was found in all gas atmospheres. This concern impedes drawing conclusions straight from gold structure behaviour and forces indirect analysis based on chemical data and structural differences between the catalyst's support and pure support without the active phase deposited on it. The only straightforward observation of the gold structure was connected with its unit cell parameter which occurred to be slightly smaller than the predicted value. Experimentally

Table 17. Summary of crystal structure dynamics of CeO_2 (the support of 9.4%$_{wt.}$ Au/ CeO_2 catalyst) as a function of gas atmosphere. For each gas atmosphere composition the average apparent lattice parameter (ALP) is calculated. sCOOX ≡ stoichiometric CO oxidation; PROX ≡ preferential oxidation (of CO).

Gas atmosphere	DP range	ALP [Å]	Std. Dev. [$\times 10^{-6}$ Å]
He	0 – 4	5.415809	393
H_2	5 – 9	5.424662	407
He	10 – 14	5.416124	513
CO	15 – 19	5.421392	220
He	20 – 24	5.415929	225
O_2	25 – 29	5.415129	195
He	30 – 34	5.415269	205
sCOOX	35 – 39	5.415285	53
He	40 – 44	5.414819	48
PROX	45 – 49	5.417063	57
sCOOX	50 – 54	5.415561	46
PROX	55 – 59	5.417067	298
He	60 – 64	5.414737	297
CO_2	65 – 69	5.415207	54
He	70 – 74	5.414262	78

it fitted within the range 4.0785 – 4.0875 Å and equalled 4.082 Å on the average, while the thermally expanded to 140-150°C structure of gold nanocrystals should exhibit lattice constant ~4.0842 Å.

The lack of gold structure dynamic lattice change indirectly suggests that reaction might take place on AuNPs perimeter. Thus, the structural perturbation might be too small to be spotted in averaged DPs.

By contrast to pure CeO_2, the structure of Au-decorated ceria was significantly influenced under both sCOOX and PROX conditions. Slight expansion could be seen also under pure CO_2. Lattice constant average increase by 0.13 pm, 0.28 pm and 0.10 pm was spotted under these gas mixtures, respectively. These changes in unit cell parameter corresponded appropriately to $CeO_{1.997}$, $CeO_{1.994}$ and $CeO_{1.998}$ stoichiometry. The biggest expansion connected with PROX conditions was certainly in some part the result of hydrogen molecules spillover (term usually referred to dissociated hydrogen atoms or radicals) from gold to ceria support. Adsorption of CO and CO_2 on cerium dioxide led also to crystal lattice expansion. However, the extent to which atomic network was stretched while reaction took place on the catalyst's surface is much lower than it was observed for pure gases. The limitation might correlate with oxygen occupation of part of the available sites on the surface, what would agree with results for pure CeO_2. Because of the running reaction of oxygen with CO, it was impossible to form a stable covering layer which

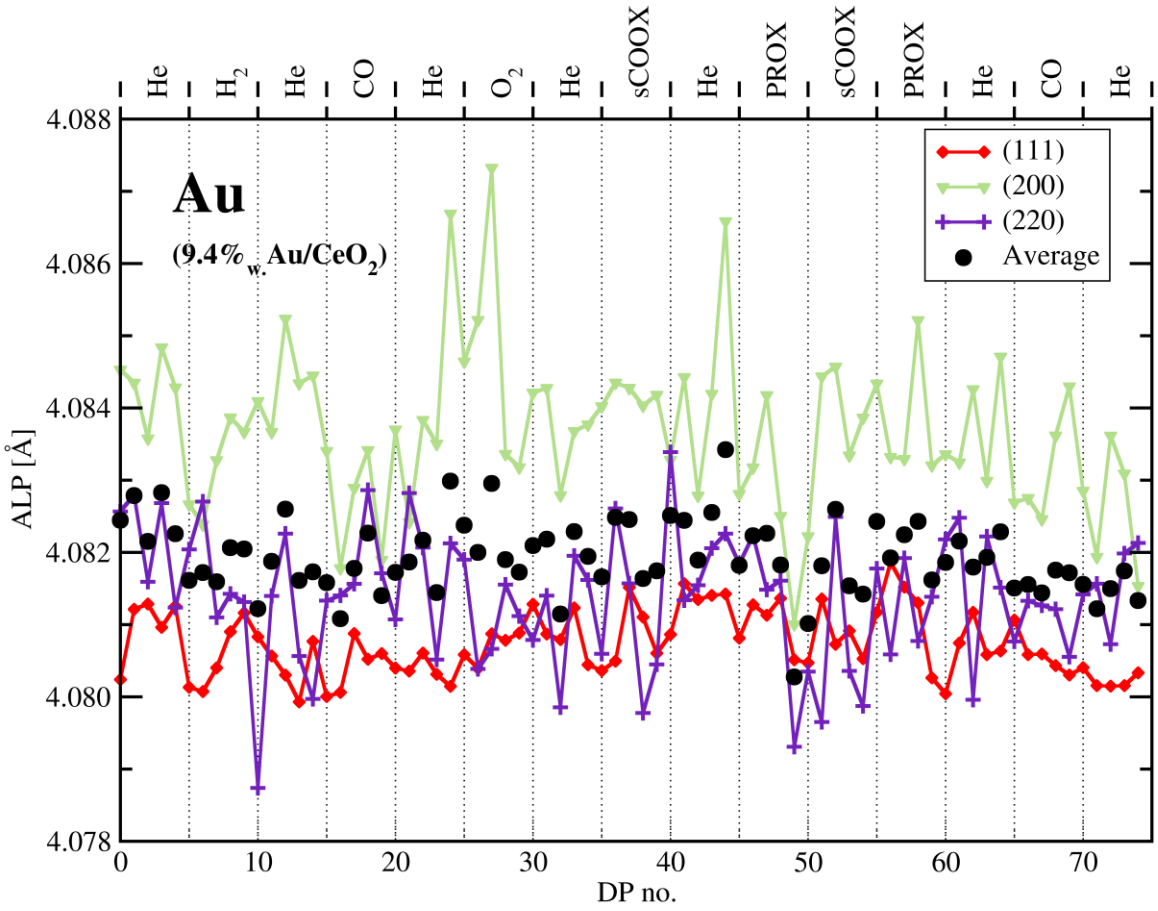

Fig. 33. Temperature-corrected apparent lattice parameter (ALP) of gold (component of 9.4%$_{wt.}$ Au/ CeO_2 catalyst) calculated from the position (scattering angle 2θ) of each diffraction peak is plotted against the index of the diffraction pattern (DP) in the series of DPs. Acquisition of one DP takes ~42 min. Gas sequence is shown above the graph. sCOOX ≡ stoichiometric CO oxidation; PROX ≡ preferential oxidation (of CO).

would fully cancel the lattice expansion. Yet an explanation is needed that will include very vigorous CO_2 production.

J. A. Rodriguez et al. presented in 2002 his research done on Au deposited on TiO_2 (110) surface which was subjected to EXAFS examination and first–principles density–functional slab calculations [3]. He concluded that in the proximity of gold the rate of oxygen vacancies exchange between the bulk and surface of TiO_2 is altered in favour of the surface. The higher concentration of O–vacancies perturbs electronically gold (among others –0.15 partial charge was found on gold) making it then more active. The evidence of this perturbation is visible also as an additional Au-induced occupied state ~1.6 eV above the TiO_2 valence band. From the DFT studies it was found that migration of O–vacancies to the surface near Au becomes exothermic ($-41.6\frac{\text{kcal}}{\text{mol}} = -1.79\frac{\text{eV}}{\text{atom}}$), while generation of surface defect is usually endothermic.

The interface of metal and its semiconductive support is sometimes referred to as Schottky junction, because a potential barrier (also called Schottky barrier, $2\phi(b) = 2(E_c - E_f)$, where E_c and E_f are the conduction band edge of the support and Fermi level of the metal phase, respectively) for electrons is formed there [112]. Although the surface may generally become terminated with oxygen and vacancies can move towards the bulk of the particle leading to nett effect of reduction of CeO_2, which means its crystal lattice

Table 18. Summary of crystal structure dynamics of gold (component of 9.4%$_{wt.}$ Au/CeO_2 catalyst) as a function of gas atmosphere. For each gas atmosphere composition the average apparent lattice parameter (ALP) is calculated. sCOOX ≡ stoichiometric CO oxidation; PROX ≡ preferential oxidation (of CO).

Gas atmosphere	DP range	ALP [Å]	Std. Dev. [$\times 10^{-6}$ Å]
He	0 – 4	4,082506	351
H_2	5 – 9	4,081856	237
He	10 – 14	4,081954	443
CO	15 – 19	4,081632	510
He	20 – 24	4,082116	652
O_2	25 – 29	4,082145	551
He	30 – 34	4,081890	516
sCOOX	35 – 39	4,082080	451
He	40 – 44	4,082578	633
PROX	45 – 49	4,081649	937
sCOOX	50 – 54	4,081843	529
PROX	55 – 59	4,082054	358
He	60 – 64	4,082042	220
CO_2	65 – 69	4,081617	146
He	70 – 74	4,081448	228

expansion, in the neighbourhood of AuNPs the local concentration of vacancies might be higher than average for the surface of CeO_2. This is, however, impossible to judge based on the structural data collected during this research. Collected data directly indicated the crystal structure expansion so characteristic for reduction of CeO_2 and the observed changes were perfectly reversible immediately after the trigger was removed.

CO oxidation reaction mechanism

Sun and Takeda et al. [114] suggested that CO oxidation kinetics is greatly enhanced by presence of water and its derivatives on the surface of the catalyst, which they related solely to gold nanoparticles. With DFT calculations, they pointed to –OH, –OOH and, especially, to –COOH species which played major role in the reaction mechanism that they proposed. Similar moieties were suggested by Bongiorno and Landman [115] in their first principles calculations performed on small Au clusters (8 – 30 atoms) immobilised on MgO (100) surface. They showed coadsorption of H_2O and O_2 resulting in proton transfer to –OOH where O–O bond was elongated by 21 %, so it was activated for the proceeding dissociation induced by approaching CO molecule from the gas phase. As they also noticed, in that case gold surface can be treated as hydrophilic and it acted as an attractor for water molecules present on MgO. This phenomenon was called *reverse–spillover*. Nevertheless, Sun and Takeda presented another route, as well, which explains CO_2 formation when no hydrogen-containing compounds were added to the feeding

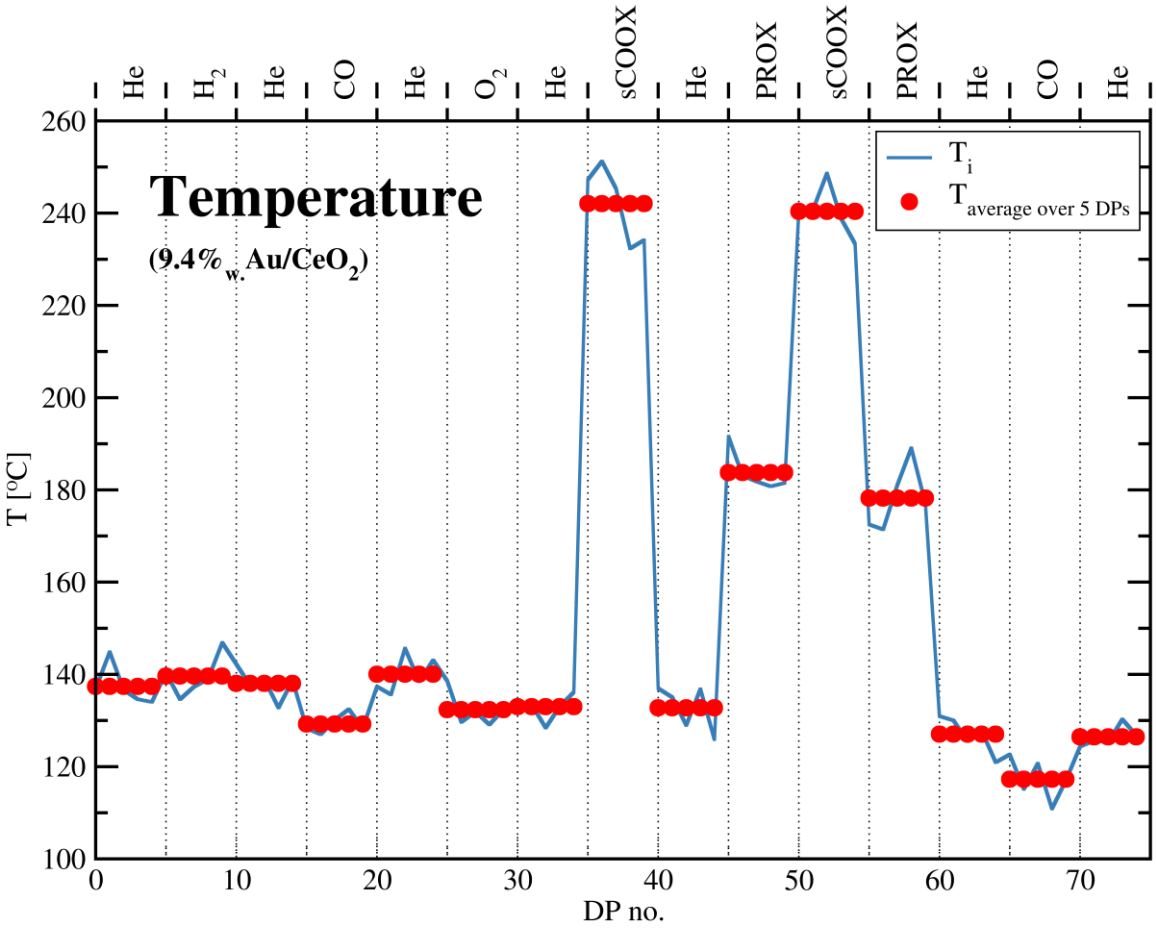

Fig. 34. Temperature profile of the specimen bed (9.4%$_{wt.}$ Au/CeO_2 catalyst) throughout the *in-operando* PXRD experiment. Values are calculated from the thermal expansion properties of "a" crystal lattice constant of crystalline quartz, which was mixed with the sample. Data are plotted against the index of the diffraction pattern (DP) in the series of DPs. Acquisition of one DP takes ~42 min. Gas sequence is shown above the graph. sCOOX ≡ stoichiometric CO oxidation; PROX ≡ preferential oxidation (of CO).

stream. Formation of all crucial moieties (important for both H_2-rich and H_2-free reactants mixture) strongly depends on the ability of the catalyst's surface to adsorb and dissociate oxygen molecules from the gas phase.

Normally this process, when conducted only on Au or CeO_2 surface, has a large energy barrier, mainly due to capabilities of both surfaces to bind O* ("*" indicates the bond with surface). This activation energy is so high that it cannot be overcome by heating the surface, because increased temperature facilitates also desorption of molecular oxygen, O_2*, adsorbed in the first step. The authors proposed a two-step reaction on gold surface between adsorbed undissiociated *CO and O_2*:

$$*CO + O_2* \leftrightarrow O*COO + * \leftrightarrow *CO_2 + O* \qquad (33)$$

This reaction has a relatively low energy barrier, 0.28 eV, and is highly exothermic – the total of 2.76 eV of heat is released.

A catalyst supported on a reducible oxide, like Au/CeO_2, creates opportunities to enhance the importance of those reaction acts, which were neglected by Sun and Takeda, as they

focused on isolated AuNPs. Active oxygen appearing on the gold surface can migrate towards CeO_2 surface. There are three possibilities of interactions between them:

- oxygen will occupy a vacancy available on ceria surface;
- oxygen will react with adsorbed and activated in this way CO molecule to form CO_2;
- oxygen will take part in cascade of other reaction acts.

All options are beneficial from the point of view of the CO oxidation reaction. The ease of oxygen transfer between the support (hence an easily reducible one) and gold nanocrystals is widely regarded as crucial for low temperature CO oxidation [105]. The second option proposed above is obvious and needs no further explanation. The first option results in creation of a new active site ready to adsorb new CO molecule. In the next step, either CO_2 will be directly formed and will desorb from the surface leaving the vacancy, or this CO molecule will remain activated for reaction with another O*. Regarding the CO adsorption experiments, this last variant rather does not lead to CO_2 formation and should be negligible in equilibrium. The net effect of O* occupying all vacancies would be a decrease of the ceria lattice parameter what is not observed. The third option cannot be approached now, as the scope of this research was to investigate structural changes of gold catalysts and not the adsorbates behaviour on the surface. Among many possible routes, formation of peroxides on the titanium (IV) oxide is noticed [111, 116], thus creating new active oxygen moieties easily available for CO molecules.

The statement that the concentration of oxygen vacancies on the CeO_2 surface during CO oxidation should be low because of their saturation with oxygen-containing species (like molecular CO and O_2 or atomic O*) is analogous to the result of *in-situ* ECM (Electrical Conductance Measuremnt) obtained for Au/TiO_2 catalyst by comparison of the conductance under CO atmosphere and during sCOOX reaction [117]. High electrical conductance $3 \cdot 10^{-5}$ S under pure CO indicated high oxygen vacancies concentration, while under COOX reaction conditions only $1.1 \cdot 10^{-8}$ S was measured, which is about 2700 times lower.

Furthermore, it was shown very recently in the studies of Water-Gas Shift (WGS) reaction over $Au/\alpha\text{-}Fe_2O_3$ catalyst [118], that if the support exposes mostly oxygen-terminated faces of $\alpha\text{-}Fe_2O_3$ (namely: {001}), the catalyst is prone to adsorb molecular H_2O (i.e. without its dissociation) and to efficiently produce only CO_2 through formation of formate groups at temperatures lower than 180°C. On the contrary, on {113} plane, which is rich with oxygen vacancies, dissociative adsorption of H_2O occurs and H_2 production (therefore WGS, not COOX, reaction occurs) starts at 140°C.

The hydrogen-assisted dissociation of oxygen, leading to formation of hydrogen-containing species (–OH, –OOH and –COOH), is also the reaction pathway that becomes much more important and probable thanks to the existence of oxide support in the catalyst composition. It is usually suggested [119] that adsorption and activation of oxygen requires CO too, so a H_2-CO-assisted activation of O_2 should be rather referred to. The gold catalyst prepared by means of wet synthesis has much water adsorbed on its surface as it could not be dried or calcinated at high temperature due to sintering of AuNPs which might then occur. Presence of H_2O even at very low concentrations, like several ppm, was reported to enhance the catalyst activity [120]. Oxide support acts then as a huge reservoir of water which does not get used during the reaction and does not

desorbs from the surface spontaneously, as well, because of too low temperature of the system.

The role of support was further studied with respect to support's isoelectric (IE) point. From the point of view of the synthesis procedure, the deposition–precipitation method benefits from weakly acidic or basic type of supports as usually any anchoring of gold precursor is favourable in water solution of pH > 7. However, it was reported [119, 121] that H^+ ions supplied by the strongly acidic support suppress catalyst's activity in CO oxidation. Hydrogen cations do not allow formation of –OH species and its derivatives, thus the importance of hydrogen-based reaction mechanisms is greatly limited.

To sum up, the role of the ceria support would be to provide extended reaction surface with ready to react adsorbed CO and to provide easy migration path for active O*. In this way, the support would increase CO_2 production rate at least 2 times, because O* produced on the gold surface results in release of at least one adsorption site on ceria that can be taken again by O_2 or CO with probability dependent on the adsorption potential, local concentrations of reagents and reaction stoichiometry. The proposed scheme can effectively reduce Au coverage by oxygen enhancing the reaction rate. It assumes that this enhancement is not dependent only on water content, unlike the kinetics of the reaction on gold alone (according to Sun and Takeda [114]).

Facing the proposed mechanism, which resembles the general Mars–van Krevelen mechanism [17], a question should be raised why gold atomic lattice in Au/CeO_2 catalyst was not influenced by interaction with the gas phase. To address this puzzle properly, first it is necessary to discuss how frequently any reaction act takes place on gold surface. If contribution of gold is just to trigger a cascade of further reaction steps which are carried out on the support's surface, the occasional interaction of gold particles with the environment will not be reflected in the averaged crystallographic image recorded in a diffraction pattern. Gold alone demonstrates activity towards CO_2 production according to possible reaction pathways shown by Sun et al. [114]. Some of them assume role of water, have low activation barrier and significant net exothermic effect. If so, gold surface ought to be highly mobile and disordered. Consequently, stress or surface roughening effects are barely detectable even under exposure to pure CO.

Structure analysis – diffraction peaks' intensity decay

Until now, structural changes were related only to changes of apparent lattice parameter calculated from the shifted diffraction peaks positions. Besides the scattering angle, other peaks' parameters describing their shape were monitored as well, including reflections intensity, full width at half maximum (FWHM) and presumptive asymmetry on the left or right side of the peak's profile.

As mentioned in Section 1.5, the decay of the intensity of the reflections of one crystallographic phase depends on:

- the structure factor;
- temperature oscillations and/or structure disorder;
- peak's multiplicity;
- polarisation of the scattered wave;
- Lorentz factor.

The last 3 terms are constant for a given structure type and diffraction geometry used during the experiment. Since, the relative intensity change among peaks of one phase in a given temperature can be caused by better ordering or progressive disordering of the atomic lattice, or slight deviations of particles' structure with respect to the reference bulk one. Qualitatively, evolution of the intensity can be measured by the ratio of detected reflection to the strongest visible in the studies angle range (see Table 19 and Table 20). Quantitative approach is based on Debye-Waller factor estimation, however its assessment may be sometimes misleading, as in the discussed case.

Table 19. Comparison of the average experimental intensities of selected gold diffraction peaks to the literature values for polycrystalline gold [122] (alter. [123]).

Miller *h k l* indices	Intensity of Au peaks [a.u]	
	reference [122]	experimental
1 1 1	100.00	100.00
2 0 0	47.92	22.44
2 2 0	28.36	15.16

Table 20. Comparison of the average experimental intensities of selected cerium (IV) oxide diffraction peaks to the literature values for polycrystalline ceria [124] (alter. [125]).

Miller *h k l* indices	Intensity of CeO_2 peaks [a.u]	
	reference [124]	experimental
1 1 1	100.00	100.00
2 0 0	27.73	29.52
2 2 0	48.63	54.25
3 1 1	35.71	41.26
2 2 2	6.31	6.49
4 0 0	5.98	6.44
3 3 1	11.84	10.86
4 2 0	7.15	5.99
4 2 2	10.51	9.79

In the case of Au/CeO_2, CeO_2 peak intensities decay resembles well the reference structure and the average displacement of atoms, 0.22 Å, is rather low. On the other hand, the intensity decay of AuNPs was ~2 times faster than for the reference gold structure. The intensity ratio of two most intense reflections is close to 0.2 which is very low comparing to polycrystalline gold diffraction pattern. Furthermore, the correlation of $-\ln I_0$ vs. $\left(\frac{\sin\theta}{\lambda}\right)^2$ (see Fig. 35), which ideally should be linear, suggests that 2 0 0 reflection has too small intensity (see the increased value of $-\ln I_0$, where I_0 is the measured intensity divided by structure factor, multiplicity and Lorentz polarization).

Table 21. Root mean square displacement of atoms $\sqrt{< u^2 >}$ from their nodes for gold and ceria structures in 9.4%$_{wt.}$ Au/CeO_2 catalyst. For comparison, the mean displacement for gold structure without considering 2 0 0 peak is included. Values calculated from Debye-Waller factor estimation.

Crystallographic phase	$\sqrt{< u^2 >}$ [Å]	$\Delta\sqrt{< u^2 >}$ [Å]
Au	0.305	0.019
Au 2 0 0 omitted	0.363	0.015
CeO_2	0.220	0.004

Although the root mean square displacement of gold atoms is bigger when the 2 0 0 peak is omitted during the analysis (Table 21), it is not possible to explain the intensity ratio of 2 0 0 to 1 1 1 peak with FCC structure disorder, strain or metal particles shape (which still have FCC atoms arrangement). This extreme ratio, approx. 0.2, is characteristic for non-periodical arrangements of atomic lattice in gold nanocrystals. There are two shapes of metal nanoparticles occasionally discussed in the literature that cannot be cut from FCC crystal lattice: icosahedron and decahedron. In the case of 9.4%$_{wt.}$ Au/CeO_2 catalyst, decahedral shape of AuNPs fits better to experimental data than icosahedron, while it provides explanation for observed intensity decay, anomalous for polycrystalline gold.

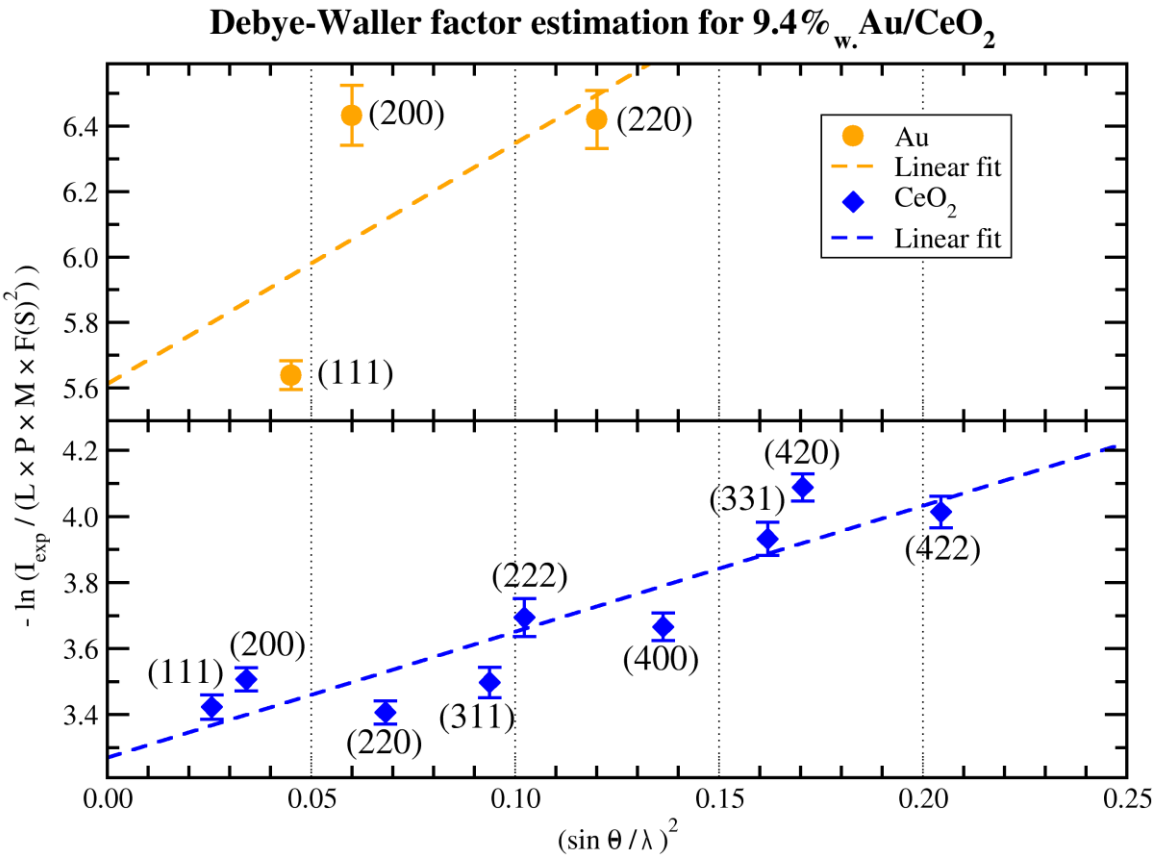

Fig. 35. The correlation of $-\ln I_0$ vs. $\left(\frac{\sin\theta}{\lambda}\right)^2$ used for estimation of the Debey–Waller factor in the case of the 9.4%$_{wt.}$ Au/CeO_2 for both gold (Au) and ceria (CeO_2) phases.

The comparison of diffraction patterns calculated according to Debye summation formula [74, 35] for energetically relaxed cuboctahedra, icosahedra and decahedra, containing similar total number of atoms, with the experimental catalyst DP is presented in Fig. 36. Only cuboctahedral shape on AuNPs cannot be assumed, because the observed 2 0 0 reflection intensity is always simply too low if 1 1 1 peak's intensity is scaled properly. Gold particles seems not to be purely icosahedrons as well, because such a shape would yield a broad scattering band between 60° – 80° 2θ and thus no clear gold peaks should be observed in this region, but it is not the case of 9.4%$_{wt.}$ Au/CeO_2 catalyst. On the contrary to icosahedral, decahedral particles show clearly separated peaks in this angular range and the intensity ratio of 1 1 1 and 2 0 0 reflections is appropriate.

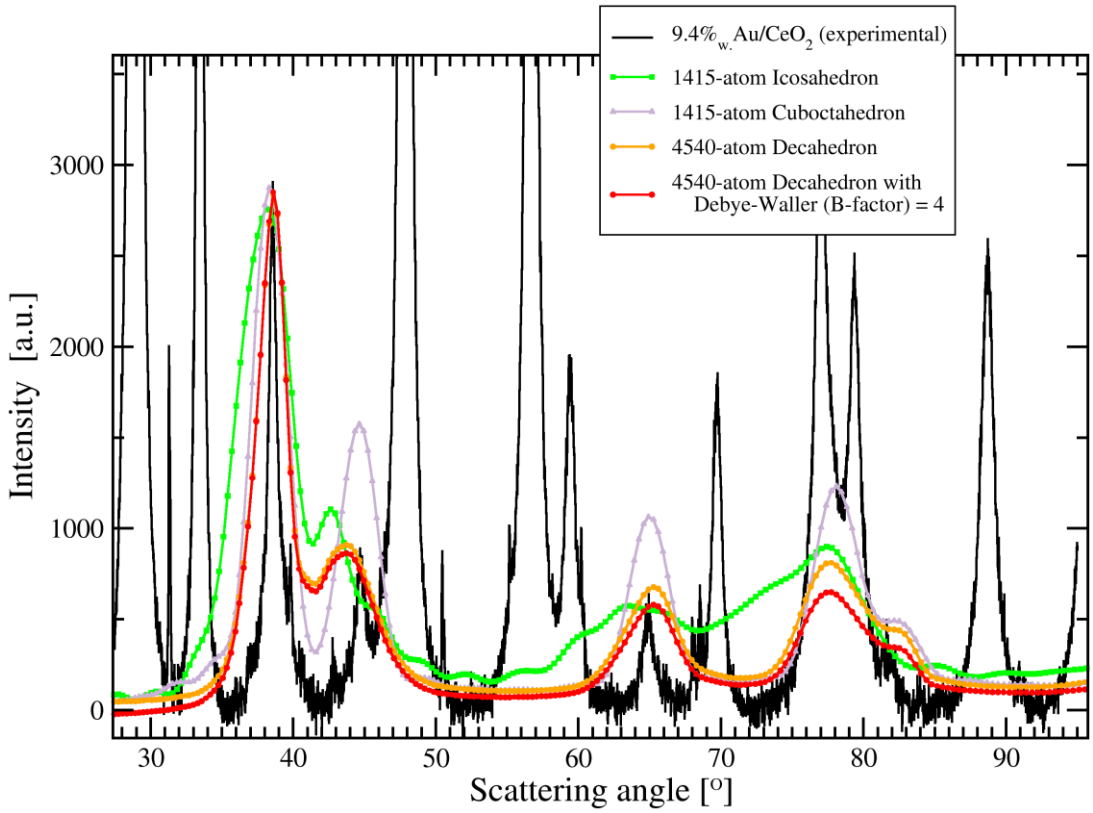

Fig. 36. The comparison of the sample experimental DP of the 9.4%$_{wt.}$ Au/CeO_2 catalyst to the simulated (using Cluster program, Section 2.6) DPs of selected model gold nanocrystals. Accounting for peak positions and relative intensity of height, the slightly disordered 4540-atom decahedron (red line) fits best to the data. Although it is clear, that the real AuNPs are larger than the models ones (hence, the peaks are narrower) – building much bigger crystal models requires much more computational resources for model energy minimisation. Refer also to Fig. 6 (page 23) for more simulated DPs.

Structure analysis – size and strain

Conclusions drawn from structure analysis may be heavily violated if the crystal object of interest is affected by stress that results in a strained atomic lattice. There is also, so called, "zero-stress strain" which frequently accompanies nanocrystals and originates, paradoxically, from full relaxation of surface energy excess of those nanocrystals. Therefore, it is important to assess the magnitude of these effects and, if necessary, take them into account. Williamson-Hall approach serves as a good tool for basic estimation of size and strain.

The 9,4%$_{wt.}$ Au/CeO_2 catalyst showed negligible strains in both gold and ceria structures. It is well visible in Fig. 37 and the results of analysis are gathered in Table 22. Generally, it is believed that if the slope of correlation of $FWHM \cdot \cos\theta$ with $\sin\theta$ is below 0.01,

the structure can be regarded as unstrained, provided that no systematic deviations along any specific crystallographic direction are detected. This slope in the case of ceric oxide equals 0.0069 ± 0.0027 and for gold it is 0.0006 ± 0.0015. The relatively big error reported for gold structure strain factor is due to poor statistics based only on 3 reflections, but they represent different crystallographic directions. Nevertheless, either of phases can be regarded on average as unstrained structures.

The Williamson-Hall analysis procedure yields also additional parameter which is mean crystallite size. These sizes for CeO_2 and Au, 20.0 ± 3.6 nm and 13.7 ± 0.8 nm, respectively, were already reported at the very beginning of this Section and are included in Table 22. The error reported for ceria mean crystallite size is high mainly because of pronounced deviations from the linear trend in the case of higher indexed reflections. This is quite common for nanocrystalline structures due to broader overlapping diffraction peaks, which deconvolution is challenging. Besides, the support of the catalyst was a commercially available cerium (IV) oxide powder and was used in the synthesis without any crystals size selection/exclusion. Thus, broad distribution of crystals' size was expected and is not surprising.

The estimated Au NPs size apparently disagrees with TEM observations (see Section 3.4.1). The principal factor is the crystal size distribution strongly affecting differences between the size average and the volume weighted size average. Typical cost effective TEM size histogram is formed on the basis of more than 100 counted crystals seen on the photographs [77]. However, adding to the resulted histogram even one larger crystal (e.g. 15 nm in size) substantially shifts the calculated volume weighted average. In practice, millions of nanocrystals contribute to the XRD peak shape whereas presence of one larger

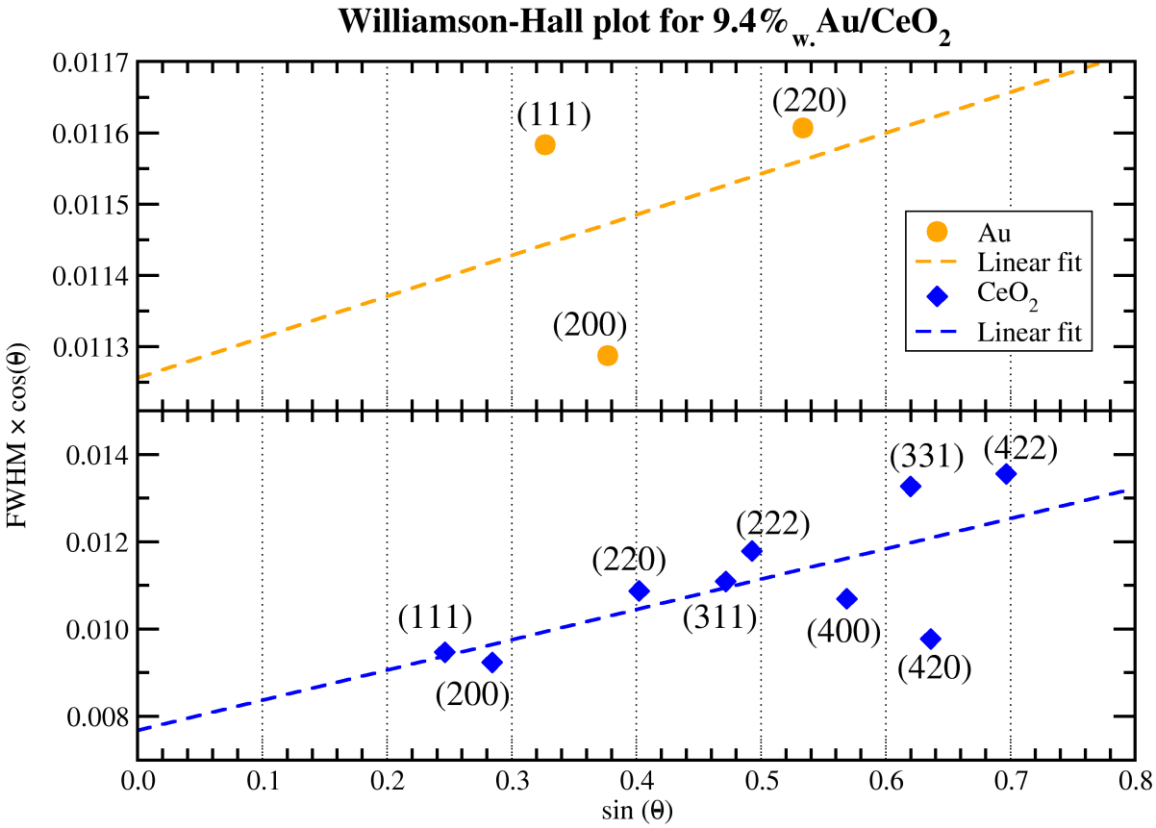

Fig. 37. The Williamson–Hall plot used for the estimation of size and strain of the gold (AuNPs) and ceria (CeO_2) nanoparticles in the $9.4\%_{wt.}$ Au/CeO_2.

per thousands of small metal nanoparticles can pass unnoticed in the TEM study. In the case of 9.4%$_{wt.}$ Au/CeO_2 catalyst adding few larger crystals in the size range 10–20 nm is sufficient to obtain agreement between XRD size and the TEM size distribution.

Table 22. The summary results of Williamson-Hall analysis of 9.4%$_{wt.}$ Au/CeO_2 catalyst. Data corresponds to Fig. 37. Slope of line fitted to correlated $FWHM \cdot \cos\theta$ and $\sin\theta$ is the measure of strain, while the intercept with OY is reciprocal to mean crystallites size.

Crystallographic phase	$C \cdot \varepsilon$	$\frac{K \cdot \lambda}{D}$	D [nm]
Au	0.0006±0.0015	0.0113±0.0007	13.7±0.8
CeO_2	0.0069±0.0027	0.0077±0.0014	20.0±3.6

3.3.4. Au/SiO_2 – structure dynamics and chemistry

The catalyst containing 7.16%$_{wt.}$ Au loaded on amorphous silica support was investigated in PXRD chamber at 160°C set on the heating block. In general, the catalyst occurred to be only moderately active in CO oxidation and it was poorly selective to CO_2 as comparable amounts of H_2O were produced during PROX reaction conditions. The characteristic behaviour of this sample was that oxidation of CO had to be triggered at first with hydrogen mixed to the gas feeding stream. Otherwise, only traces of CO_2 production could be spotted. Precise MS data are shown in Fig. 38 and Table 23. Williamson-Hall analysis returned the mean size of gold crystallites of 4.1 ± 0.7 nm (for more details please refer to "Structure analysis – stress and strain" subsection). Crystal structure dynamics of gold phase remained hard for interpretation, similarly to the case of Au/CeO_2. Insights on this are presented in subsection "Structure analysis – lattice constant" and "– diffraction peaks' intensity decay", in Fig. 40 and Table 24.

Chemical performance

The most distinguishable feature of 7.16%$_{wt.}$ Au/SiO_2 catalyst regarding its activity in CO oxidation was stimulation by the presence of hydrogen in the stream. Generally, the specimen was exposed to hydrogen for several hours prior to exposure to stoichiometric CO oxidation reaction conditions for the first time. This did not, however, grant to obtain reasonable CO_2 production. MS 44 signal, which corresponds to CO_2^+ ion, remained over 1 order of magnitude lower than CO^+. Although it increased with time, it was a very weak trend (please note that the time period between 35 and 40 DPs in Fig. 38 lasted for about 4-5 hours). Detected traces of residual water seemed not to stipulate the catalyst performance.

The situation changed completely when the specimen was exposed to PROX reaction conditions. The presence of H_2 resulted in both H_2O and CO_2 production with similar yields. The overall conversion of carbon monoxide did not reach as high level as in the case of Au/CeO_2 catalyst. Nevertheless, oxidation of CO and H_2 led to the *light-off* phenomenon [86] as well. The temperature of the specimen bed rose by approx. 60°C during first attempt of PROX reaction, but only by approx. 40°C during the second.

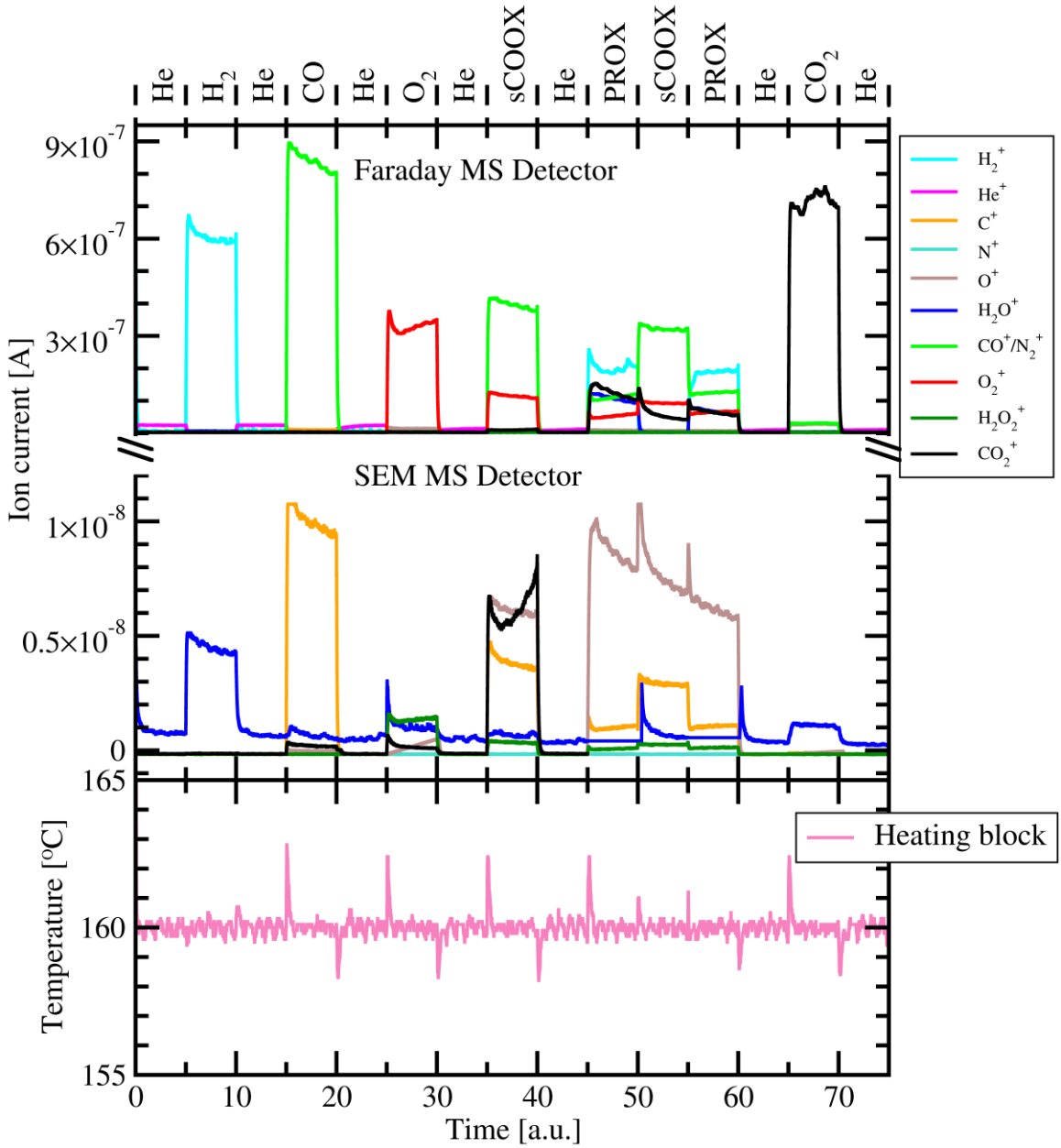

Fig. 38. Mass spectrometry (MS) analysis of composition of the gas stream leaving the PXRD chamber with 7.16%$_{wt.}$ Au/SiO_2 and the actual temperature of the heating block. MS signals corresponding to relevant cations are shown. Data are plotted against time normalized to time required to acquire one diffraction pattern (DP; approx. 42 min). sCOOX ≡ stoichiometric CO oxidation; PROX ≡ preferential oxidation (of CO).

When hydrogen was removed from the gas feeding stream, i.e. second exposure to sCOOX reaction conditions was performed, carbon dioxide was still produced despite the immediate water level drop. The initial increase in m/z = 44 signal occurred due to rapid change of pressure in the MS chamber after hydrogen vanished from the gas stream. The *light-off* phenomenon remained visible, but, as water was no longer produced, temperature of the catalyst was only approx. 20°C higher than under helium atmosphere.

After the whole PROX-sCOOX-PROX sequence was examined, it was evident that the catalyst underwent progressive deactivation with regard to conversion to either of CO_2 and H_2O. The reason of this loss of activity was not studied in detail. The gold structure

Table 23. Outlet gas composition and reaction yields analysis for the sCOOX and PROX reactions carried out on 7.16%$_{wt.}$ Au/SiO_2 catalyst in the PXRD chamber. sCOOX ≡ stoichiometric CO oxidation; PROX ≡ preferential oxidation (of CO).

Compound	Ion current [× 10^{-6} A]			$\eta_{\rightarrow CO_2}$ [%]			$\eta_{\rightarrow H_2O}$ [%]
	(before PROX) sCOOX	sCOOX	PROX	(before PROX) sCOOX	sCOOX	PROX	PROX
CO	0.40	0.320	0.112	1.2	9.1	43.4	-
O_2	0.115	0.093	0.050	2.1	14.3	28.1	38.1
CO_2	0.0069	0.120	0.045	-	-	-	-
H_2O	0.00	0.000	0.105	-	-	-	-
Selectivity to CO_2, S_{CO_2} [%]:						42.5	

did not change significantly – peaks' intensity ratios and FWHM remained constant throughout the whole experiment, i.e. all 75 acquired DPs.

Generally, from the chemical point of view 7.16%$_{wt.}$ Au/SiO_2 catalyst is not a good candidate for further studies of preferential oxidation of CO. Its selectivity as well as activity would require to be largely improved before the catalyst can gain properties

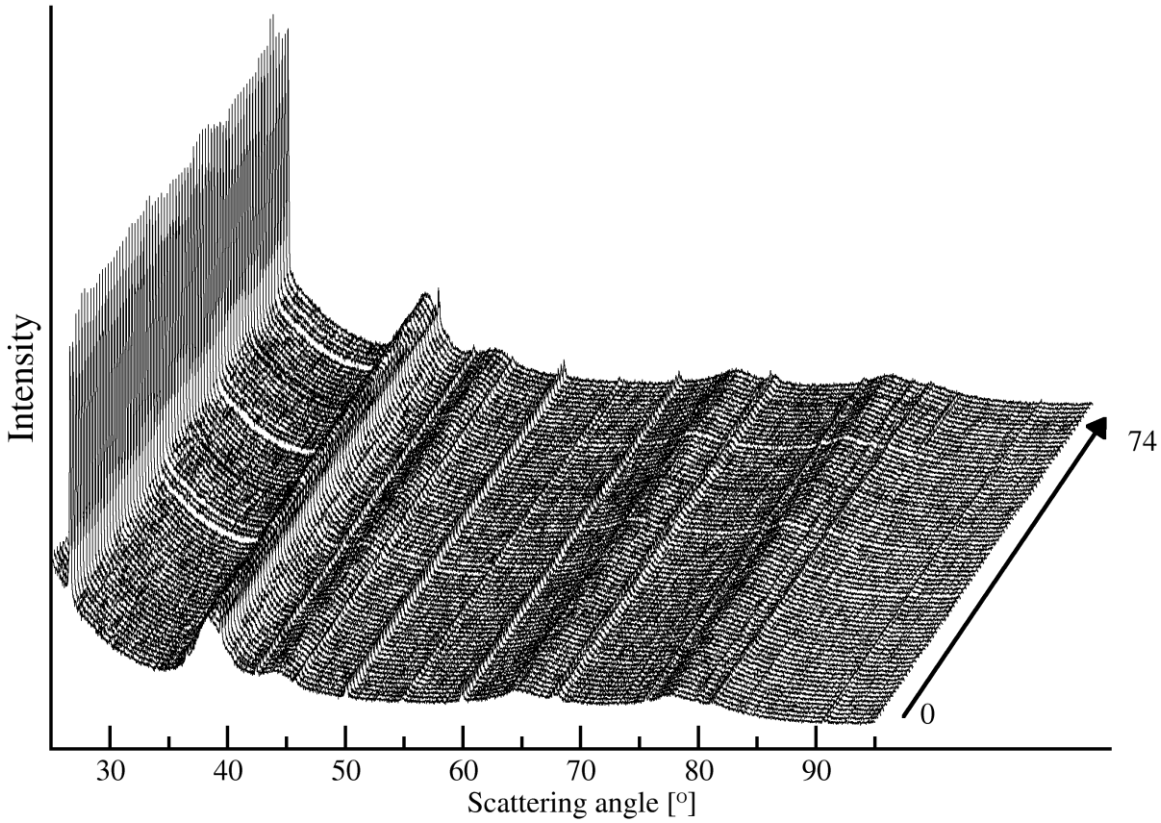

Fig. 39. The overview on the 75 collected diffraction patterns of the 7.16%$_{wt.}$ Au/SiO_2 during the *in-operando* PXRD-MS experiment.

comparable to e.g. Au/CeO_2 system. What is worth notice is that the chemical output measured in the PXRD chamber reflects excellently the real performance of the catalyst. Data are in good agreement with the one presented in Section 3.2.3 for the continuous flow reactor.

Comparison of Au/CeO_2 and Au/SiO_2 catalysts, both supported on oxide materials, reveals how important for the catalyst's properties are its interactions and mutual influence of metal phase and its support. Then the commonly adopted approach, that small gold crystals, preferably smaller than 10 nm or better 5 nm, are the key of the gold-containing catalyst to be efficient, is a very rough and shallow one. Similar concerns are occasionally raised in the literature, as very recently did O. Bondarchuk et al. concluding his studies on CeO_2 and SiO_2 supported gold catalysts [126] or a few years earlier M. A. Centeno et al. at the end of his article in Catalysis Letters [105].

Structure analysis – lattice constant

In the analysis of Au crystal structure, the thermal expansion was taken into account and the obtained lattice constant values were recalculated to a common temperature (average temperature measured during DPs 0 – 4 under helium in Fig. 41) using thermal expansion coefficient of gold reported in Section 2.5.5.

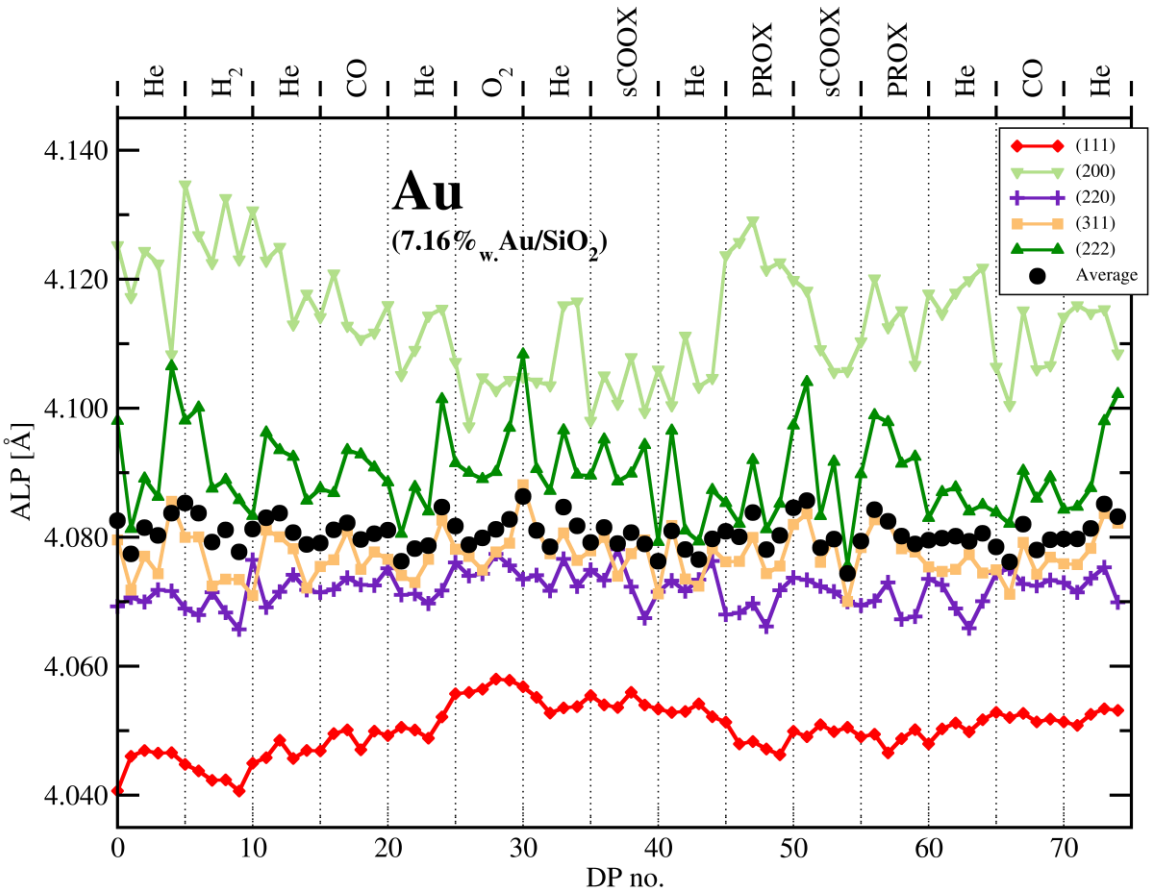

Fig. 40. Temperature-corrected apparent lattice parameter (ALP) of gold (component of 7.16%$_{wt.}$ Au/SiO_2 catalyst) calculated from the position (scattering angle 2θ) of each diffraction peak is plotted against the index of the diffraction pattern (DP) in the series of DPs. Acquisition of one DP takes ~42 min. Gas sequence is shown above the graph. sCOOX ≡ stoichiometric CO oxidation; PROX ≡ preferential oxidation (of CO).

Table 24. Summary of crystal structure dynamics of gold (component of 7.16%$_{wt.}$ Au/SiO_2 catalyst) as a function of gas atmosphere. For each gas atmosphere composition the average apparent lattice parameter (ALP) is calculated. sCOOX ≡ stoichiometric CO oxidation; PROX ≡ preferential oxidation (of CO).

Gas atmosphere	DP range	ALP [Å]	Std. Dev. [$\times 10^{-6}$ Å]
He	0 – 4	4.080718	2636
H_2	5 – 9	4.080452	2589
He	10 – 14	4.081575	2223
CO	15 – 19	4.080882	1080
He	20 – 24	4.079460	3627
O_2	25 – 29	4.080670	1703
He	30 – 34	4.081490	2530
sCOOX	35 – 39	4.080034	1271
He	40 – 44	4.078827	1938
PROX	45 – 49	4.080553	2386
sCOOX	50 – 54	4.079529	4677
PROX	55 – 59	4.081457	2368
He	60 – 64	4.079987	521
CO_2	65 – 69	4.078949	2475
He	70 – 74	4.082352	2331

Changes happening to the atomic lattice were found to be difficult to interpret. The overall average values of gold crystal unit cell constant calculated over all 5 reflections equalled almost exactly 4.0800 Å and did not vary by more than 0.0025 Å from this value. There was also no clear and unambiguous expansion nor contraction of gold structure upon exposure to any of the used gases, including sCOOX and PROX reactions conditions when considerable CO_2 and H_2O production was observed.

Examination of every single diffraction peak position did not shed more light on evolution of gold structure in this catalyst influenced by surface phenomena. Peaks' tops are rather randomly distributed around the average values.

Throughout the whole experiment gold nanocrystals did not sinter, although the vast majority was smaller than 5 nm. FWHM of 1 1 1, 2 2 0 and 3 1 1 peaks remained constant. In the case of the other two reflections, 2 0 0 and 2 2 2, their FWHM oscillated much, but around their average values. No clear correlation of these oscillations with the gas atmosphere composition could be derived. It is expected, that one of the reasons of this noisy behaviour of FWHM in these two examples lies in the fact that these peaks overlaid with lower-angle peaks which were more intense.

The other, more important, reason which caused problems in obtaining a stable fit of FWHM to 2 0 0 and 2 2 2 diffraction peaks' shapes was the additional intensity occurring

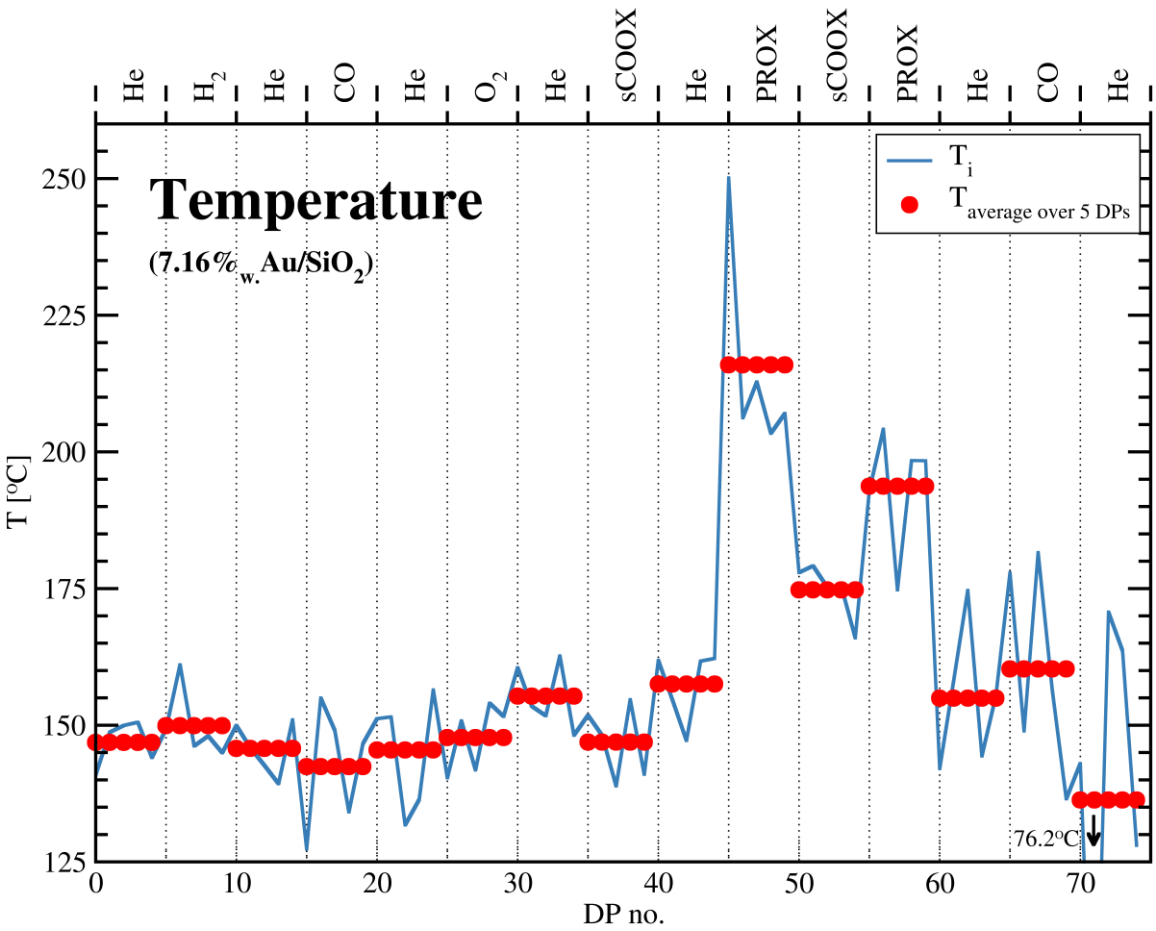

Fig. 41. Temperature profile of the specimen bed (7.16%$_{wt.}$ Au/SiO_2 catalyst) throughout the *in-operando* PXRD experiment. Values are calculated from the thermal expansion properties of "a" crystal lattice constant of crystalline quartz, which was mixed with the sample. Data are plotted against the index of the diffraction pattern (DP) in the series of DPs. Acquisition of one DP takes ~42 min. Gas sequence is shown above the graph. sCOOX ≡ stoichiometric CO oxidation; PROX ≡ preferential oxidation (of CO).

between the two pairs of reflections: 1 1 1–2 0 0 and 3 1 1–2 2 2. It was hard, or even impossible, to explain this excessive intensity with just FCC-structured nanocrystals and additional stress or disorder introduced to the model particles. Further details on this issue are given in the next subsections "Structure analysis – diffraction peaks' intensity decay" and "– stress and strain".

Structure analysis – diffraction peaks' intensity decay

The excessive intensity noticed between 1 1 1–2 0 0 and 3 1 1–2 2 2 neighbouring diffraction peaks (mentioned in the previous subsection) is also accompanied by rapid decay of intensities of subsequent reflections (refer to Table 25) which is unusual in such extent for FCC structure metals.

The Debye-Waller analysis yielded at first a negative slope of correlation of $-\ln I_0$ vs. $\left(\frac{\sin\theta}{\lambda}\right)^2$ (see Fig. 42). This slope became positive after 2 0 0 reflection was excluded from calculations. Then the structure of gold seemed to be totally ordered. Gold atoms were not displaced much from the lattice nodes, as the average deviation from ideal positions was assessed at 0.1 Å.

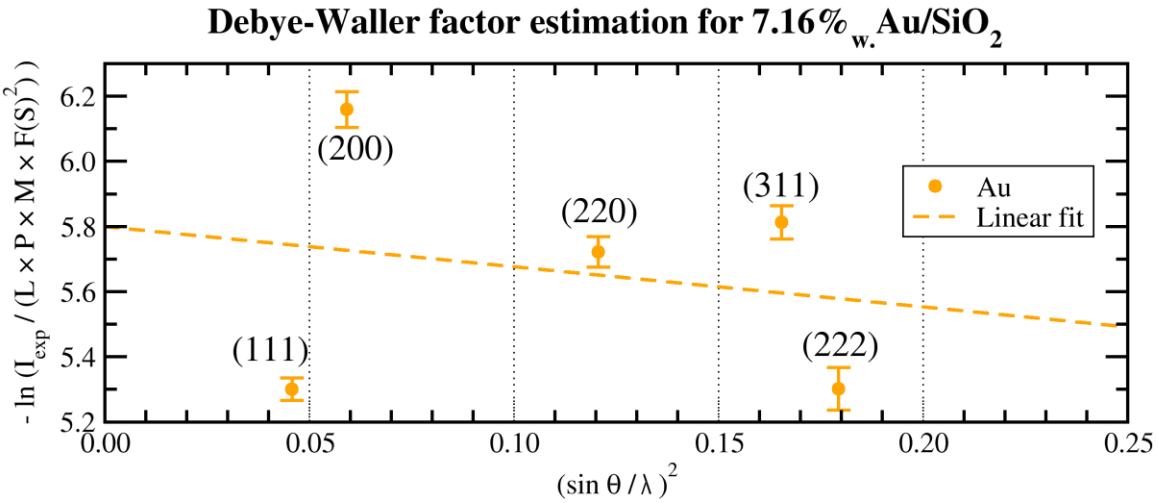

Fig. 42. The correlation of $-\ln I_0$ vs. $\left(\frac{\sin\theta}{\lambda}\right)^2$ used for estimation of the Debey–Waller factor in the case of the 7.16%$_{wt.}$ Au/SiO_2 catalyst for the gold (Au) crystal phase.

Such an approach could not be accepted, because no reflection might be omitted in the analysis without providing a reason. Assuming totally different concept, that the structure was heavily strained and that low 2 0 0 peak intensity was an anisotropic feature, did not enable to agree the fitted model with the experimental data.

However, the rapid intensity decay mimics the case of Au/CeO_2 catalyst. The major difference between gold phases supported on CeO_2 and SiO_2 is the mean size of AuNPs, 14 nm vs. 4 nm respectively, which is reflected in the peaks' breadth.

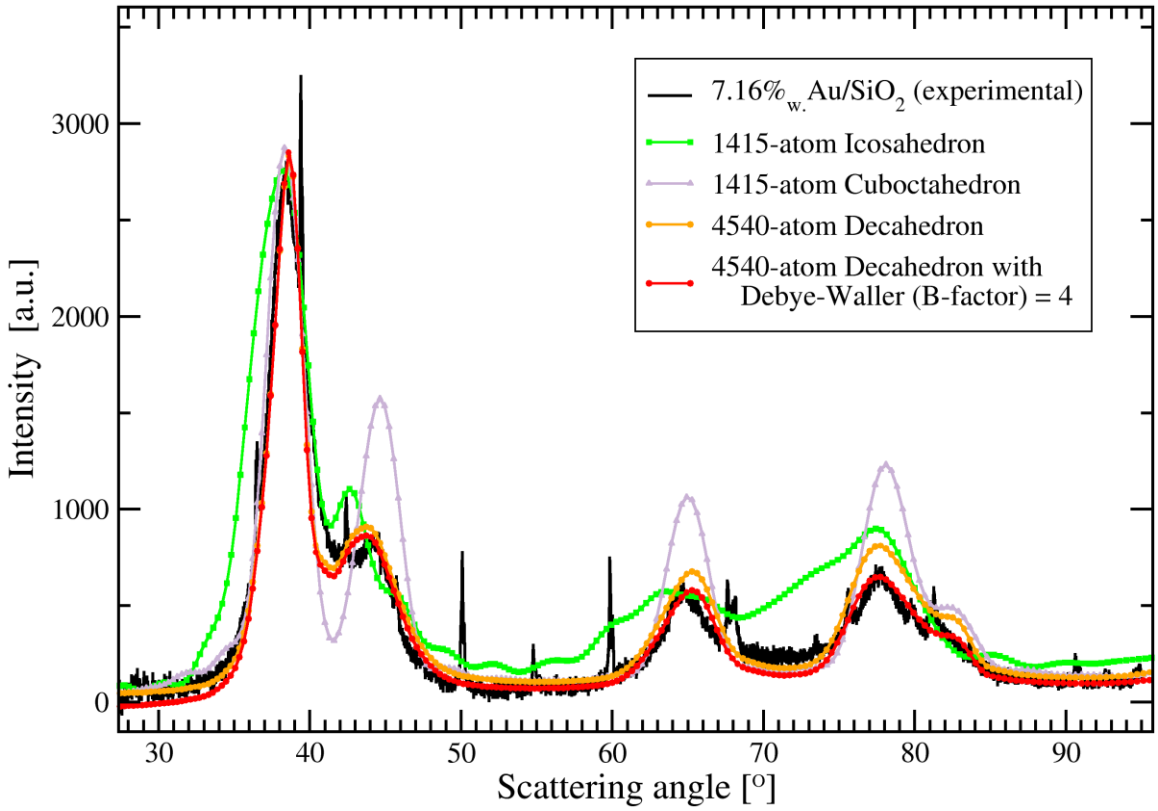

Fig. 43. The comparison of the sample experimental diffraction pattern of the 7.16%$_{wt.}$ Au/SiO_2 catalyst to the simulated (using Cluster program, Section 2.6) DPs of selected model gold nanocrystals. Accounting for peak positions, shapes and relative intensity of height, the slightly disordered 4540-atom decahedron (red line) fits the best to the data.

This unnaturally small ratio of subsequent peaks (with respect to the first most intense one), like 0.2 ratio of 2 0 0 to 1 1 1 diffraction peak, in the case of a structure, that supposedly should be face–centred cubic, recall non-periodical arrangements of atomic lattice in gold nanocrystals – similarly as in specimen of CeO_2-supported catalyst. Out of the two shapes of AuNPs containing 5-fold symmetry, decahedra suited again better the experimental diffraction patterns than icosahedra. The choice was based on the fact that icosahedral shape of clusters and atoms ordering inside them result in broad scattering bands above $2\theta = 50°$ rather than isolated peaks with clearly defined maxima, even if they overlap strongly each other (please refer to Fig. 43).

On the other hand, decahedral gold clusters are free from these issues. The diffraction peaks obtained using Debye summation formula applied to a model relaxed decahedra AuNPs appear near the positions characteristic for FCC structures and are clearly distinguishable. With the decreasing size of gold decahedron, the peaks become not only broader, but also shift their maxima. The low-angle peaks which apparently coincide with 1 1 1 and 2 0 0 reflections from FCC structure, approach closer to each other. As some narrow distribution of gold nanocrystals sizes was expected (and confirmed with Williamson-Hall analysis and TEM investigation), the smallest AuNPs could well participate in increasing the observed intensity between these reflections. The same phenomenon is valid of peaks resembling 3 1 1 and 2 2 2 reflections. The visualisation of the presented explanation for rapid peaks' intensity decay and excessive scattering intensity observed in some parts of the experimental patterns is shown in Fig. 43. The theoretical diffraction pattern for classical cuboctahedral gold cluster is also included for convenient comparison why this model failed this time to describe experimental data.

Table 25. Comparison of the average experimental intensities of selected gold diffraction peaks to the literature values for polycrystalline gold [122, 123].

Miller *h k l* indices	Intensity of Au peaks [a.u]	
	reference [122]	experimental
1 1 1	100.00	100.00
2 0 0	47.92	21.73
2 2 0	28.36	21.94
3 1 1	31.29	24.24
2 2 2	8.94	12.00

Table 26. Root mean square displacement of atoms $\sqrt{< u^2 >}$ from their nodes for gold structure in 7.16%$_{wt.}$ Au/SiO_2 catalyst. For comparison, the mean displacement for gold structure without considering 2 0 0 peak is included. Values calculated from Debye-Waller factor estimation.

Crystallographic phase	$\sqrt{< u^2 >}$ [Å]	$\Delta\sqrt{< u^2 >}$ [Å]
Au	< 0.00	- - -
Au 2 0 0 omitted	0.138	0.012

Structure analysis – size and strain

Size and strain analysis is based on the dependence of FWHM on the scattering angle. A relaxed structure with no strains is expected to present constant values of $FWHM \cdot \cos\theta$. As mentioned briefly in subsection "Structure analysis – lattice constant", in the two pairs of reflections, peaks of lower intensity overlapped with the more intense neighbours. In addition, there was strong asymmetry of peaks: right-hand side for lower angle and left-hand side for higher angle peaks. It was found that this asymmetric shape might be the consequence of gold clusters atomic lattice ordering exhibiting 5-fold symmetry followed by a range of clusters sizes distribution.

The observed phenomena resulted in difficulties in automatic machine analysis of the DPs. Especially, FWHM values for 2 0 0 and 2 2 2 reflections varied a lot from one pattern to the other. These values were, however, quite randomly distributed and, after averaging, formed a well–visible trend in Fig. 44. The rather huge error, reaching 50%, in the slope coefficient (which is proportional to the strain) was thanks to 2 2 0 diffraction peak, of which the result of FWHM · cos θ multiplication seemed to be too high.

If this fact will be temporarily neglected, the gold phase appeared to be a little bit strained. Bearing in mind that gold particles are of nanometric size and no strong anisotropy of FWHM was observed (which would suggest particles shape elongated in a given crystallographic direction), this strain may be the consequence of, so called, *zero-stress strain*. It indicates the stress coming from the structure relaxation rather than induced by external forces (for instance like poor quality epitaxy on the support or bending, squeezing forces). Very small crystals commonly experience this phenomenon, as not fully-coordinated atoms that form the surface constitute large fraction of the total number of atoms. The energy excess connected with the empty coordination spheres of those atoms is then dissipated on the whole structure of a cluster, thus leading to appearance of wide distribution of interatomic distances on a very short length scale and, consequently, strain. This chain of interactions was the base for this research as any surface interactions are detected indirectly by investigation of the average structure evolution.

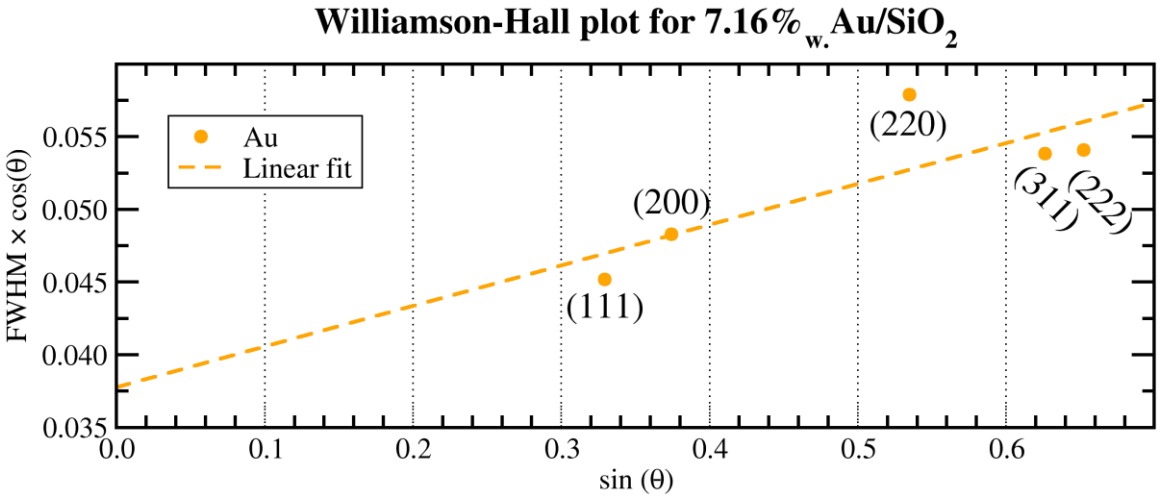

Fig. 44. The Williamson–Hall plot used for the estimation of size and strain of the gold nanoparticles (AuNPs) in the 7.16%$_{wt.}$ Au/SiO_2.

Table 27. The summary results of Williamson-Hall analysis of 7.16%$_{wt.}$ Au/SiO_2 catalyst. Data corresponds to Fig. 44. Slope of line fitted to correlated $FWHM \cdot \cos\theta$ and $\sin\theta$ is the measure of strain, while the intercept with OY is proportional to mean crystallites size.

Crystallographic phase	$C \cdot \varepsilon$	$\frac{K \cdot \lambda}{D}$	D [nm]
Au	0.0280±0.0118	0.0378±0.0062	4.1±0.7

Moving attention back to 2 2 0 reflection, this is actually the only peak that lays in the angular region of relatively smooth background (also well subtracted by the method of division of the experimental DP by the reference background pattern) and far from other reflections. FWHM of this peak should be the most reliable one. Hence, a justified suspicion arose that Voigt (or XVoigt) analytical functions and the preliminary tentative assumption of FCC structure of gold were not appropriate to describe the experimental data, in particular the overlapping with extra intensity pairs of reflections. Crystallography of aperiodic structures, like 5-fold symmetric decahedron, differs critically from classical approach and diffraction patterns evolve substantially with the changing size of cluster, particularly when this cluster contains only several hundred or a few thousands of atoms. Because of lack of ready-to-use and well-established tools devoted to analysis of such cases, it was decided to still attempt to apply standard DPs analysis used normally in this research, i.e. fitting of XVoigt functions to experimental diffraction peaks' profiles. Additionally, to cover the newly discovered obstacles, atomistic simulations of decahedral gold clusters' models were conducted. The models were subjected to atomic lattice energy optimisation and minimisation, so relaxed gold nanocrystals were obtained. The conclusions were already presented in the subsection above.

CO oxidation reaction mechanism

Activity of 7.16%$_{wt.}$ Au/SiO_2 catalyst consisting of 4.1 ± 0.7 nm gold crystals encountered great dependence on hydrogen availability in the gas stream. Without H_2, the pure stoichiometric mixture of CO and O_2 was not oxidised to CO_2. Situation changed completely after the gas composition was enriched with hydrogen at the cusp of acquisition of 44th and 45th diffraction patterns. This should be a straightforward suggestion in favour of the work of Sun and Takeda et al. [114], which was widely referred to and described in Section 3.3.3. devoted to Au/CeO_2 system.

There was, however, vital difference in performance of Au/SiO_2 catalyst in comparison to the ceria-supported one – water was obtained in quantities similar to carbon dioxide amount. The mechanism presented earlier benefited from the hydrogen-containing species, but, at the same time, extensive hydrogen involvement and competing reactions were hindered. Here, hydrogen underwent vigorous transformations, out of which water was the dominant visible result and participated largely to the heat effect (mind the temperature difference: 60°C or 40°C during PROX against 20°C during second sCOOX cycle).

Large demand on H_2O by SiO_2 based Au catalysts in order to see improved activity in CO oxidation has been already noticed by Date and Haruta et al. [10], but AuNPs had around 8.2 nm in diameters (i.e. 2 times larger than in 7.16%$_{wt.}$ Au/SiO_2 described here). With their research they were able to conclude that the reaction on such insulating support

takes place on the gold crystals' surface as no contribution from SiO_2 surface oxygen is expected. Therefore, H_2O must be a prerequisite in the reaction mechanism, because it is indispensable for convenient and energetically reasonable adsorption of oxygen on gold surface, following numerous studies mentioned already in this work [114, 115, 11].

Currently described Au/SiO_2 system seemed to deactivate in time and ion current of m/z = 44 Ms signal (CO_2^+ ion) decreased twice from the beginning of 45^{th} to the end of 59^{th} DP. Meanwhile, signals 28 and 32 increased accordingly. Tanaka [11, 119, 121] proposed a reaction mechanism very similar to the other discussed earlier in this work, but added a positive and negative *feedback cycle* based on results from Polymer Electrolyte Hydrogen Fuel Cell measurement setup (PEFC). *Positive feedback* was directly connected to the presence of H_2O and formation of intermediates containing hydrogen. *Negative feedback* was imposed by H^+ ions prevented those deserved intermediates to form, made unstable and to decompose. SiO_2 with its low isoelectric (IE) point can easily serve as supply of H^+. However, the explanation of the source of deactivation remains open for further studies.

3.3.5. Au/C – structure dynamics and chemistry

The $20\%_{wt.}$ Au/C catalyst was spread on the porous glass plate and mounted in the sample holder integrated with heating block in PXRD chamber. The heater temperature was set to 160°C after the chamber was purged of air with helium.

The purpose of examination of this catalyst was to check performance of only gold nanopartciles unaffected or imperceptibly affected by support properties. The need to use carbon as the volumetric phase of the catalyst was dictated by the fact that it was nearly impossible to carry out studies on pure dry gold nanoparticles. Carbon served as a medium separating gold particles from each other and preventing their agglomeration or sintering. Without carbon support, AuNPs would have certainly agglomerated which would consequently lead to hardly predictable properties of such a catalyst sample. Not to mention also a rather high cost of one specimen, as much gold precursor would be used to produce decent amount of the AuNPs in total.

Briefly, the catalyst showed little activity in CO oxidation and its selectivity to CO_2 with regard to H_2O during PROX reaction conditions was not impressive as well. A very distinct phenomenon was total loss of activity when conditions were changed from PROX to sCOOX reaction, but activity was recovered again after hydrogen was added again to the stream (i.e.: under next exposure to PROX reaction atmosphere). Relevant MS data are shown in Fig. 45 and Table 28. Williamson-Hall analysis returned the mean size of gold crystallites of 6.2 ± 2.0 n. For more comments on this large error please refer to "Structure analysis – size and strain" subsection. Crystal structure dynamics remained hard for interpretation, similarly to two previous cases of Au/CeO_2 and Au/SiO_2. Insights on this are presented in subsection "Structure analysis – lattice constant", in Fig. 48 and Table 29.

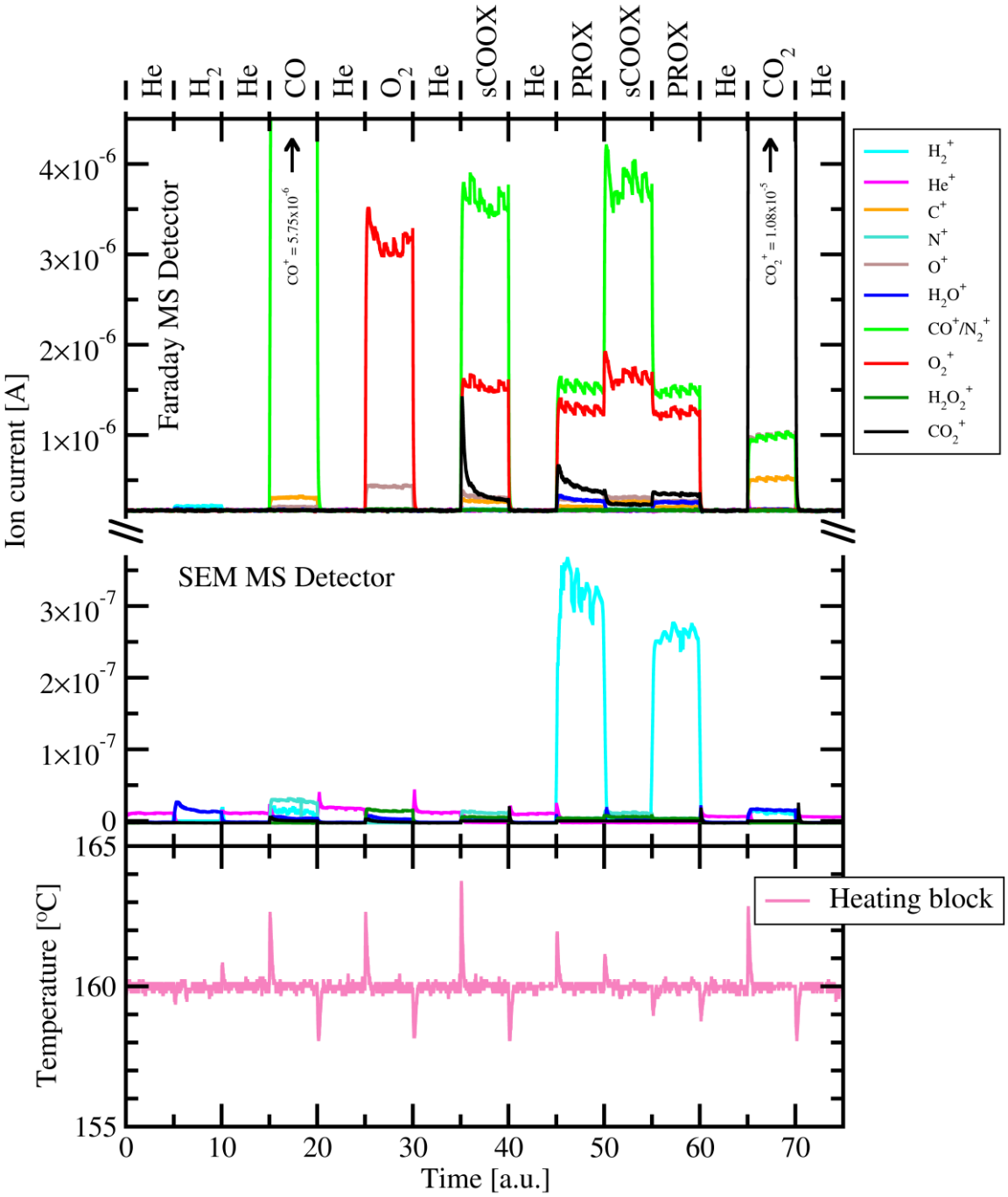

Fig. 45. Mass spectrometry (MS) analysis of composition of the gas stream leaving the PXRD chamber with 20%$_{wt.}$ Au/C and the actual temperature of the heating block. MS signals corresponding to relevant cations are shown. Data are plotted against time normalized to time required to acquire one diffraction pattern (DP; approx. 42 min). sCOOX ≡ stoichiometric CO oxidation; PROX ≡ preferential oxidation (of CO).

Chemical performance and CO oxidation reaction mechanism

The activity of the 20%$_{wt.}$ Au/C catalyst in CO oxidation was much smaller than it is for the two previously described catalysts supported on CeO_2 and SiO_2. Low production rate of CO_2 did not allow to observe the *light-off* phenomenon. Temperature assessed by quartz "*a*" lattice constant was in the range 147°C – 159°C. It was observed that temperature of the specimen bed was always a few degrees higher under helium atmosphere than for the other gases introduced before or after the given period of

Table 28. Outlet gas composition and reaction yields analysis for the sCOOX and PROX reactions carried out on 20%$_{wt.}$ Au/C catalyst in the PXRD chamber. sCOOX ≡ stoichiometric CO oxidation; PROX ≡ preferential oxidation (of CO).

Compound	Ion current [× 10^{-6} A]		$\eta_{\rightarrow CO_2}$ [%]		$\eta_{\rightarrow H_2O}$ [%]	
	sCOOX	PROX	sCOOX	PROX	sCOOX	PROX
CO	3.61	1.55	5.2	14.5	-	-
O_2	1.54	1.27	5.9	8.3	0.0	9.4
CO_2	0.28	0.37	-	-	-	-
H_2O	0.00	0.27	-	-	-	-
Selectivity to CO_2, S_{CO_2} [%]:				47.0		

exposure to helium. This inert gas has relatively good heat conduction properties what was reflected in Fig. 45 in the graph presenting temperature of the heating block – as discussed earlier introduction of helium was usually followed by a negative spike on the temperature curve while other gases noticed positive spikes.

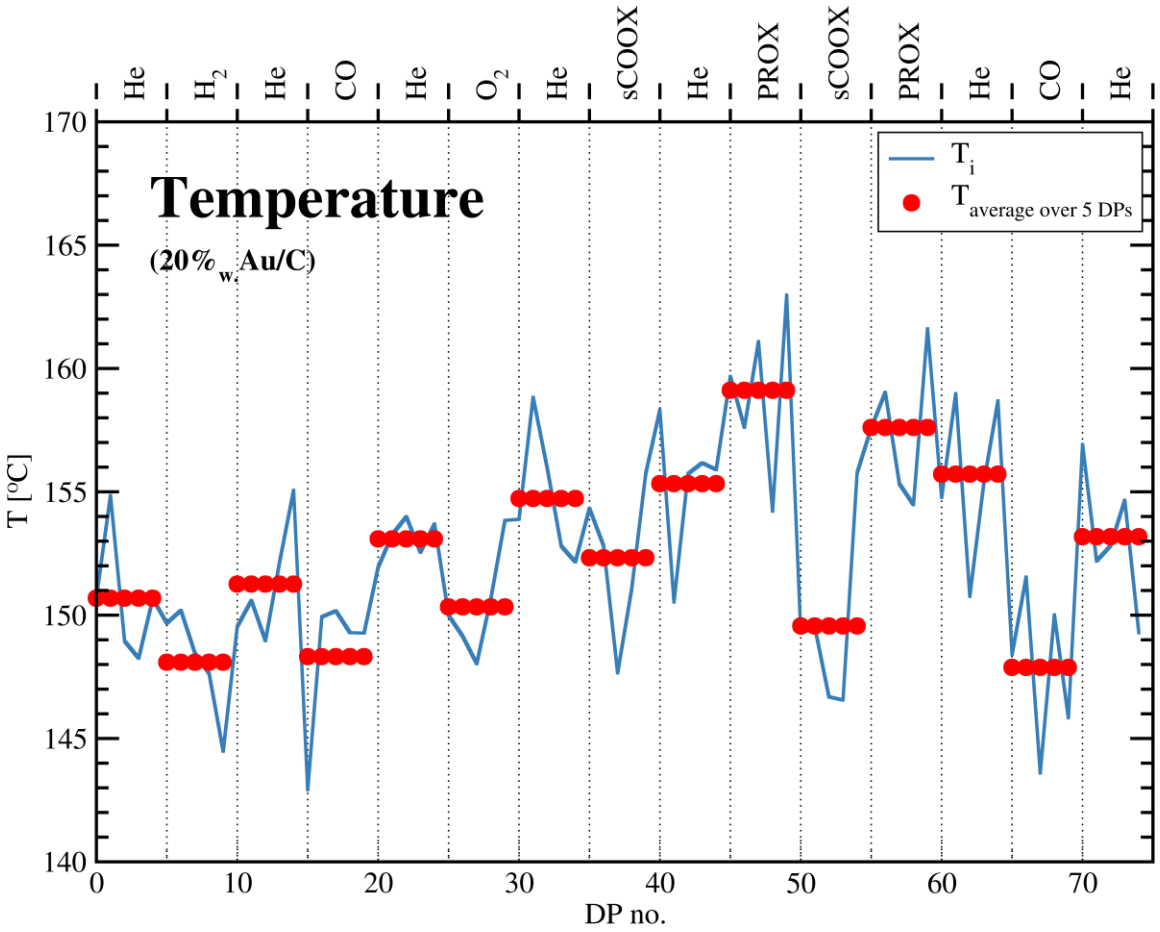

Fig. 46. Temperature profile of the specimen bed (20%$_{wt.}$ Au/C catalyst) throughout the *in-operando* PXRD experiment. Values are calculated from the thermal expansion properties of "a" crystal lattice constant of crystalline quartz, which was mixed with the sample. Data are plotted against the index of the diffraction pattern (DP) in the series of DPs. Acquisition of one DP takes ~42 min. Gas sequence is shown above the graph. sCOOX ≡ stoichiometric CO oxidation; PROX ≡ preferential oxidation (of CO).

At the beginning of 35th DP when stoichiometric CO and O_2 mixture was introduced to the PXRD chamber, m/z = 44 MS signal (characteristic for carbon dioxide) increased almost to the level of oxygen cation (m/z = 32), but immediately started to decrease and reached plateau at the end of 39th DP. This effect was not repeated during next PROX nor sCOOX reaction conditions. Prior to first exposure to reaction gas mixture required for stoichiometric oxidation of carbon monoxide the catalyst was kept under oxygen and then helium atmosphere. It could not be excluded that some oxygen residues were not removed by purging with helium. It is, however, more expected that the pristine surface of gold exhibited some feature or features (e.g. some ions might be present) which enabled rapid conversion of CO to CO_2 for a very short period of time. It was not possible to explore this initial jump in m/z = 44 signal with the set of techniques used in this research.

Gold nanoparticles' activity in CO oxidation seemed to depend on the content of water in the reaction environment. As no other origin of H_2O was expected, it has to be synthesized during PROX by the catalyst itself from elemental hydrogen and oxygen. Examination of the sequence PROX–sCOOX–PROX clearly shows higher concentration of CO_2 during both PROX reaction conditions than under sCOOX.

The carbon support is believed not to contribute to the reaction mechanism, because it cannot adsorb O_2 nor CO efficiently and it cannot act as the source (donor) of atomic oxygen species. Hence, the whole activity was attributed to the surface of gold. Reaction mechanism similar to the one presented by Sun and Takeda et al. [114] seems the most reasonable to explain the activity of this catalyst. Facing the MS data which clearly showed production of CO_2 for several hours (> 20 h in total) the surface of gold was certainly not blocked by e.g. ligands which were used as gold colloid stabilizing agents during the catalyst's synthesis.

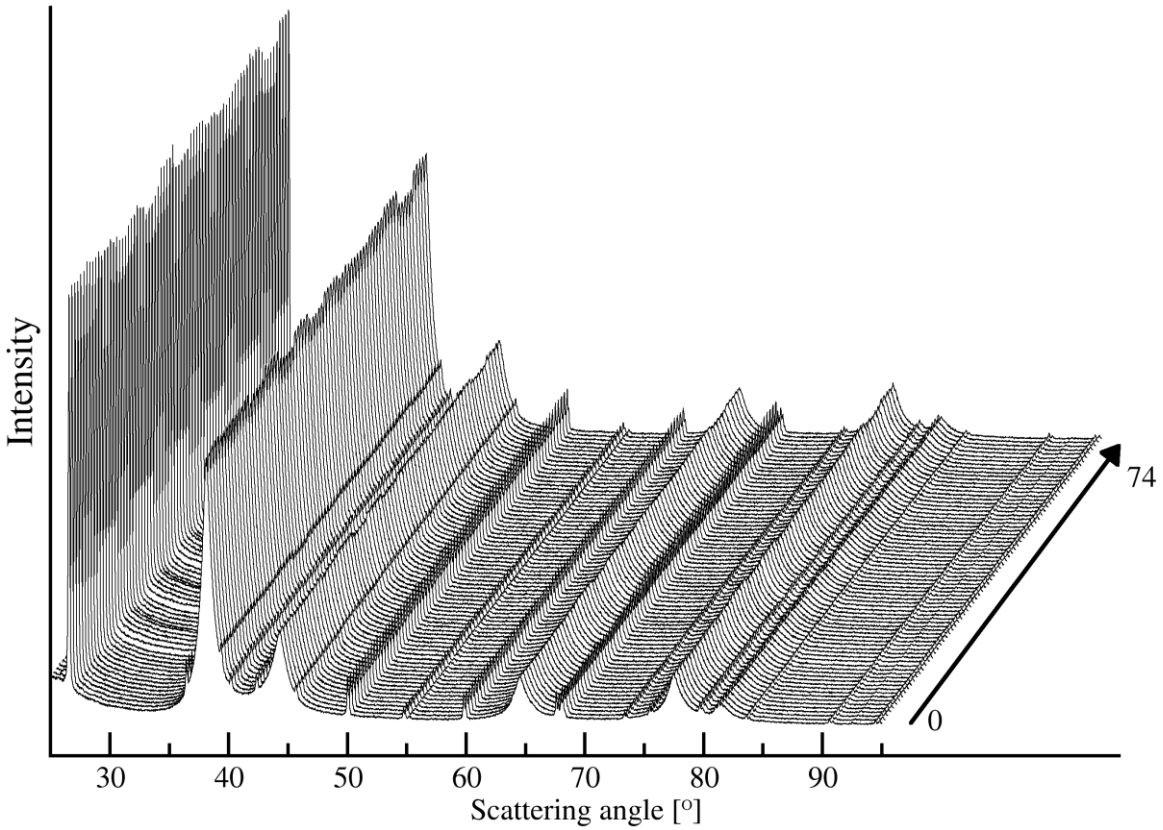

Fig. 47. The overview on the 75 collected diffraction patterns of the 20%$_{wt.}$ Au/C during the *in-operando* PXRD-MS experiment.

The main purpose of studying the 20%$_{wt.}$ Au/C catalyst was to emphasise the importance of the support in gold catalysis and to compare the efficiency of sole gold nanoparticles (supported on an inert material) with those benefiting from appropriate supporting materials. To conclude, AuNP deposited on carbon occurred to be the least active catalyst out of all three studied in this research.

Structure analysis – lattice constant

The structure analysis was based on a background–subtracted intensity profile. Background handling method was described in Section 2.5.4. Briefly, the experimental diffraction pattern of the catalyst was divided by the pattern of bare support (here: carbon Vulcan XC 72). The baseline in the resulting pattern is the angle–dependent X-Rays absorption function characteristic for the catalyst with respect to radiation absorption of the support. This function was sufficiently well described by a straight line. Hence, subtraction of the absorption function followed by multiplication again by the pure support pattern yielded a profile closely resembling the diffractogram of only gold phase.

It was, however, visible that the carbon support was influenced by texture phenomenon. Especially the 0 0 2 peak at around $2\theta \cong 25°$ differed much in the relative intensity and width what appeared as deep negative band after the initial division of the patterns (i.e.

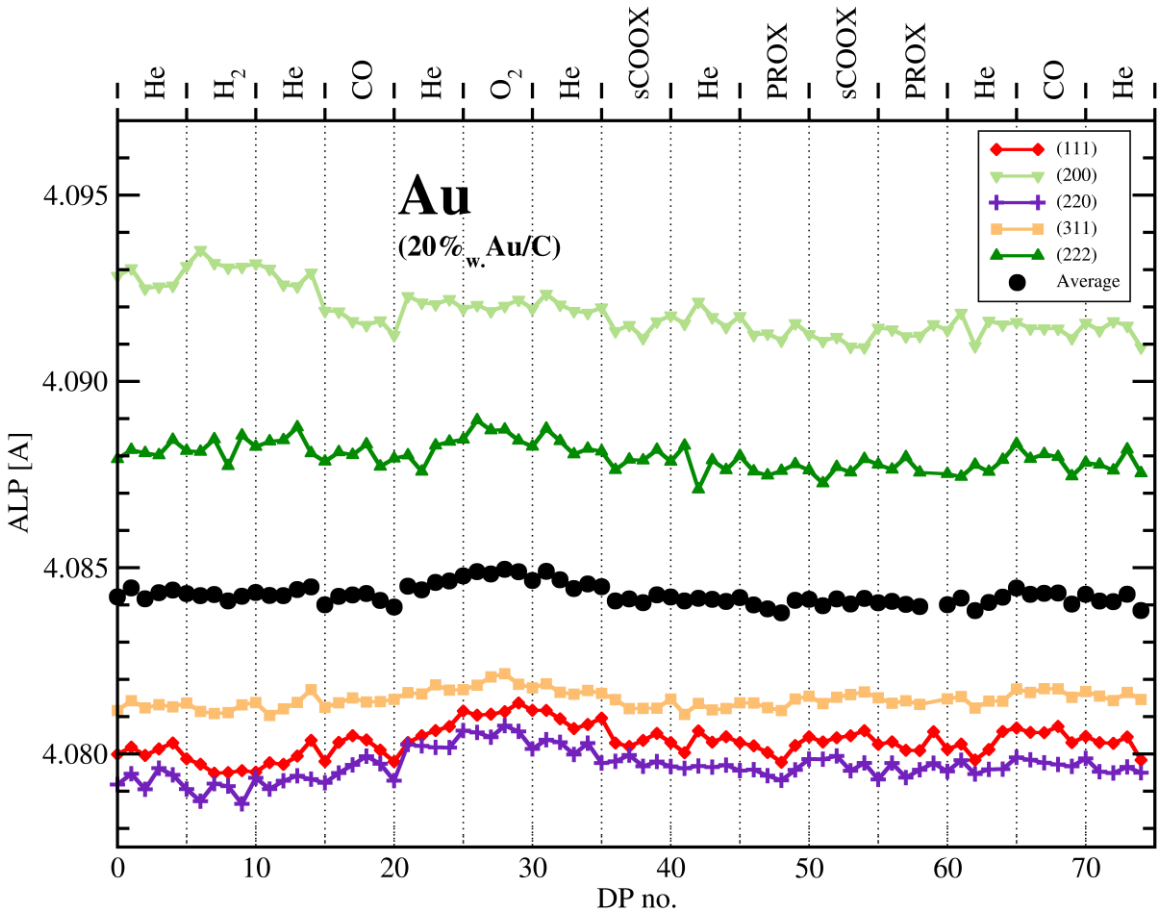

Fig. 48. Temperature-corrected apparent lattice parameter (ALP) of gold (component of 20%$_{wt.}$ Au/C catalyst) calculated from the position (scattering angle 2θ) of each diffraction peak is plotted against the index of the diffraction pattern (DP) in the series of DPs. Acquisition of one DP takes ~42 min. Gas sequence is shown above the graph. sCOOX ≡ stoichiometric CO oxidation; PROX ≡ preferential oxidation (of CO).

Table 29. Summary of crystal structure dynamics of gold (component of 20%$_{wt.}$ Au/C catalyst) as a function of gas atmosphere. For each gas atmosphere composition the average apparent lattice parameter (ALP) is calculated. sCOOX ≡ stoichiometric CO oxidation; PROX ≡ preferential oxidation (of CO).

Gas atmosphere	DP range	ALP [Å]	Std. Dev. [$\times 10^{-6}$ Å]
He	0 – 4	4.084336	127
H_2	5 – 9	4.084215	76
He	10 – 14	4.084348	117
CO	15 – 19	4.084230	81
He	20 – 24	4.084536	107
O_2	25 – 29	4.084892	51
He	30 – 34	4.084644	196
sCOOX	35 – 39	4.084148	90
He	40 – 44	4.084131	40
PROX	45 – 49	4.083949	145
sCOOX	50 – 54	4.084083	99
PROX	55 – 59	4.084020	70
He	60 – 64	4.084075	164
CO_2	65 – 69	4.084233	142
He	70 – 74	4.084080	179

first step of the background evaluation procedure, Section 2.5.4). It is then still as open question how much the scattering on carbon phase affected the results of the analysis of the gold phase. A reasonable assumption was made considering the origin of the 0 0 2 peak of carbon that the other peaks remained negligibly changed. 0 0 2 reflection comes from the distance between sheets of carbon atoms arranged in hexagonal structure in graphite. Bonds connecting these sheets are much weaker than bonds within each sheet. The former are vulnerable to break under mechanical force (thus sheets can be exfoliated producing smaller carbon stacks) and to allow intercalation of small guest molecules. The other interplanar distances in graphite structure cannot be changed so easily. Specimen preparation requires the powder catalyst to be pressed onto the porous glass plate what was always done manually and there was no control over used force. Graphite domains tend adopt preference orientation parallelly to the (002) planes (graphene sheets) under pressure applied to the sample – (002) planes orient perpendicularly to the vector of applied force. Since, the 0 0 2 peak distortions occurred independently from other carbon reflections (neglecting low intensity second order 0 0 4 peak).

Bearing in mind low activity of 20%$_{wt.}$ Au/C catalyst, it was not surprising that the structure of gold did not evolve much during the experimental cycle. The average lattice constant of gold phase across all 75 DPs was established at 4.084266 ± 0.000264 Å, i.e. it was constant within ± 0.03 pm (see Fig. 48).

The high precision of fitting of the peaks' maxima was even not affected by the large overlap of 1 1 1 – 2 0 0 and 3 1 1 – 2 2 2 pairs. It is, however, significant that in both cases insertion of two XVoigt functions was not sufficient to cover the excessive intensity between those peaks which remained underestimated by the automatic script.

The analysis of each and every diffraction peak did not reveal new information regarding the lattice constant of gold phase. The fact that Apparent Lattice Parameter was slightly different when calculated from different reflections is common for nanometerials [36] and was experienced for all three catalysts described in this work.

The variable that showed some coherent behaviour correlating with the gas exchange sequence was the FWHM of the 2 0 0 peak of gold. The breadth of this peak decreased by ~0.1° when the catalyst was exposed to CO, O_2, sCOOX, PROX and CO_2 comparing to He and also H_2 as there was no change noticed in the He–H_2–He sequence. The neighbouring 1 1 1 peak did not experience similar alternations. This repetitive oscillations of 2 0 0 peak's FWHM suggested considerable anisotropic change of the mean length of columns of atoms along [200] direction when the surface of gold crystals interacted with non-inert gas molecules. The distribution of interplanar distances should adapt accordingly to preserve the mean value and peak's maximum position (no alternations of 2θ position of the top were noticed).

This trace of structure dynamics was not confirmed for other reflections, so a question emerged whether the observed effects were not a misleading noise introduced unintentionally during data analysis. Voigt function is a convolution of Gaussian and

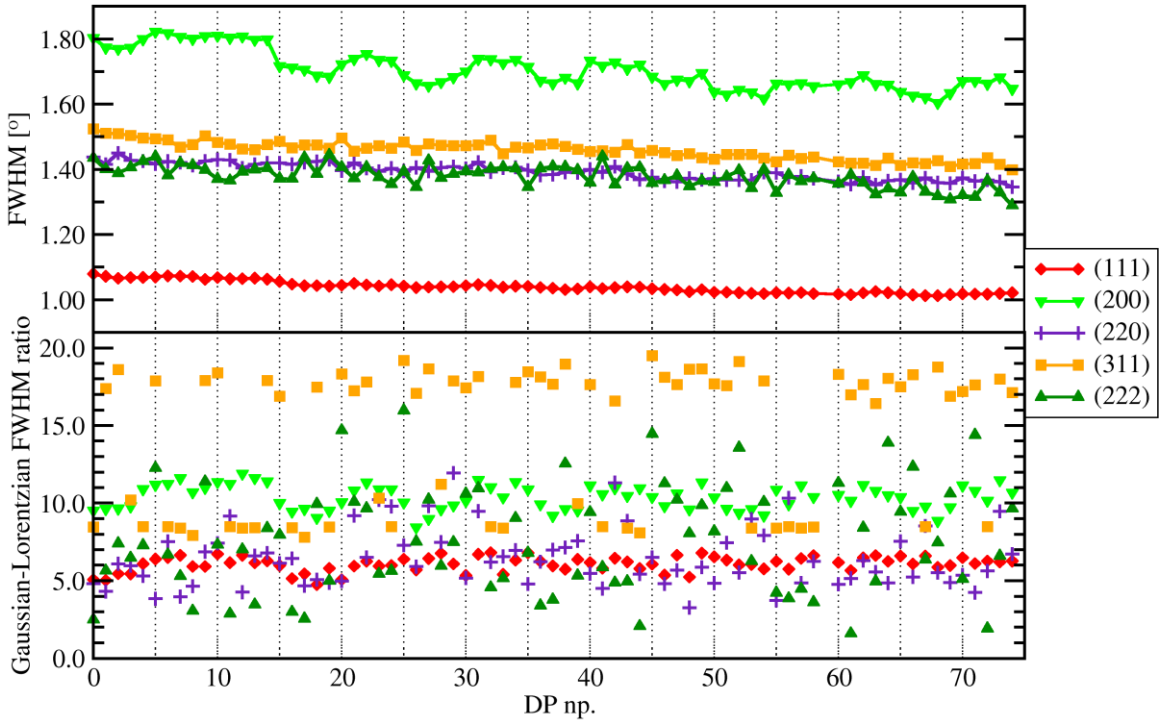

Fig. 49. The values of Full Width at Half Maximum (FWHM) of the peak height and the ratio of Gaussian to Lorentzian contribution to the XVoigt peak profile for gold nanoparticles (AuNPs) in the 20%$_{wt.}$ Au/C catalyst. These values were reported by the automatic fitting algorithm described in Section 2.5.4. Data have been plotted against the index of the diffraction pattern (DP) in the series of DPs. Acquisition of one DP takes ~42 min.

Lorentzian function. All of the Voigt function variable parameters were unconstrained during fitting of the model to experimental data. Although intensity of diffraction patterns was not corrected for absorption of X–rays in the gas atmosphere of variable composition in the PXRD chamber, in general little changes in the peaks' positions were spotted. On the other hand, the automatic analysis procedure reported the oscillating ratio of widths of Gaussian and Lorentzian functions contributing to the XVoigt function describing 2 0 0 gold reflection. These alternations correlated with the interval of gas exchange in the PXRD chamber, similarly to FWHM of the discussed peak.

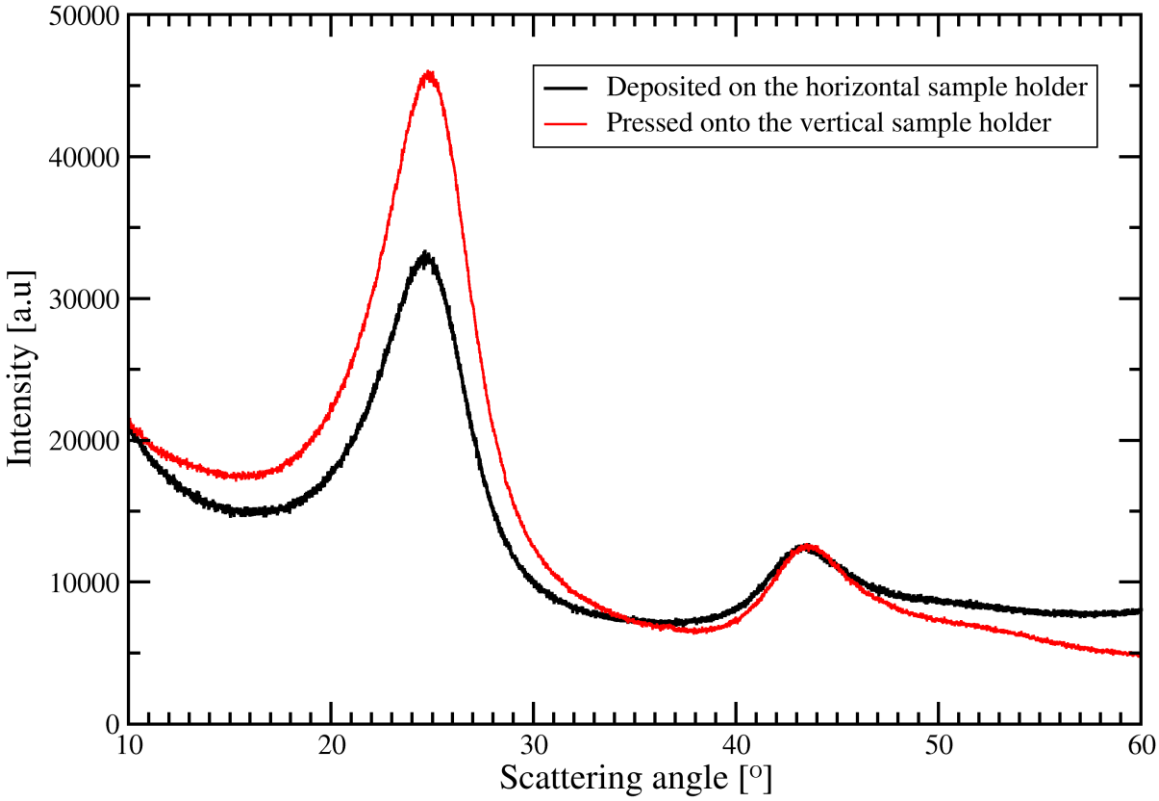

Fig. 50. The comparison of diffraction patterns of the same carbon material (Vulcan XC72) measured using two different sample holders: horizontal and vertical. The vertical orientation of the sample required to press it firmly onto the holder, so the graphite domains orient preferably and result in a change in the relative peak intensities and background level. This phenomenon is called *texture* in X-Ray diffractometry. Similar effect of the intensities ratio change can be obtained after suspending the carbon material in different solvents and subsequent low-temperature drying – the origin is in the varying capability of carbon to sorb in its volume the molecules of different solvents.

It seemed that the evolution of 2 0 0 peak breadth was either the effect of fitting method (Levenberg–Marquardt algorithm) or the change in the background profile under different gas environment. Diffraction patterns profiles of the same carbon material: one fresh and the other dried after suspending in water, differ noticeably, although they both exhibit the same scattering bands. Especially reflections 1 0 *l* (i.e.: 1 0 0, 1 0 1, 1 0 2) and 0 0 4 are interesting in this context. Similarly, influence of gas atmosphere composition might slightly influence DP profile. In the case of the analysis of 2 0 0 Au peak, some role might play the additional scattering observed in the angular range between 1 1 1–2 0 0 pair of peaks, which is discussed in the next subsection.

On balance, however the question concerning 2 0 0 peak's FWHM is still open and awaits answer and evidence, most probably some tiny differences in the extracted peak's profile (especially the shape of the peak's slope) affected the fitting factors (Gaussian and Lorentzian widths contributing to Voigt function and, thus, observed Voigt's FWHM) to such an extent that the final result corresponded to another neighbouring minimum of fitting factors (for which the integrated differential curve yielded lower value).

Structure analysis – diffraction peaks' intensity decay

Similarly to the cases of two other studied systems: Au/CeO_2 and Au/SiO_2, in the series of reflections of the gold phase the intensity decay is much faster than expected for the FCC structure (see Table 30). Additional high scattering was observed in the angular range between 1 1 1–2 0 0 and 3 1 1–2 2 2 pairs of peaks, so that more functions than usually need for 2 diffraction peaks in each case would be necessary to model these scattering bands.

The approach to estimate of the Debye–Waller factor assuming the FCC structure of gold crystals resulted in the average displacement of Au atoms for crystal lattice nodes of 0.230 Å (corresponds to 5.6% of the unit cell constant) with very low error of 0.002 Å (i.e. 0.02 pm). Despite the suggested disorder in gold nanocrystals' lattice, the correlation of $-\ln I_0$ and $\left(\frac{\sin\theta}{\lambda}\right)^2$ is very high (see small $\sqrt{< u^2 >}$ value) and assumption of FCC structure (and e.g. cuboctahedral or truncated octahedral particles shape) might be seriously considered. Close examination of the Fig. 51 revealed the imperfections of the applied model. Both 1 1 1 and 2 2 2 reflections (first and last on the plot) had too high amplitude regarding the three other diffraction peaks. Hence the intensity ratios were disturbed and deviated much from the literature sequence (see Table 30).

The decrease of consecutive peaks' intensities quicker than expected for FCC–type of atoms ordering and excessive scattering bands reminded the situation met in Au/SiO_2 and Au/CeO_2 catalysts. The size regime of gold crystals is very similar, as the mean diameter estimated by Williamson–Hall approach equalled 9.7 nm while TEM micrographs present crystals size distribution centred around approx. 3 nm with the majority of particles being smaller than 6 nm.

The attempt to model experimental data with non–periodical atomic lattice, preferably containing 5–symmetry, seemed to be the solution explaining the phenomena observed in diffraction patterns of carbon–supported gold nanoparticles. Even though peaks' intensities and shapes showed features which are odd for FCC structures, no new peaks were visible in the diffractograms. Recalling back the theoretical scattering intensity profile of icosahedra, additional reflection would be inevitably acquired in between those found in positions similar to regular bulk gold structure if icosahedral nanocrystals were the dominating fraction of particles. Consequently, the purely icosahedral model of gold nanocrystals was likely to be disqualified.

Then the decahedral shape of AuNPs is put up again as the leading candidate. Scattering from a decahedron cluster does not generate peaks in positions varying much from those for FCC structure. 1 1 1– and 2 0 0–like peaks (2θ positions around 38° and 44.4°) are cluster size–dependent. With the decreasing size of the nanocrystals they approach each other and, naturally, get broader. When nanocrystals grow in diameter, the diffraction

pattern resembles a perfect F m$\bar{3}$m space group, but the modulation of peak intensities remains odd, i.e. characteristic for decahedral particles. Thus, using decahedron–based model the experimental diffraction patterns could be modelled with the highest agreement.

Table 30. Comparison of the average experimental intensities of selected gold diffraction peaks to the literature values for polycrystalline gold [122, 123].

Miller *h k l* indices	Intensity of Au peaks [a.u]	
	reference [122]	experimental
1 1 1	100.00	100.00
2 0 0	47.92	30.97
2 2 0	28.36	16.90
3 1 1	31.29	17.69
2 2 2	8.94	6.17

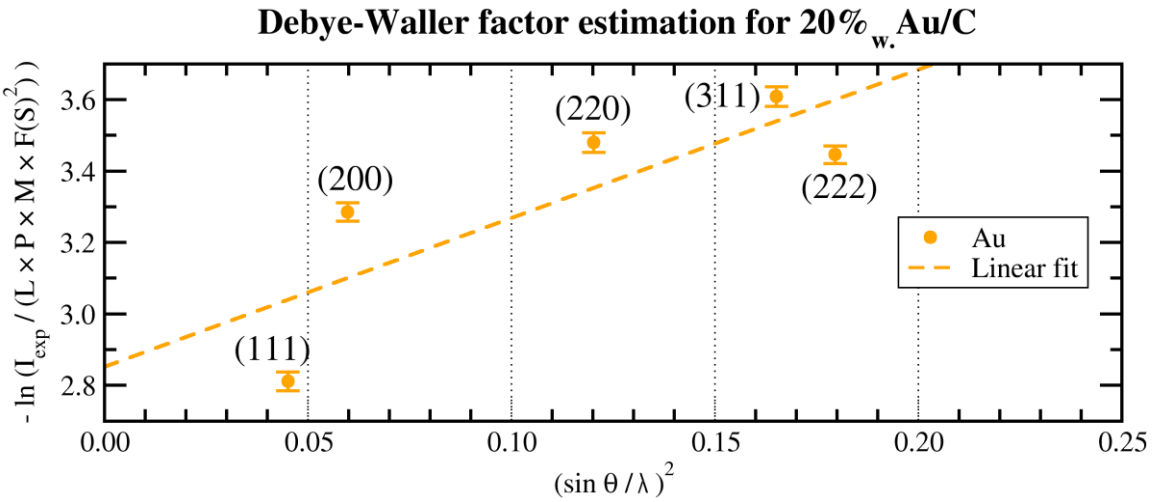

Fig. 51. The correlation of $-\ln I_0$ vs. $\left(\frac{\sin\theta}{\lambda}\right)^2$ used for estimation of the Debey–Waller factor in the case of the 20%$_{wt.}$ Au/C catalyst for the gold (Au) crystal phase.

Table 31. Root mean square displacement of atoms $\sqrt{< u^2 >}$ from their nodes for gold structure in 20%$_{wt.}$ Au/C catalyst. For comparison, the mean displacement for gold structure without considering 2 0 0 peak is included. Values calculated from Debye-Waller factor estimation.

Crystallographic phase	$\sqrt{< u^2 >}$ [Å]	$\Delta\sqrt{< u^2 >}$ [Å]
Au	0.230	0.002

Structure analysis – size and strain

The crucial parameter in the size and strain analysis considered by most of the analytical approaches – including the one proposed by Williamson and Hall [46] – is FWHM (or integral width) and its dependence on the scattering angle 2θ. A relaxed crystal lattice should preferably result in constant values of $FWHM \cdot \cos\theta$ calculated for each diffraction peak. In the "Structure analysis – lattice constant" subsection the evolution of the 2 0 0 peak width only has been already discussed. Further comments on peaks' shapes pointed to 1 1 1–2 0 0 and 3 1 1–2 2 2 reflection pairs, because excessive intensity was observed in those angle ranges, which initially might be regarded as asymmetry of the peaks' width – bigger on the right or left hand side, respectively. A suggestion was made which explained this observation with specific shape of gold nanocrystals, containing 5–fold symmetry, and incorporation of crystals size distribution.

Williamson–Hall approach is independent of the crystal lattice model, so from this point of view there were no obstacles to perform this analysis. In the classical definition both size and strain should cause a Lorentzian peak to become broader, but even if this condition is not fulfilled, the method can be still valuable by giving general trends and recommending further investigation.

Initial attempt to fit a line to all reflections of gold showed the negative slope of $FWHM \cdot \cos\theta$ vs $\sin\theta$ correlation, –0.00842 with huge error ±182%, which could not be interpreted properly according to the theory. Evidently, 2 0 0 peak greatly disturbed the trend. Bearing in mind the model fitting problems and behaviour of Gaussian–Lorentzian FWHM ratio contributing to Voigt function, this reflection was excluded from second calculation attempt. Then the factor corresponding to microstrain equalled 0.0057±0.0062. It suggested a rather unstrained structure as completely flat line was also allowed within the error bar. However, factor above 0.01 should encourage a deeper investigation of the sample.

The points on the plot, even though there are only 5 of them, are hardly scattered in a random way, but rather lay on a curved line. Generally, the Stokes–Wilson approximation involved in Williamson–Hall theory requires strain to be constant over sufficiently large distances. Naturally, in a small nanoparticle the maximum length scale is very limited. Then anisotropy of crystal size (i.e. irregular shape) and/or strain distribution is usually considered, but in collected data there was only one pair of reflections that belongs to the same family – 1 1 1 and 2 2 2. Hence, anisotropy of strain was hard to assess, nevertheless in [111] direction the strain–dependent slope factor of 0.0034 was obtained, so a relatively small value.

It is worth to mention that an energetically relaxed decahedral AuNP (with lowest energy per atom) subjected to Williamson–Hall analysis occurred to be strained. In other words: the most energetically favourable atomic structure in nano–sized decahedron is a strained one! The strain is, however, decreasing with rising nanoparticle size so that the Williamson–Hall slope falls well below 0.01 for decahedra of more than 10 000 atoms.

Simultaneously with estimation of strain, the mean size of crystals can be obtained. When 2 0 0 reflection was omitted, the average size of AuNPs was assessed at 9.7 ± 2.1 nm. The {111} diffraction peaks family suggest almost the same value – 9.6 nm. Recalculation of each peaks' FWHM to average crystals size using Scherrer equation [127] resulted in

spread values between 6.8 and 9.1 nm, with the simple average at 7.2 nm. TEM measurements showed that the majority of crystals is smaller than this and the crystals size distribution has maximum population at approx. 3 nm. Calculation of a volume weighted average of this distribution is very sensitive to undersampled sizes larger than 10 nm. Assumption of few larger crystals per about 100 counted can easily result in a perfect agreement between XRD and TEM data. Good statistics of the TEM histogram is however costly and a focus on the smallest NPs is a matter of choice in TEM imaging.

To conclude, the most important result obtained following classical Williamson–Hall approach was that no obvious strain was detected which would violate other conclusions regarding the gold phase structure. It is however undoubtful, that AuNPs could not be properly characterised based standard FCC structure assumption, but deeper investigation was inevitable and was presented in previous subsections.

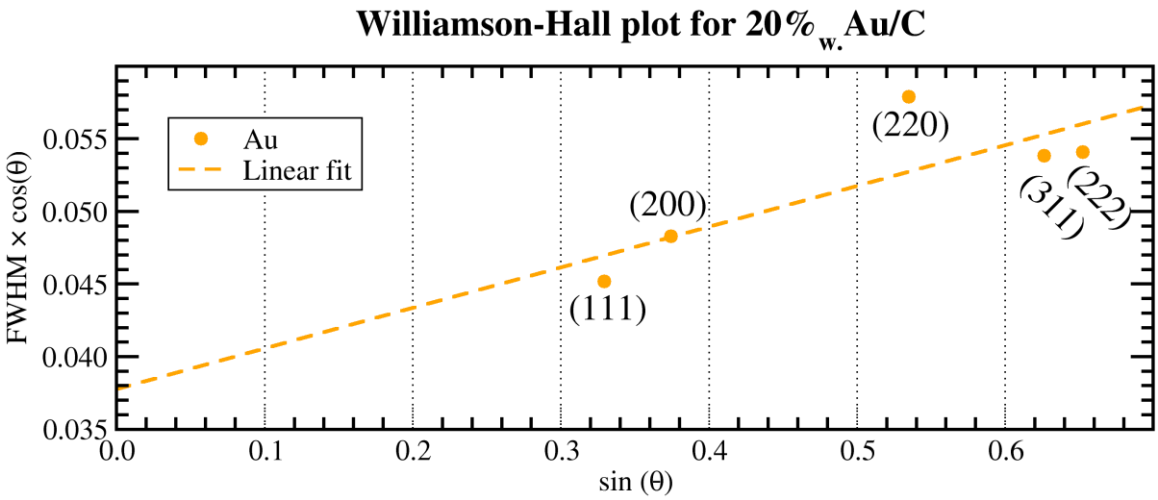

Fig. 52. The Williamson–Hall plot used for the estimation of size and strain of the gold (AuNPs) in the 20%$_{wt.}$ Au/C.

Table 32. The summary results of Williamson-Hall analysis of 20%$_{wt.}$ Au/C catalyst. Data corresponds to Fig. 52. Slope of line fitted to correlated $\mathrm{FWHM} \cdot \cos\theta$ and $\sin\theta$ is the measure of strain, while the intercept with OY is inversely proportional to mean crystallites size.

Crystallographic phase	$C \cdot \varepsilon$	$\frac{K \cdot \lambda}{D}$	D [nm]
Au 2 0 0 omitted	0.0057±0.0062	0.0159±0.0034	9.7±2.1
Au only {111}	0.0034	0.0160	9.6

3.4. *ex–situ* TEM studies

Characterisation of catalysts using Transmission Electron Microscopy (TEM) under ultra high vacuum (UHV) aimed at obtaining description regarding:

a) distribution (spread) of gold nanoparticles on the surface of the support, i.e. whether the catalyst structure is uniform or metal particles tend to group and/or to agglomerate;
b) distribution of crystals' size (average diameter) which was then compared with the mean size obtained from the analysis of X-Ray diffraction patterns (DPs);
c) shape of gold particles which was crucial for proper and accurate analysis of DPs;
d) crystals structure at atomic level (the observed projection of the atomic lattice was usually closely bound to particles' shape).

Ex–situ investigation was also an inevitable step for planning of *in–operando* experiments. Below there are presented the results of examination in transmission and/or scanning–transmission mode – they will be referred to as TEM and STEM, respectively. TEM mode was much more feasible to use for studies of these powder samples. FEI Titan Cubed 80–300 microscope was equipped with image corrector devoted to TEM mode. STEM mode enables better image contrast based on atomic number of the elements and their crosssection on scattering of electrons which was especially suitable for Au/SiO_2 catalyst. JEOL JEM–ARM 200 F had the probe corrector, so higher resolution images were obtained in STEM mode. However, more time was required to align the device and to acquire good quality images as it was challenging considering concentrated electron beam and insulating SiO_2 support.

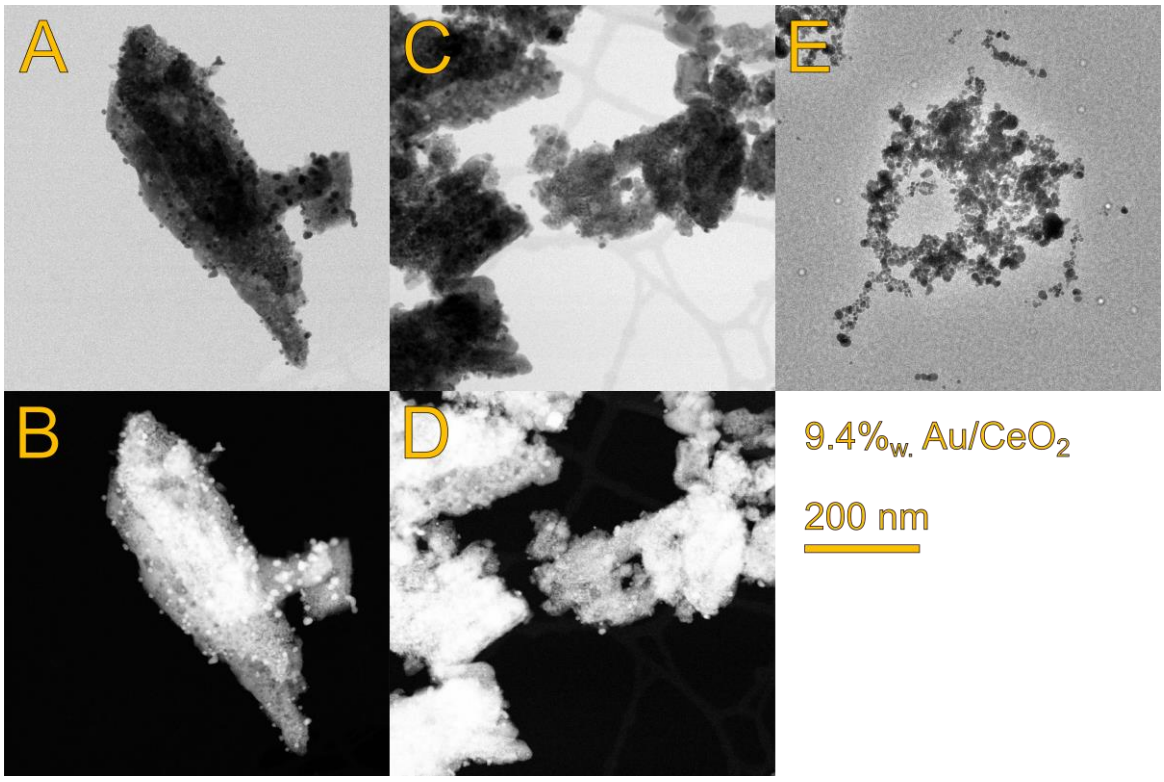

Fig. 53. Bright field (A, C) and dark field (B, D) STEM images, and TEM image (E) presenting an overview on the specimen of the $9.4\%_{wt.}$ Au/CeO_2 catalyst deposited on TEM copper grid covered with holey amorphous carbon film.

3.4.1. Au/CeO_2 – morphology characterisation

A general view on the 9.4%$_{wt.}$ Au/CeO_2 catalyst specimen is shown in Fig. 53.Gold nanocrystals were uniformly distributed on the surface of the support – cerium (IV) oxide (see Fig. 54). No gold crystals deposited inside ceria particles were spotted. The experimentally established crystals' size distribution (CSD) was very wide, however, the population frequency in the histogram was centred at 3 nm (see Fig. 56; histogram step was 0.5 nm). Naturally for the deposition–precipitation type of wet synthesis methods, bigger AuNPs, which diameter reached 20–25 nm, were also noticed (see Fig. 55). Despite a few larger particles, it is evident both in the micrographs and in X–Ray diffraction patterns (wide FWHM and even wider bottom part of each diffraction peak), that the fraction of smallest nanocrystals is dominant. Thus, the CSD histogram reflects well the gold phase characteristics.

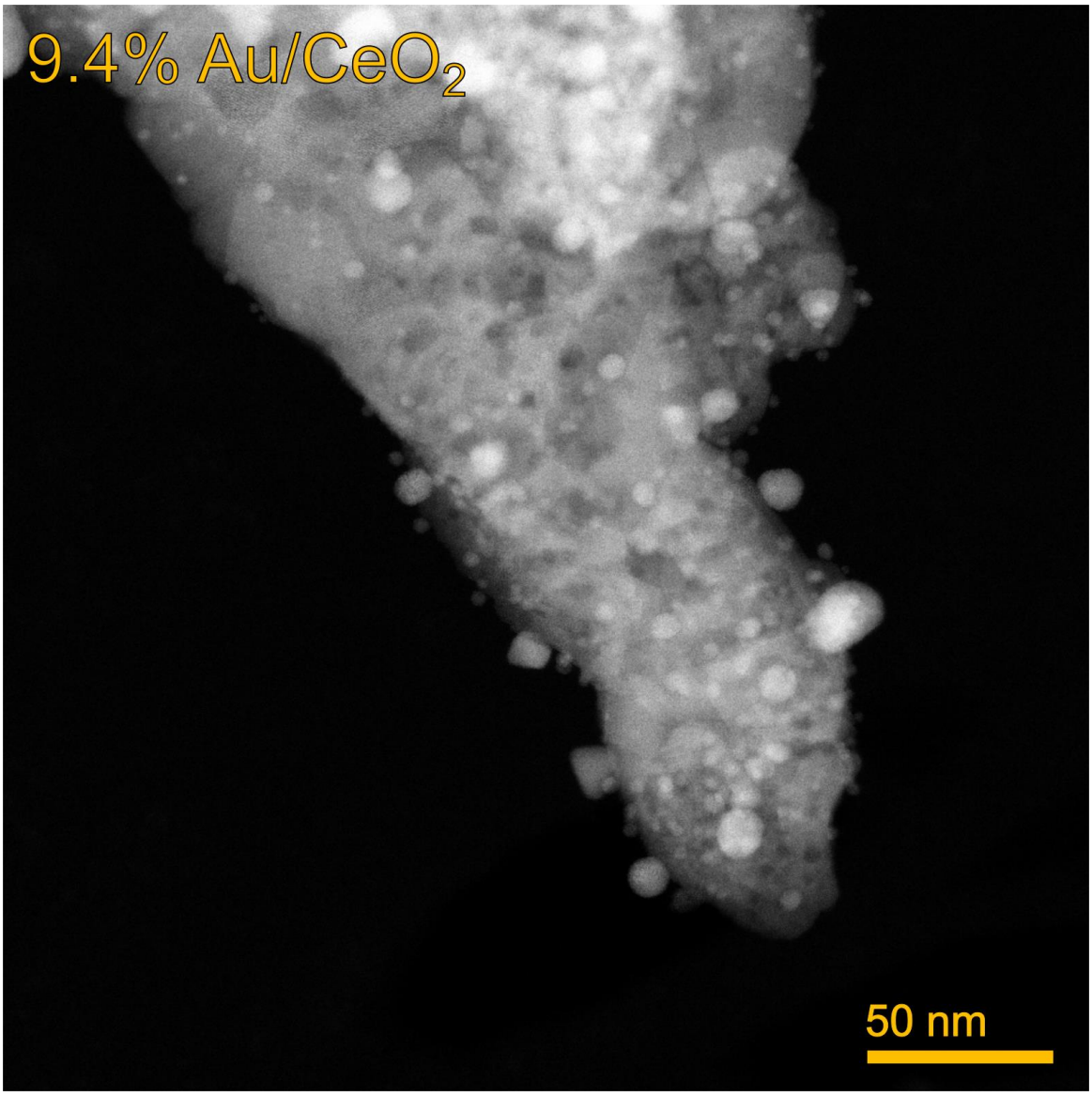

Fig. 54. A dark field STEM overview image of 9.4%$_{wt.}$ Au/CeO_2 catalyst presenting irregular shape of overlapping support particles and gold nanocrystals in the size range 2–25 nm. Gold scatters the electrons better than cerium (IV) oxide (dominant phase regarding mass fraction), so it appears in the image as brighter particles. As known from EDX and PXRD examination, AuNPs are smaller than CeO_2 particles.

Ceric oxide was in the form of crystalline nanoparticles (no amorphous phase supporting AuNPs was found) out of which the vast majority was below 50 nm in diameter (cf. Section 3.3.3 Subsection "Structure analysis – stress and strain" – mean volume–weighted CeO_2 crystal size was about 20 nm). The exact CSD histogram was not established, because of two reasons:

a) commercially available CeO_2 was used – there was no intention and plan to influence the form and state of the support, so it was used "as delivered";
b) CeO_2 particles tended to agglomerate and overlap each other on the TEM holey carbon–coated grid, which made it impossible to properly distinguish grains' boundaries.

Particles of CeO_2 seemed to be single crystals, although sometimes aggregated or twinned, and contained no pores.

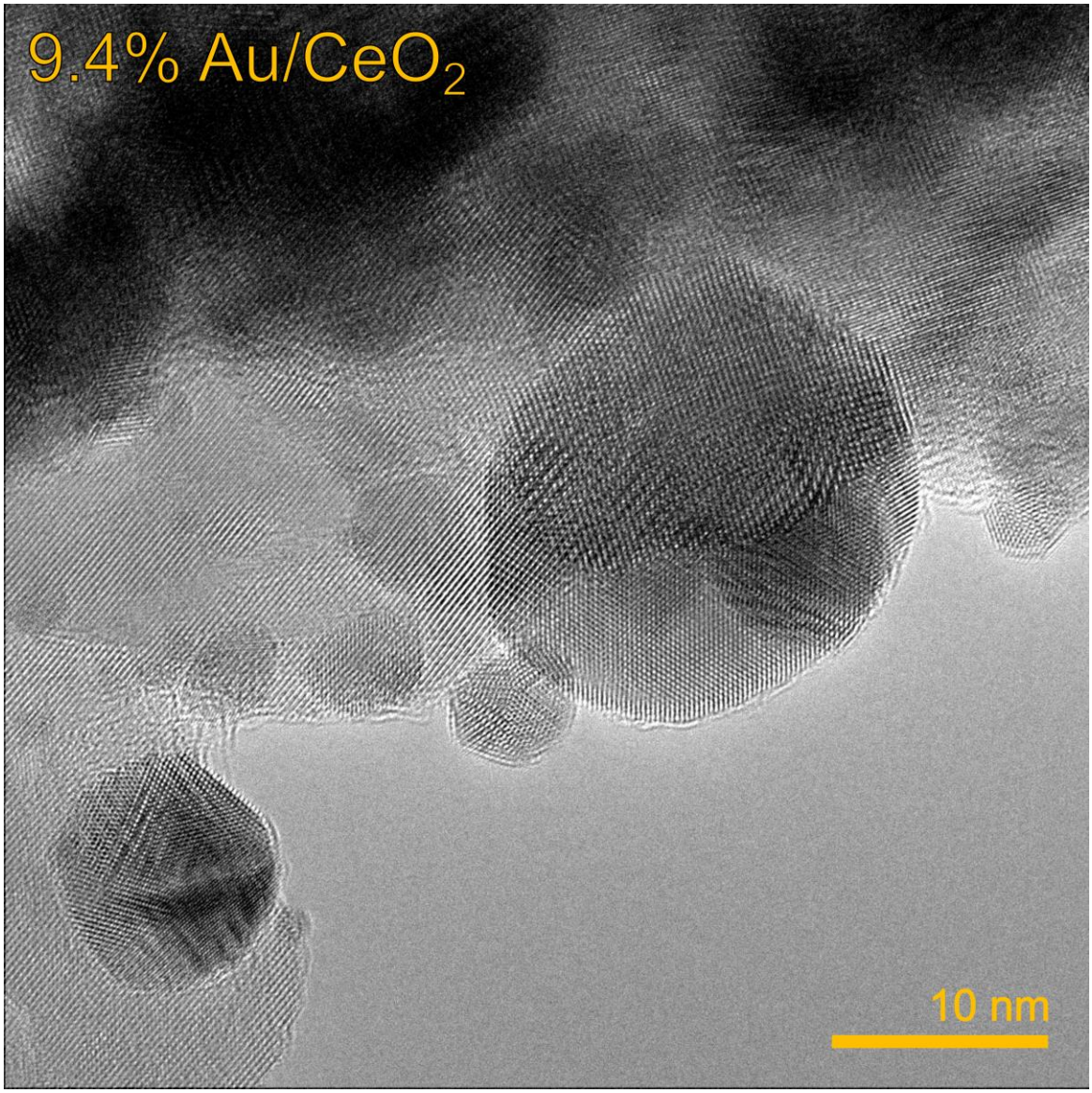

Fig. 55. A TEM image of 9.4%$_{wt.}$ Au/CeO_2 catalyst presenting gold nanoparticles of the diameter below 5 nm up to 20 nm (the biggest particle in the centre of the image). Many of them exhibited complicated atomic lattice projection, however they were reminiscent of icosahedral or decahedral AuNP oriented at the proper angle with respect to their 5–symmetry axis. The image was acquired slightly underfocus to emphasise grains' boundaries.

Detection of characteristic X–Ray radiation excited in the specimen by the microscope's electron beam (Energy–Dispersive X–Ray Spectroscopy, abbrev.: EDX or EDS) allowed to clearly distinguish between gold and ceria nanocrystals. It was easily demonstrated that virtually all small particles located at the verge of observed agglomerates contained only gold which was in line with the expectations based on the image diffraction and phase contrast in both TEM and STEM modes (see Fig. 57).

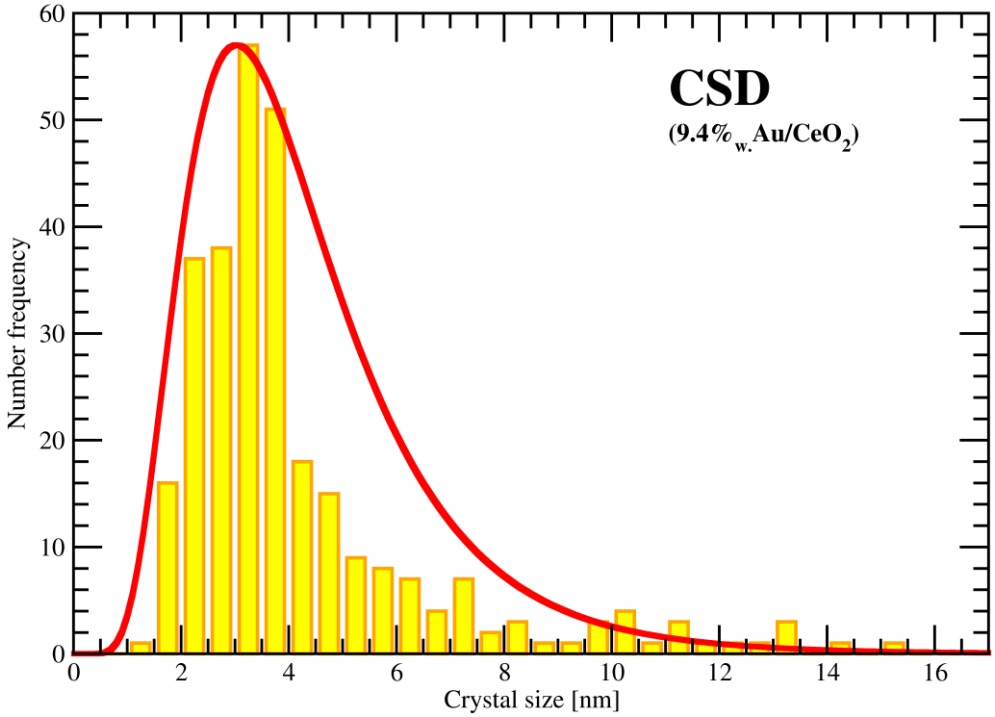

Fig. 56. Histogram showing gold crystals size distribution (CSD) in the 9.4%$_{wt.}$ Au/CeO_2 catalyst. The graph was limited to 17 nm on the OX axis for better presentation of results, because very little number of larger crystals was spotted. Yellow bars – number of observed crystals within the given size range; red line – scaled to number frequency axis log–normal analytical function fitted to the experimental results, parameters: average of natural logarithm of crystals' sizes = 1.33 and its standard deviation = 0.48.

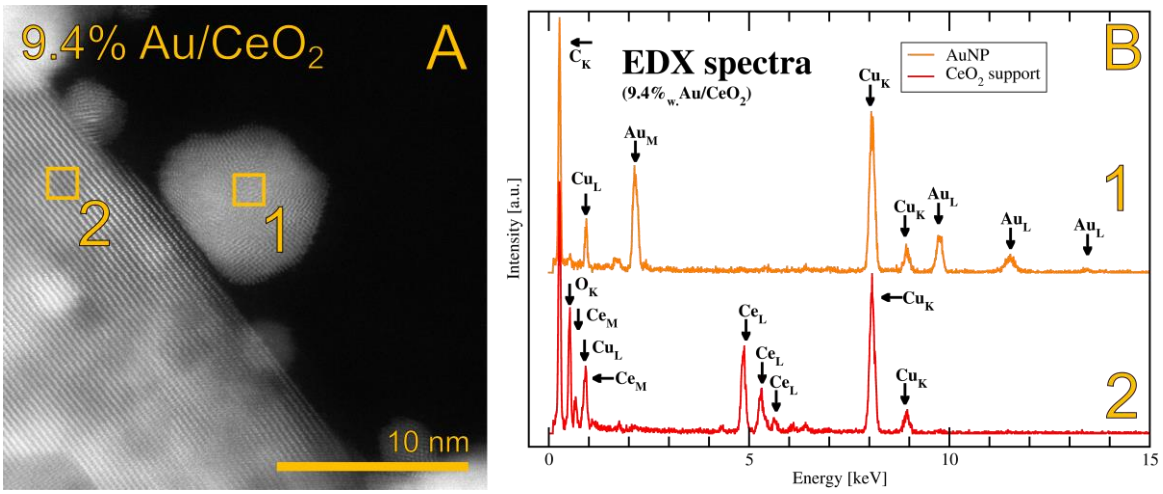

Fig. 57. A dark field STEM image (A) of gold nanoparticle (AuNP) deposited on cerium (IV) oxide (CeO_2) and EDX spectra (B) acquired from two illuminated by the beam selected areas labelled "1" and "2" showing that the particle in the middle of the image is purely made of Au (only X–Ray lines characteristic for gold are visible) and it is supported on pure CeO_2 (only lines of Ce and O). No traces of other contaminants are detected. Peaks indicating the presence copper (Cu) and carbon (C) originate from the TEM grid, which is made of holey carbon film covering copper mesh.

3.4.2. Au/CeO_2 – structure characterisation

Following PXRD studies, gold crystals exhibiting 5–fold symmetry were also observed during TEM investigation. Additionally, other crystals which showed the classical FCC structure projection were also spotted.

The later ones were mostly trapezoidally–shaped particles (possibly e.g.: hemi-cuboctahedra or "face"-oriented decahedra – the evaluation of the later was included in Section 3.4.4 devoted to Au/SiO_2 catalyst) exhibiting (100), (110) and/or (111), rarely e.g. (311), faces to the environment (see Fig. 60). Subjective observation was that there were fewer of these particles than the ones with visible evidence of the presence of 5–fold symmetry. FCC metal particles, which crystallize in highly symmetrical space groups, are more likely to preferentially orient themselves along a chosen crystallographic axis, so that the projection of atomic lattice in TEM micrograph shows an ordered network of fringes or spots, or a discrete diffraction pattern. In the case of Au/CeO_2 catalyst, large number of, presumably, gold particles presented features characteristic for Multiply Twinned Particles (MTPs) or were visible in the image only because of phase contrast.

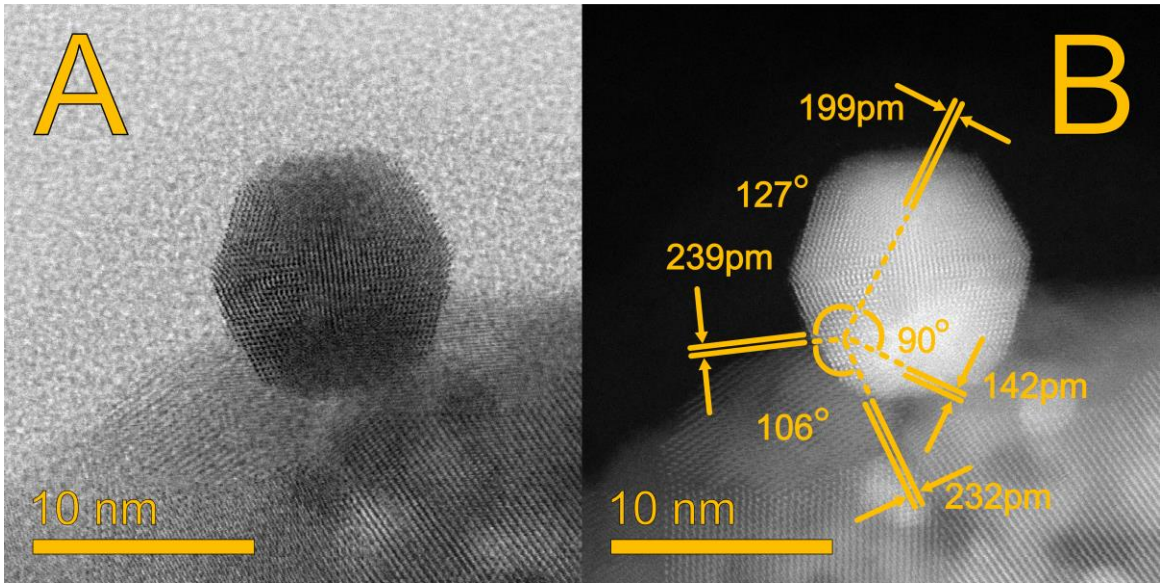

Fig. 58. Bright (A) and dark (B) field STEM images of icosahedral gold nanoparticle in the "edge" orientation found in the 9.4%$_{wt.}$ Au/CeO_2 catalyst specimen. Structure analysis (look at part B) revealed interplanar distances close to FCC structure of bulk gold – zone axis identified for this subdomain corresponds to [110]. Deviations from ideal literature values were expected, as Multiply Twinned Particles (MTPs) can be regarded as joint clusters that are energetically relaxed and, thus, severely strained.

Metal particles which contain 5–fold symmetry axes are frequently referred to in the literature as MTPs or rarely as non–crystallographic particles [128, 129, 45, 42, 44, 130, 40]. The most common shapes of MTPs are decahedron and icosahedron. The term Multiply Twinned Particle was coined on the basis of the inner structure of those crystals. They seem to consist of several subunits, like tetrahedra in the case of decahedral particles, in which ordering of atoms resembles very closely a seriously strained FCC structure [44]. However, because of the "twinning" and small over size of the particle, surface relaxation leads to additional diffraction phenomena (extra peaks, peak's splitting and/or broad scattering bands) not known for standard full–FCC–structured nanocrystals [43]. Relaxation causes also slight shift of those peaks which are located in

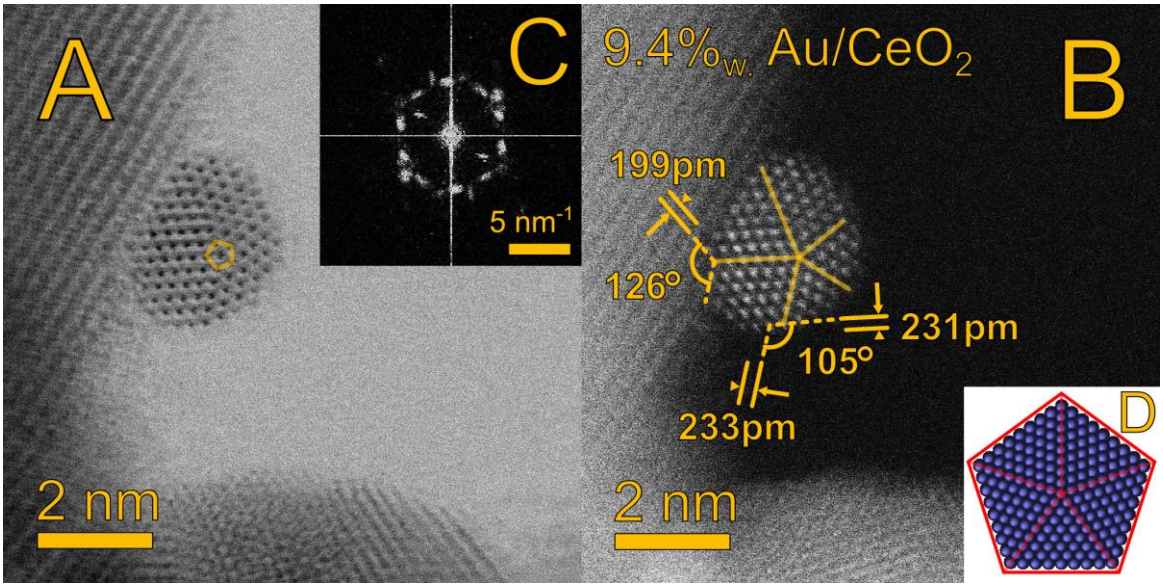

Fig. 59. A bright field (A) and dark field (B) STEM image of a decahedral gold nanoparticle (9.4%$_{wt.}$ Au/CeO_2) together with an r–FFT image (C) of the whole area and a model (D) of decahedron in the "top" orientation (i.e. along 5–fold symmetry axis). The model, however, does not account for eccentricity ($-1 < \beta < 1$, [44]) of the experimentally observed decahedron, i.e. when the 5–fold axis is not in the centre of the particle.

positions close to typical for FCC structure. The interplanar distance measurement yields values that deviates from the literature data for bulk gold by 0.1-0.2 Å. Elemental analysis (EDX or EELS) becomes the most certain and undisputable way to prove the composition of the analysed particle.

A common feature of MTPs is the limited number of preferential orientations resulting in straightforward identification of the particles' structures. Decahedral particles exhibit perfectly ordered lattice in TEM micrographs when the projection is along the 5–fold axis (see Fig. 59). Unlike decahedron, characteristic structure projections of icosahedron in TEM are when one of its triangular faces or whichever edge (ref.: "face" or "edge" orientation) are perpendicular to the electron beam [45] [40] (see Fig. 58 and Fig. 62). Projections of various possible orientations of both decahedron and icosahedron are presented and compared with experimental images in the work of Kirkland et al. [41]. In order to prove that the observed projection originates from an icosahedral gold nanoparticle, a TEM image (see Fig. 61) of a gold icosahedron tilted to lie on the edge (i.e.: "edge" orientation) was simulated using the QSTEM program [78]. The result points to 3 distinct features of this orientation, which are visible in the experimental micrograph and the image by Hofmeister [45]:

a) there are lattice fringes in the centre, $d = 2.36$ Å (distance not marked in Fig. 58B to maintain image legibility);
b) 4 domains with clearly visible ordering of atoms – atomic planes parallel to the nearest boundary of the particle, $d = 2.32$ Å, and planes perpendicular to the fringes mentioned in point "a", $d = 2.39$ Å;
c) 2 structurally unresolved areas near the particle's boundaries, in the axis of the fringes in the centre.

Regarding the substantial representation of MTPs containing 5–fold symmetry axes and breaking out of classical diffraction theory, it was hard to describe the typical epitaxial relationships between gold and cerium (IV) oxide. Some examples of structures

orientation at their interface were determined at the basis of FCC–structured AuNPs found in the specimen. Two most common orientations were:

a) Au (111) [110] || CeO_2 (100) [310];
b) Au (111) [321] || CeO_2 (210) [211].

The first one is quite well–recognised in the field of Au/CeO_2 catalysis and it is presented in Fig. 60. The second is not mentioned frequently, however, structures match each other reasonably well with low misfit parameter: 2.35 Å for Au (111) against 2.42 Å for CeO_2 (210). Generally, analysed gold particles expose largely (111) planes to the environment (other facets have smaller area), what is usually observed for similar specimens (e.g. [77, 131])

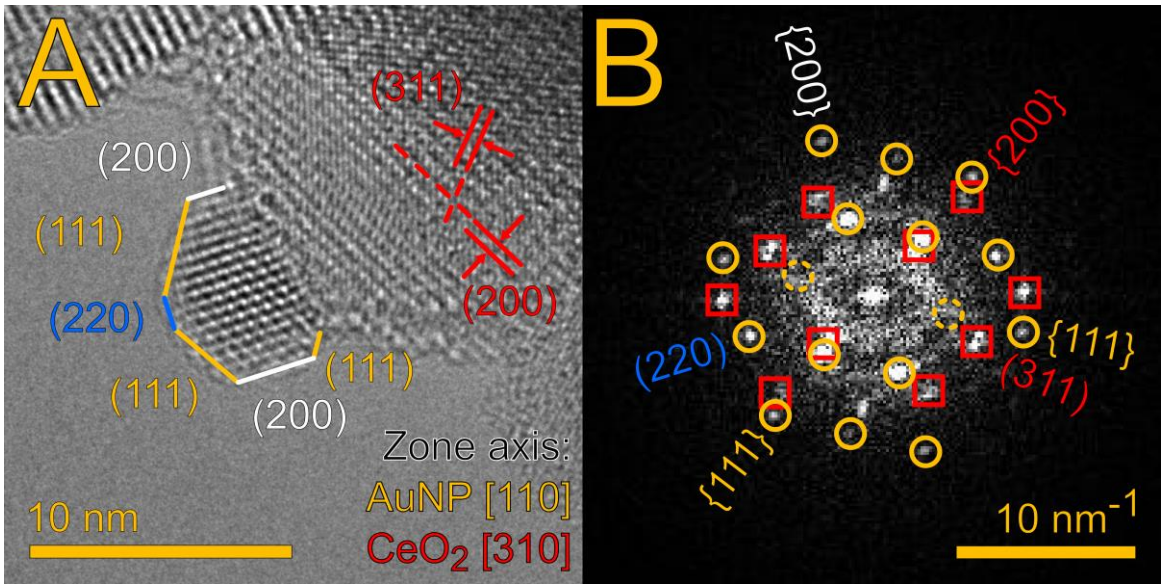

Fig. 60. A TEM image (A) and its reduced Fast Fourier Transformed (r-FFT) image (B) showing a gold nanoparticle with FCC structure deposited on cerium (IV) oxide support. They are oriented along [110] and [310] crystallographic direction, respectively. AuNP is terminated with (111), (100) and (110) faces. The resulting epitaxial relation between the metal and its support: Au (111) [110] || CeO_2 (100) [310], is typical for this system. On r-FFT, orange circles mark Au planes in reciprocal space and red squares mark CeO_2 ones.

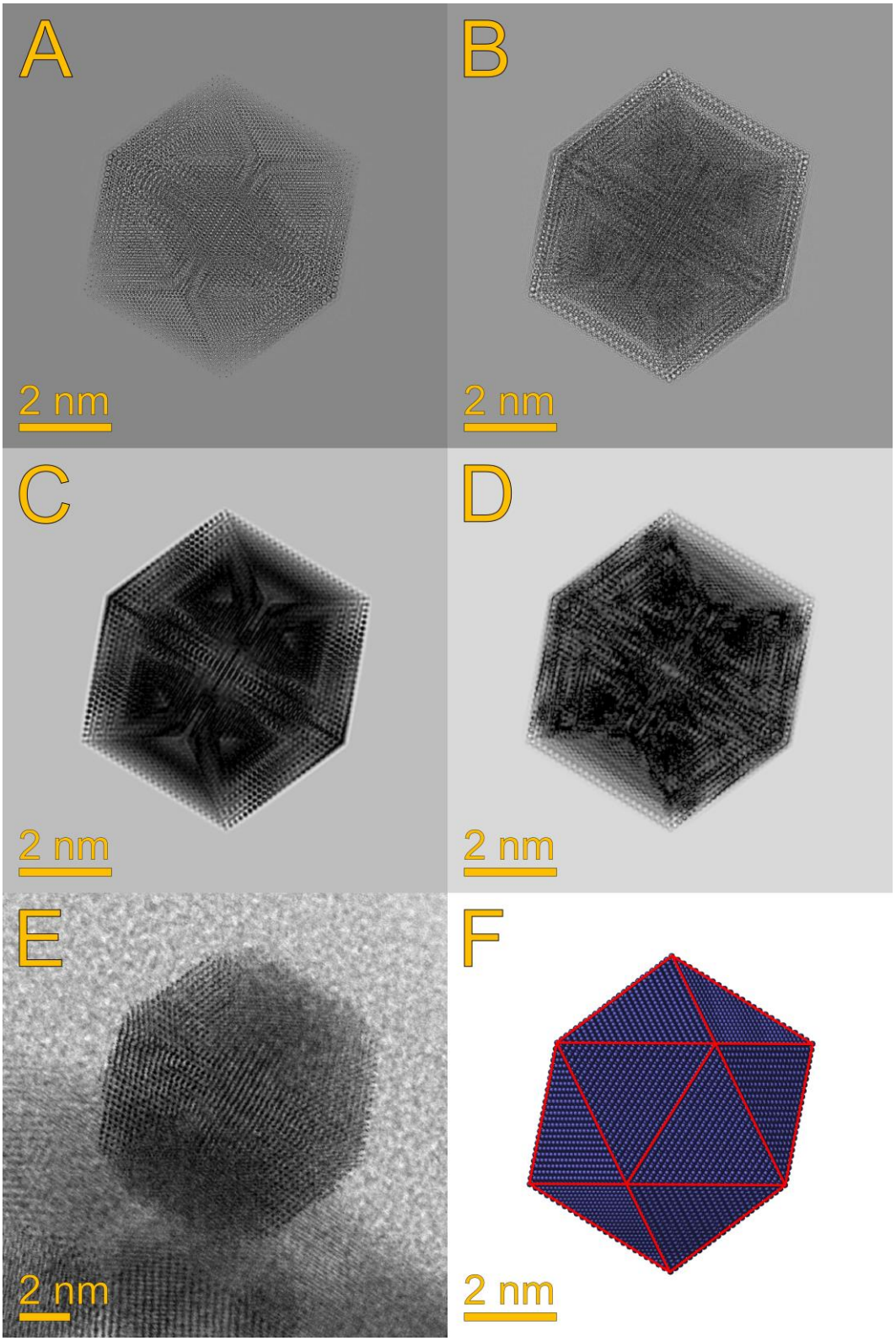

Fig. 61. Simulated TEM images (C, D) from the wave functions (A, B) calculated for the model energetically relaxed icosahedral gold nanoparticle (F) oriented in "edge" position (the particular "edge" is the red line in the centre of the particle) using the QSTEM program [78], which is based on the potential multislice algorithm. Real TEM image (E) of AuNP supported on CeO_2 is included for comparison – its structural analysis is presented in Fig. 58. Image D presents the result of simulation performed on the wave function propagated through the whole particle, while image C is based on the wave function propagated through only ¼ of the particle thickness (in Z direction, perpendicular to the image plane). For technical details regarding the simulation procedure please refer to Section 2.9.4.

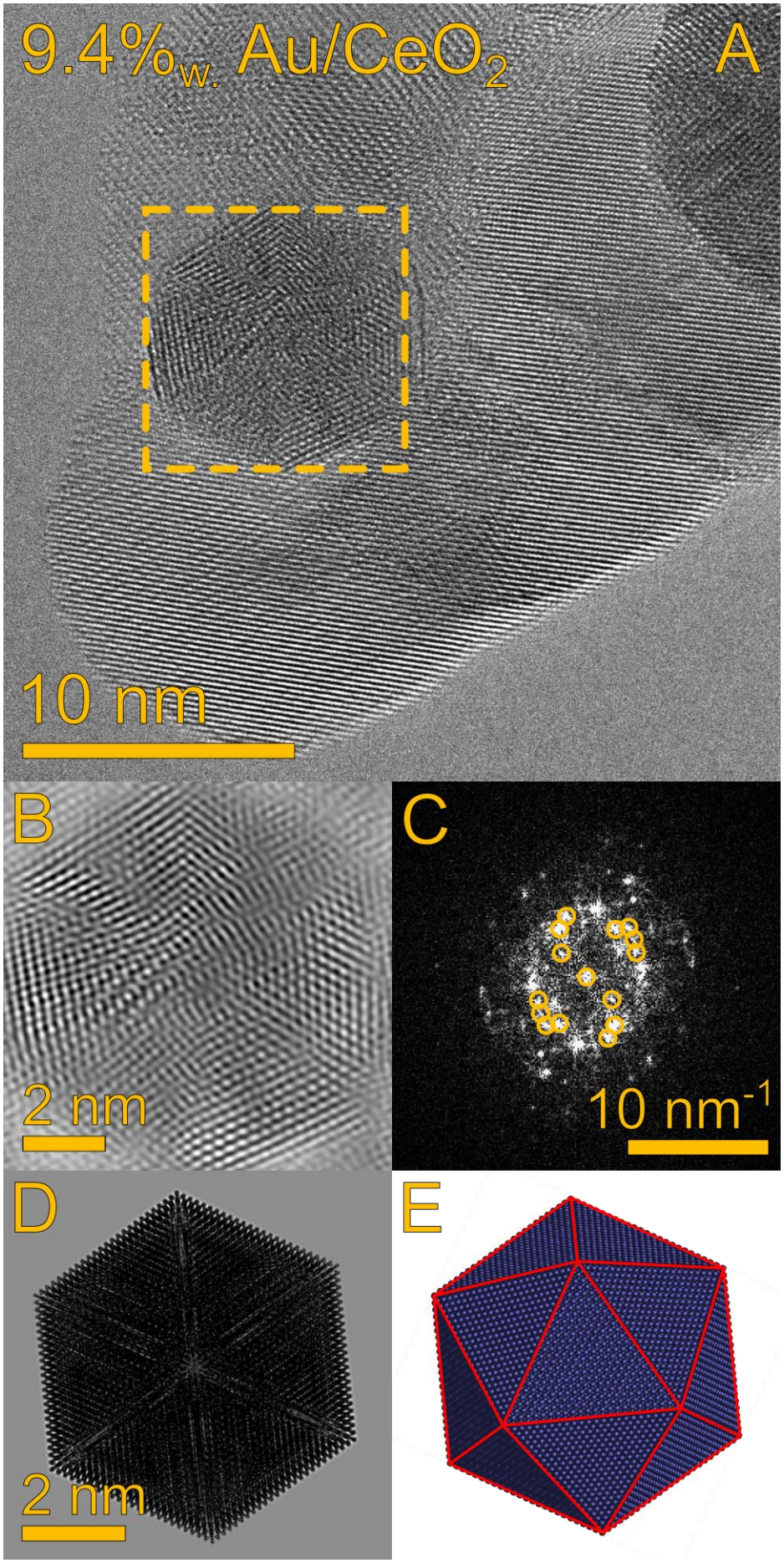

Fig. 62. A TEM image (A) of a "face"–oriented (lying on one of the triangular sides – refer to model crystal in image E) gold icosahedral nanoparticle (marked by the orange) surrounded by cerium (IV) oxide. The image B shows an FFT–filtered from noise enlarged view of the AuNP, whose structure symmetry projection is compared with image D – the result of TEM image simulation (QSTEM program [78], based on the model in image E) – and excellently agrees with the projection of an icosahedral nanoparticle oriented in such way reported by H. Hofmeister [45], Flueli et al. [40] and Kirkland et al. [41]. Image C is the FFT image of the analysed AuNP reciprocal space with marked spots identified as contributing to image formation of the AuNP.

3.4.3. Au/SiO_2 – morphology characterisation

Thanks to the synthesis method based on ion exchange between the water solution containing $Au(H_2N(CH_2)_2NH_2)_2^{3+}$ and the acidic surface of SiO_2, which granted uniform coverage of the catalyst's support with the precursor of the active phase, gold nanoparticles in a ready–to–use material were evenly distributed on the silica grains (see Fig. 63). Utilizing the big contrast in electron scattering of gold, which is a heavy element with high atomic (Z) number), silicon and oxygen, which are both very light elements, together with gold crystallinity against amorphous silica, STEM imaging mode was particularly suitable for microscopic investigations of this catalyst (compare Fig. 65 with Fig. 63).

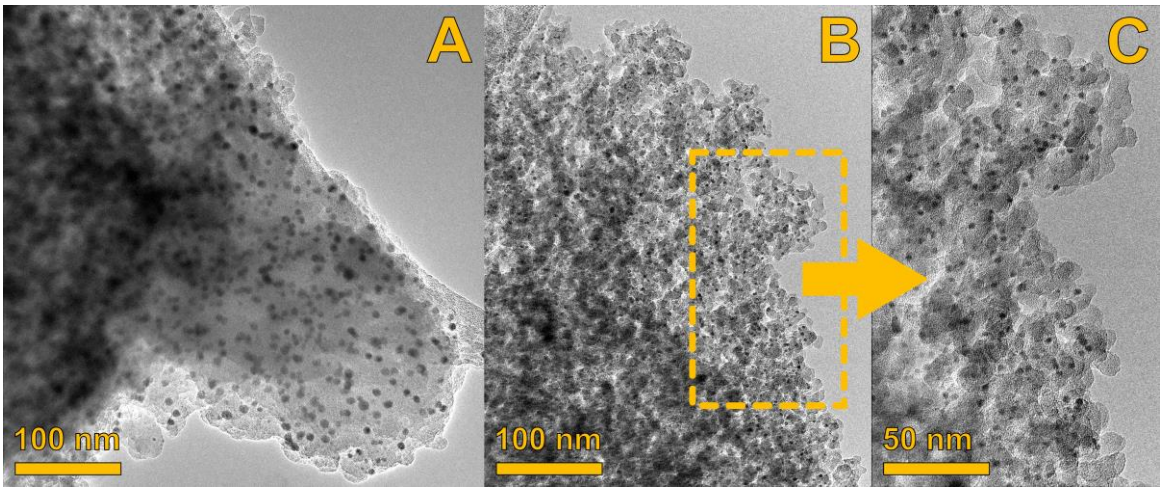

Fig. 63. TEM overview images (A–C) of 7.16%$_{wt.}$ Au/SiO_2 catalyst presenting amorphous SiO_2 support with deposited gold nanoparticles (dark spots, as crystalline gold scatters electrons much better than silica). Virtually all AuNPs visible in these images have below 10 nm in diameter and most of them do not even exceed 5 nm – refer to Fig. 64 for detailed description of Crystals' Size Distribution (CSD).

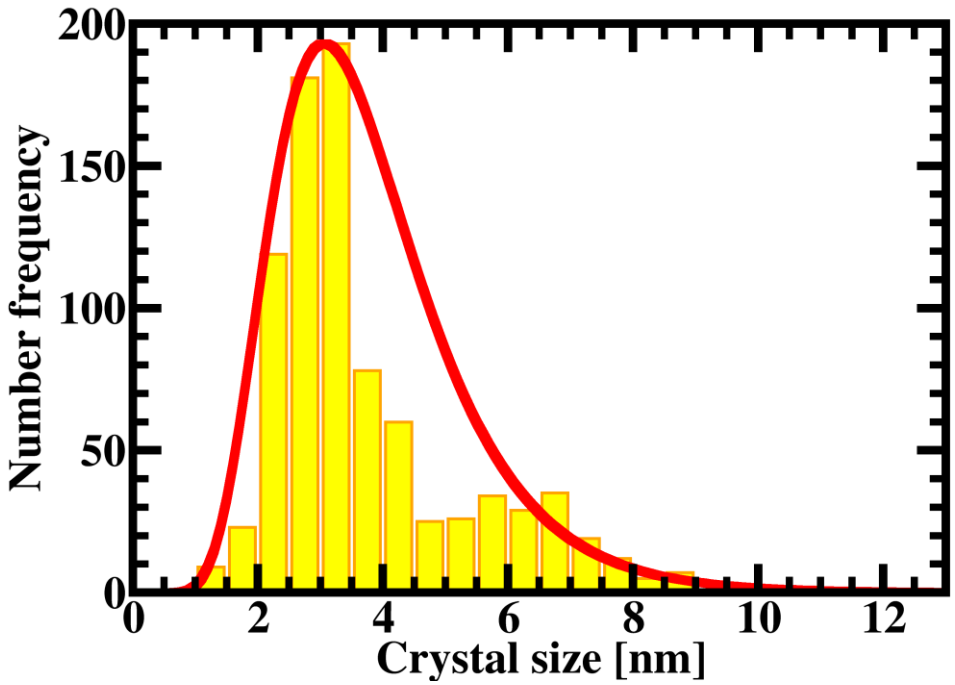

Fig. 64. Histogram showing gold crystals size distribution (CSD) in the 7.16%$_{wt.}$ Au/SiO_2 catalyst. In fact, no AuNPs larger than 12 nm were spotted. Yellow bars – number of observed crystals within the given size range; red line – scaled to number frequency axis log–normal analytical function fitted to the experimental results, parameters: average of natural logarithm of crystals' sizes = 1.25 and its standard deviation = 0.39.

Each gold nanocrystal occupied detached location on the silica and, thus, was excellently separated from other neighbours. Overlap of AuNPs occurred seldom, if ever, and it still remained uncertain whether crystals were or not in different places and this rare phenomenon was just an impression created by the flat projection of the specimen morphology. It remained beyond the capabilities of electron microscopy to determine if AuNPs were deposited in some part inside pores of silicon oxide. Judging from the edges of catalyst agglomerates, which were the thinnest part of such aggregates, gold crystals seemed to be mostly deposited on the surface, directly exposed to the environment.

The width of PXRD peaks of the gold phase pointed out to the very small volume-weighted size of crystals – 4.1±0.7 nm (refer to Section 3.3.4 – stress and strain analysis). Examination of electron micrographs showed similarly very narrow distribution of crystals' sizes with the maximum at around 3 nm and only a few observed particles which diameter exceeded 8 nm (see Fig. 64).

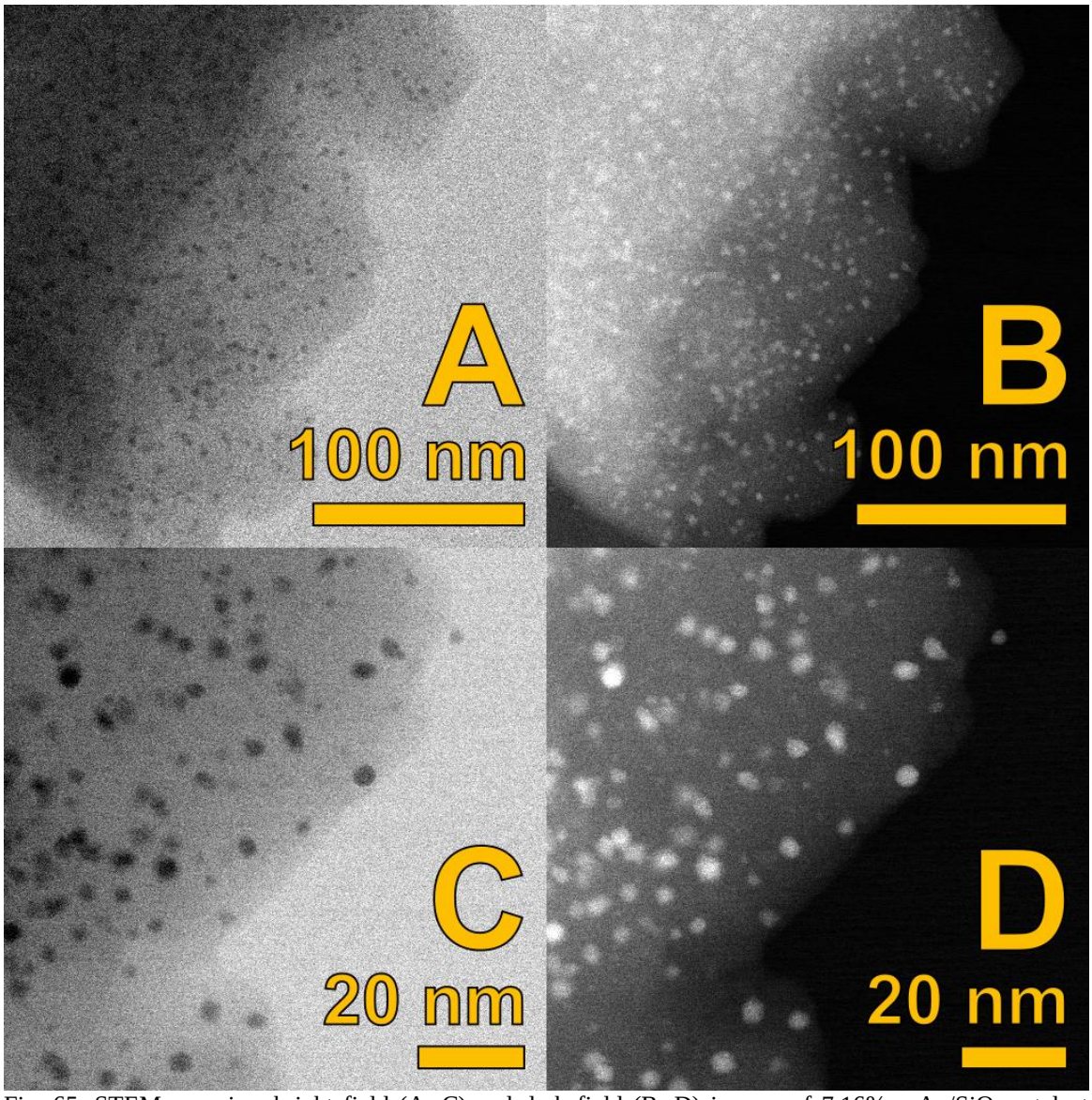

Fig. 65. STEM overview bright field (A, C) and dark field (B, D) images of 7.16%$_{wt.}$ Au/SiO_2 catalyst presenting amorphous SiO_2 support (grey shadow) with deposited gold nanoparticles (images A, C – black, B, D – white of light–grey spots, as crystalline gold scatters electrons much better than silica). Similarly to TEM images (Fig. 63), AuNPs visible in these images clearly reflect the results presented in the CSD histogram (Fig. 64).

SiO_2 support, on the contrary to CeO_2, could not be characterised, because it was an amorphous phase. Silica was supplied by Davison® and the 150 – 180 μm (80 – 100 mesh) fraction was used for the catalyst synthesis.

3.4.4. Au/SiO_2 – structure characterisation

Atomic structure investigation of the Au/SiO_2 catalyst was a very challenging part of the TEM studies done on this sample. Silica is an insulating material. It gained quickly and held the electric charge when illuminated by the electron beam. Thanks to the probe corrector of the JEOL microscope in the STEM mode, it was possible to decrease the beam electric current while preserving point–to–point resolution necessary for atomic lattice imaging. The catalyst specimen was able to dissipate quickly enough the accumulating excessive charge input by the beam with lower electron flux.

As suggested by the PXRD results, the shape of gold nanoparticles deposited on silica and their crystal lattice ordering should also exhibit 5–fold symmetry. Such particles were

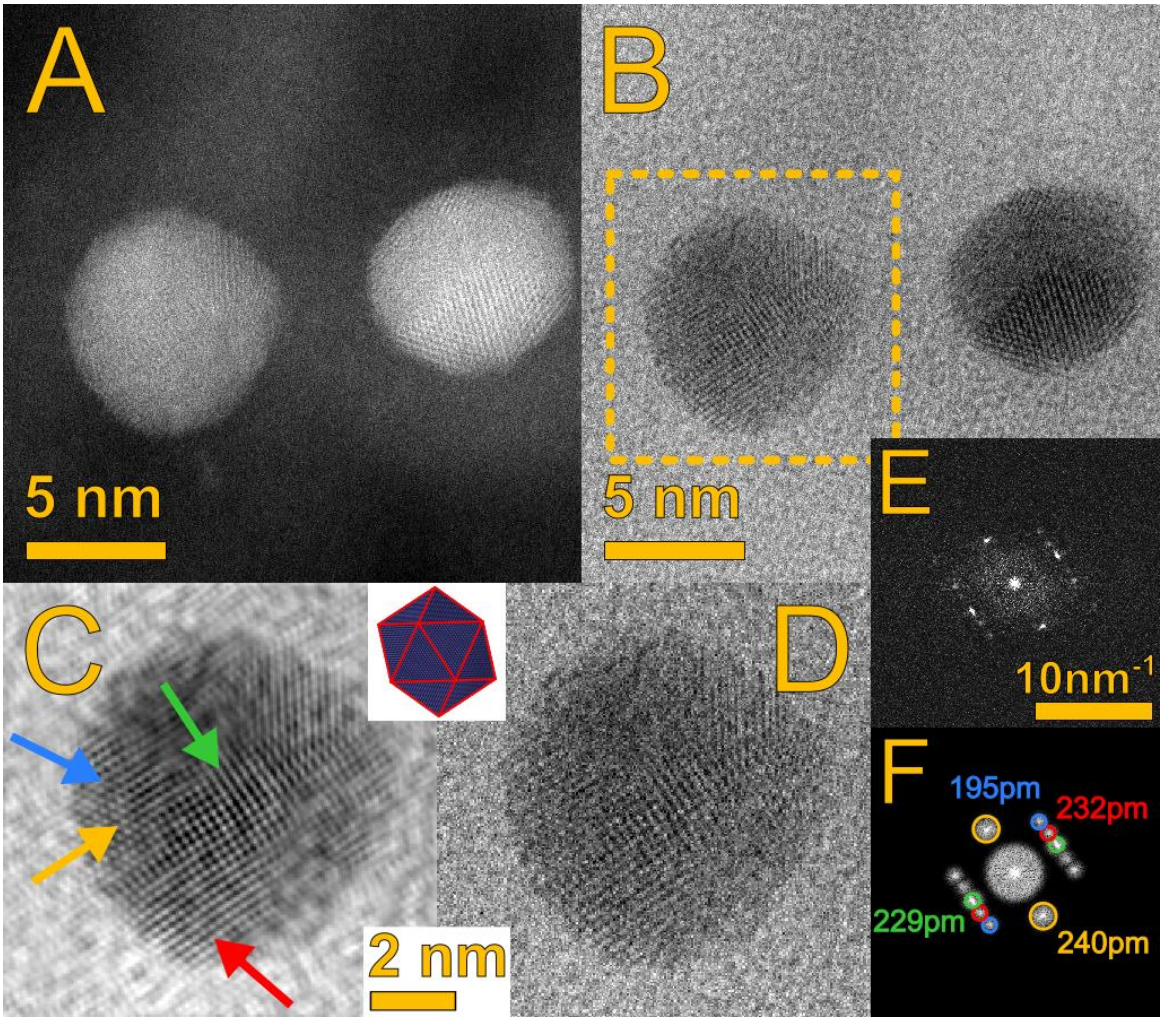

Fig. 66. Dark (A) and bright (B) field STEM images of icosahedral gold nanoparticles found in the 7.16%$_{wt.}$ Au/SiO_2 catalyst specimen. The "edge"–orientated particle marked with the orange square is enlarged in image D, while image E presents r–FFT view of this area. Image C shows the filtered–from–noise (refer to r–FFT image F) structure of this AuNP, which, despite some visible artefacts, helps to recognise planes (colourful arrows correspond to marks in image F) characteristic for icosahedron "edge" orientation (displayed in the insert between images C and D). This Multiply Twinned gold Particle is probably slightly tilted from the ideal zone axis.

observed (see Fig. 66), although many nanocrystals with hexagonal ordering of atoms, as on (111) plane of an FCC crystal, were identified as well (see Fig. 67).

Icosahedra or decahedra were expected as Multiply Twinned Particles (MTPs) containing 5–fold symmetry crystals, similarly as it was in the case of Au/CeO_2 catalyst. On the contrary to the ceria supported system, AuNPs on silica substrate were generally smaller in diameter. Most probably, it was a serious obstacle in high resolution observation of their atomic structure. Icosa– and decahedron's structure projections are considered as complicated (refer to e.g.: Fig. 61 in Section 3.4.2) with many subdomains of atoms' ordering, what makes it the more difficult to obtain a clear image the smaller the observed crystal is. In these terms, decahedra are favoured over icosahedra, because there are two projections: "face" and "top", which appearance on the micrographs do not depend on the size of the imaged particle (see Fig. #TEM-Au-SiO2-model-face-top-decahedra and Fig. 59). A particle has to be, however, oriented ideally in the zone axis for the clear structure projection to be visible, as tiniest tilts result in a blurred uninterpretable view in the electron microscope.

The "top" view of a decahedron presents 5 times twinned FCC–like structure displayed along [110] direction. As discussed thoroughly by Liang and Yu [44], for the reference FCC bulk gold structure, the angle between {111} set of planes is 70.53°, so twinning of FCC domains with the boundary being the (111) plane would result in a missing 7.35° gap. In a decahedral particle, where atomic lattice is strained with respect to the ideal one, this angle grows to 72° and such structure expansion fills the free space. Purely geometrical consideration of this phenomenon was published by Marks in 1984 [132], after he observed MTPs in 1981 [133]. Now the effect of strain occurring as a consequence of such structure and surface relaxation, which is frequently neglected or underestimated, is studied in terms of its influence on, or being the reason for, the catalytic properties of AuNPs [128].

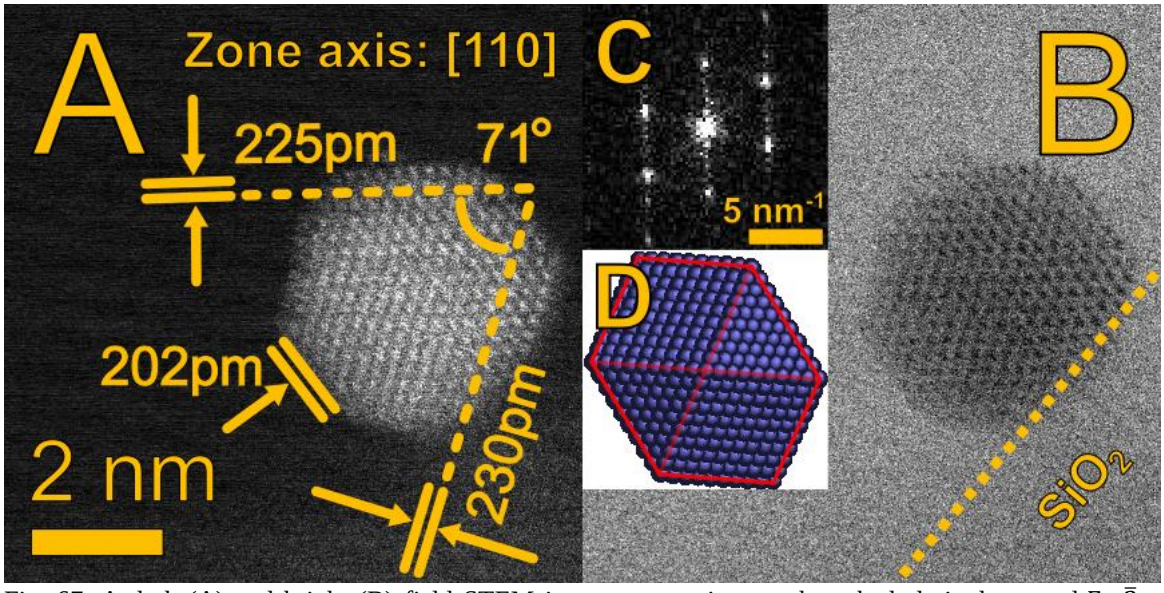

Fig. 67. A dark (A) and bright (B) field STEM images presenting a cuboctahedral single crystal $Fm\bar{3}m$ (FCC) gold nanoparticle seen along [110] crystallographic direction, which was found in the $7.16\%_{wt.}$ Au/SiO_2 catalyst specimen. Image C shows the r-FFT (reciprocal space) of the particle's lattice. Image D is a model cuboctahedron oriented accordingly (not scaled to images A and B).

The “face”–oriented decahedra (Fig. 68.A and D; they have been already mentioned in Section 3.4.2) need closer discussion. Structure projection resembles very well FCC atoms’ ordering of the (111) plane (i.e. when looking in the [111] crystallographic direction, see Fig. 68.C and F). The two most distinguishable sets of planes that can be identified in the decahedron’s “face” projection are {110}/{220} and {211}/{422}. The measured interplanar distances are close to literature values for bulk gold, 2.88/1.44 Å and 1.67/0.83 Å respectively. The 1 1 0 and 2 1 1 reflections are forbidden ones in the $Fm\bar{3}m$ space group, because their structure factors equal zero. It is worth also to mention that the 0.83 Å value is very close to the resolution of most of modern electron microscopes. Thus, it may be challenging to observe atomic lattice with sufficient resolution. The projection of FCC structure along [111] direction should not be confused with the one along [110] direction. They look very similar at first sight, but in the latter one there are easy–to–spot very characteristic interplanar distances: 2.04 Å of {200} and 2.35 Å of {111} planes family, which is not present in the crystal terminated by the (111) plane. This serves as the critical condition during (S)TEM image analysis to discriminate between [111]– and [110]–oriented crystal.

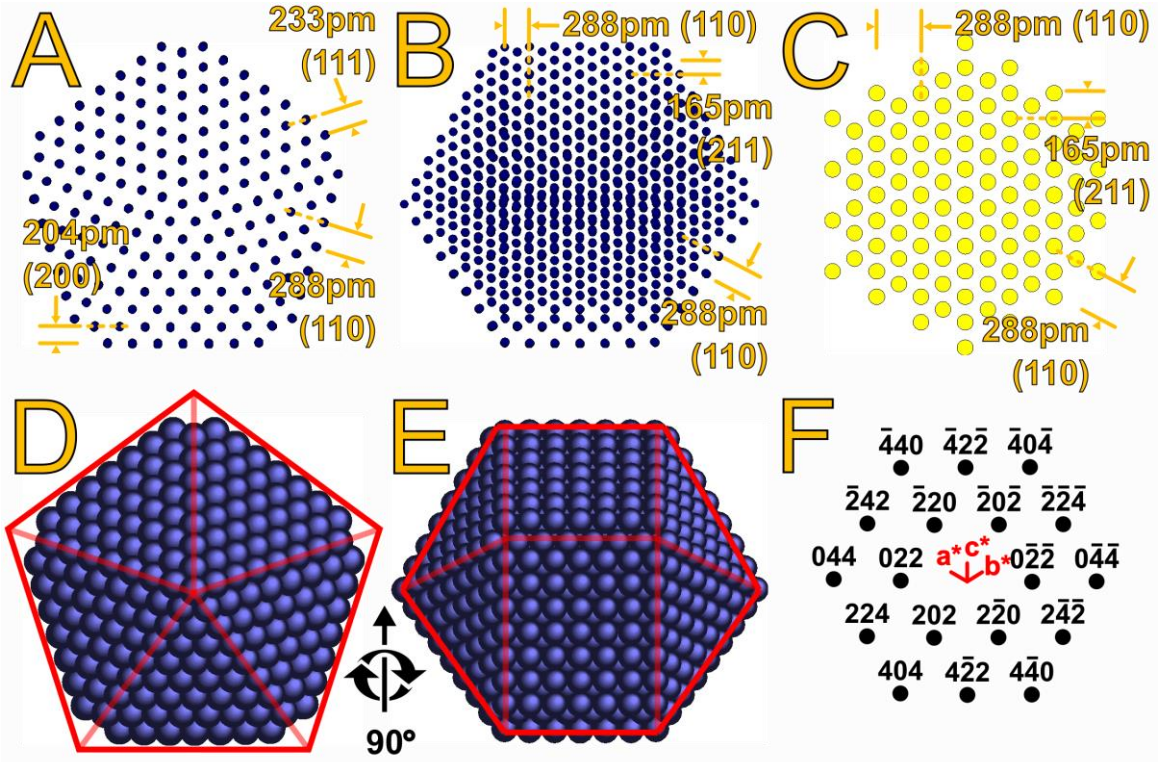

Fig. 68. #TEM-Au-SiO2-model-face-top-decahedra-FCC[111]. Comparison of gold decahedron and bulk FCC gold structure projections. “Top”–oriented decahedron (images A, D) shows 5 twinned strained FCC-like seen along [110] domains – the angle between {111} set of planes is 72.00° while for reference FCC structure it is 70.53°. “Face”–oriented view is obtained by rotating the “top” one by 90° while a chosen truncated face needs to stay perpendicular to the image plane (images B, E). It is possible then to notice projection which thanks to twinned nature of decahedron resembles excellently FCC structure view along [111] direction (for direct comparison presented in image C; reciprocal space view in image F).

The concept of observation of overlapped structures of twinned crystals which results in projection of closer packed lattice than the original structure of each of the twins was utilised in the work of Kuwauchi and Takeda et al. [134]. In the Supporting Information to their article they presented a particle consisting of two perfect FCC gold domains twinned on the (111) plane. After rotation by 60° along the [111] direction, planes (311)

and (220) became visually dominant in the structure projection, although it was the effect of overlaid lattices. The major differences between their case and the structure of a decahedron are the strained lattice of decahedron (angles are not preserved with respect to reference bulk material) and twinning of 5 subcrystals. Hence, the TEM image of such oriented decahedron mimics another zone axis of FCC unit cell and the contrast usually worsens with the increasing distance from the particle's edge.

3.4.5. Au/C – morphology characterisation

Fig. 69 presents the overview of the 20%$_{wt.}$ Au/C catalyst morphology. The amorphous carbon (Vulcan XC72) support, which show weak graphite features, is hardly visible in the micrographs, because the contrast profile in the images must account for strongly scattering gold nanoparticles. At the interface of the support and vacuum or the very thin (20 nm) layer of carbon covering the copper TEM grid one can see the subtle boundaries or differences in the texture, as Vulcan carbon looks more grainy and less uniform, plain.

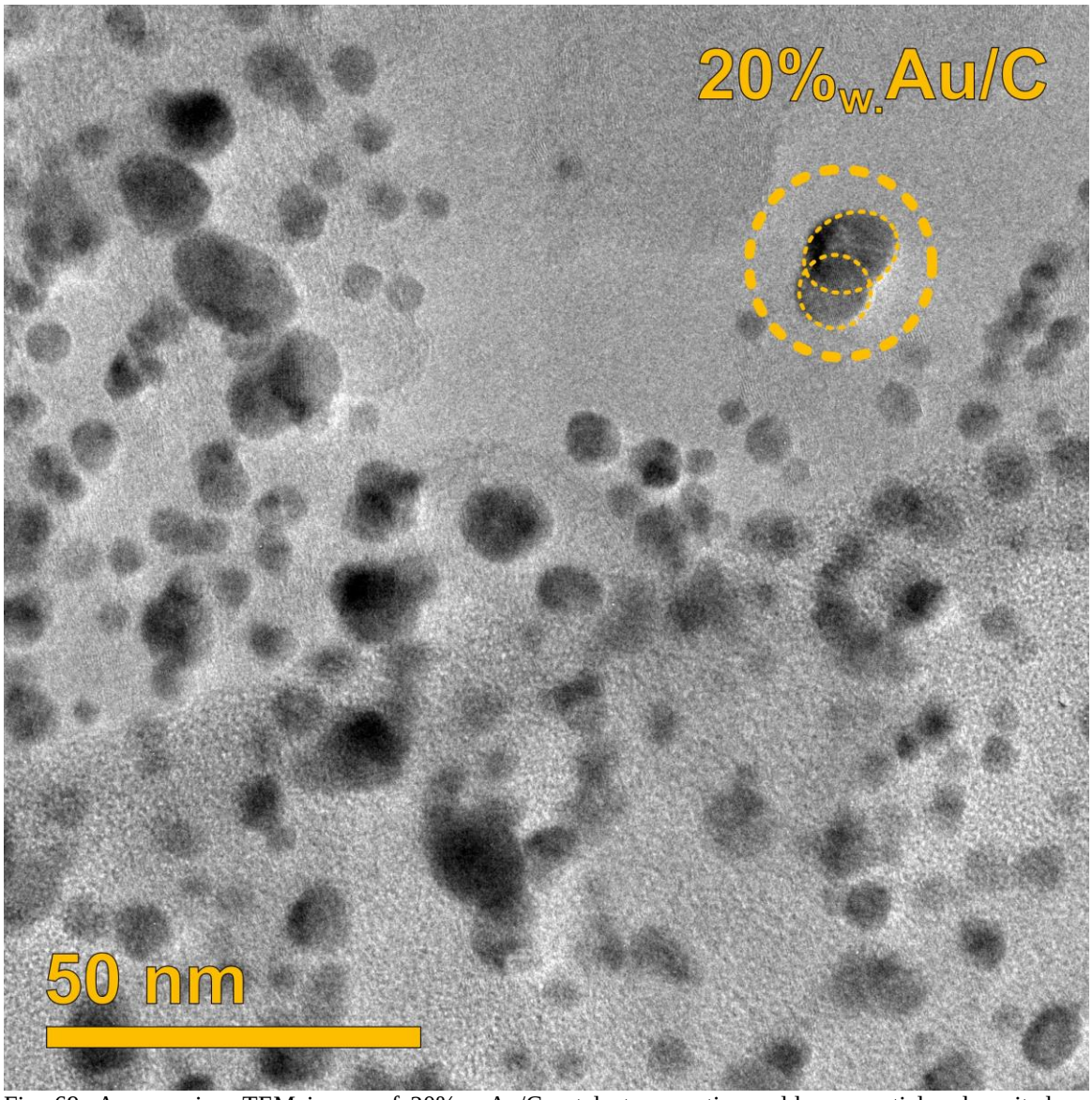

Fig. 69. An overview TEM image of 20%$_{wt.}$ Au/C catalyst presenting gold nanoparticles deposited on amorphous carbon (Vulcan XC72). Most of AuNPs visible in the image are smaller than 10 nm, but larger ones can be occasionally noticed. Mind that some of the particles overlap with the others (e.g. in the marked area), thus increasing erroneously the observed particle's diameter (such doubtful cases were not accounted for in the CSD analysis, Fig. 71).

Gold nanoparticles were homogeneously dispersed on the carbon matrix. The high loading of gold phase (20%$_{wt.}$), despite the low density of carbon compared with gold, and small average size of crystals resulted in frequent overlap of AuNP. Most probably it did not affect the chemical properties of this catalyst, because the structures of neighbouring crystals were randomly oriented. Atomic resolution studies (next Section 3.4.6) suffered, however, from such morphology of the catalyst.

The characteristic X–Ray radiation excited in the specimen by the electron beam was collected from the area shown in the Fig. 69. The spectrum presented in Fig. 70 testifies that the catalyst is free from contaminants and contains gold as the only metal. The same result was obtained from the XPS analysis (Section 2.8).

The experimentally measured crystal size distribution (CSD) has its peak at 3 – 3.5 nm. This corresponds very well with the broad diffraction reflections observed during the *in-operando* PXRD-MS studies. In the micrographs larger crystals were also observed, although their population is small and the fraction of smallest particles with diameter less than 5 nm is dominant.

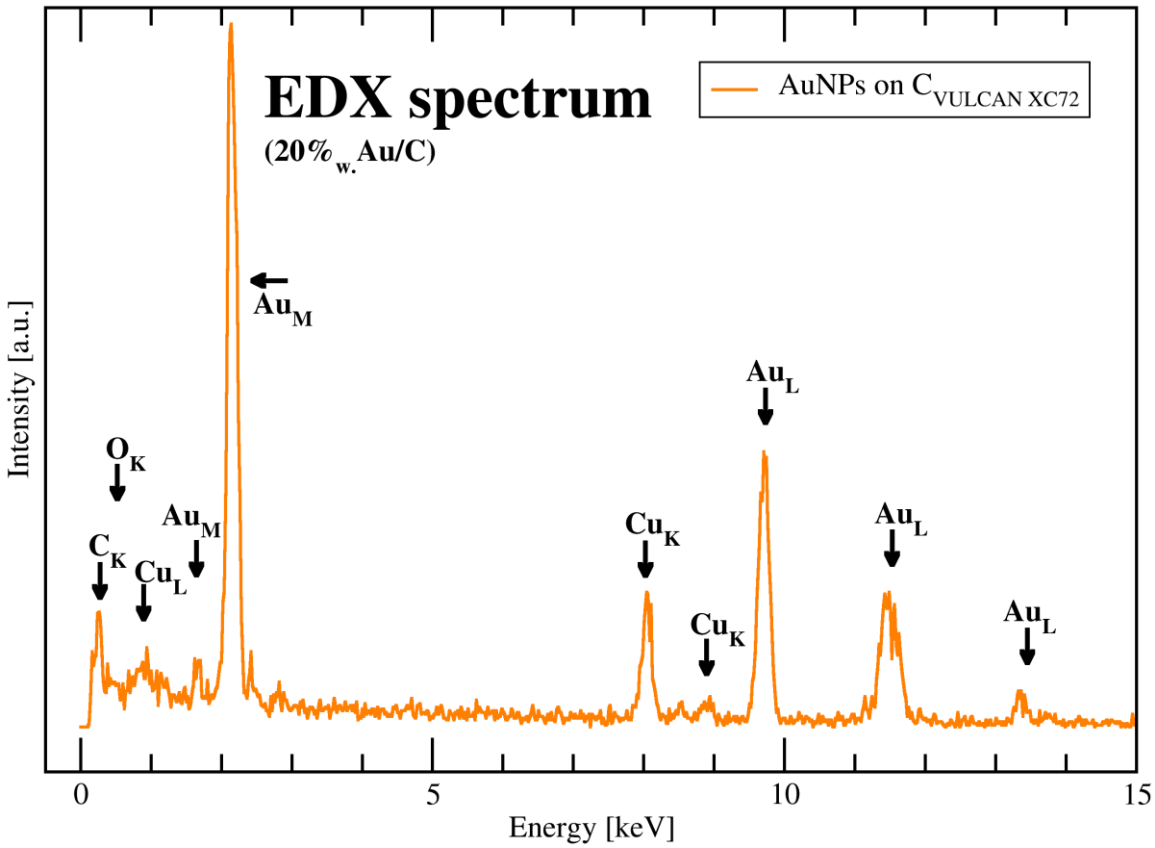

Fig. 70. An EDX spectrum of gold nanoparticles (AuNP) deposited on carbon Vulcan XC 72 acquired from the area visible in Fig. 69 (sample holder was tilted along its axis by 22° to efficiently collect X–Ray radiation emitted by the specimen). There were no other elements detected apart from gold (Au), carbon (C) and copper (Cu; the TEM grid – the specimen's substrate – was made of copper covered by thin holey amorphous carbon layer). No traces of contaminants were detected.

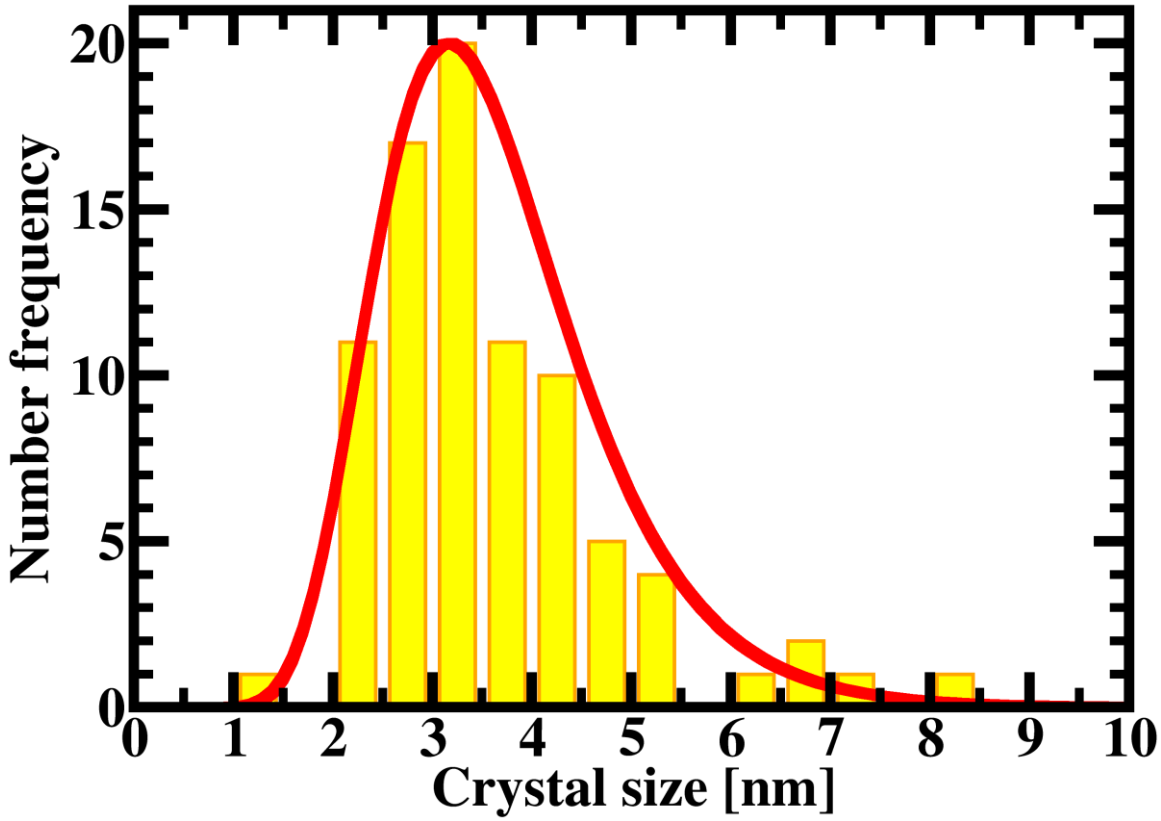

Fig. 71. Histogram showing gold crystals size distribution (CSD) in the 20%$_{wt.}$ Au/C catalyst. The graph was limited to 10 nm on the OX axis for better presentation of results, because only individual larger crystals were spotted. Yellow bars – number of observed crystals within the given size range; red line – scaled to number frequency axis log–normal analytical function fitted to the experimental results, parameters: average of natural logarithm of crystals' sizes = 1.23 and its standard deviation = 0.31.

3.4.6. Au/C – structure characterisation

Atomic structure analysis of the 20%$_{wt.}$ Au/C catalyst was slightly hampered by the high loading of gold phase. Little number of AuNPs exhibiting their lattices well–oriented in one of preferred zone axis and not interfering with another overlapping neighbour were spotted.

Fortunately, the investigation of AuNPs was not limited only to the ideal case. Successful attempt to filter the structure projection of the "edge"–oriented icosahedron is presented in the Fig. 73. Such an arrangement of planes is exceptional for icosahedron and it was frequently observed in this sample as well as in the other two catalysts (see Fig. 58, Fig. 61, Fig. 62 and Fig. 66).

Besides, apart from Multiply Twinned Particles (MTPs), two twinned crystals and single nanocrystals, Fig. 72 and Fig. 74 respectively, were observed. In the case of two latter types of particles, the FCC structure could be easily identified. The lattice spacings usually slightly deviated from the literature values for bulk gold, what was expected regarding the small size of the crystals. The limited resolution of the microscope and its camera (pixel size) allowed to measure the lattice spacings with the accuracy up to 0.05 – 0.10 Å – technically the ideal point-to-point resolution is ~100 pm and the averaging on the observed real few-nanometre nanocrystal could be performed on approx. 10 fringes. On balance, the certain zone axis could be undoubtedly identified on the basis of measured interplanar distances and arrangement of planes.

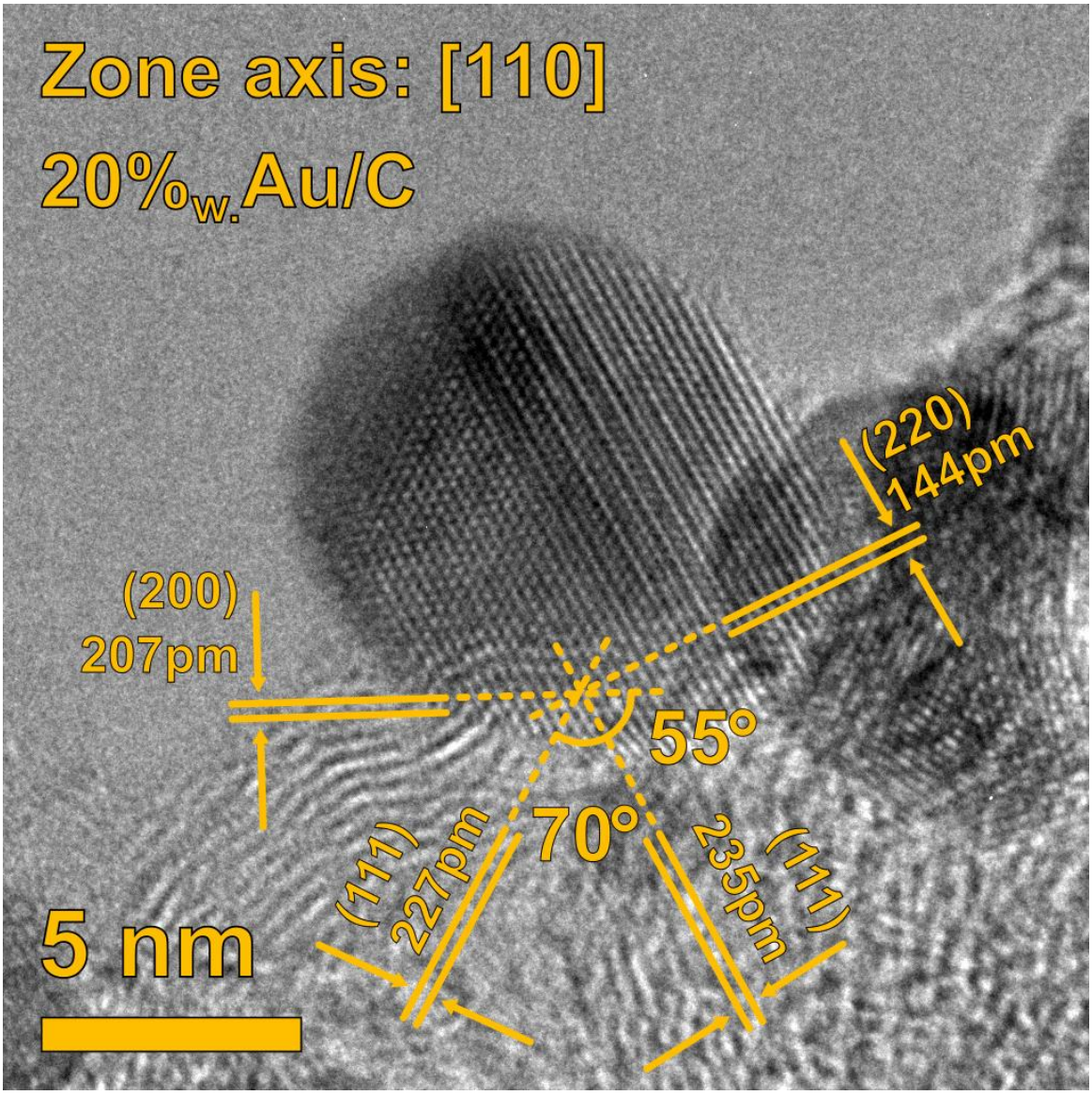

Fig. 72. A TEM image of a 10 nm twinned gold nanoparticle. The left part well-oriented along [110] direction FCC exhibits interplanar distances characteristic for the projection of the (111) plane.

The general observed trend concerning the internal structure of gold nanocrystals prepared by the modified Turkevich method was that larger crystals (approaching 10 nm and larger) were single crystals with FCC atoms' ordering, while smaller ones tended to be twinned or multiply twinned. The crystallisation mechanism did not lie within the scopes of this research. The formation and growth of seeds remains unclear. However, above 10 nm in diameter decahedral or icosahedral AuNPs scatter X–Rays under almost the same angles as FCC single crystals, so it is an important indication that crystal properties of these non–periodic structures are hardly preserved at bigger distances (long range ordering). The precise limit of the size of crystals containing 5–fold symmetry axis could not be specified. The purely experimental observations gave only a diffused approx. 5 nm range where single particles and MTPs coexist with each other. Such a broad intermediate zone is of the order of the total size of the smallest fraction of crystals, thus full quantification of this phenomenon was not possible.

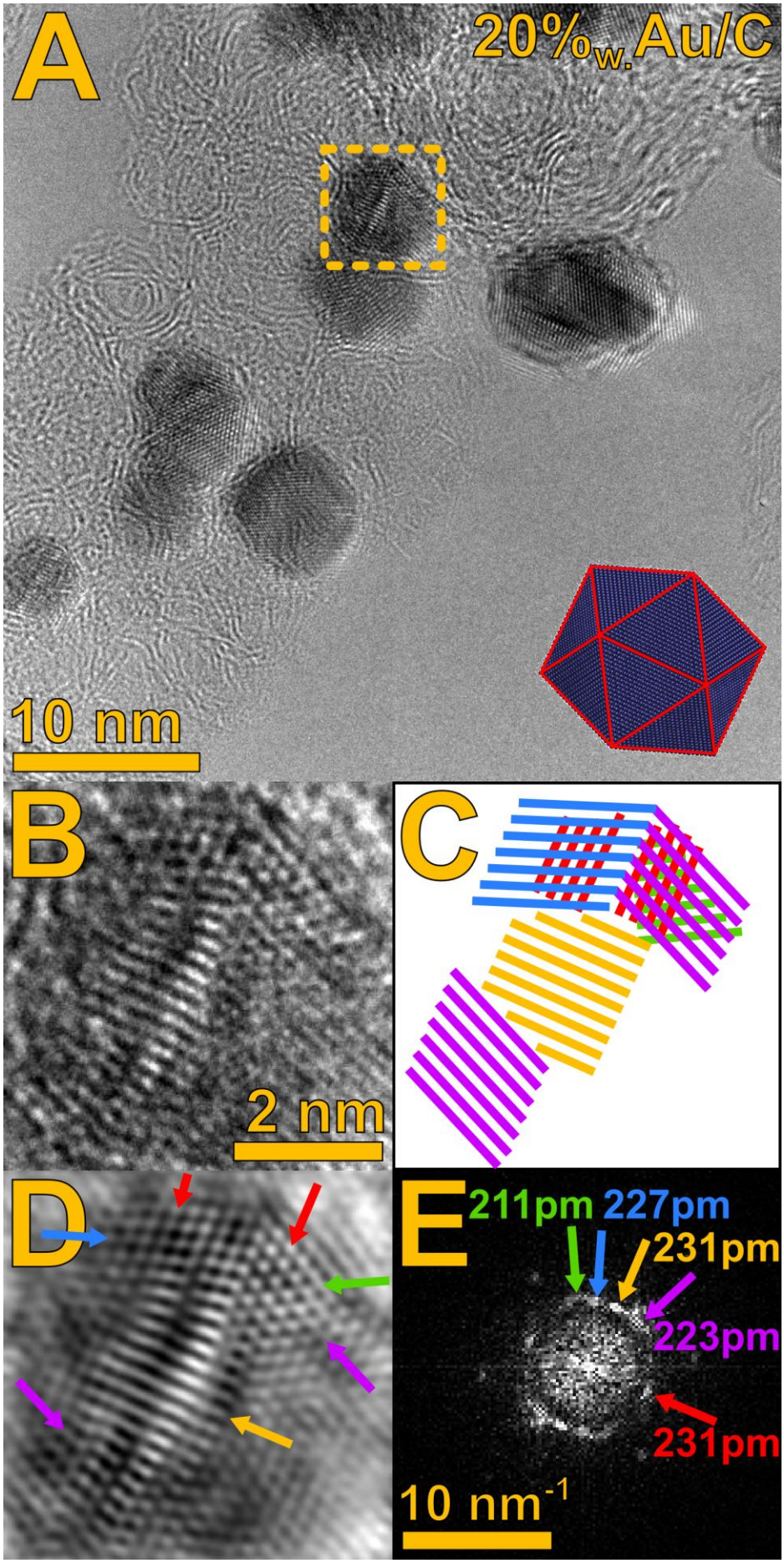

Fig. 73. A TEM image (A) of gold nanoparticles, one of which is a ~5 nm icoisahedron, found in the 20%$_{wt.}$ Au/C catalyst specimen. The "edge"–orientated particle marked with the orange square is enlarged in image B, while image E presents its r–FFT view. Image D shows the filtered–from–noise (refer to r–FFT image E) structure of this AuNP with some additional artefacts that should be neglected. The identified planes are marked with arrows and are schematically shown in image C. The characteristic "edge" orientation of icosahedron (presented in the insert in image A) can be recognised.

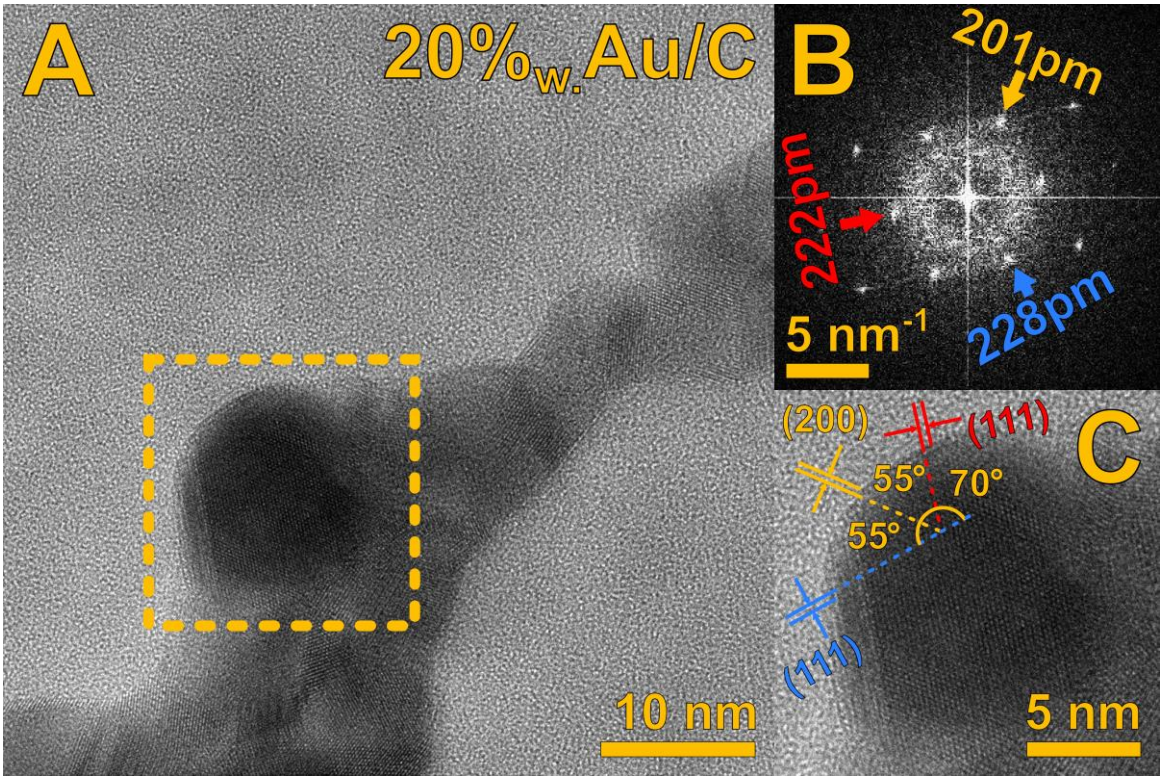

Fig. 74. A TEM image (A) of a 13 nm gold nanoparticle (enlarged in the image C) deposited on the amorphous carbon substrate. The r–FFT image (B) confirms clearly the presence of highly-ordered FCC atomic lattice oriented along [110] crystallographic direction.

3.5. *in–operando* TEM studies of 9.4%$_{wt.}$ Au/CeO_2

For the *in–operando* Transmission Electron Microscopy coupled with Mass Spectrometry (*in–operando* TEM–MS) studies the 9.4%$_{wt.}$ Au/CeO_2 catalyst was chosen. This catalyst was found to be the most active one out of the 3 investigated. High catalytic activity was vital, because the design of the microreactor was optimised considering best conditions for microscopy and electron spectroscopy on the expense of aspects related to engineering of chemical reactors. In addition, *in–operando* PXRD–MS experiments revealed several interesting phenomena accompanying catalytic activity of this system (e.g.: crystal lattice expansion, suspected shape of particles), which seemed promising to be examined under high magnification.

Thorough research on the chemical performance of the ceria–supported gold nanoparticles and the impact of the electron beam on the output of chemical reactions and specimen's structure and morphology preceded the main part of experiments. The results have been already described in Sections 2.10.3 and 2.10.4, respectively. In brief, under the atmosphere of CO and O_2 mixed in the ratio 2 : 1 (by volume) and 20 $\mu L \cdot min^{-1}$ gas stream Au/CeO_2 sample deposited in the microreactor mounted in the dedicated TEM holder was catalytically inactive below approx. 300°C. Hence, 200°C was chosen for studies of the inactive state of the catalyst, while its surface was prevented from being contaminated by the material originating from gas molecules decomposed by the beam. Above the activation temperature, the concentration of CO_2 linearly increased with the rising temperature. At 400°C the conversion of CO to CO_2 reached 1–2% which was significant enough to testify that the oxidation of carbon monoxide carried on with the aid of the catalyst. The empty microreactor was check to stay inert up to 600°C.

The overall low yield of CO_2 production and necessity to heat the specimen to higher temperatures were attributed to differences in design of ordinary chemical reactors or PXRD measurement chamber and the microreactor mounted in the commercial *in-operando* TEM setup. The two factors claimed to be crucially responsible for the discrepancies were: small total amount of the catalyst deposited in the microreactor; and the transfer of heat from the heater to the catalyst grains and gas reagents. The studies done in the transmission mode required thin layer of the specimen to be deposited on the microreactor's windows. Temperature conditions were maintained by the heater embedded in only one of the walls of the microreactor. Gaseous reagents were supplied at the room temperature directly to heated zone and the surface of the catalyst. The net effect of the mentioned factors (which may not be the mere reasons for the observed circumstances) on the chemical performance of the Au/CeO_2 catalyst was impossible to be reliably evaluated, as even the manufacturer of the setup still evaluates and develops the performance of the its product.

In general, *in–operando* TEM–MS studies give relevant data which agree well with conclusions drawn on the basis of experiments done with other techniques. The specific working procedures are just characteristic for this approach, but undoubtfully provide valuable knowledge about the investigated material.

3.5.1. Low magnification imaging

Visual investigation of the 9.4%$_{wt.}$ Au/CeO_2 catalyst at relatively low magnification (Low-MAG), × 61 000, aimed at seeking global morphology changes happening to the sample during the course of CO oxidation reaction. The phenomena which were foreseen included gold particles mobility on the support surface, crystals shape change (faceting, loosing sharpness of the edges) and radical switch of contrast of the object in the image (contrast loss might indicate amorphization of, initially crystalline, particles; while contrast gain might imply crystallisation of matter).

Of special interest was oscillatory behaviour of these features. Alternations could happen either under reaction conditions or under inert atmosphere. In the first case, they would be related to reaction acts happening at the catalyst surface. The latter scenario would suggest stabilisation of the surface by interactions with reagents, while surface layers atoms would be very mobile, perhaps in a quasi-melted state, in the absence of adsorbates. Oscillations observed regardless of the gas atmosphere might point to the influence of the electron beam on the sample, which would impede the research until solution to such problem would be found.

The specimen was heated to 400°C in order to study the active state of the catalyst under reaction conditions. The results were compared with the state of the observed aggregate in He environment. Although 360 images with 10 s time interval were recorded in both condition sets, they presented a very steady picture of the macroscale morphology of the catalyst – no mobility of, especially, AuNPs was observed – see Fig. 75 and Fig. 76.

Preservation of the catalyst macrostructure coincides well with the expectations regarding catalyst stability. Its chemical performance remained at high level – close to 100% CO conversion – for long time-on-stream. Consequently, the degradation of the catalyst should not occur and binding of AuNPs to CeO_2 support (preferably through good epitaxy) may be claimed as strong enough.

Similarly, the AuNPs shape remained faceted regardless of the gas atmosphere. The *in-operando* PXRD studies suggested only negligible evolution of gold structure, so stable faceted shape of crystals observed in TEM agreed well with those results. The fact that crystals were clearly terminated with crystallographic planes supported the idea of particles shape modelling with polyhedra, as well.

This experiment served also as additional proof for the resistance of the studied catalyst against electron beam influence when the dose and illumination time were limited appropriately.

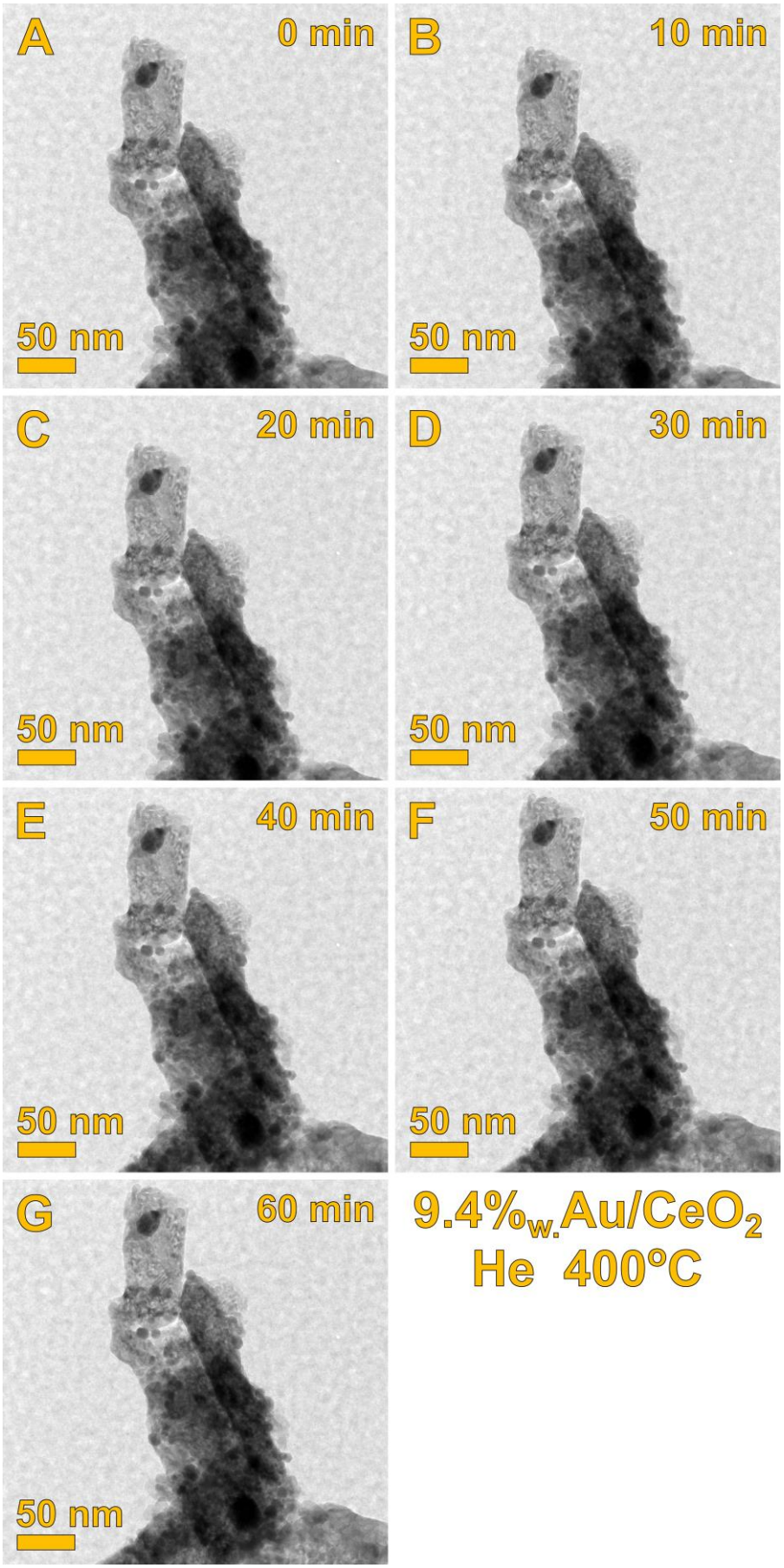

Fig. 75. Selected low magnification (× 61 000) images (from a series acquired at constant 10 s interval) of the 9.4%$_{wt.}$ Au/CeO_2 catalyst exposed to He atmosphere at 400°C.

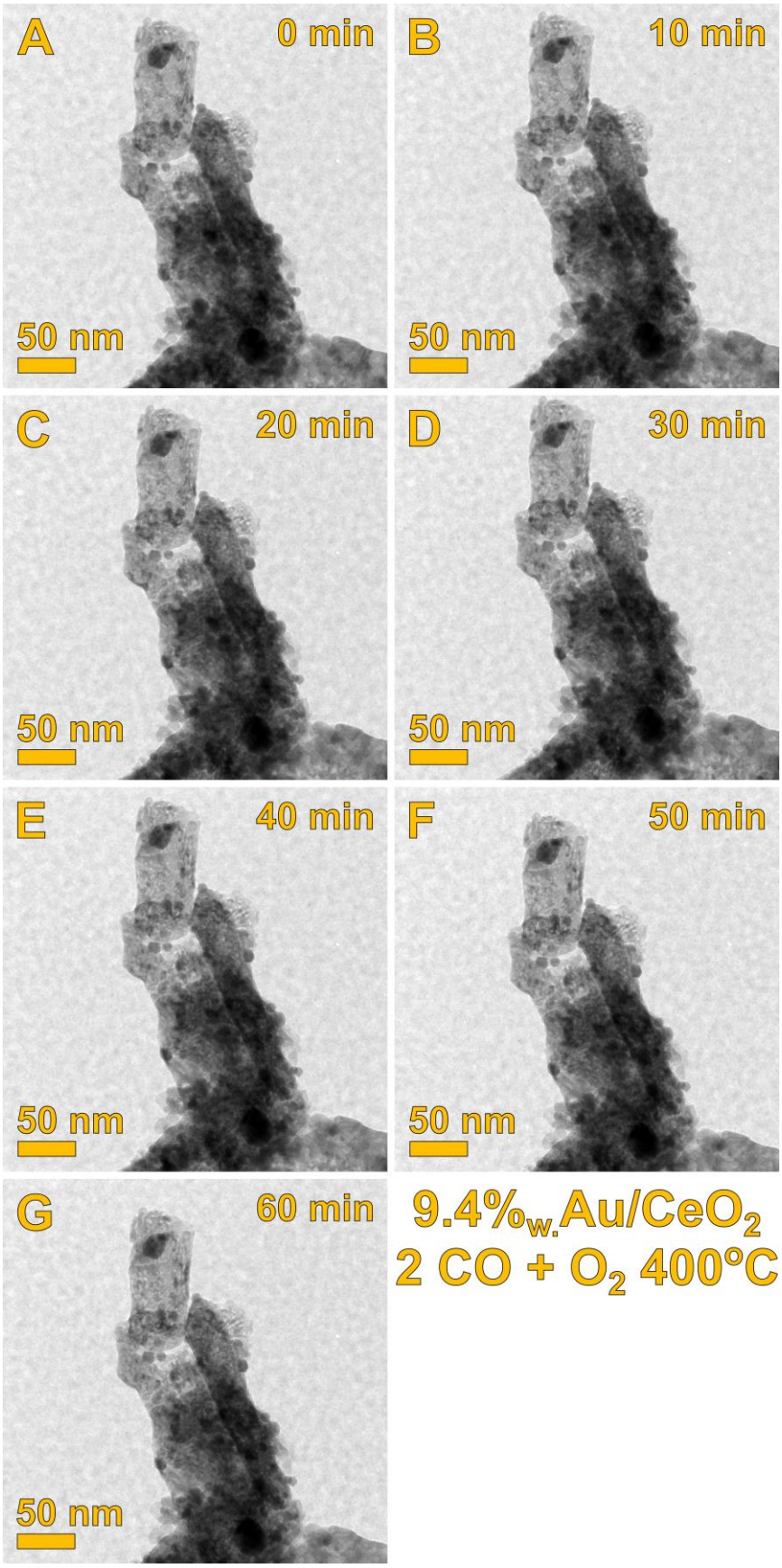

Fig. 76. Selected low magnification (× 61 000) images (from a series acquired at constant 10 s interval) of the 9.4%$_{wt.}$ Au/CeO_2 catalyst exposed to stoichiometric CO oxidation reaction reagents mixture at 400°C.

3.5.2. High resolution imaging – low electron beam dose conditions

High resolution imaging of the 9.4%$_{wt.}$ Au/CeO_2 catalyst was a natural extension of studies done at, relatively, low magnification (see Section 3.5.1). Herein, it was possible to concentrate on individual nanocrystals (see Fig. 79 and Fig. 80) or small aggregates containing just a couple of particles (Fig. 77 and Fig. 78). The specimen was exposed to pure He environment and stoichiometric CO oxidation reaction conditions at 400°C.

It is worth to notice that no contamination (usually growing carbon-based amorphous layer) was not experienced also during this part of research. Hopefully, sample drop-casting from water solution and the *in-situ* oxygen pre-treatment prior to TEM investigation allowed to successfully remove any pollutants from the surface and pores of the E-chips (microreactor) and the catalyst. No disproportionation of CO was spotted as well, although studies of localized surface plasmon resonance mediated decomposition of CO to carbon and CO_2 on preferred sites of gold nanoprisms excited only by finely focused electron beam were carried out [135].

The first glimpse comparison of Fig. 77 and Fig. 78 reveals that the relative orientation of crystals with respect to the electron beam slightly varied after gases were exchanged. This misorientation was expected, but no adjustment of microreactor holder tilt was applied. Any attempts to recover all previously simultaneously observed projections of atomic lattices were usually unsuccessful, because the relative positions between gold and ceria crystals were not ideally preserved. Prolonged trials would only excessively expose the studied area to electron beam, which was generally avoided as much as possible. The readily obtained imaging conditions were sufficient to examine potential faceting processes and, occasionally, to characterise atomic lattice parameters.

The later task was challenging regarding the shallow depth of focus of the microscope at high magnification. Depth of focus itself is inversely proportional, among other factors, to the order of magnification, so it is a commonly experienced difficulty. The experimental observation was that the focus of atomic structures of nanocrystals was cyclically lost and gained without readjustment of the microscope lenses. Consequently, undisturbed fluent tracking of dynamic changes of the crystal structure was impossible. It was, however, achievable to monitor the outer shape of nanocrystals and eventual reorientation of those crystals in time (judging by the analysis of lattice fringes observed in some images). Such investigations are presented in Fig. 79 and Fig. 80.

Image A and B in Fig. 79 show an icosahedral gold nanoparticle exhibiting characteristic arrangement of crystal planes. Analysis of all images in the series recorded under He and sCOOX reaction conditions confirmed that the AuNP was rigidly bound to the neighbouring CeO_2 substrate. The epitaxial relationship (however hard to determine because of both non-crystallographic character of icosahedron and lack of an image of its perfect zone axis projection) was preserved throughout the whole experiment. Actually, the whole visible aggregate was not subjected to any damage despite rather high electron beam dose used during this part of studies – thus it served as the final proof of the safe level of electrons flux in the case of Au/CeO_2 catalyst. Furthermore, the faceting of the AuNP from Fig. 79 remained stable and did not transform noticeably upon the gas exchange from He to the mixture CO : O_2 = 2 : 1 (by volume). Generally, the shapes of visible AuNPs were preserved during the experiment.

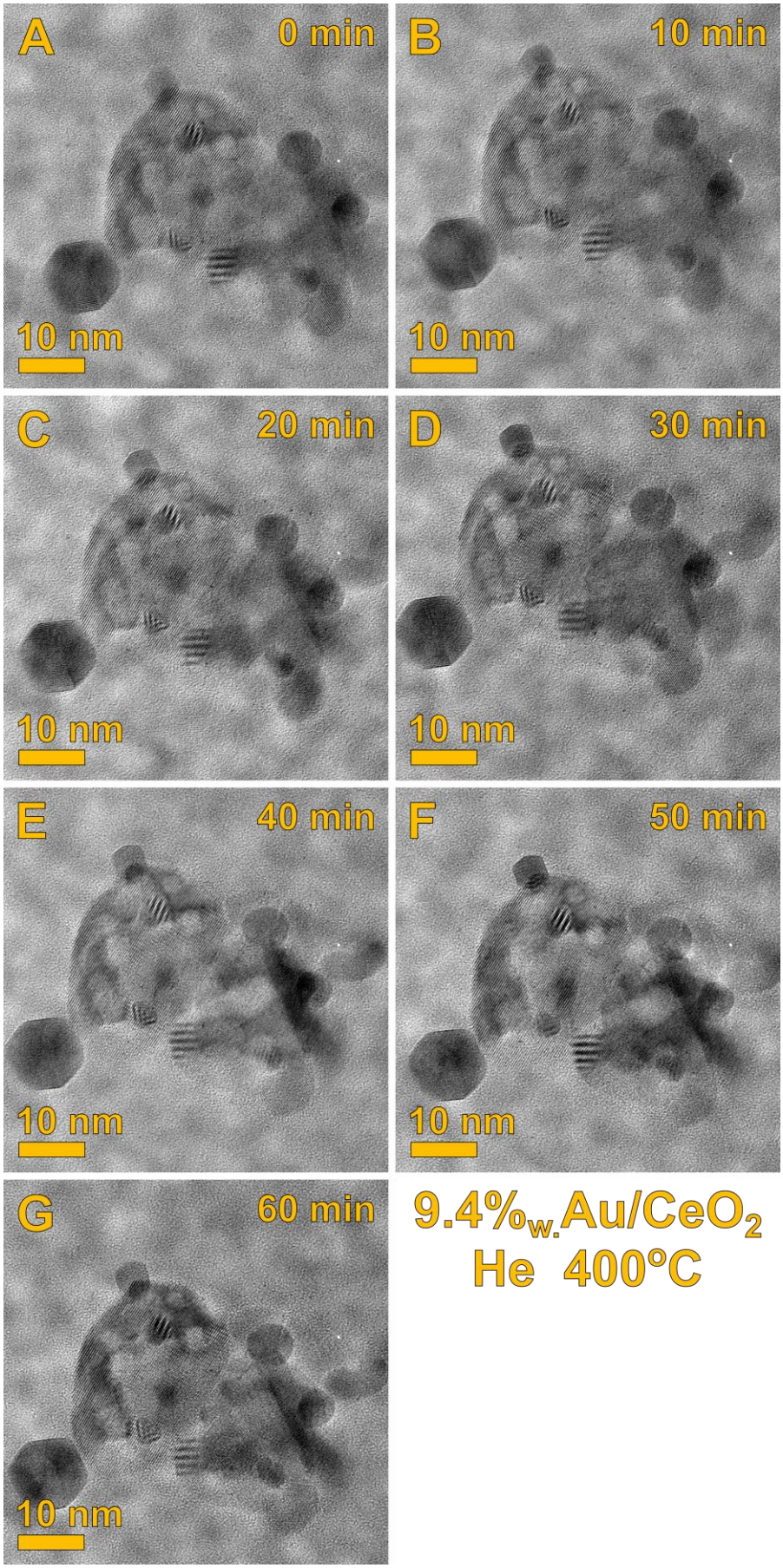

Fig. 77. Selected high resolution images (from a series acquired at constant 10 s interval; magnification × 380 000) of the 9.4%$_{wt.}$ Au/CeO_2 catalyst exposed to He atmosphere at 400°C.

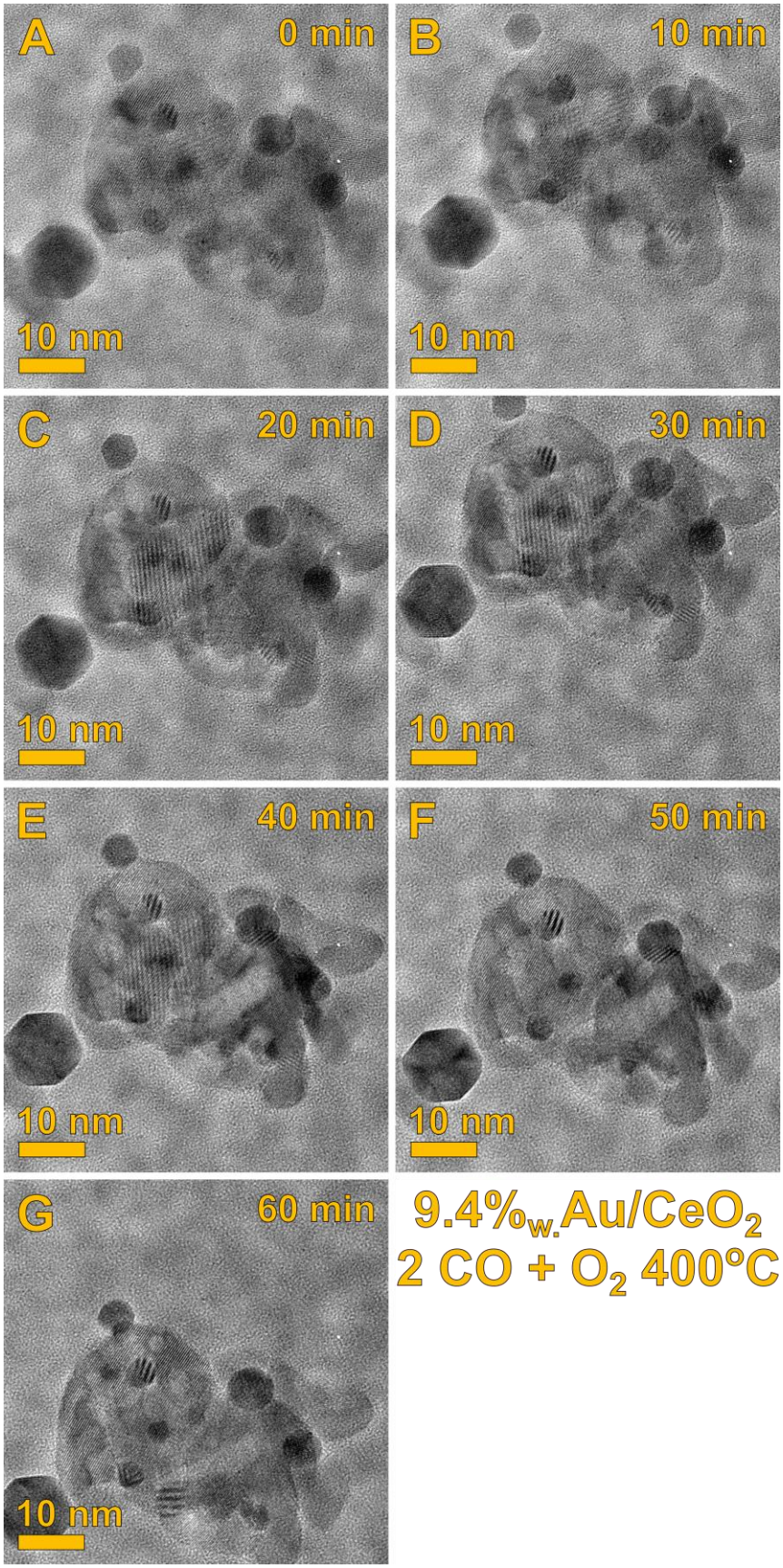

Fig. 78. Selected high resolution images (from a series acquired at constant 10 s interval; magnification × 380 000) of the 9.4%$_{wt.}$ Au/CeO_2 catalyst exposed stoichiometric CO oxidation reaction reagents mixture at 400°C.

The only exception was the 6 nm gold nanocrystal which was bound to ceria support in Fig. 80. Following images in Fig. 78, starting from image E, the particle seemed to become round (i.e. lost clear faceting) and started to increase overlap with the CeO_2 support. Most probably this was just a misleading impression as the aggregate went out of focus. This fact was especially evident judging by the Fresnel fringe around the dark 10 nm AuNP close to the bottom left corner of the image (analysed in Fig. 79). Comparison with the images in Fig. 77 clearly shows that during the experiment the projection of cerium dioxide structure became frequently less sharp near the verges. The fact that lattice fringes observed in micrographs only represent the crystal structure which they originate from, but not necessarily depict the exact positions atoms or atomic planes, should be borne in mind always during the analysis. Similarly, the sample going out of objective lens focus may disappear from the field of view.

On balance, high resolution imaging of the Au/CeO_2 catalyst confirmed conclusions drawn after evaluation of low magnification and X-Ray diffraction data that no global changes to the shape of crystals and their arrangement occurs under reaction conditions. The performed experiments pointed also to limited application of the real image studies when changes happening to the crystal structure at the picometre scale are of the interest of the research. The choice of electron diffraction techniques is strongly advised.

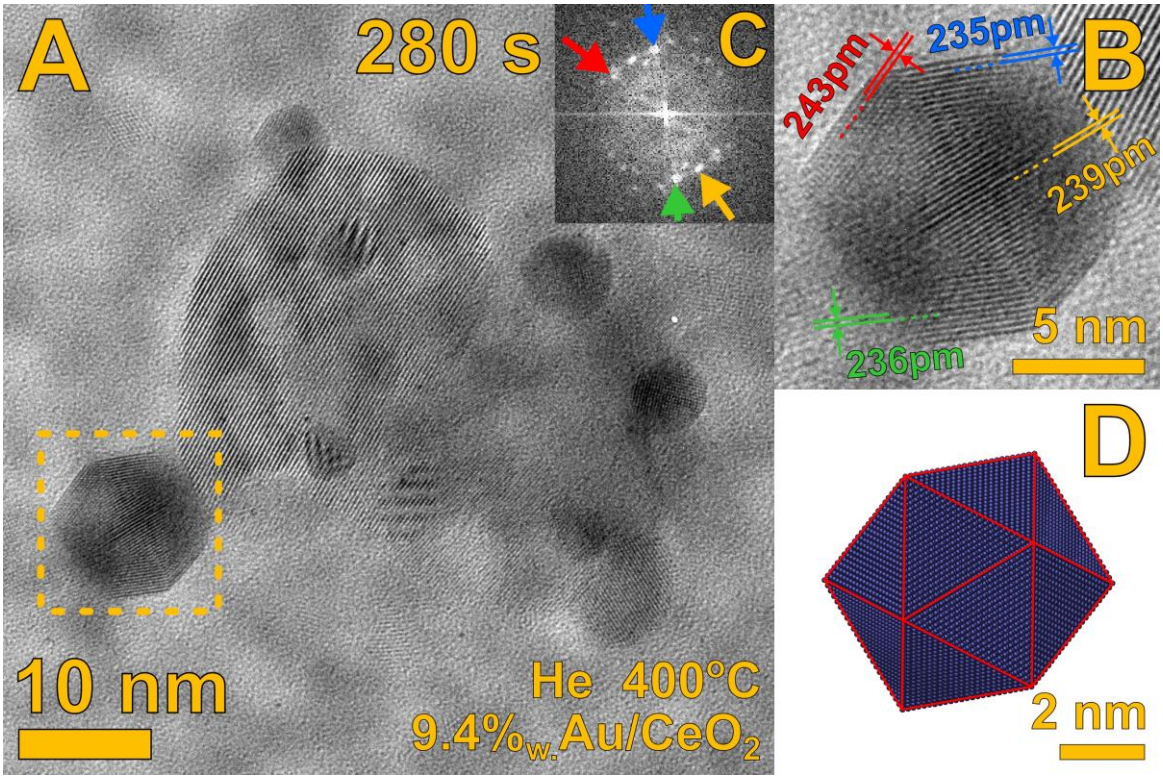

Fig. 79. A selected high resolution image (A), one from the series represented in Fig. 77 recorded under pure He atmosphere at 400°C, of a-few-particle agglomerate of the 9.4%$_{wt.}$ Au/CeO_2 catalyst sample. An icosahedral gold nanoparticle exhibiting characteristic lattice fringes is marked with the orange square and is enlarged in image B. Its r-FFT pattern is presented in image C. Image D shows the refence model of a gold icosahedron appropriately oriented in space.

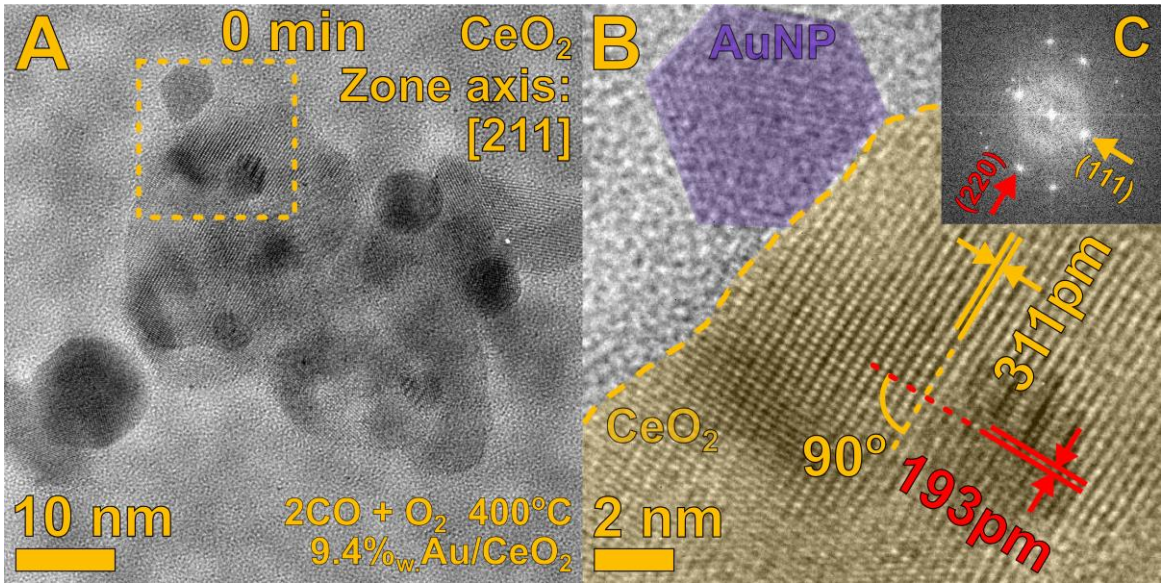

Fig. 80. Image A is a reproduced image from Fig. 78.A presenting a-few-particle agglomerate of the $9.4\%_{wt.}$ Au/CeO_2 catalyst sample exposed to stoichiometric CO oxidation reaction mixture at 400°C. Area marked with the orange square is enlarged in image B which shows atomic lattice of the catalyst support, CeO_2, oriented along [211] zone axis. Image C is the r-FFT pattern of CeO_2 structure projection.

3.5.3. High resolution imaging – high (excessive) electron beam dose conditions

Generally, *in–operando* TEM–MS experiments were focused on investigation of the specimen while minimising damages induced by the electron beam. However, when the pre-specimen shutter was omitted (post–specimen shutter was still inevitable, because the buffer of the camera would be oversaturated, or even destroyed, if it was permanently illuminated by the beam) and a selected gold nanoparticle was constantly exposed to a focused beam (approx. 870 000 $\frac{e}{nm^2 \cdot s}$), several interesting states were observed. The experiment described in this Section was performed during initial microreactor chemical tests, exactly during exposure to the gas mixture of He : CO : O_2 = 89 : 10 : 1 (by volume) at 400°C. The focused beam illuminating only a few tens of nanometres area did not caused the MS signal 44 to change. Additional reminder: this gas mixture was not the optimal one for CO to CO_2 conversion.

The initially round 21 nm AuNP randomly oriented in space underwent a few steps of shape change and structure reordering and came back to the initial state after 810 seconds. The evolution of shape was the easiest to track. The most obvious change was bulging of the particle's edges which was accompanied by creation of notches at the borders of the expanded region (it is very well noticeable in Fig. 82.j). The area of the nanocrystal (or better say: its "volume") that was subjected to such a change was as big as roughly $\frac{1}{5}$ of the whole particle. In numerous images (Fig. 82.d, f and h) the contrast between parts of the crystal suggested presence of 5–fold symmetry axis, which further pointed to decahedral shape of this crystal (comparatively: icosahedron does not exhibit 5–fold symmetry in any structure projection, because there are 6 such axes in this polyhedron). Appearance of the notches might indicate, that the observed crystal occasionally adopt the shape of Marks decahedron (m–decahedron, [132] [128] [43]). M–decahedron is based on a truncated decahedron (frequently called Ino–decahedron, i–decahedron [136]), i.e. the classic decahedron is cut with planes parallel to the 5–fold axis and verges of the

triangular faces, so that new square or rectangular faces are created on the polyhedron's perimeter. Additionally, m–decahedron requires re-entrant cut of the edges formed by the new rectangular faces. The depth of this cut and the whole shape of m–decahedron are described by a 3–number notation: $m \times n \times p$ (refer to Fig. 81 and [43]), where m, n, p define the length of appropriate edges (either by number of atoms or units of length).

The energy provided by the electron beam (heat and/or electric charge) induced cyclic reordering of the atomic lattice of the observed crystal. In numerous frames, e.g. in Fig. 82.h lattice fringes could be spotted. The range of the measured spacings at different times was quite broad, 2.24 – 2.69 Å, but the structure of this crystal had never enough time to relax and equilibrate.

Investigation of a gold nanoparticle which was heavily affected by the interaction with the electron beam did not correspond directly to the state of the catalyst during CO oxidation reaction conditions. It was although shown, that the structure of even a randomly oriented particle could be checked and, thus, selected characteristic features of its outer shape and internal arrangement could be established. While the electron beam influence was attempted to be minimised at all times during microscopic investigation of the catalyst's specimen, application of excessive electrons dose enabled to assess to what extent the obtained results might be corrupted in this way.

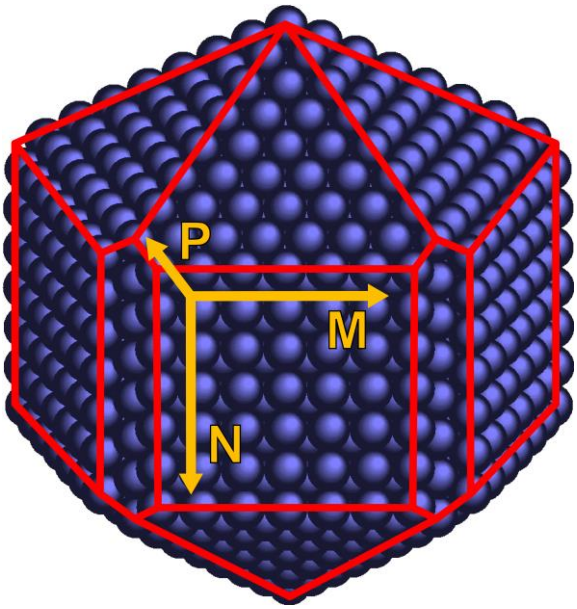

Fig. 81. A model of a Marks decahedron (m–decahedron, [132]) with re-entrant (111) facets (in "p" direction). For the description of this m–decahedron notation used e.g. by Cleveland [43] can be used, $m \times n \times p$, which defines the size of the truncated faces ($m \times n$) and the depth of concavity (p) – in this case it look in the following way: m–decahedron 7 × 7 × 1 atoms.

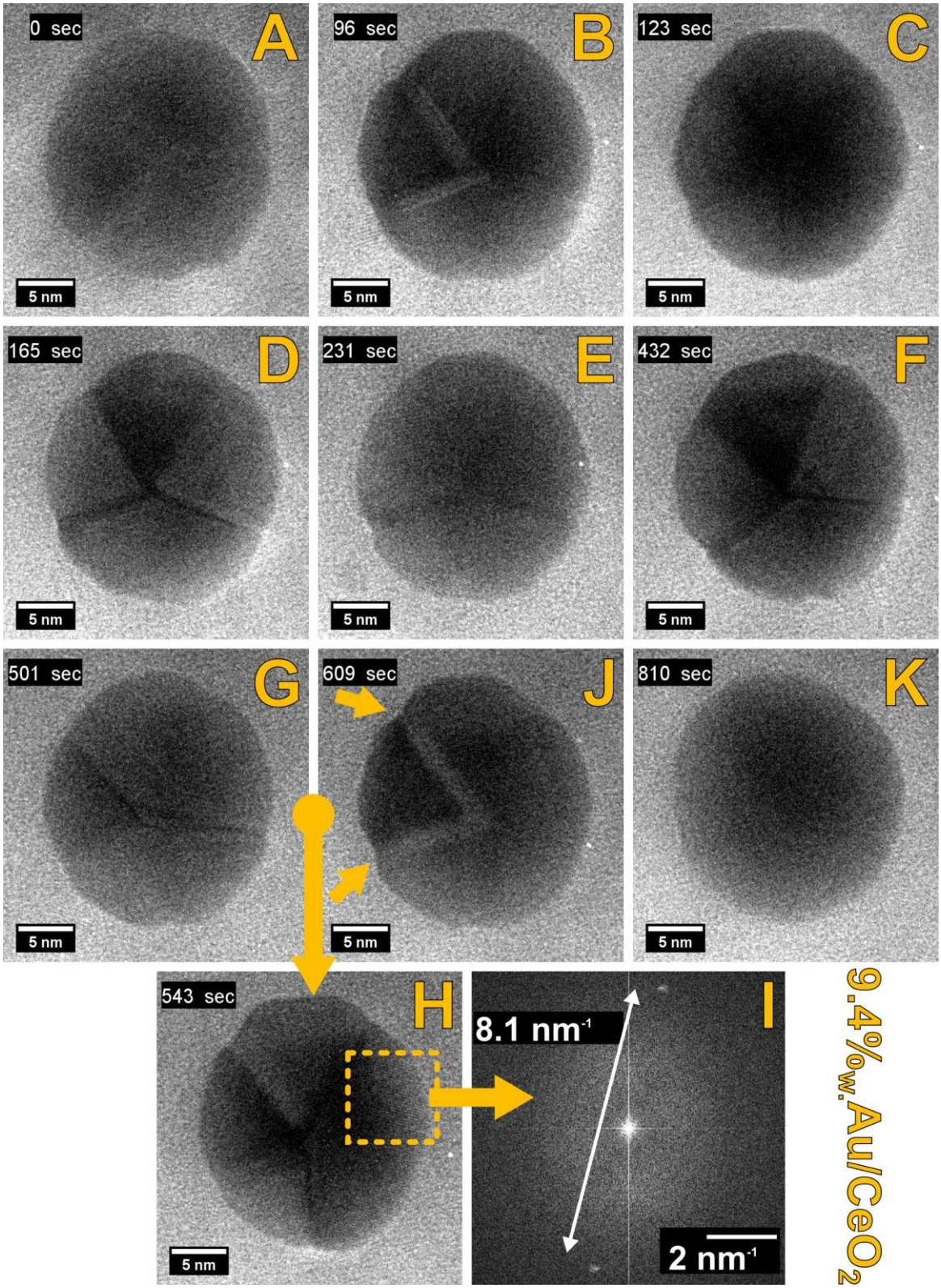

Fig. 82. Series of selected TEM images presenting the evolution of a gold nanoparticle illuminated constantly (no pre–specimen shutter was used) by a focused electron beam, i.e. flux of electrons equalled ~870 000 e · nm^{-2} · s^{-1}. Changes did not happen at regular time intervals. Altering crystal lattice expansion and/or structure reconstruction (e.g.: amorphisation–recrystallisation, melting–solidifying) resulted in bulging of the particle's verges accompanied by appearance of notches (visible in images B, D, F, H and J, where they are marked with an arrow). Worth of notice are traces of 5–fold symmetry axis (visible especially in images D, F and H) which suggests that this was a Multiply Twinned Particle (MTP), possibly a decahedron. Image I presents an r–FFT of the area marked in image H where atomic lattice fringes were spotted. They corresponded to 2.47 Å spacing, but range 2.24 – 2.69 Å was observed.

3.5.4. Electron diffraction

Electron diffraction studies were utilised to obtain higher precision in interplanar spacing measurement in comparison with imaging under either TEM or STEM mode. Typical point-to-point resolution of the real image obtained with a high resolution TEM microscope is 0.5 – 1.0 Å. The effectively measured interplanar distance can be reported with 1–2 orders of magnitude higher precision thanks to formation of high resolution image from several interfering beams. Precision can be further improved statistically by measuring the sum of spacings between several neighbouring planes and dividing the resulting value by the number of planes. The latter approach has, however, limited applications to studies of nanoparticulate materials, because only about 10 – a few tens of planes can be observed within one crystal oriented in the preferred zone axis.

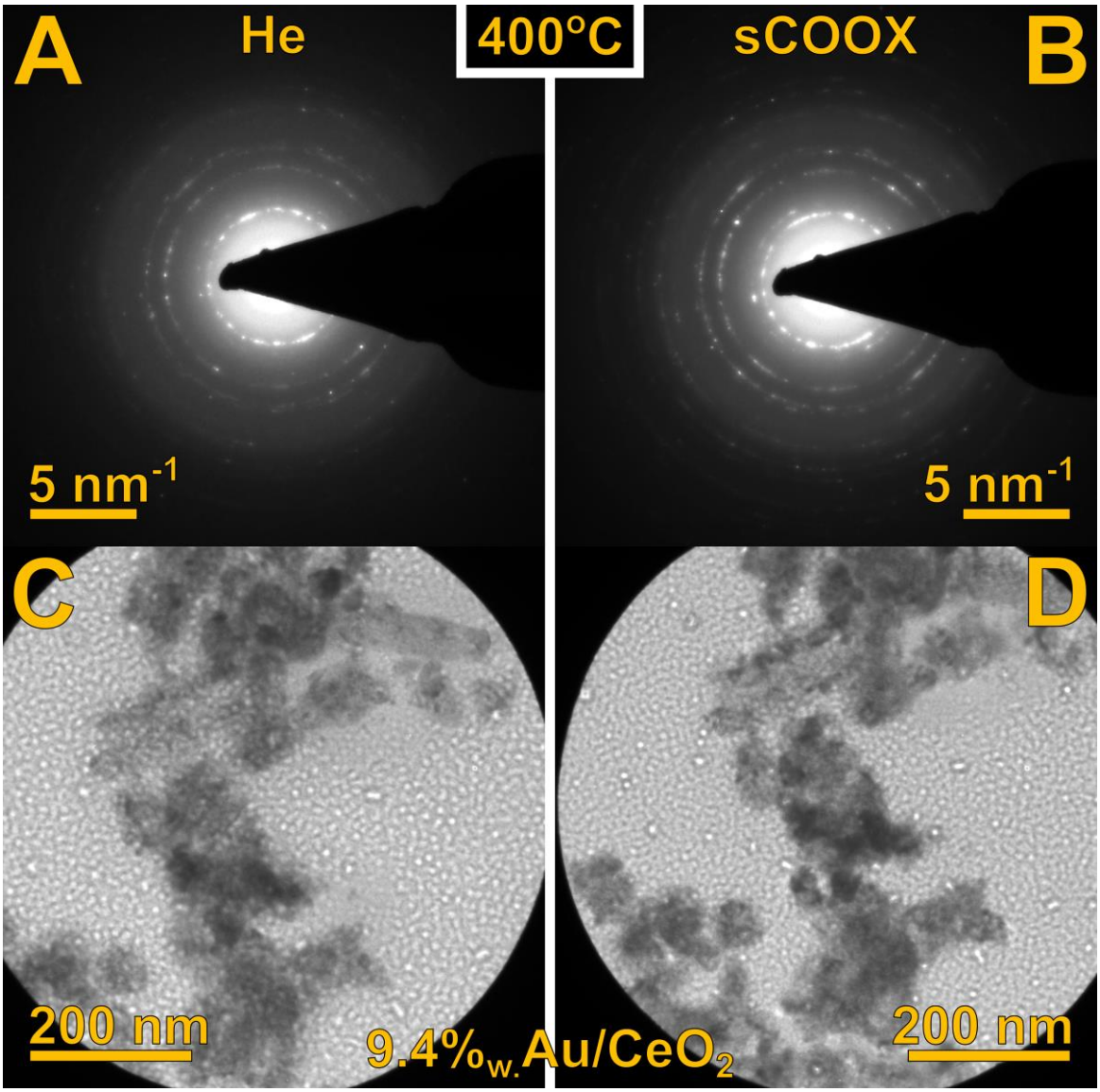

Fig. 83. Comparison of first acquired Electron Diffraction Patterns (EDPs, images A and B) and TEM images (C and D) showing the area selected for electron diffraction studies (SAED). The sample did not move noticeably in the plane of the image during the 1 hour experiment. In EDPs, the exchange of gases (which included pumping of the microreactor) and slightly different illuminated area are reflected in the intensity and position of individual visible reflections. However, the Debye–Scherrer rings were statistically equally well-represented in both cases.

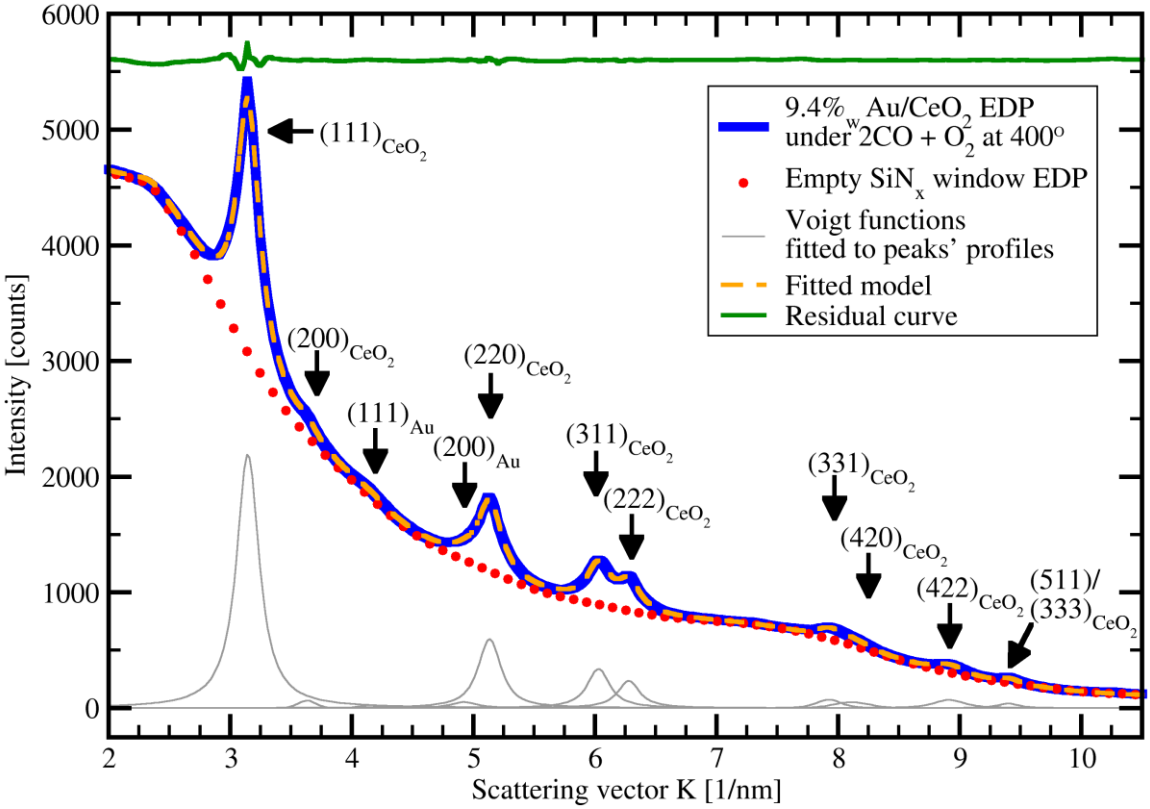

Fig. 84. The azimuthally averaged Electron Diffraction Pattern (EDP) of 9.4%$_{wt.}$ Au/CeO_2 catalyst exposed to the stoichiometric CO oxidation (sCOOX) reaction mixture at 400°C. The subtracted background is the scaled EDP of an empty Si_3N_{4-x} E-chip window. Diffraction peaks were fitted using Voigt functions. Reflection originating from gold (Au) and the 4 0 0 CeO_2 peak (should be observed at ~7.39 nm^{-1}) were too weak to be taken into account during structure analysis.

A flattened (azimuthally averaged) 2D electron diffraction pattern (Fig. 84) acquired at the 245 mm distance between the sample and 4 MP (megapixel, also called 2 K ≡ 2048 × 2048 pixels) camera (Gatan® BM–UltraScan) offers readily 0.0215 nm^{-1} point-to-point resolution, which equals to the real space resolution linearly changing from 0.0239 Å to 0.0022 Å in the most useful range of spacings 3.0 – 1.0 Å (approx. 3.0 – 10.0 nm^{-1}). Naturally, it can be improved by fitting peaks' shapes with analytical functions, e.g. Voigt functions.

For collection of relevant electron diffraction data, it is crucial to maintain parallel illumination of the investigated area. Otherwise, the calibration of the microscope's camera becomes invalid and the Debye-Scherrer rings become broadened and displaced. Electron diffraction studies are also free from uncertainties originating from the mechanism of real atomic resolution image formation – fringes (or lattices of interlacing fringes) only correspond to the real atomic planes, but do not represent the true positions of atoms (compare e.g. Fig. 61.E and F which shows how a known icosahedral nanoparticle looks like in the micrograph).

The average character of electron diffraction data excludes the study of individual nanocrystals. In the *in-operando* experiments, EDPs acquired under different conditions, either varying gas atmosphere composition or temperature, are rarely identical (refer to Fig. 83). Differences arise due to ease of position change of specimen particles lying on the E-chip's Si_3N_{4-x} window. These windows are very elastic and bulge easily. The gas exchange procedure includes pumping of the microreactor to provide efficient purging of

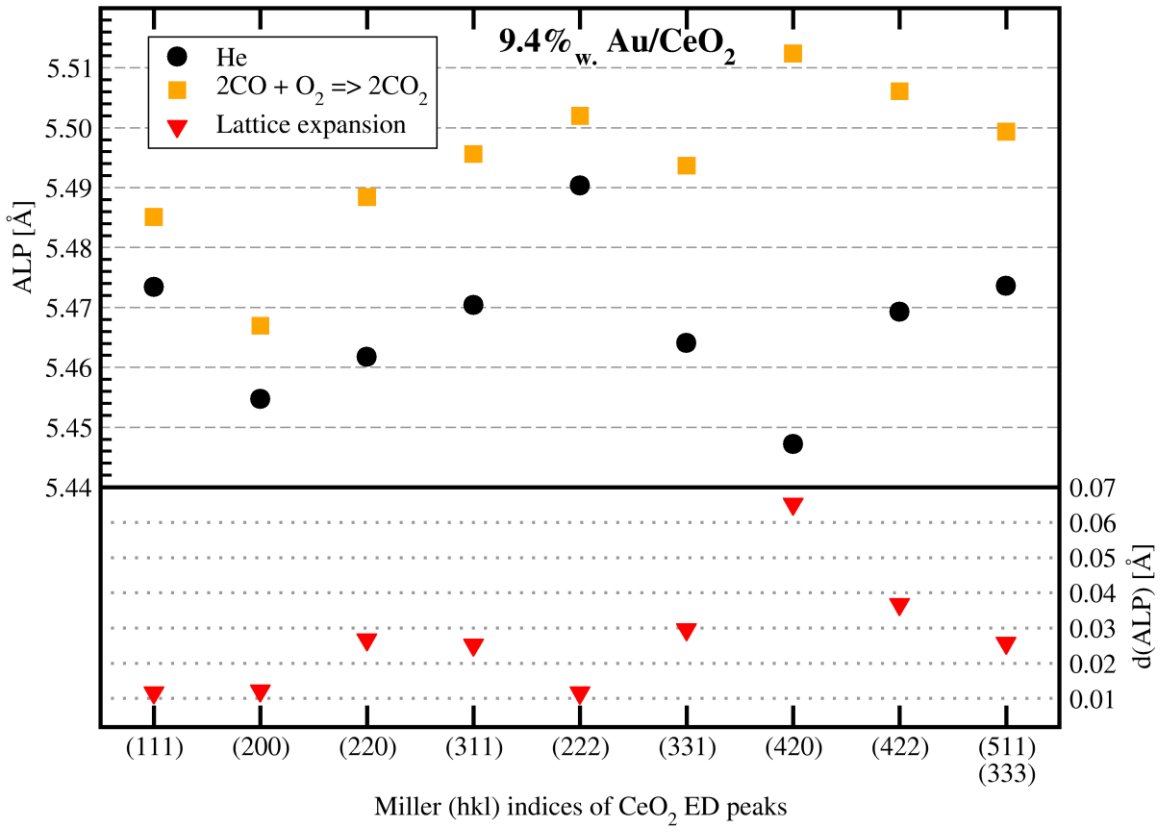

Fig. 85. Comparison of Apparent Lattice Parameter (ALP) of cerium (IV) oxide, which serves as the support in the 9.4%$_{wt.}$ Au/CeO_2 catalyst, observed in electron diffraction studies (ED) under He atmosphere and CO oxidation (sCOOX) reaction gas mixture at 400°C. ALP was recalculated from the positions of *h k l* peaks visible on the azimuthally averaged EDP. These peaks' positions corresponded to electron scattering semi–angle on selected crystallographic planes of ceric oxide particles illuminated by the electron beam. Please refer to Table 33 for exact values.

Table 33. Comparison of Apparent Lattice Parameter (ALP) of cerium (IV) oxide (component of 9.4%$_{wt.}$ Au/CeO_2 catalyst) under He atmosphere and CO oxidation (sCOOX) reaction gas mixture at 400°C, investigated by electron diffraction (ED). ALP was recalculated from the positions of *h k l* peaks visible on the azimuthally averaged EDP. Please refer also to Fig. 85.

	400°C		
	ALP [Å]		
h k l	He	sCOOX	Δ ALP [Å]
1 1 1	5.473	5.485	0.012
2 0 0	5.455	5.467	0.012
2 2 0	5.462	5.488	0.027
3 3 1	5.470	5.496	0.025
2 2 2	5.490	5.502	0.012
3 3 1	5.464	5.494	0.030
4 2 0	5.447	5.512	0.065
4 2 2	5.469	5.506	0.037
5 1 1) / / 3 3 3	5.474	5.499	0.026

the volume with the new mixture. Heating of the microreactor causes its walls and windows to expand thermally. Hence, the orientation of specimen can change with respect to the electron beam direction. Although much more limited number of crystals is illuminated by the electron beam and contributes to formation of EDP than it is in the case of X-Ray beam in the powder X-Ray diffractometer, this number is usually sufficient to ensure observation of the vast majority of diffraction rings (actually: traces of cones), but their relative intensities are distorted. Fortunately, this fact does not prevent structural analysis based on reflections' positions. However, marginal asymmetries of peaks' shapes may be experienced and may attempt to influence the analysis results, what needs to be borne in mind and examined if necessary.

The 9.4%$_{wt.}$ Au/CeO_2 catalyst loaded onto the E-chip heated up to 400°C was exposed to He atmosphere and stoichiometric mixture of CO and O_2 suitable for CO oxidation reaction. In each case, 360 EDPs were acquired with a 10 s interval. The EDP on an empty window was also recorded. All EDPs were examined in order to spot significant differences which may indicate severe disturbance of the experiment conduct – no such symptoms were noticed. Then, in brief, only 7 EDPs collected after every 10 min were selected for manual structure dynamics analysis. After determining the centre and ellipticity distortion parameter of each selected EDP, they were azimuthally averaged to yield the dependence of intensity on scattering vector, $I = f(K)$. As such, the EDPs acquired under the same gas environment were further averaged to obtain smoother experimental curve which was then appropriate enough for peak shape and position analysis – Voigt functions were used to model peaks' profiles. The model established for stoichiometric CO oxidation reaction conditions is presented in Fig. 84.

Commonly for all attempts of EDPs acquisition, peaks originating from AuNPs had very low intensity (amplitude) and reliable analysis of gold phase remained impossible. The loading of gold in the catalyst was quite high – 9.4%$_{wt.}$. For the electron diffraction studies, it was necessary to choose catalyst agglomerates which were thin enough to enable the electron beam to pass through. Any AuNPs larger than approx. 20 nm (it is only an arbitrary limit) absorbed the beam too much. The size of catalyst aggregates imposed application of 40 or 10 μm selected area (SA) diffraction aperture (40 μm SA was used). Any larger SA allowed too much of scattering from empty areas of Si_3N_{4-x} window to contribute to the EDP, thus decreasing the ratio of the reflection to background signal. Powder X-Ray diffraction is free from such limitations and probe the whole volume of the specimen within the penetration depth, which is higher than for negatively charged accelerated electrons.

Similarly to *in-operando* PXRD-MS studies, structure dynamics analysis focused, then, on cerium (IV) oxide phase. The comparison of results obtained under He atmosphere and 2 CO + O_2 gas mixture are presented in Fig. 85 and Table 33. The apparent lattice parameter (ALP) was recalculated assuming $Fm\bar{3}m$ crystal space group from the peak's position which corresponds to the interplanar spacing of certain *(hkl)* plane and is a function of the observed unit cell constant "*a*" and *h, k, l* Miller indices.

CeO_2 structure expanded significantly under sCOOX reaction conditions with respect to state under He atmosphere, from 0.012 to even 0.065 Å for 4 2 0 peak (i.e.: 1.2 - 6.5 pm). The structure expansion detected by X-Ray diffraction was the highest under pure H_2 and equalled 0.88 pm, while under pure CO it was 0.55 pm (see Sections 3.3.2 and 3.3.3).

The large base (He–exposed) ALP value, 5.447 – 5.490 Å, can be also noticed. A close look on the EDP shown in Fig. 84 reveals, that some peaks positions might be established with serious uncertainties, because their amplitudes were low and/or they overlapped with a neighbouring intense peak. This applies mostly to 4 2 0 reflection, for which the obtained ALP difference is the highest.

Additionally, there was no internal temperature probe included in the specimen, as quartz was in PXRD experiments, but supposedly the temperature of the sample did not vary much from the set 400°C. Then, correction for structure thermal expansion down to room temperature, 25°C ($\Delta T = 375°C$), would decrease the ALP values by 0.0165Å, which would be still much higher than the literature value of 5.411 Å.

It was expected that another mechanism was responsible for additional lattice expansion. CeO_2 is a reducible material that starts to convert Ce^{4+} ions to Ce^{3+} under fairly mild favourable conditions. Charging of specimen under the highly energetic electron beam is a known phenomenon [137]. Here, electric charge (precisely: absorbed electrons) accumulated in a ceria particle might result in partial reduction of Ce^{IV} to Ce^{III} and, consequently, to crystal structure expansion (as discussed previously, following [89, 90, 91, 98, 99, 3]). Such a state would be maintained only under electron beam illumination, but research using electron microscope cannot be performed with the beam turned off. The electron beam–stimulated partial reduction of cerium (IV) oxide has been studied already [9, 138]. It was reported that transition of Ce^{4+} to Ce^{3+} ions occurs below 1 minute from the time the irradiation began [8]. Other *in-situ* TEM studies described surface reconstruction of ceric oxide which evolved with time (or actually with the total accumulated electron dose) and the re-entrant faces appeared on the corners of particles [139]. The oxidation state of cerium ions causes even changes in contrast on TEM or STEM images what can serve as a qualitative benchmark for the redox behaviour of CeO_{2-x} particles [140].

If more Ce^{3+} ions were formed inside the ceria particles, it would result in spontaneous redistribution of oxygen vacancies driven by appearing deficit of positive charge. Most probably oxygen anions concentrated near the particle's surface in order to minimise repulsion energy among them [100]. In this way, they became more abundant for gaseous CO, which, as suggested from *in-operando* PXRD studies, tend to bind to them. The equilibrium of oxygen moieties and oxygen vacancies might be shifted towards concentrating oxygen anions on the nanocrystals surface and the detected ALP expansion between He and sCOOX reaction condition should be further increased.

Provided that the equation 32 (Section 3.3.2, [91]) remains valid, the degree of CeO_{2-x} reduction can be calculated, Table 34. First, the structure under helium will be considered. After the temperature correction was introduced, ceria underwent reduction by 2.1 – 6.8 % (see Table). When exposed to reaction conditions, ceric oxide was reduced by further 1.3 - 4.0 %. When those contributions to structure expansion were summed, it occurred that CeO_{2-x} was reduced by no more than 8.5 %. Such a degree of reduction can still be attributed solely to surface effects, as the roughly estimated fraction of atoms building the surface of a 14 nm particle (see Section 3.3.2) was about 10 %. It is expected that the fluorite structure of CeO_{2-x} is preserved for $x < 0.15$ [141].

In-operando electron diffraction studies performed on the $9.4\%_{wt.}$ Au/CeO_2 catalyst in CO oxidation reaction showed the promising potential of this technique. Application of

nanobeam ED may even widen the perspectives of investigation of single nanocrystals with high precision. Parallelly, several difficulties appeared during experiments. Fundamental issues, like effect of electron beam on easily reducible materials, must be deeply studied. Herein, new questions were formed and new opportunities for experiments were opened.

To propose some course of action, partial reduction of CeO_{2-x} will be shortly discussed. One of possible ways to determine, to what extent the electron beam can temporarily convert Ce^{IV} to Ce^{III}, is to compare the fractional molar ratio of these ions under non-aggressive conditions. X-Ray Photoelectron Spectroscopy (XPS, sometime called Electron Spectroscopy for Chemical Analysis, ESCA), seems a good candidate to study the non-influenced sample. It uses "soft" aluminium X-Ray radiation which may be weak enough to preserve the pristine state of cerium ions. Additionally, advanced methods of cerium peaks deconvolution are known [85, 142]. On the other hand, electron beam influenced sample can be studied in the electron microscope itself, provided that it is equipped with Electron Energy Loss Spectrometer (EELS). Accurate analysis of the spectrum should be based on measurements of reference materials containing separately Ce^{IV} and Ce^{III} ions, which should be just a matter of proper choice of compounds resistant to the beam irradiation. If sufficient precision of results is obtained, the answer on how much CeO_2 can be reduced inside the electron microscope should be readily available. The task of EELS investigation has been already covered [8, 139, 141, 143], but up to now collected data were rather qualitative than quantitative.

Table 34. Percentage of partial reduction, *x*, of cerium (IV) oxide, CeO_{2-x}, when heated up to 400°C under He or sCOOX reaction atmosphere compared to the reference structure examined in air at room temperature (RT).

Comparison between:	Percentage of reduction *x* of CeO_{2-x} [%]		
h k l	Air, RT → He, 400°C	He, 400°C → sCOOX, 400°C	Air, RT → sCOOX, 400°C
1 1 1	5.0	1.3	6.3
2 0 0	3.0	1.3	4.3
2 2 0	3.7	2.9	6.6
3 3 1	4.7	2.7	7.4
2 2 2	6.8	1.3	8.1
3 3 1	4.0	3.2	7.2
4 2 0	2.1	7.1	9.2
4 2 2	4.5	4.0	8.5
5 1 1 / / 3 3 3	5.0	2.8	7.8

4. Conclusions

This research was focused on the dynamic structure changes of the surface of heterogeneous catalysts based on nanocrystalline gold. These changes were induced by the chemical reactions running in the presence of the catalysts: stoichiometric oxidation of CO by the molecular oxygen (sCOOX) and preferential oxidation of CO in the presence of H_2 (PROX). Three catalysts containing gold nanoparticles (AuNPs) deposited on different supports: cerium (IV) oxide ($9.4\%_{wt.}$ Au/CeO_2), silica ($7.16\%_{wt.}$ Au/SiO_2) and carbon ($20\%_{wt.}$ Au/C), were selected for this research. The assumed hypothesis suggested that the interaction with adsorbents results in the immediate perturbation of the initially relaxed structure of the catalyst surface. Such perturbations were detected in the PXRD and TEM experiments.

Ceria decorated with AuNPs was the most interesting sample. It was the most efficient catalyst reaching over 80% conversion of CO to CO_2 with high selectivity against H_2O production (in PROX reaction). The PXRD and TEM results confirmed that ceric oxide is an easily-reducible material and even more prone to reduction when neighbouring AuNPs. Ceria crystal lattice expanded under the atmosphere of CO, H_2 and under the electron beam too. Ce^{3+} cation has larger radius than the Ce^{4+} ion, so the detected crystal structure expansion is the bigger, the higher is the concentration of Ce^{3+}. Ceria surface served as a large adsorption site for CO and it bound activated oxygen moieties. Pure CeO_2 was inactive in CO oxidation under studied reaction conditions and remained unaffected by the hydrogen atmosphere at ~150°C.

The Au/SiO_2 and Au/C catalysts, although were found to be less active towards CO oxidation, were vital for the understanding of the reaction mechanism. The reactivity of the catalyst supported on silica was positively influenced by the presence of water vapour in the gas atmosphere. The metal-support interactions (MSI) differed substantially between the reducible semiconducting CeO_2 and non-reducible insulating SiO_2. Despite being the oxide compounds, their role in the COOX reaction mechanism was different as SiO_2 could hardly facilitate CO activation or O_2 dissociation. The Au/C catalyst with its rather inert carbon support was a perfect reference mark of the catalytic activity of the bare gold nanocrystals.

The electron microscopy clearly confirmed the structure expansion of CeO_2 under sCOOX reaction conditions. However, although the imaging conditions were carefully chosen and they did not influence the chemical activity results, the electron beam probably changed temporarily the electronic structure of the irradiated sample – there was evidence that additional part of Ce^{4+} ions in ceria were reduced to Ce^{3+}. Detailed study on and evaluation of this issue is necessary in the future.

Fascinating aspect of this research was the discovery of gold Multiply Twinned Particles (Au MTPs). They were noticed in each catalyst sample. AuNPs were deposited on the supports using three completely different methods which were not optimised regarding the AuNPs shape: deposition-precipitation with subsequent reduction of the $Au(OH)_4^-$ complex (Au/CeO_2); reduction with H_2 of the Au-ethyldiamine complex anchored by ion exchange with the support surface (Au/SiO_2); and immobilisation of the gold particles colloid (Au/C). Au MTPs were directly observed in TEM micrographs (also during *in-operando* experiments) and affected noticeably the X-Ray diffraction patterns. The proper description of all corresponding phenomena was challenging, but successful.

5. References

[1] T. Takei, T. Akita, I. Nakamura, T. Fujitani, M. Okumura, K. Okazaki, J. Huang, T. Ishida, M. Haruta, *Adv. Catal.*, vol. 55, pp. 1-126, 2012.

[2] S. A. Cotton, Chemistry of Precious Metals, London: Blackie Academic and Professional, 1997.

[3] J. A. Rodriguez, G. Liu, T. Jirsak, J. Hrbek, Z. Chang, J. Dvorak, A. Maiti, *J. Am. Chem. Soc.*, vol. 124, no. 18, p. 5242, 2002.

[4] M. Haruta, *CATTECH*, vol. 6, no. 3, p. 102, 2002.

[5] J. T. Miller, A. J. Kropf, Y. Zha, J. R. Regelbuto, L. Delannoy, C. Louis, E. Bus, J. A. van Bokhoven, *J. Catal.*, vol. 240, p. 222, 2006.

[6] S. A. Ansari, M. M. Khan, M. O. Ansari, S. Kalathil, J. Lee, M. H. Cho, *RSC Adv.*, vol. 4, p. 16782, 2014.

[7] U. R. Pillai, S. Deevi, *Appl. Catal. A*, vol. 299, p. 266, 2006.

[8] Y. Ding, Y. C. Pradel, M. Liu, Z. L. Wang, *J. Appl. Phys.*, vol. 120, p. 214302, 2016.

[9] A. C. Johnston-Peck, W.-C. D. Yang, J. P. Winterstein, R. Sharma, A. A. Herzing, *Micron*, vol. 115, p. 54, 2018.

[10] M. Date, M. Okumura, S. Tsubota, M. Haruta, *Angew. Chem. Int. Ed.*, vol. 43, p. 2129, 2004.

[11] K. Tanaka, *Catal. Today*, vol. 154, p. 105, 2010.

[12] M. W. Chase Jr., "NIST-JANAF Thermochemical Tables, Fourth Edition," *J. Phys. Chem. Ref. Data, Monograph*, vol. 9, pp. 1-1951, 1998.

[13] M. Haruta, T. Kobayashi, H. Sano, N. Yamada, *Chem. Lett.*, vol. 16, no. 2, p. 405, 1987.

[14] M. Haruta, *Faraday Discuss.*, vol. 152, p. 11, 2011.

[15] M. S. Scurell, *Gold Bull.*, vol. 50, no. 1, p. 77, 2017.

[16] H. J. Freund, G. Meijer, M. Scheffler, R. Schloegl, M. Wolf, *Angew. Chem. Int. Ed.*, vol. 50, p. 10064, 2011.

[17] P. Mars, D. W. Krevelen, *Chem. Eng. Sci.*, vol. 3, no. 1, p. 41, 1954.

[18] X. Liu, *J. Am. Chem. Soc.*, vol. 24, p. 10251, 2012.

[19] M. A. Saqlain, A. Hussain, M. Siddiq, A. A.Leitao, *Appl. Catal. A*, vol. 519, p. 27, 2016.

[20] Y.-G. Wang, D. C. Cantu, M.-S. Lee, J. Li, V.-A. Glezakou, R. Rousseau, *J. Am. Chem. Soc.*, vol. 138, no. 33, p. 10467, 2016.

[21] T. Ishida, H. Koga, M. Okumura, M. Haruta, *Chem. Rec.*, vol. 16, p. 2278, 2016.

[22] J. Z. Zhang, Q. Kuang, Y. Jiang, Z. Xie, *Nano Today*, vol. 11, no. 5, p. 661, 2016.

[23] E. Bus, J.T. Miller, J.A. van Bokhoven, *J. Phys. Chem. B*, vol. 109, p. 14581, 2005.

[24] A. Corma, M. Boronat, S. Gonzalez, F. Illas, *Chem. Commun.*, p. 3371, 2007.

[25] L. Barrio, P. Liu, J. A. Rodrigez, J. M. Campos-Martin. G. L. J. Fierro, *Chem. Phys.*, vol. 125, p. 64715, 2006.

[26] P. Claus, *Applied Catalysis*, vol. 291, p. 222, 2009.

[27] J. Guzman, B.C. Gates, *Angew. Chem.*, vol. 42, p. 690, 2003.

[28] X. Zhang, F.X. LlabresiXamena, A. Corma, *J. Catal.*, vol. 265, p. 155, 2009.

[29] T. Fujitani, I. Nakamura, T. Akita, M. Okumura, M. Haruta, *Angew.Chem.*, vol. 48, p. 9515, 2009.

[30] G. C. Bond, *J. Mol. Catal. A*, vol. 156, p. 1, 2000.

[31] H. Y. Kim, H. M. Lee, G. Henkelman, *J. Am. Chem. Soc.*, vol. 134, no. 3, p. 1560, 2012.

[32] B. Palosz, *Phase Transitions*, vol. 76, p. 171, 2003.

[33] Z. Kaszkur, M. Zielinski, W. Juszczyk, *J. Appl. Cryst.*, vol. 50, p. 585, 2017.

[34] A. Taneda, Y. Kawazoe, *J. Magn. Soc. Jpn.*, vol. 23, p. 679, 1999.

[35] B. E. Warren, X-Ray Diffraction, Addison-Wesley Publishing Company Inc., 1969.

[36] Z. Kaszkur, *Zeitschrift fuer Kristallographie*, vol. 23, p. 147, 2006.

[37] B. Mierzwa, Z. Kaszkur, "Combined XRD-EXAFS Software Tools for Metal Nanoclusters," in *Applied Crystallography: Proceddings of the XIX Conference*, Singapore, World Scientific Publishing Co. Pte. Ltd., 2003, p. 162.

[38] A. P. Sutton, J. Chen, *Phil. Mag. Lett.*, vol. 61, p. 139, 1990.

[39] Z. Kaszkur, W. Juszczyk., D. Lomot, *Phys. Chem. Chem. Phys.*, vol. 17, p. 28250, 2015.

[40] M. Flueli, R. Spycher, P. A. Stadelmann, P. A. Buffat, J.-P.Borel, *Europhys. Lett.*, vol. 6, no. 4, p. 349, 1988.

[41] A. I. Kirkland, D. A. Jefferson, D. Tang, P. P. Edwards, *Proc. R. Soc. Lond. A: Math. Phys. Sci.*, vol. 434, no. 1891, p. 279, 1991.

[42] Z.-A. Li, M. Spasowa, Q. M. Ramasse, M. E. Gruner, C. Kisielowski, M. Farle, *Phys. Rev. B*, p. 161406, 2014.

[43] C. L. Cleveland, U. Landman, T. G. Schaaf, M. N. Shafigullin, *Phys. Rev. Lett.*, vol. 79, no. 10, p. 1873, 1997.

[44] C. Ling, Y. Yu, *IUCrJ*, vol. 6, p. 447, 2019.

[45] H. Hofmeister, "Fivefold Twinned Nanoarticles," *Encyclopedia of Nanoscience and Nanotechnology*, vol. X, pp. 1-22, 2003.

[46] G. K. Williamson, W. H. Hall, *Acta Metall.*, vol. 1, p. 22, 1953.

[47] B. E. Warren, L. Averbach, *J. Appl. Phys.*, vol. 21, p. 595, 1950.

[48] B. E. Warren, L. Averbach, *J. Appl. Phys.*, vol. 23, p. 497, 1952.

[49] Z. Kaszkur, B. Mierzwa, J . Pielaszek, *J. Appl. Cryst.*, vol. 38, p. 266, 2005.

[50] D. B. Williams, C. B. Carter, Transmission Electron Microscopy. A Textbook for Materials Science, New York: Springer, 2009.

[51] M. Tanaka, "Glosary of TEM Terms," JEOL Ltd., 2019. [Online]. Available: www.jeol.co.jp/en/words/emterms.

[52] P. Brouwer, Theory of XRF, Almelo, The Netherlands: PANalytical B.V., 2006.

[53] R. E. van Grieken, A. A. Markowicz, Handbook of X-Ray Scpectrometry, New York, USA: Marcel Dekker Inc., 2002.

[54] "Microscopy Australia, MyScope Training," Australian Centre for Microscopy & Microanalysis, The University of Sydney, Australia, 2017. [Online]. Available: myscope.training.

[55] M. Zielinski, Master Thesis, Warsaw University of Technology, Faculty of Chemistry, Poland, 2015.

[56] J. Turkevich, P. C. Stevenson, J. Hillier, *Disc. Farad. Soc.*, vol. 11, p. 55, 1951.

[57] K. C. Grabar, K. J. Allison, B. E. Barker, R. M. Bright, K. R. Brown, R. G. Freeman, A. P. Fox, C. D. Keating, M. D. Musick, M. J. Natan, *Langmuir*, vol. 12, no. 10, p. 2353, 1996.

[58] N. Kristian, X. Wang, *Electrochem. Commun. 10 (2008) p.12*, vol. 10, p. 12, 2008.

[59] E. Frota Jr., A. Purgatto, J. J. Linares, *Chem. Eng. Trans.*, vol. 41, p. 253, 2014.

[60] Y. L. Lam, M. Boudart, *J. Catal.*, vol. 50, p. 530, 1977.

[61] B. P. Block, J. C Bailar, *J. Am. Chem. Soc.*, vol. 73, p. 4722, 1951.

[62] W. J. Louw, W. Robb, *Inorg. Chim. Acta*, vol. 3, no. 1, p. 29, 1969.

[63] K. Kitada.US Patent 6087516.

[64] J. Brynestad, Iron and Nickel Carbonyl Formation in Steel Pipes and Its Prevention - Literature survey, Oak Ridge, Tennessee, USA: National Technical Information Service, U.S. Department of Commerce, 1976.

[65] M. Wojdyr, *J. Appl. Cryst.*, vol. 43, p. 1126, 2010.

[66] R.J.Wells, *J. Quant. Spectrosc. Radiat. Transfer*, vol. 62, p. 29, 1999.

[67] L. Levien, C. T. Prewitt, D. J. Weidner, *Am. Mineral.*, vol. 65, p. 920, 1980.

[68] S. Sameshima, M. Kawaminami, Y. Hirata, *J. Ceram. Soc. Jpn.*, vol. 110, no. 7, p. 597, 2002.

[69] S. Stecura, W. J. Campbell, "Thermal Exapnsion and Phase Inversion of Rare-Earth Oxides," *U.S. Dept. of the Interior, Bureau of Mines*, 1961.

[70] Z. Kaszkur, *J. Appl. Cryst.*, vol. 33, p. 87, 2000.

[71] T. P. Martin, T. Bergmann, H. Göhlich, T. Lange, *Z. Phys. D.*, vol. 19, no. 4, p. 25, 1991.

[72] Z. Kaszkur, B. Mierzwa, *Phil. Mag. A*, vol. 77, p. 781, 1998.

[73] W. H. Press, S. A. Teukolsky, W. T. Vetterling, B. P. Flannery, Numerical Recipes, Cambridge University Press, 1986.

[74] P. Debye, *Annalen der Physik*, vol. 351, no. 6, p. 809, 1915.

[75] Mass Spectrometry Data Center, National Institute of Standard and Technology (NIST), USA.

[76] S. N. Foner, R. L. Hudson, *J. Chem. Phys.*, vol. 36, p. 2676, 1962.

[77] M. A. Malecka, L. Kepinski, *J. Microsc.*, vol. 237, no. 3, p. 282, 2010.

[78] C. Koch, "Determination of core structure periodicity and point defect density along dislocations," Dissertation for the degree of Doctor of Philosohy, Arizona State University, 2002.

[79] Protochips Inc., [Online]. Available: www.protochips.com.

[80] Air Liquide Deutschland GmbH, Safety Data Sheet: Carbon Monoxide, 2018.

[81] C. A. Schneider, W. S. Rasband, K. W. Eliceiri, *Nat. Methods*, vol. 9, no. 7, p. 671, 2012.

[82] J. Schindelin, I. Arganda-Carreras, E. Frise, V. Kaynig, M. Longair, T. Pietzsch, S. Preibisch, C. Rueden, S. Saalfeld, B. Schmid, J. Y. Tinevez, D. J. White, V. Hartenstein, K. Eliceiri, P. Tomancak, A. Cardona, *Nat. Methods*, vol. 9, no. 7, p. 676, 2012.

[83] C. Gammer, C. Mangler, C. Rentenberger, H.P. Karnthaler, *Scripta Materialia*, vol. 63, p. 312, 2010.

[84] M. Zhu, I. E. Wachs, *ACS Catal.*, vol. 6, no. 2, p. 722, 2016.

[85] L. Ilieva, P. Petrova, G. Pantaleo, R. Zanella, L. F. Liotta, V. Georgiev, S. Boghosian, Z. Kaszkur, J. W. Sobczak, W. Lisowski, A. M. Venezia, T. Tabakova, *Appl. Catal. B,* vol. 188, p. 154, 2016.

[86] G. C. Bond, C. Louis, D. T. Thompson, Catalysis by Gold. Catalytic Science Series - Vol. 6, Singapore: Imperial College Press, 2006.

[87] W. Mizerski, Tablice chemiczne, Warszawa: Adamantan, 2004.

[88] O. H. Laguna, M. A. Centeno, F. Romero-Sarria, J. A. Odriozola, *Catal. Today.*, vol. 172, p. 118, 2011.

[89] G. Brauer, K. A. Gingerich, *J. Inorg. Nucl. Chem.*, vol. 16, no. 1, p. 87, 1960.

[90] S. R. Bishop, D. Marrocchelli, C. Chatzichristodoulou, N. H. Perry, M. B. Mogensen, H. L. Tuller, E. D. Wachsman, *Annu. Rev. Mater. Res.*, vol. 44, p. 205, 2014.

[91] M. Mogensen, N. M. Sammes, G. A. Tompsett, *Solid State Ionics,* vol. 129, p. 63, 2000.

[92] S. J. Hong, A. V. Virkar, *J. Am. Ceram. Soc.*, vol. 78, p. 433, 1995.

[93] D. Marrocchelli, S. R. Bishop, J. Kilner, *J. Mater. Chem. A,* vol. 1, p. 7673, 2013.

[94] D. Marrocchelli, S. R. Bishop, H. L. Tuller, G. W. Watson, B. Yildiz, *Phys. Chem. Chem. Phys.*, vol. 14, p. 12070, 2012.

[95] D. Marrocchelli, S. R. Bishop, H. L. Tuller, B. Yildiz, *Adv. Funct. Mater.*, vol. 22, p. 1958, 2012.

[96] E. A. Kummerle, G. Heger, *J. Solid Stae Chem.*, vol. 147, p. 485, 1999.

[97] O. S. Bezkrovnyi, P. Kraszkiewicz, M. Ptak, L. Kepinski, *Catal. Commun.*, vol. 117, p. 94, 2018.

[98] S. Tsunekawa, K. Ishikawa, Z.-Q. Li, I. Kawazoe, A. Kasuya, *Phys. Rev. Lett.*, vol. 85, no. 16, p. 3440, 2000.

[99] T. Desaunay, G. Bonura, V. Chiodo, S. Freni, J.-P. Couzinie, J. Bourgon, A. Ringuede, F. Labat, C. Adamo, M. Cassir, *J. Catal.*, vol. 297, p. 193, 2013.

[100] C. Binet, A. Bardi, J.-C. Lavalley, *J. Phys. Chem. C,* vol. 98, p. 6392, 1994.

[101] M. A. Malecka, J. J. Delgado, L. Kepinski, J. J. Calvino, S. Bernal, G. Blanco, X. Chen, *Catal. Today,* vol. 187, p. 56, 2012.

[102] M. Li, X. Wang, F. Cardenas-Lizana, M. A. Keane, *Catal. Today,* vol. 279, p. 19, 2017.

[103] D. Andreeva, V. Idakiev, T. Tabakova, L. Ilievaa, P. Falaras, A. Bourlinos, A.Travlos, *Catal. Today,* vol. 72, p. 51, 2002.

[104] T. Tabakova, F. Boccuzzi, M. Manzoli, D. Andreeva, *Appl. Catal. A,* vol. 252, p. 385, 2003.

[105] M. A. Centeno, C. Portales, I. Carrizosa, J. A. Odriozola, *Catal. Lett.*, vol. 102, no. 3-4, p. 289, 2005.

[106] J. Erkelens, C. Kemball, A. K. Galway, *Trans. Far. Soc.*, vol. 59, p. 1181, 1963.

[107] G. C. Bond, P. A. Sermon, G. Webb, D. A. Buchanan, P. B. Wells, *J. Chem. Soc., Chem. Commun.*, p. 444b, 1973.

[108] J. E. Bailie, G. J. Hutchings, *Chem. Commun.*, p. 2151, 1999.

[109] C. Milone, R. Ingoglia, A. Pistone, G. Neri, F. Frusteri, S. Galvagno, *J. Catal.*, vol.

222, no. 2, p. 348, 2004.
[110] J. A. Rodriguez, P. Liu, J. Hrbek, J. Evans, M. Perez, *Angew. Chem. Int. Ed.*, vol. 46, p. 1329, 2007.
[111] I. X. Green, W. Tang, M. Neurock, J. T. Yates Jr., *Angew. Chem. Int. Ed.*, vol. 50, p. 10186, 2011.
[112] J. C. Frost, *Nature*, vol. 334, no. 6183, p. 577, 1988.
[113] T. Akita, M. Okumura, K. Tanaka, M. Kohyama, M. Haruta, *Catal. Today*, vol. 117, p. 62, 2006.
[114] K. Sun, M. Kohyama, S. Tanaka, S. Takeda, *J. Phys. Chem. C*, vol. 122, p. 9253, 2018.
[115] A. Bongiorno, U. Landman, *Phys. Rev. Lett.*, vol. 95, no. 10, p. 106102, 2005.
[116] T. Fujitani, I. Nakamura, *Angew. Che. Int. Ed.*, vol. 50, p. 10144, 2011.
[117] Y. Maeda, Y. Iizuka, M. Kohyama, *J. Am. Chem. Soc.*, vol. 135, p. 906, 2013.
[118] L. Gu, Y. Zeng, Y. Feng, W. Jiang, W. Ji, H. Arandiyan, C.-T. Au, *ChemCatChem*, 2019, DOI: 10.1002/cctc.201900576.
[119] K. Tanaka, M. Shou, H. He, X. Sie, X. Zhang, *J. Phys. Chem. C*, vol. 113, p. 12427, 2009.
[120] S. Alayoglu, A.U. Nilekar, M. Mavrikakis, B. Eichhorn, *Nat. Mater.*, vol. 7, p. 333, 2008.
[121] K. Tanaka, M. Shou, H. He, C. Zhang, D. Lu, *Catal. Lett.*, vol. 127, p. 148, 2009.
[122] R. W. G. Wyckoff, *Crystal Structures*, vol. 1, pp. 7-83, 1963.
[123] T. Swanson, *Natl. Bur. Stand (U.S.)*, vol. 539, p. 33, 1953.
[124] R. W. G. Wyckoff, *Crystal Structures*, vol. 1, pp. 239-444, 1963.
[125] *JCPDS PDF #34-394*, ICDD.
[126] O. Bondarchuk, S. Shaikhutdinov, H.-J. Freund, *J. Phys. Chem. C*, vol. 123, p. 12376, 2019.
[127] P. Scherrer, "Bestimmung der Grosse und der Inneren Struktur von Kolloidteilchen Mittels Rontgenstrahlen," *Nachrichten von der Gesellschaft der Wissenschaften, Gottingen, Mathematisch-Physikalische Klasse*, vol. 2, p. 98, 1918.
[128] M. J. Walsh, K. Yoshida, A. Kuwabara, M. L. Pay, P. L. Gai, E. D. Boyes, *Nano Lett.*, vol. 12, p. 2027, 2012.
[129] M. J. Walsh, K. Yoshida, P. L. Gai, E. D. Boyes, *J. Phys.: Conf. Ser.*, vol. 241, p. 012058, 2010.
[130] A. Slabon, *IUCrJ*, vol. 6, p. 344, 2019.
[131] T. Akita, M. Okumura, K. Tanaka, M. Kohyama, M. Haruta, *J. Mater. Sci.*, vol. 40, p. 3101, 2005.
[132] L. D. Marks, *Philos. Mag. A*, vol. 49, p. 81, 1984.
[133] L. D. Marks, D. J. Smith, *J. Cryst. Growth*, vol. 54, no. 3, p. 425, 1981.
[134] Y. Kuwauchi, H. Yoshida, T. Akita, M. Haruta, S. Takeda, *Angew. Chem. Int. Ed.*, vol. 51, no. 31, p. 7729, 2012.
[135] W.-C. D. Yang, C. Wang, L. A Fredin, P. A. Lin, L. Shimomoto, H. J. Lezec, R. Sharma, *Nature Mat.*, vol. 18, p. 614, 2019.
[136] S. Ino, *J. Phys. Soc. Jpn.*, vol. 21, p. 346, 1966.
[137] R. F. Egerton, P. Li, M. Malac, *Micron*, vol. 35, p. 399, 2004.

[138] A. C. Johnston-Peck, J. S. DuChene, A. D. Roberts, W. D. Wei, A. A. Herzing, *Ultramicroscopy,* vol. 170, p. 1, 2018.

[139] R. Wang, S. I. Mutinda, *Chem. Phys. Lett.,* vol. 517, p. 186, 2011.

[140] A. C. Johnston-Peck, J. P. Winterstein, A. D. Roberts, J. S. DuChene, K. Qian, B. C. Sweeny, W. D. Wei, R. Sharma, E. A. Stach, A. A. Herzing, *Ultramicroscopy*, vol. 162, p. 52, 2016.

[141] R. Wang, P. A. Crozier, R. Sharma, *J. Phys. Chem. C,* vol. 113, p. 5700, 2009.

[142] A. M. Venezia, L. Liotta, G. Pantaleo, R. Zanella, J. Sobczak, W. Lisowski, *Int. J. Hydrogen Energy*, vol. 44, no. 1, p. 233, 2019.

[143] R. Wang, P. A. Crozier, R. Sharma, J. B. Adams, *Nano Lett.*, vol. 8, no. 3, p. 962, 2008.

I would like to acknowledge:

Zbigniew Kaszkur, PhD., DSc., Assoc. Prof. IPC PAS – supervision, teaching and numerous pieces of advice

Wojciech Juszczyk, PhD. – laboratory and technical support

Ilia Smirnov, MSc. – fruitful discussions and graphical design support

Bogusław Mierzwa, PhD. – data analysis and programming

Dmytro Lisovytskiy, PhD. – technical support

Piotr Dluzewski, PhD., DSc., Assoc. Prof. IP PAS – foundations in electron microscopy (IP PAS, Warsaw, Poland)

Thomas Lunkenbein, Dr. – support in in-operando electron microscroscopy (FHI MPG, Berlin, Germany)

Milivoj Plodinec, PhD. – support in in-operando electron microscroscopy (FHI MPG, Berlin, Germany)

Mark-Georg Willinger, Dr. support in in-operando electron microscroscopy (FHI MPG, Berlin, Germany)

Prof. Christain Ricolleau – support in electron microscroscopy (Université Paris Diderot – Paris 7, France)

Guillaume Wang – support in electron microscroscopy (Université Paris Diderot – Paris 7, France)

Jaysen Nelayah, Assistant Prof. – support in electron microscroscopy (Université Paris Diderot – Paris 7, France)

My parents, Ewa and Slawomir – who I can always count on

Magdalena and Pawel Majewscy, both PhDs – who introduced me to and then supported in the world of science

Without these people, and others that have not been mentioned here, everything would be much more difficult and, certainly, less pleasant.

I would like to acknowledge:

Zbigniew Kaszkur, PhD., DSc., Assoc. Prof. IPC PAS – supervision, teaching and numerous pieces of advice

Wojciech Juszczyk, PhD. – laboratory and technical support

Ilia Smirnov, MSc. – fruitful discussions and graphical design support

Bogusław Mierzwa, PhD. – data analysis and programming

Dmytro Lisovytskiy, PhD. – technical support

Piotr Dluzewski, PhD., DSc., Assoc. Prof. IP PAS – foundations in electron microscopy (IP PAS, Warsaw, Poland)

Thomas Lunkenbein, Dr. – support in in-operando electron microscroscopy (FHI MPG, Berlin, Germany)

Milivoj Plodinec, PhD. – support in in-operando electron microscroscopy (FHI MPG, Berlin, Germany)

Mark-Georg Willinger, Dr. support in in-operando electron microscroscopy (FHI MPG, Berlin, Germany)

Prof. Christain Ricolleau – support in electron microscroscopy (Université Paris Diderot – Paris 7, France)

Guillaume Wang – support in electron microscroscopy (Université Paris Diderot – Paris 7, France)

Jaysen Nelayah, Assistant Prof. – support in electron microscroscopy (Université Paris Diderot – Paris 7, France)

My parents, Ewa and Slawomir – who I can always count on

Magdalena and Pawel Majewscy, both PhDs – who introduced me to and then supported in the world of science

Without these people, and others that have not been mentioned here, everything would be much more difficult and, certainly, less pleasant.